LATE QUATERNARY INDO-PACIFIC CLIMATE: MONSOONS AND WARM CURRENTS

EDITED BY: Hema Achyuthan, Min-Te Chen and Shengfa Liu
PUBLISHED IN: Frontiers in Earth Science

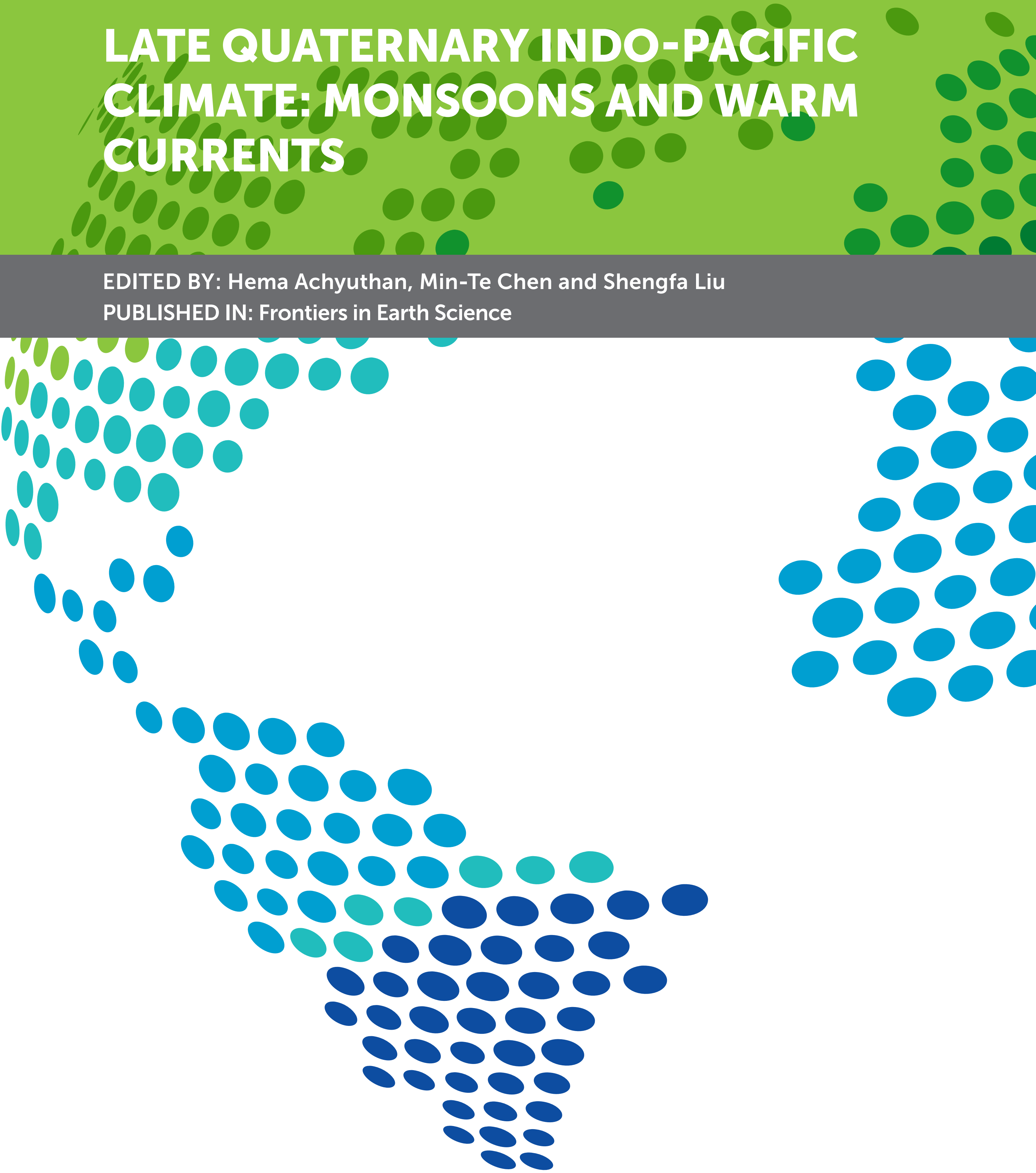

frontiers Research Topics

ISSN 1664-8714
ISBN 978-2-88974-905-8
DOI 10.3389/978-2-88974-905-8

About Frontiers

Frontiers is more than just an open-access publisher of scholarly articles: it is a pioneering approach to the world of academia, radically improving the way scholarly research is managed. The grand vision of Frontiers is a world where all people have an equal opportunity to seek, share and generate knowledge. Frontiers provides immediate and permanent online open access to all its publications, but this alone is not enough to realize our grand goals.

Frontiers Journal Series

The Frontiers Journal Series is a multi-tier and interdisciplinary set of open-access, online journals, promising a paradigm shift from the current review, selection and dissemination processes in academic publishing. All Frontiers journals are driven by researchers for researchers; therefore, they constitute a service to the scholarly community. At the same time, the Frontiers Journal Series operates on a revolutionary invention, the tiered publishing system, initially addressing specific communities of scholars, and gradually climbing up to broader public understanding, thus serving the interests of the lay society, too.

Dedication to Quality

Each Frontiers article is a landmark of the highest quality, thanks to genuinely collaborative interactions between authors and review editors, who include some of the world's best academicians. Research must be certified by peers before entering a stream of knowledge that may eventually reach the public - and shape society; therefore, Frontiers only applies the most rigorous and unbiased reviews.
Frontiers revolutionizes research publishing by freely delivering the most outstanding research, evaluated with no bias from both the academic and social point of view.
By applying the most advanced information technologies, Frontiers is catapulting scholarly publishing into a new generation.

What are Frontiers Research Topics?

Frontiers Research Topics are very popular trademarks of the Frontiers Journals Series: they are collections of at least ten articles, all centered on a particular subject. With their unique mix of varied contributions from Original Research to Review Articles, Frontiers Research Topics unify the most influential researchers, the latest key findings and historical advances in a hot research area! Find out more on how to host your own Frontiers Research Topic or contribute to one as an author by contacting the Frontiers Editorial Office: frontiersin.org/about/contact

LATE QUATERNARY INDO-PACIFIC CLIMATE: MONSOONS AND WARM CURRENTS

Topic Editors:
Hema Achyuthan, Anna University, Chennai, India
Min-Te Chen, National Taiwan Ocean University, Taiwan
Shengfa Liu, First Institute of Oceanography, Ministry of Natural Resources, China

Citation: Achyuthan, H., Chen, M.-T., Liu, S., eds. (2022). Late Quaternary Indo-Pacific Climate: Monsoons and Warm Currents. Lausanne: Frontiers Media SA. doi: 10.3389/978-2-88974-905-8

Table of Contents

frontiers
in Earth Science

ORIGINAL RESEARCH
published: 12 April 2021
doi: 10.3389/feart.2021.631815

Sedimentary Responses to Climate Changes and Human Activities Over the Past 7400 Years in the Western Sunda Shelf

Kaikai Wu[1,2,3], Xuefa Shi[2,3]*, Zhanghua Lou[1]*, Bin Wu[2], Jingrui Li[3], Hui Zhang[2], Peng Cao[2] and Che Abd. Rahim Mohamed[4]

[1] Ocean College, Zhejiang University, Zhoushan, China, [2] Key Laboratory of Marine Geology and Metallogeny, First Institute of Oceanography, Ministry of Natural Resources, Qingdao, China, [3] Laboratory for Marine Geology, Qingdao National Laboratory for Marine Science and Technology, Qingdao, China, [4] Faculty of Science and Technology, National University of Malaysia, Bangi, Malaysia

High-resolution records of grain size, major and trace elements, and Sr-Nd isotopes of Core K17 from the western Sunda Shelf were investigated to evaluate the response of weathering and terrigenous input to climatic changes and human activities over the past 7400 years. Sr-Nd isotopic results indicate that the Kelantan River is the main source of sedimentary material in the study core since the mid-Holocene. Chemical weathering levels are represented by the chemical index of alteration (CIA), α^{Al}Na, and K_2O/Al_2O_3 ratios; and geochemical and grain size proxies (including TiO_2/CaO, Rb/Sr ratios, and grain size end-member) were used to establish variations of terrigenous input into the study core since 7400 cal yr BP. Based on these records, the evolution of weathering and terrigenous input processes in the western Sunda Shelf can be divided into four stages. During stage 1 (7400–3700 cal yr BP), increasing precipitation and decreasing temperature jointly balanced the relatively stable weathering and terrigenous sediment supply. Dramatically decreasing weathering rates were consistent with less rainfall and lower temperatures during stage 2 (3700–2600 cal yr BP). Heavy rainfall played a more important role than low temperature in controlling weathering and erosion, leading to increasing terrigenous input in stage 3 (2700–1600 cal yr BP). Because of the decoupling between weathering, erosion, and climate in the late Holocene (stage 4, since 1600 cal yr BP), increasing agriculture and related human activities likely dominated weathering and erosion relative to climate changes. Furthermore, the initial time at which human activity overwhelmed natural processes in the southern South China Sea (SCS) is similar to that in the northern SCS. Our results highlight that human activities during the past 1600 years have gradually overwhelmed natural climatic controls on weathering and erosion processes in the western Sunda Shelf.

Keywords: geochemistry, climate change, human activity, weathering, Sunda Shelf

OPEN ACCESS

Edited by:
Min-Te Chen,
National Taiwan Ocean University,
Taiwan

Reviewed by:
Nadia Solovieva,
University College London,
United Kingdom
Pai-Sen Yu,
Taiwan Ocean Research Institute,
Taiwan
Shiming Wan,
Institute of Oceanology, Chinese
Academy of Sciences (CAS), China

****Correspondence:***
Xuefa Shi
xfshi@fio.org.cn
Zhanghua Lou
iwr@zju.edu.cn

Specialty section:
This article was submitted to
Quaternary Science, Geomorphology
and Paleoenvironment,
a section of the journal
Frontiers in Earth Science

Received: *21 November 2020*
Accepted: *25 March 2021*
Published: *12 April 2021*

Citation:
Wu K, Shi X, Lou Z, Wu B, Li J,
Zhang H, Cao P and
Rahim Mohamed CA (2021)
Sedimentary Responses to Climate
Changes and Human Activities Over
the Past 7400 Years in the Western
Sunda Shelf.
Front. Earth Sci. 9:631815.
doi: 10.3389/feart.2021.631815

INTRODUCTION

Continental weathering and erosion are critical processes controlling the delivery of sediments and solutes from the land to the ocean, shaping the terrestrial landscape, and regulating atmospheric CO_2 (Raymo and Ruddiman, 1992; Bi et al., 2015; Wan et al., 2015; Hu et al., 2020). Climate is a critical factor influencing weathering and erosion, because warm and humid conditions can typically enhance weathering intensity and erosion rates (White and Blum, 1995; West et al., 2005; Hu et al., 2020). Additionally, anthropogenic processes can alter landscapes and result in weathering and erosion pattern changes (Hu et al., 2013; Huang et al., 2018). Acquiring knowledge about the interactions between past climate, human activity, and weathering and erosion changes is important for comparing and understanding the present and future interactions among these systems (Huang et al., 2018).

Some studies on the interaction between climate change, human activities, and weathering and erosion have been performed in different locations in the northern South China Sea (SCS) regions and around the world (Corella et al., 2013; Hu et al., 2013; Wan et al., 2015; Huang et al., 2018). A general consensus is that human activities have dramatically influenced the natural environment and overwhelmed climate signals in sedimentary archives during the late Holocene (Wan et al., 2015; Huang et al., 2018). However, for the southern SCS, anthropogenic impacts have not been distinguished from natural variability in tropical Southeast Asia (Tan et al., 2019).

The Southeast Asia, located in tropical region, is characterized by intense rainfall and high temperatures that generally provide the highest global weathering and erosion rates (McLennan, 1993; Milliman et al., 1999; Liu et al., 2012), and thus it makes Southeast Asia a natural laboratory for studying the interactions between climate change, human activities, and weathering and erosion. As the largest low-latitude continental shelf, the Sunda Shelf is a huge sink of terrigenous sediments from rivers on surrounding regions due to its extremely low gradient (Hanebuth et al., 2011). Located in the central part of Southeast Asia, the Malay Peninsula yields and discharges large amounts of sediments by small mountainous rivers into the Sunda Shelf, up to ca. 35 Mt/yr (Liu et al., 2012), making the Peninsula an important provenance for the southern SCS region (Liu et al., 2016; Jiwarungrueangkul et al., 2019b; Wu et al., 2019). Moreover, the fluvial discharge in this region is largely influenced by the Asian–Australian monsoon, which influences rainfall and temperature through seasonal changes (Wang et al., 2011; Liu et al., 2012). Marine sediments record abundant environmental change signals during production, transportation, and deposition, including tectonics, climate, and human activities (Li et al., 2019). Studying the response of sedimentary records to rainfall and temperature in the western Sunda Shelf is of great significance for understanding the evolution characteristics of tropical monsoon in the geological history. Furthermore, the Sunda Shelf is located in the intersection of the Indian Ocean and the Pacific Ocean, and the ocean circulation system is very complex and interconnected, which is important for the study of the inter-oceanic material and energy cycle (Wu et al., 2020). Additionally, human activities, such as agriculture, began in peninsular Malaysia at least 2000 years ago (Liang et al., 2011) and influenced natural river sediment compositions and sediment yields (Kamarudin et al., 2015; Wang et al., 2017). Exploring long-term climate change and the impact of human activity on past weathering and erosion rates in the Peninsula will improve our understanding of landscape dynamics (Hu et al., 2020). High-resolution sedimentary archives from the western Sunda Shelf may shed light on the details of the complicated interaction of climate changes, human activities, and weathering and erosion in the Southeast Asia.

Numerous studies on the Sunda Shelf primarily focus on the impact of sea level change on sedimentary processes and biogeography evolution since the Last Glacial Maximum (Pelejero et al., 1999; Hanebuth et al., 2000, 2011; Voris, 2000; Steinke et al., 2003). Since ca. 7–8 ka, the coastline reached its modern position, and sea level was relatively stable with little fluctuation (Steinke et al., 2003); therefore, the impact of sea level on sedimentation was negligible. Estuary and coastal deposits formed when sea level was at its latest transgressional and highstand stages since 8 ka (Hanebuth et al., 2011; Zong et al., 2012). Thus, the estuary/coastal region is an ideal location to preserve records of regional erosion and weathering in the tropical Malay Peninsula influenced by climate change and human activities since the mid-Holocene on the western Sunda Shelf. However, well-preserved records for the middle and late Holocene in the western Sunda Shelf are scarce.

In this study, we present high-resolution grain size, major and trace element geochemistry, and Sr-Nd isotopes from Core K17 from the inner Sunda Shelf in the southern SCS. The primary objective is to evaluate sediment provenance and to explore the interactions between climate changes, human activities, and weathering and erosion on the western Sunda Shelf over the past 7400 years.

REGIONAL SETTING

The Kelantan River, located in the northeastern Malay Peninsula (**Figure 1B**), is the second largest river on the Peninsula with a length of 335 km and flows from south to north into the SCS. It originates from the "Main Range" of the peninsular Malaysia near Gunong Korbu at an elevation of approximately 2100 m, and its gradient drops less than 100 m over the last 100 km (Koopmans, 1972). The river has a drainage area of 12,691 km^2, mean annual rainfall of 2500 mm, mean annual runoff of 1500 mm, and mean sediment load of 13.9×10^6 t (Liu et al., 2012; **Table 1**). Principal surrounding rivers include the Chao Phraya (Thailand), Mekong (Indochina Peninsula), and Pahang (peninsular Malaysia).

As a part of Sundaland, peninsular Malaysia has been tectonically stable since the Mesozoic, with few strong tectonic activities (Hutchison, 1968). Topographically, 90% of the coastal plain is less than 75 m above mean sea level. Most river drainage is covered by Quaternary alluvium; the Mesozoic granites underlie the alluvial coastal plain and outcrop on both sides of the Kelantan River Valley (Awadalla and Noor, 1991).

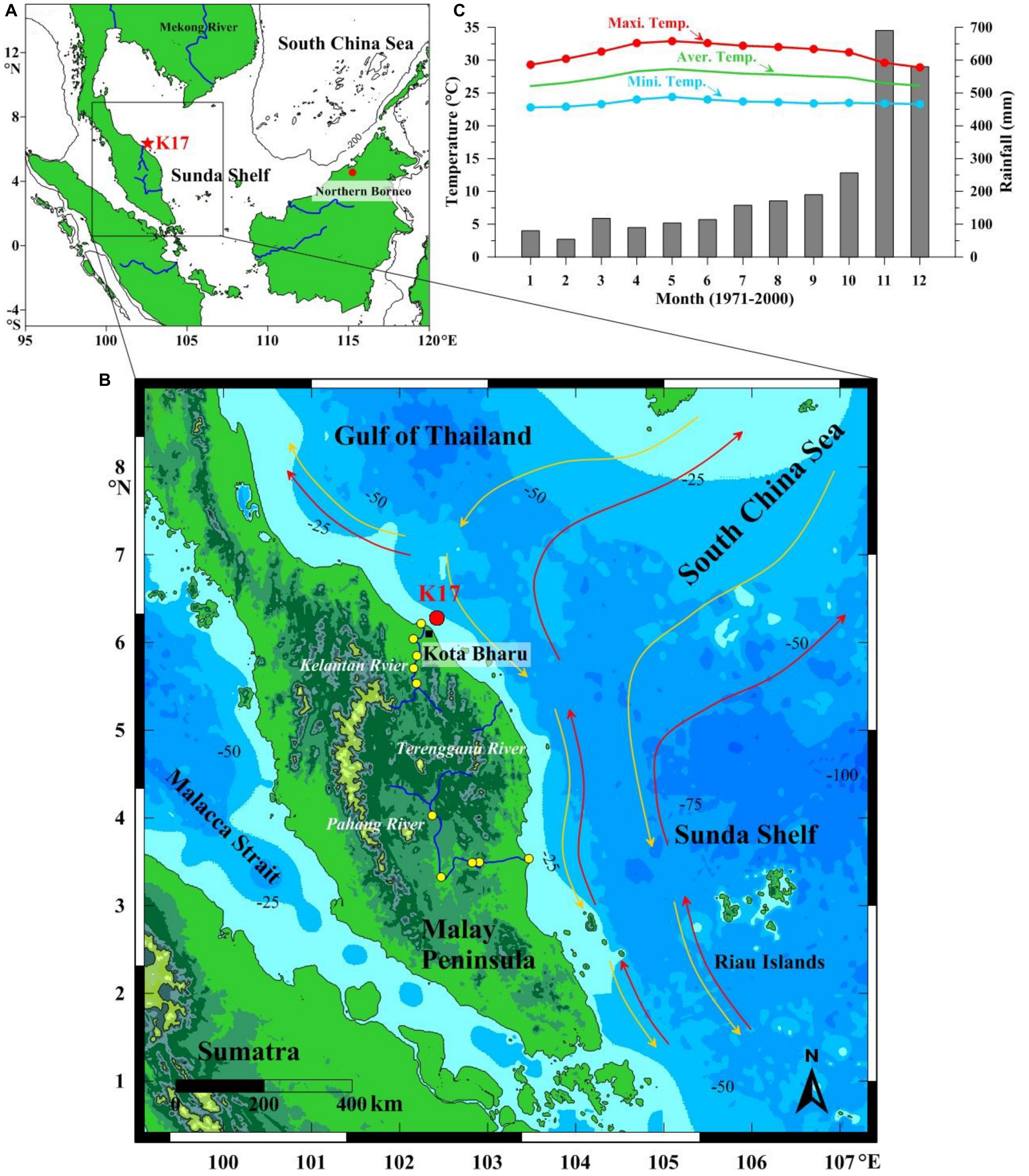

FIGURE 1 | (A) Locations of K17 (red star) and paleoclimate records from stalagmites (red dots) referenced in the text: Northern Borneo (Partin et al., 2007). **(B)** Geographic setting and prevalent hydrography of the western Sunda Shelf. Hydrography was modified from Tangang et al. (2011). The red and yellow arrows show the southwest and northeast monsoon currents, respectively. The locations of Core K17 and Sr-Nd sites of Kelantan and Pahang rivers are exhibited by red dot and yellow dots, respectively. **(C)** Regional monthly average precipitation (gray bars) and temperature over Kota Bharu from 1971 to 2000. Temperature and rainfall data are from the World Weather Information Service (http://www.worldweather.org).

Various types of Paleozoic sedimentary and metamorphic rocks are found between the eastern and western granitic masses. Shale and quartzite are the predominant sedimentary rock types (Awadalla and Noor, 1991).

The climate in peninsular Malaysia is controlled by the East Asian–Australian monsoon (Wang et al., 2005, 2011; Liu et al., 2012) with small seasonal temperature variations (**Figure 1C**) but substantially different characteristics between

TABLE 1 | Basic information of main rivers drained into the western Sunda Shelf (Liu et al., 2012, 2016).

River name	Length (km)	Annual rainfall (mm)	Drainage area (km^2)	Annual runoff (mm/year)	Suspended sediment discharge (Mt/year)
Kelantan River	280	875	12,691	1500	13.9
Pahang River	459	2170	29,300	947	20.4
Mekong River	4180	1570	790,000	590	160
Chao Phraya River	1252	1487.3	160,000	188	11

the wet and dry seasons (Wang et al., 2011). From October to January, the region is controlled by the southwesterly East Asian monsoon and receives abundant rainfall (the wet season) (**Figure 1C**). In other periods, the river basin is controlled by the northeasterly Australian monsoon, and the weather is relatively dry with less precipitation (the dry season) (Liu et al., 2012).

The water depth of the Kelantan River estuary ranges from 5 to 25 m, and the slope of the sea floor adjacent to the estuary is extremely gentle. Furthermore, the surface circulation in the southern SCS is primarily controlled by the monsoon (Tangang et al., 2011; **Figure 1B**). The entire southern SCS experiences cyclonic circulation during the northeast monsoon period (winter), whereas the surface current direction is opposite during the southwest monsoon period (summer) (Tangang et al., 2011). Tides are irregular with diurnal to semidiurnal tides (1.5:1). The mean spring range and maximum tidal range are 0.6 and 1.2 m, respectively (Raj et al., 2007).

MATERIALS AND METHODS

Materials

The gravity Core K17 (6.2°N, 102.34°E; 133 cm) was collected at a water depth of 11.4 m on the Kelantan River estuary of the northeastern Malay Peninsula during the R.V. DISCOVERY cruise in 2017 (**Figure 1**). The lithology of Core K17 is primarily olive gray homogeneous silt and sandy silt in the upper 10 cm (**Figure 2**). The lower section from a depth of 10–50 cm is composed of olive gray and dark greenish interlaid sandy silt with a 6 cm thick high sand and a biological debris layer between depths of 36 and 42 cm; below 42 cm to the base, the core primarily consists of dark greenish gray homogeneous sandy

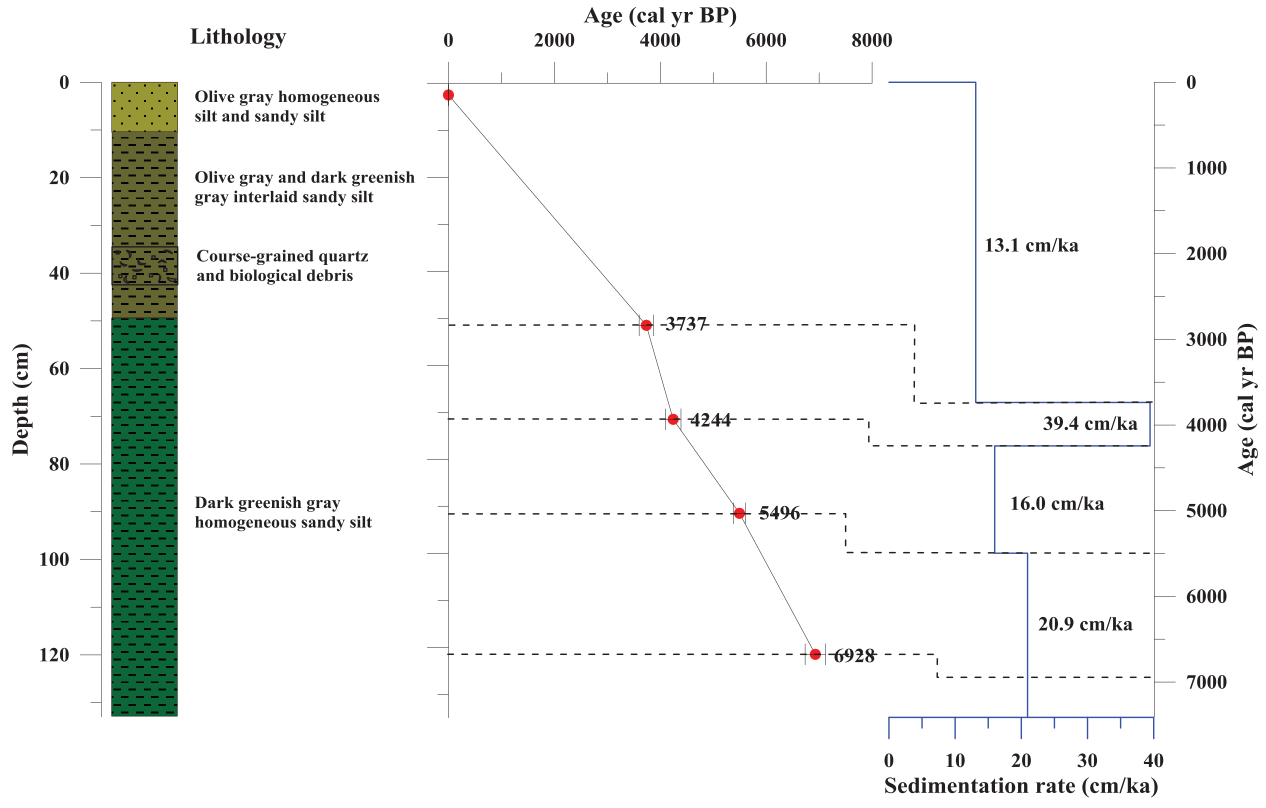

FIGURE 2 | Lithology and age model of Core K17 showing lithological description, foraminiferal AMS ^{14}C dating, and sedimentation rate.

silt (42–133 cm). A total of 132 samples were subsampled at 1 cm intervals for grain size, geochemical elements, and Sr-Nd isotope analyses.

AMS^{14}C Analyses

The chronology of Core K17 was established using AMS^{14}C data (**Figure 2** and **Table 2**). Because of the estuarial location and low carbonate content (<10%), there were few planktonic foraminifera. We picked more than 4 mg of mixed benthic foraminiferal species for five samples from the core. The raw radiocarbon ages were corrected for a local reservoir age of −15 ± 38 years (Southon et al., 2002) and converted to calendar ages using Calib Rev 7.0.4 (Reimer et al., 2013). The AMS^{14}C dating was performed at the Beta Analytic Laboratory, United States.

Grain Size Analyses

The grain size distribution of 132 samples of Core K17 was determined using a Malvern 2000 Mastersizer Particle Size Analyzer with a measurement range and resolution of 0.02–2000 μm and 0.01 Φ, respectively, at the First Institute of Oceanography (FIO), Ministry of Natural Resources (MNR), Qingdao, China. Bulk sediments were treated with an excess of 30% H_2O_2 and 3 mol/L HCl for 24 h at 25°C to remove organic matter and carbonates, respectively. Then, the samples were washed with distilled water until excessive H_2O_2 and HCl were completely removed before measurement. The relative error of the repeated measurements was less than 3%.

Geochemical Element Analyses

The geochemical element concentrations of 122 samples of Core K17 were analyzed using inductively coupled plasma optical emission spectrometry (ICP-OES; SiO_2, Al_2O_3, K_2O, Na_2O, Fe_2O_3, TiO_2, MgO, CaO, P_2O_5, MnO, and Sr) and inductively coupled plasma-mass spectrometry (ICP-MS; Rb, Cu, and Pb) at FIO. Approximately 50 mg of ground bulk sediment was digested with ultrapure HNO_3 and HF (1:1) in a Teflon digestion tank at 195°C for 48 h before measurement (Li et al., 2019). The standard material GSD-9 was assessed once after every 10 samples to provide quality control of accuracy and precision, and the relative standard deviations of analyzed elements were less than 5%.

Sr-Nd Isotope Analyses

The Sr and Nd isotopes of 10 decarbonated samples of Core K17 were determined using a Thermo Scientific multi-collector-inductively coupled plasma-mass spectrometer (MC-ICP-MS Nu plasma) at FIO. The samples were decarbonated using 0.25 N acetic acid and centrifuged and rinsed three times using Milli-Q purified water to eliminate traces of the carbonate fraction. Subsequently, the samples were completely dissolved in a $HF–HNO_3–HClO_4$ mixture (Li et al., 2018). Sr and Nd isotopes were extracted from the solution using a standard ion-exchange procedure. $^{88}Sr/^{86}Sr = 0.1194$ and $^{146}Nd/^{144}Nd = 0.7219$ were adopted to calibrate the mass bias during the Sr and Nd isotope measurements, respectively. Repeated analyses of the NBS987 standard yielded $^{87}Sr/^{86}Sr = 0.71031 \pm 0.00000777$ (1σ), and the JNdi-1 standard yielded $^{143}Nd/^{144}Nd = 0.512115 \pm 0.00000556$ (1σ), which is well within the recommended range.

RESULTS

Chronological Framework

The ages of this downcore were calculated by linear interpolation among five dated sediment layers, and the basal age was 7400 cal yr BP (**Figure 2**), which was calculated by linear extension after 6298 cal yr BP based on the same sedimentary rate with upper section under similar sedimentary environment. The ages were reported in years before present (yr BP). The linear sedimentation rates vary in the range of 13–39 cm/ka, with an average of 18 cm/ka (**Figure 2**). The sedimentation rates of the Middle Holocene (average 22 cm/ka) were relatively higher than those during the Late Holocene (average 13 cm/ka), and the highest sedimentation rate occurred during 3700–4200 cal yr BP, with a value of 39 cm/ka. The average time resolution of Core K17 was 56 yr/cm.

Grain Size Compositions and End-Member Extraction

The sediment fractions of the studied core are primarily silt (37–82%), with a secondary amount of sand (5–51%) and clay (4–25%) (**Figure 3**). According to Folk's classification (Folk et al., 1970), the sediment types are characterized by sandy silt, similar to the western Sunda Shelf (Wu et al., 2020). The mean grain size (Mz) of this downcore ranges from 3.4 to 6.8 Φ (average of 5.4 Φ). The sorting coefficient varies from 1.3 to 3.2, which is classified as poorly sorted. The mean grain size and sorting coefficient show a sudden increase of approximately 2900 cal yr BP (**Figure 3**).

TABLE 2 | AMS^{14}C dating age model of Core K17.

Depth (cm)	Sample ID	Sample material	Conventional AMS^{14}C age (yr BP)	Calendar age (cal yr BP)	Depth interval (cm)	Sedimentation rates (cm/ka)
2-3	Beta-505054	Foraminifera	103.55 ± 0.39 pMC	0	0–2.5	0
51-52	Beta-505056	Foraminifera	3780 ± 30	3737	2.5–51.5	13.1
71-72	Beta-505057	Foraminifera	4150 ± 30	4244	51.5–71.5	39.4
91-92	Beta-505058	Foraminifera	5130 ± 30	5496	71.5–91.5	16.0
121-122	Beta-505060	Foraminifera	6410 ± 60	6928	91.5–121.5	20.9

pMC, percent modern carbon.

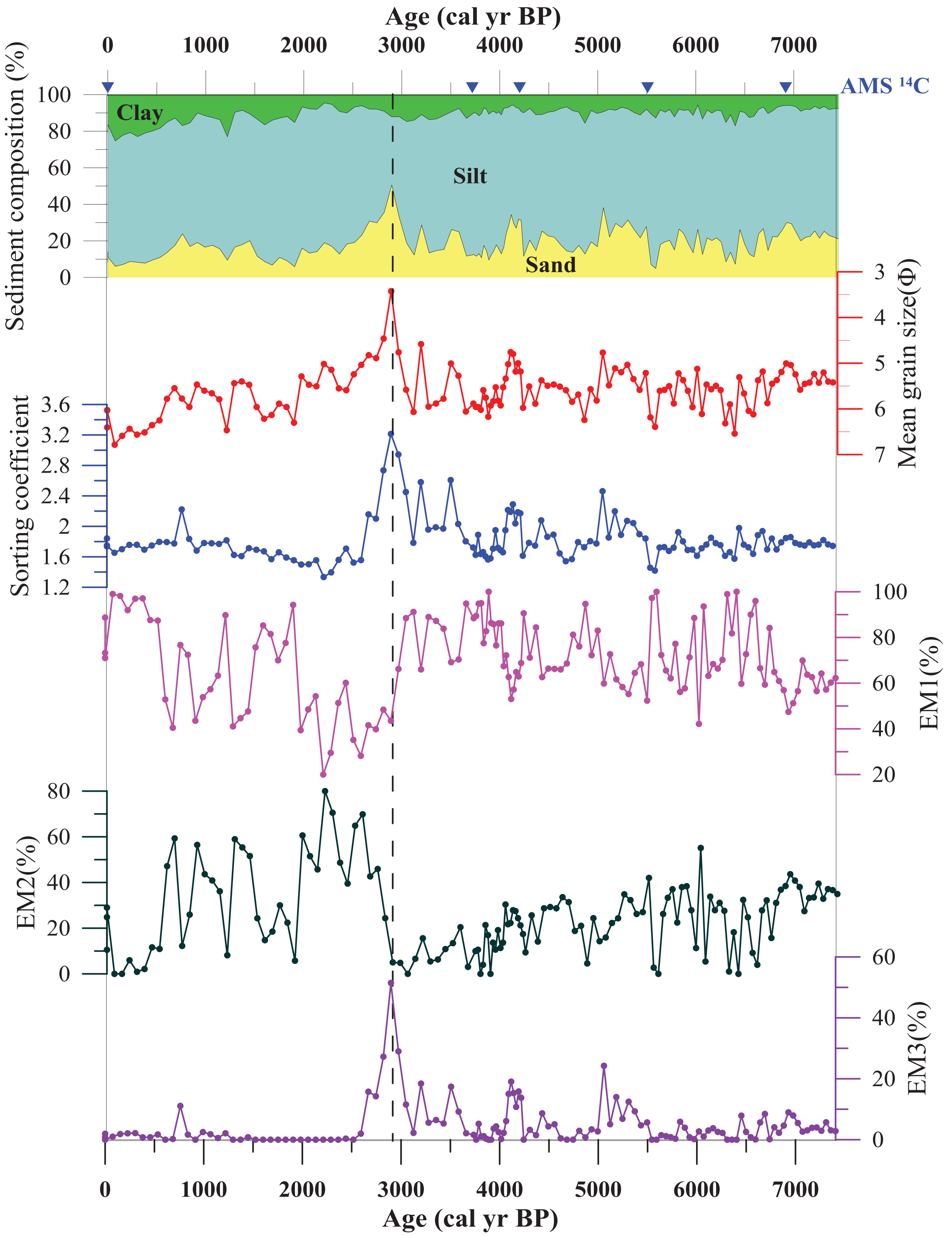

FIGURE 3 | Variations in grain size of Core K17.

An inversion algorithm was used to extract grain size end-members (Joussain et al., 2016; Li et al., 2019), and the results display a three-end-member model that explains more than 95% of the variance (**Figure 4A**). The fine end-member EM1 varies widely range of −0.9 to 10.4 Φ and explains more than 80% of the variance (**Figure 4B**). EM2 varies within the wide size range between 1.37 and 8.4 Φ, and the coarse end-member EM3 varies in the size range from −0.9 to 5.7 Φ. The proportions of the finest end-member EM1 vary in a large range from 20 to 100% (average ∼70%) (**Figure 3**), and the proportions of the EM2 vary from 0 to 80% (average ∼25%). The coarsest end-member EM3 varies between 0 and 51% with an average value of ∼5%. EM1 and EM2 display opposite patterns from the mid-Holocene to the present (**Figure 3**). The EM3 variation shows a generally similar trend compared with the mean grain size.

Geochemical Element Concentrations

The major and trace elements of Core K17 sediment are illustrated in **Figure 5**. Major elements include SiO_2 (48.9–82.1%), Al_2O_3 (3.7–15.4%), CaO (2.1–19.1%), K_2O (0.8–2.2%), Na_2O (0.5–1.6%), and TiO_2 (0.3–0.9%); trace elements are Rb (54.8–118.0 μg/g), Sr (116.4–726.4 μg/g), Cu (5.6–17.4 μg/g), and Pb (19.8–51.4 μg/g). The temporal patterns of Al_2O_3, K_2O, Na_2O, TiO_2, Rb, Pb, and Cu are basically similar in their distribution (**Figure 5**), having a drastic decrease of approximately 2900 and 3900 cal yr BP; SiO_2 displays almost the opposite character to those elements, and CaO and Sr have similar temporal distribution patterns, with an abrupt change of 2600 cal yr BP.

Sr-Nd Isotopic Compositions

The $^{87}Sr/^{86}Sr$ and εNd values of the silicate fraction of Core K17 are listed in **Table 3**. The $^{87}Sr/^{86}Sr$ ratios ranged from 0.72018 to 0.72636, and the εNd values varied from −10.28 to −7.06. The $^{87}Sr/^{86}Sr$ ratios exhibited a slight decreasing tendency, and the εNd values showed no significant variation during the studied timescale, except for one point (1–2 cm) of the core.

DISCUSSION

Provenance Discrimination

Sr-Nd isotopes are one of the widely used proxies to determine sediment provenance (Wei et al., 2012; Cao et al., 2015). However, the isotopic composition of marine sediments could be affected by authigenic, biogenic, and grain-size effects during the transport and deposition processes (Bayon et al., 2002; Dou et al., 2012; Hu et al., 2020) and, therefore, should be eliminated before using Sr-Nd isotopes to trace provenance.

Although the grain-size effect is very common for geochemical compositions (Wu et al., 2019), the $^{87}Sr/^{86}Sr$ ratios and εNd values are not significantly correlated with mean grain size (**Figure 6A**), indicating that the grain-size effect is negligible for Sr-Nd isotopes. Furthermore, there are no significant correlations between the $^{87}Sr/^{86}Sr$ and εNd values and the Fe_2O_3 values in this core sediment (**Figure 6B**), suggesting that authigenic Fe oxides or oxyhydroxides have little influence on isotopic composition. $^{87}Sr/^{86}Sr$ ratios are possibly controlled by the carbonate content, resulting from the isomorphic substitution between Ca in calcium carbonate and Sr from seawater (Hu et al., 2013). However, a very low correlation is observed between the $^{87}Sr/^{86}Sr$ ratios and CaO values (**Figure 6C**). Therefore, Sr-Nd isotopic compositions of these core sediments are considered reliable for tracing sediment provenances at the study site.

The potential sediment sources surrounding Core K17 include the Kelantan River and Pahang River in the Malay Peninsula, the

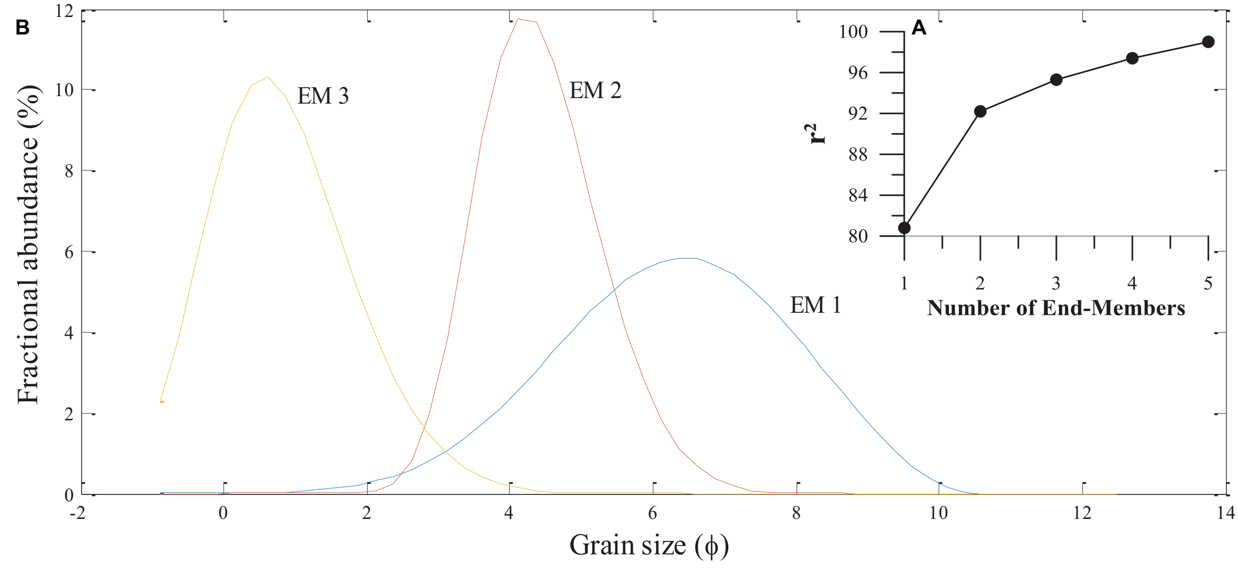

FIGURE 4 | (A) Fraction of data variance explained by the unmixing model vs. numbers of end-members. **(B)** Volume percent vs. grain-size (Φ) diagram of the three end-members (EM1, EM2, and EM3) identified in Core K17.

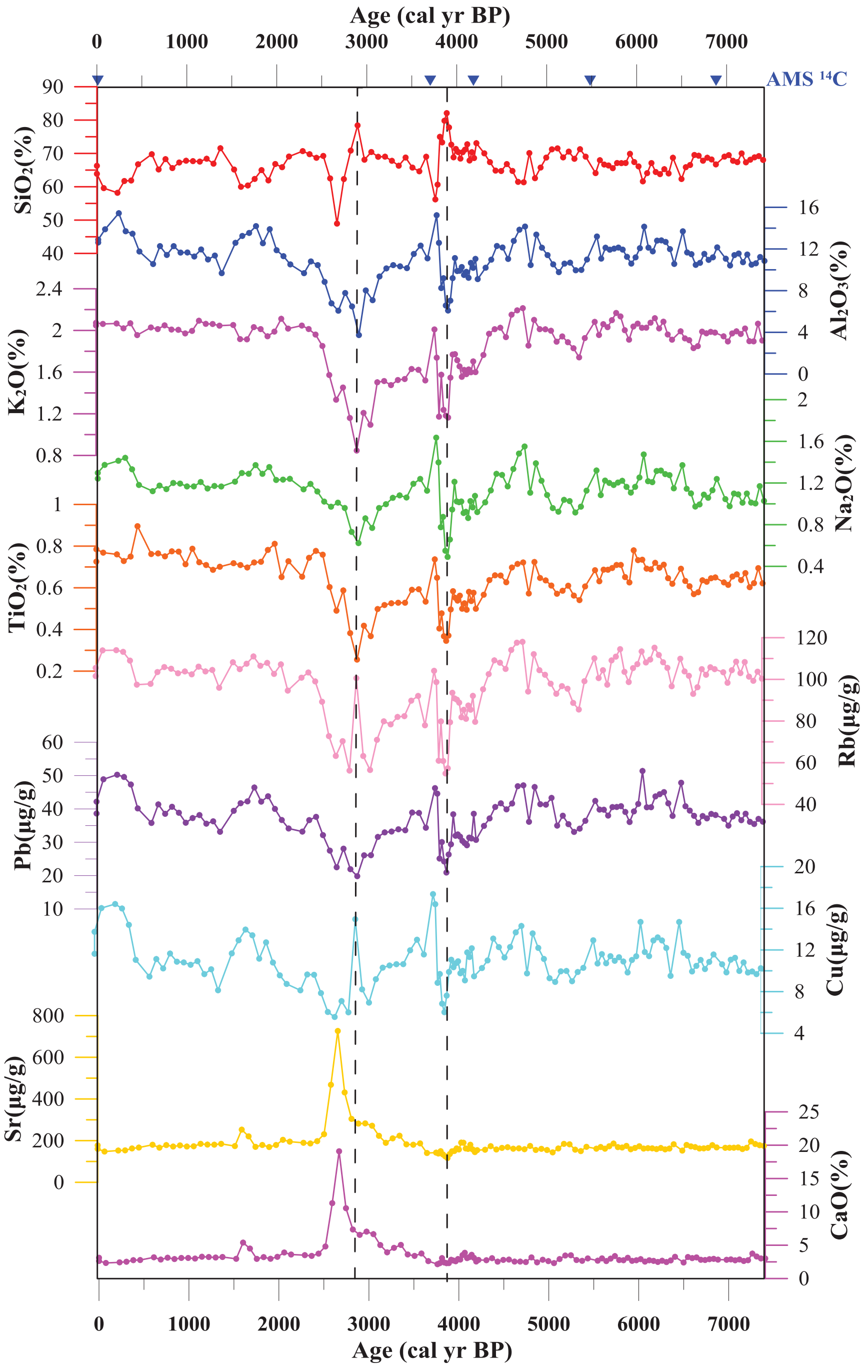

FIGURE 5 | Variations in major and trace elements of Core K17.

Mekong River in the Indochina Peninsula, the Chao Phraya River and other rivers in the Gulf of Thailand, and rivers in Borneo. The ^{87}Sr/^{86}Sr ratios are plotted against εNd values in Core K17 and potential provenances in the surrounding regions (**Figure 7**). Most of the εNd values and ^{87}Sr/^{86}Sr ratios of Core K17 are concentrated in the range of the Kelantan River, whereas the other three points fall in the field of the Mekong River, close to the range of the Kelantan River in **Figure 7**.

It seems that both the Kelantan River and Mekong River are the sediment sources of the Core K17. These three samples all fall in or close to the overlapping part of Kelantan River and Mekong River, which are 10–11, 20–21, and 30–31 cm sediment layers, respectively. The grain sizes of these three samples are coarser than the average grain size of other Sr-Nd sediment layers in this core. Sr-Nd values from other older samples all fall in the Kelantan River. Therefore, these three coarser samples may not

TABLE 3 | Sr and Nd isotopes of sediments in the Core K17 and potential river end members.

Sediment location	Depth (cm)	Age (cal yr BP)	^{87}Sr/^{86}Sr	^{143}Nd/^{144}Nd	ε Nd	Data sources
K17	1–2	0	0.72636	0.512276	−7.06	This study
K17	10–11	610	0.72066	0.512111	−10.28	This study
K17	30–31	2135	0.72056	0.512117	−10.16	This study
K17	40–41	2898	0.72018	0.512119	−10.12	This study
K17	50–51	3660	0.72151	0.512157	−9.38	This study
K17	70–71	4218	0.72150	0.512140	−9.71	This study
K17	80–81	4807	0.72150	0.512158	−9.36	This study
K17	100–101	5925	0.72093	0.512139	−9.73	This study
K17	120–121	6880	0.72101	0.512153	−9.46	This study
K17	130–131	7358	0.72196	0.512131	−9.89	This study
Kelantan River	Surface	_	0.72031	0.512132	−9.87	This study
Kelantan River	Surface	_	0.72307	0.512202	−8.51	This study
Kelantan River	Surface	_	0.72971	0.512225	−8.06	This study
Kelantan River	Surface	_	0.72721	0.512206	−8.43	This study
Kelantan River	Surface	_	0.72285	0.512285	−6.89	This study
Pahang River	Surface	_	0.74043	0.512130	−9.91	This study
Pahang River	Surface	_	0.74230	0.512128	−9.95	This study
Pahang River	Surface	_	0.73603	0.512141	−9.69	This study
Pahang River	Surface	_	0.74255	0.512156	−9.40	This study
Pahang River	Surface	_	0.74366	0.512136	−9.79	This study
Tha Chin River	Surface	_	0.720434	0.511878	−14.82	Wu et al., unpublished
Tha Chin River	Surface	_	0.734096	0.511903	−14.33	Wu et al., unpublished
Mae Klong River	Surface	_	0.753236	0.511820	−15.95	Wu et al., unpublished
Mae Klong River	Surface	_	0.743226	0.511840	−15.56	Wu et al., unpublished
Bang Pakong River	Surface	_	0.716848	0.512086	−10.77	Wu et al., unpublished
Bang Pakong River	Surface	_	0.719631	0.512132	−9.87	Wu et al., unpublished
Chao Phraya River	Surface	_	0.722863	0.512055	−11.36	Wu et al., unpublished
Chao Phraya River	Surface	_	0.718993	0.512067	−11.15	Wu et al., unpublished
Mekong River	Surface	_	0.720276	0.512131	−9.89	Liu et al., 2007
Mekong River	Surface	_	0.720699	0.512115	−10.2	Liu et al., 2007
Mekong River	Surface	_	0.721307	0.512082	−10.85	Liu et al., 2007
Mekong River	Surface	_	0.722173	0.512104	−10.42	Liu et al., 2007
Mekong River	Surface	_	0.721801	0.512098	−10.53	Liu et al., 2007
Offshore Borneo	Surface	_	0.717031	0.512216	−8.23	Wei et al., 2012
Offshore Borneo	Surface	_	0.709882	0.512282	−6.95	Wei et al., 2012
Offshore Borneo	Surface	_	0.715360	0.512200	−8.54	Wei et al., 2012
Offshore Borneo	Surface	_	0.720602	0.512189	−8.76	Wei et al., 2012
Offshore Borneo	Surface	_	0.719912	0.512191	−8.72	Wei et al., 2012

eNd = 10,000 × (^{143}Nd/^{144}Nd/0.512638−1).

be transported from the Mekong River. In fact, the Core K17 is close to the Kelantan estuary; approximately 13.9 Mt/year of sediment from the Kelantan River is discharged into the SCS (Liu et al., 2016), most of which is deposited in the estuary, with the remainder transported to the western Sunda Shelf (Koopmans, 1972; Wang et al., 2020). Our recent work used geochemical and mineral evidence to reveal that fine-grained modern sediment from the Kelantan River can be transported to the central Sunda Shelf (Wu et al., 2020). Although the Mekong River delivers approximately 160 Mt/year to the SCS, approximately 80% of the Mekong-delivered sediment is trapped within the delta area (Xue et al., 2010). Large amounts of Mekong River sediments are deposited near the Mekong River mouth in summer, and only a small fraction of these sediments are re-suspended and dispersed toward the southwest into the Gulf of Thailand during the northeast monsoon (Xue et al., 2012). During the last glacial period with a low relative sea level, sediments from the Mekong River were directly input into the southern SCS by the paleo-Mekong River and not discharged into the Sundaland (Jiwarungrueangkul et al., 2019b). Additionally, the distribution of clay mineral assemblages in the surface sediments of the SCS indicates that most of the kaolinite, accounting for more than 50% of clay minerals offshore of Malaysia, is from the Malay Peninsula and not the Mekong River (Liu et al., 2016). Therefore, we suggest that the Kelantan River is the primary provenance of Core K17.

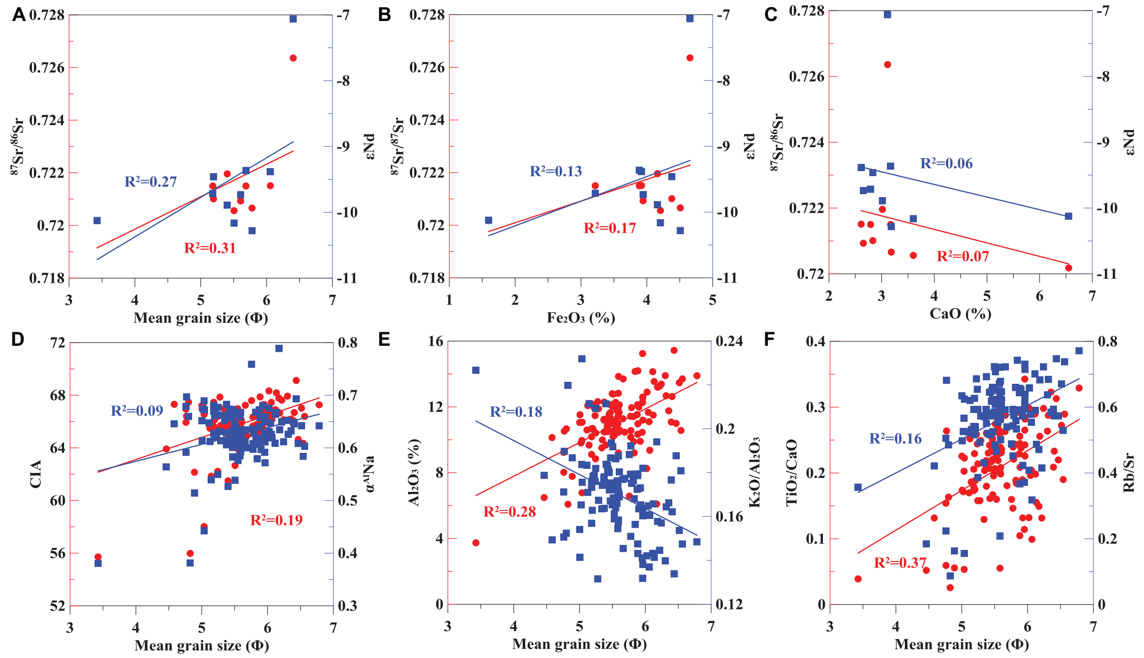

FIGURE 6 | Correlation analysis of Sr-Nd isotopic compositions, mean grain size, Fe_2O_3, MnO, and CaO concentrations, and weathering and terrigenous input indicators in Core K17. **(A–C)** Correlations between Sr-Nd isotopic compositions and mean grain size, Fe_2O_3 and CaO concentrations in core K17, respectively. **(D–F)** Correlations between mean grain size and chemical weathering indicators (CIA, a^{Al}Na and K_2O/Al_2O_3), and terrigenous input indicators (TiO_2/CaO and Rb/Sr ratios) in core K17, respectively.

Sedimentary Responses to Climate Changes and Human Activities Over the Past 7400 cal yr BP

Weathering and Terrigenous Input Indicators

Chemical weathering is an important process for modifying the mineral and chemical compositions of terrigenous sediments (Hu et al., 2020). The degree of chemical weathering under specific environmental conditions is primarily controlled by climate (White and Blum, 1995). Generally, high temperatures and heavy precipitation favor more intense chemical weathering, whereas low temperatures and less precipitation hinder the reactions involved in chemical weathering (White and Blum, 1995; Huang et al., 2018). Here, the chemical index of alteration (CIA), α^{Al}Na, and the K_2O/Al_2O_3 ratio were used to estimate chemical weathering intensity and variation. The CIA [defined as CIA = $Al_2O_3/(Al_2O_3 + CaO^* + Na_2O + K_2O) \times 100$, molar proportions; CaO* refers to the CaO content of the silicate fraction] and α^{Al}Na [defined as $\alpha^{Al}Na = (Al/Na)_{sediment}/(Al/Na)_{UCC}$, molar proportions] are widely used to estimate the chemical weathering intensity recorded in sediments (Nesbitt and Young, 1982; Garzanti et al., 2013; Liu et al., 2020). Higher CIA and α^{Al}E values correspond to stronger chemical weathering intensity. CaO* in CIA is corrected by comparing the molar contents of CaO with Na_2O, and the lower value is regarded as the CaO content in the silicate fraction (Singh et al., 2005; Liu et al., 2020). K_2O is preferentially leached in aqueous fluids compared to the immobile Al_2O_3 during the chemical weathering process (Nesbitt and Young, 1982); therefore, a lower K_2O/Al_2O_3 ratio could indicate increased chemical weathering related to strengthened monsoon rainfall, according to the basic principles of silicate weathering (Wei et al., 2004; Clift et al., 2014; Jiwarungrueangkul et al., 2019a).

TiO_2/CaO and Rb/Sr ratios were used to evaluate the variation of terrigenous sediment input related to erosion in this study (Jiwarungrueangkul et al., 2019b; Li et al., 2019). The Ti content in terrigenous sediments is stable in hypergenesis, and the Ti in marine sediments is widely believed to be primarily derived from the input of terrestrial clastic materials (Chen et al., 2013; Li et al., 2019). CaO in marine sediment primarily originates from biogenic input; thus, the TiO_2/CaO ratio can reflect the relative magnitudes of terrigenous clastics and biogenic inputs (Clift et al., 2014; Cao et al., 2015). Rb and Sr are primarily distributed in minerals bearing K (e.g., mica and K-feldspar) and Ca (e.g., carbonate), respectively; thus, Rb/Sr ratio can be used as another indicator of terrigenous sediment input (Li et al., 2019). Higher TiO_2/CaO and Rb/Sr ratios reflect enhanced terrigenous input to the core.

In previous studies, the finest end member was usually interpreted as fluvial/terrigenous input (Stuut and Lamy, 2004; Wan et al., 2007). Due to the dominant fraction of EM1 in the three end members and the overwhelming terrigenous element concentrations (e.g., SiO_2 and Al_2O_3; **Figure 3**) of sediments in Core K17, the finest end-member EM1 was interpreted as fluvial terrigenous sediment input from the Kelantan River in this study.

To ensure that chemical weathering and terrigenous input indicators are reliable for use in the study region, other factors,

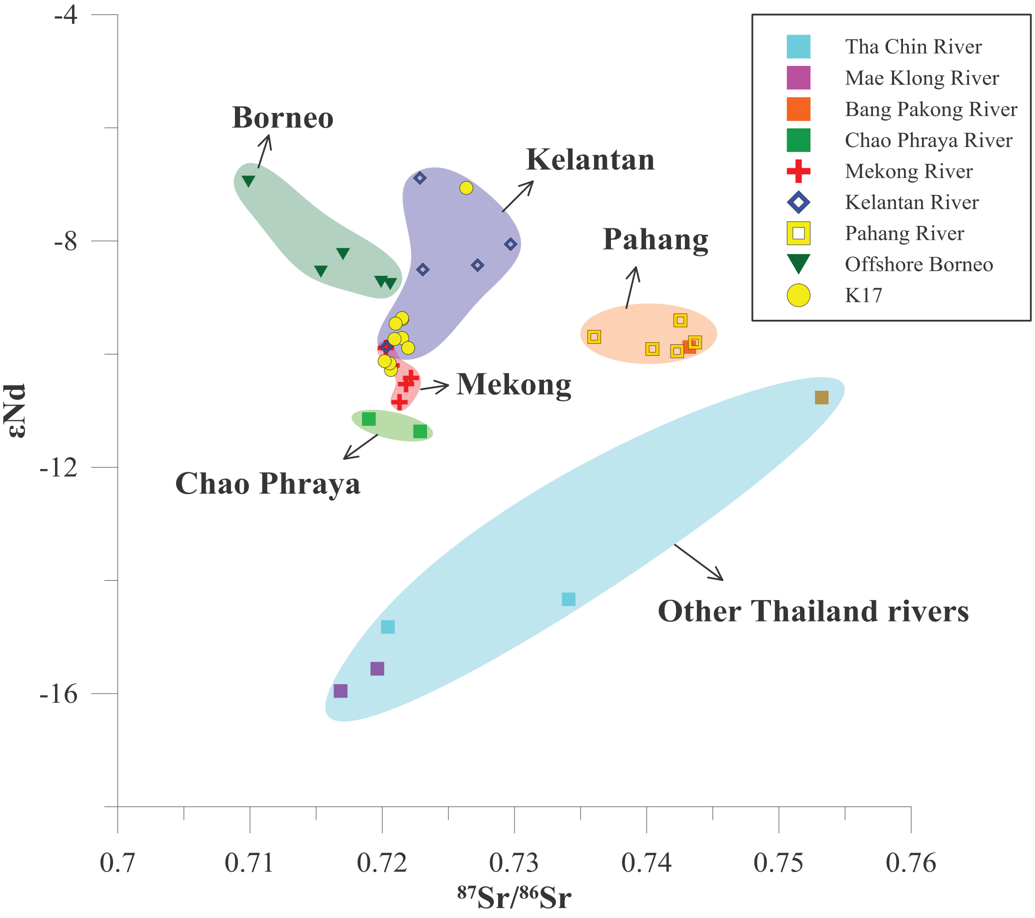

FIGURE 7 | The $^{87}Sr/^{86}Sr$ ratios versus εNd values plot for the Core K17, with sediments of Mekong River (Liu et al., 2007), Borneo offshore (Wei et al., 2012), Chao Phraya River and other Thailand rivers (Wu et al., unpublished), and Pahang and Kelantan River (this study).

including provenance changes, sea-level change, and hydraulic sorting by oceanic currents need to be considered (Hu et al., 2020). Because of the relatively constant source of Core K17 (**Figure 7**), provenance changes could not significantly influence weathering and terrigenous indicators. Sea level change played an important role in controlling terrigenous sediment input to the southern SCS before or during the early Holocene (Jiwarungrueangkul et al., 2019a) but is relatively constant with a weak fluctuation since ca. 7–8 ka on the Sunda Shelf, when the coastline reached a modern position (Steinke et al., 2003; Hanebuth et al., 2011). Thus, the influence of sea level changes is negligible. There were no significant correlations between the mean grain size and weathering and erosion indicators (i.e., CIA, K_2O/Al_2O_3, $\alpha^{Al}Na$, TiO_2/CaO, and Rb/Sr; **Figures 6D–F**), suggesting that these indicators are not influenced by transport processes or hydraulic sorting.

Climatic and Anthropogenic Impacts on the Weathering and Terrigenous Input Processes Over the Past 7400 cal yr BP

Monsoon rainfall intensity and temperature variations in the study area could lead to typical changes in chemical weathering and erosion over time (Huang et al., 2018; Li et al., 2019). Based on temporal variations in weathering and terrigenous input related to erosion processes (**Figure 8**), we suggest a four-stage sedimentary evolution in Core K17 over the last 7400 cal yr BP.

The first stage corresponds to a period of 7400–3700 cal yr BP. Stable CIA, $\alpha^{Al}Na$, and K_2O/Al_2O_3 values indicate stable chemical weathering during this period (**Figures 8C–E**). The relatively stable TiO_2/CaO and Rb/Sr ratios during this interval suggest relatively stable terrigenous sediment input (**Figures 8G,H**). Furthermore, EM1 displays a relatively stable pattern but contains fluctuations that indicate constant Kelantan River discharge due to stable chemical weathering and terrigenous input (**Figure 8F**). The monsoon precipitation from the $\delta^{18}O$ record gradually increased from 7400 to ca. 5000 cal yr BP and remained stable with heavy rainfall during 5000–3700 cal yr BP (Partin et al., 2007; Carolin et al., 2016; **Figure 8A**), contributing to more intense chemical weathering and terrigenous sediment input from the Kelantan River drainage. However, the temperature gradually decreased during this interval (**Figure 8B**), apparently reducing weathering and sediment input. Therefore, the relatively stable chemical weathering and terrigenous sediment input were probably

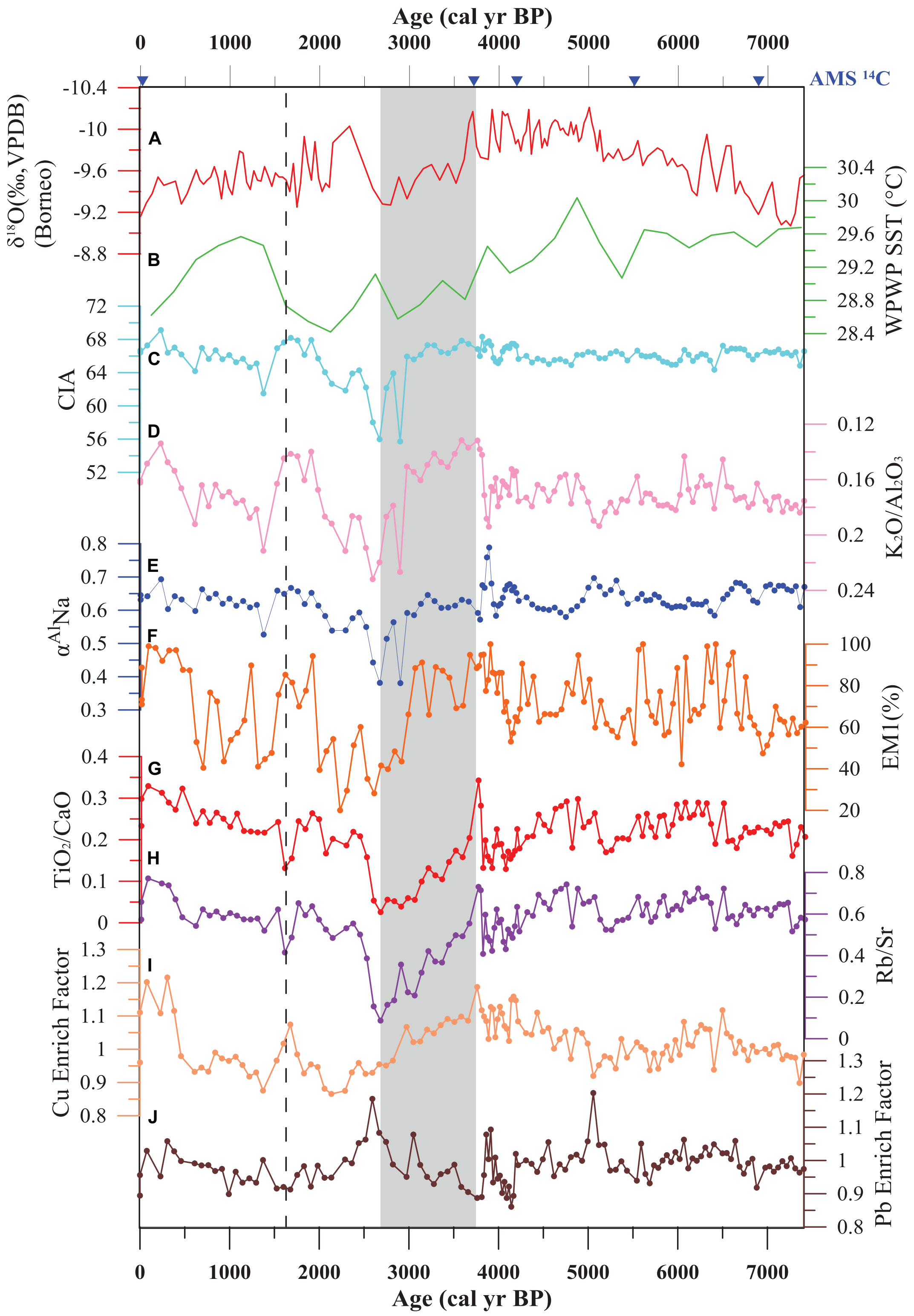

FIGURE 8 | Comparison of the Core K17 records with other representative paleoclimate records since 7400 cal yr BP: **(A)** Rainfall patterns from Borneo cave stalagmite δ^{18}O (Partin et al., 2007); **(B)** sea surface temperature (SST) of the Western Pacific Warm Pool (WPWP; Stott et al., 2004); **(C)** CIA from Core K17; **(D)** K_2O_3/Al_2O_3 from Core K17; **(E)** αAlNa from Core K17; **(F)** EM1 volume from Core K17; **(G)** TiO_2/CaO from Core K17; **(H)** Rb/Sr from Core K17; **(I)** Cu enrichment factor from Core K17; and **(J)** Pb enrichment factor from Core K17. The shadow area represents the interval of the second stage. The dotted line represents the boundary of third stage and fourth stage.

balanced by increasing rainfall and decreasing temperatures during this period.

The second stage ranged from 3700 to 2700 cal yr BP. Decreasing CIA, $\alpha^{Al}Na$, and K_2O/Al_2O_3 values suggest weaker chemical weathering and less sediment production in this interval. Less terrigenous sediment input is indicated by decreasing TiO_2/CaO and Rb/Sr ratios. Less monsoon rainfall and decreasing temperature led to weaker chemical weathering and less sediment transport to the western Sunda Shelf during this period (Stott et al., 2004; Partin et al., 2007). Due to weaker chemical weathering, fine EM1 also displayed a decreasing trend, corresponding to less Kelantan River discharge to the western Sunda Shelf during this interval. Additionally, weaker chemical weathering and less precipitation in this period were reported in the Pearl River estuary (Hu et al., 2013; Huang et al., 2018) and the Red River estuary (Wan et al., 2015) in the northern SCS, probably indicating the synchronous variations of climate change during this period in the SCS.

The third stage spanned 2700–1600 cal yr BP. Increasing CIA, $\alpha^{Al}Na$, and K_2O/Al_2O_3 values suggest stronger chemical weathering in this interval, and TiO_2/CaO and Rb/Sr ratios show an increasing trend, indicating more terrigenous sediment input. Heavy rainfall during this period possibly played a more important role than lower temperature and resulted in more intense chemical weathering and terrigenous sediment input. Therefore, EM1 also showed an increasing pattern similar to chemical weathering, indicating increasing river input.

The fourth stage corresponds to the interval since 1600 cal yr BP. Increasing CIA, $\alpha^{Al}Na$, and K_2O/Al_2O_3 values indicate stronger chemical weathering, which contributed to the production of more terrigenous sediment from the Kelantan River; decreasing monsoon precipitation from $\delta^{18}O$ records (Partin et al., 2007; Carolin et al., 2016) hindered river sediment production and transportation into the western Sunda Shelf in this period. Increasing TiO_2/CaO and Rb/Sr ratios suggest increasing terrigenous sediment input. EM1 also indicates increasing river discharge with fluctuations corresponding to stronger chemical weathering and increasing rainfall. Less precipitation and falling temperature with increasing weathering and erosion suggest no direct relationship between weathering and erosion and precipitation and temperature in this interval. Thus, climate change cannot be solely responsible for weathering/erosion changes since 1600 cal yr BP. A similar decoupling relationship between climate and weathering/erosion was reported in the Pearl River estuary (Huang et al., 2018) and the Red River estuary (Wan et al., 2015) in the northern SCS. We suggest that human activities have dominated chemical weathering and terrigenous input relative to climate change since 1600 cal yr BP. The Malay-Thai Peninsula contains many archeological sites from 6000 to 600 cal yr BP and had become a primary region of settlement in the early historic period during 2000–1400 cal yr BP (Horton et al., 2005), indicating that human society in the Malay Peninsula formed at least as early as 2000 cal yr BP. Since ca. 2000 cal yr BP, rice cultivation has been common in Southeast Asia (Liang et al., 2011). During 2000–1000 cal yr BP, both sides of the Malay Peninsula were important centers of East–West trade, and small-scale agricultural centers were established in some river basins (Liang et al., 2011). Agricultural development caused partial soil erosion, corresponding to the general increase in chemical weathering and terrigenous input (CIA, $\alpha^{Al}Na$, K_2O/Al_2O_3, TiO_2/CaO, Rb/Sr, and EM1) in Core K17 during this period (**Figure 8**).

Enrichment factor (EF) is widely used to discriminate natural and anthropogenic sources and to elevate environmental contamination (Wan et al., 2015). EF is calculated using the following equation: $EF = (X_{sample}/Al_{sample})/(X_{baseline}/Al_{baseline})$, where X_{sample} ($X_{baseline}$) and Al_{sample} ($Al_{baseline}$) are heavy metal concentrations and aluminum contents of samples (background references), and average elements concentration of samples below 84 cm depth (older than 5000 cal yr B P.) is chosen as the baseline, which is regarded as not influenced by anthropogenic process. Our results show that the EF values of Cu and Pb increased dramatically after 1600 cal yr BP (**Figures 8I,J**), which is closely related to mining and metalworking activities due to increasing requirements of tools for agriculture, corresponding to an increasing impact of human activities. There is a long history of tin and gold mining in Peninsular Malaysia at least before the 9th century (Balamurugan, 1991), related metal elements such as Cu and Pb are very common in tin or gold deposits. Burning of trees to smelt metals in the ancient could strengthen weathering and erosion since 1600 cal yr BP. Furthermore, the enrichment of Cu and Pb seems to be related to the disposal of sewage effluent, indicating an increase in human activity (Hu et al., 2013, 2020; Huang et al., 2018). Relatively higher enrichment of Cu and Pb were also observed in some sediment sequences before 1600 cal yr BP (**Figures 8I,J**), perhaps reflecting fluvial erosion related to harsh weather conditions during this period (Hu et al., 2020), such as flooding, which occurs frequently in the Kelantan River basin (Koopmans, 1972). However, more research is needed to clarify these mechanisms. The initial time at which human activity overwhelmed natural processes in our study is similar to that in the Pearl River Delta (2000 cal yr BP) (Huang et al., 2018), the Red River drainage (1800 cal yr BP) (Wan et al., 2015), and Taiwan (1500 cal yr BP) (Hu et al., 2020). Therefore, since 1600 cal yr BP, increased human activity has been the dominant influence on the natural landscape of Kelantan River drainage by agriculture and related mining activities. Compared the established variations in erosion and weathering rates from Sunda Shelf with other studies from the Southeast Asia, especially in the northern SCS (Wan et al., 2015; Huang et al., 2018), our results show a similar variation trend with them, but the accurate changing periods between these studies have some differences. It is worth noting that, after about 2000 cal yr BP, they all display a remarkable increasing trend. Therefore, we believe the Southeast Asia have similar variations trend in erosion and weathering rates, and human activities overwhelming the nature in erosion and weathering share a similar period in the Southeast Asia.

CONCLUSION

Provenance analysis from Sr-Nd isotopic evidence for Core K17 in the western Sunda Shelf suggests that the Kelantan

River is the major sediment contributor. The sediment succession of Core K17 can be divided into four stages according to chemical weathering and terrigenous input indicators. During stage 1 (7400–3700 cal yr BP), increasing precipitation and decreasing temperature jointly controlled relatively stable chemical weathering and terrigenous sediment input. Dramatically decreasing weathering and terrigenous input during stage 2 (3700–2700 cal yr BP) coincides well with less precipitation and lower temperature, resulting in weaker weathering and erosion. The period of 2700–1600 cal yr BP corresponds to the third stage, in which heavy rainfall played a more important role than low temperature in controlling weathering and erosion and led to increasing terrigenous input. For the late Holocene (stage 4, since 1600 cal yr BP), weathering and sediment inputs in the study core have likely been dominantly influenced by human activities due to decoupling between weathering/erosion and climate change and increasing agriculture and mining activities.

DATA AVAILABILITY STATEMENT

The raw data supporting the conclusions of this article will be made available by the authors, without undue reservation.

AUTHOR CONTRIBUTIONS

KW interpreted the data and wrote the manuscript. XS conceived and designed the project. KW and BW recovered the sediment core. KW and HZ did the experiments about the grain size, geochemistry, and isotopes. PC and CR collected the samples in the field. ZL, BW, and JL revised the manuscript. All authors contributed to the article and approved the submitted version.

FUNDING

This work was supported by the National Program on Global Change and Air-Sea Interaction (GASI-GEOGE-03 and GASI-02-SCS-CJB01), the Natural Science Foundation of China-Shandong Joint Fund for Marine Science Research Centers (U1606401), the Scientific and Technological Innovation Project Financially supported by Qingdao National Laboratory for Marine Science and Technology (2015ASKJ03), the China–Malaysia cooperation project "Effect on variability of seasonal monsoon on sedimentary process in Peninsular Malaysia waters," and the Taishan Scholar Program of Shandong.

ACKNOWLEDGMENTS

We thank staff of National University of Malaysia, crew of "R.V. DISCOVERY," and Xisheng Fang, Xin Shan, Haitao Zhang, and Taoyu Xu from the First Institute of Oceanography, Ministry of Natural Resources for sample collection on board, and Xingquan Sun and Wenxing Ye from the Ocean University of China for sample pretreatment.

REFERENCES

Awadalla, S., and Noor, I. M. (1991). Induced climate change on surface runoff in Kelantan Malaysia. *Int. J. Water Resour. Dev.* 7, 53–59. doi: 10.1080/07900629108722492

Balamurugan, G. (1991). Tin mining and sediment supply in Peninsular Malaysia with special reference to the Kelang River basin. *Environmentalist* 11, 281–291. doi: 10.1007/BF01266561

Bayon, G., German, C. R., Boella, R. M., Milton, J. A., Taylor, R. N., and Nesbitt, R. W. (2002). An improved method for extracting marine sediment fractions and its application to sr and nd isotopic analysis. *Chem. Geol.* 187, 179–199. doi: 10.1016/S0009-2541(01)00416-8

Bi, L., Yang, S., Li, C., Guo, Y., Wang, Q., Liu, J. T., et al. (2015). Geochemistry of river-borne clays entering the east china sea indicates two contrasting types of weathering and sediment transport processes. *Geochem. Geophys. Geosyst.* 16, 3034–3052. doi: 10.1002/2015GC005867

Cao, P., Shi, X., Li, W., Liu, S., Yao, Z., Hu, L., et al. (2015). Sedimentary responses to the Indian Summer Monsoon variations recorded in the southeastern Andaman Sea slope since 26 ka. *J Asian Earth Sci.* 114, 512–525. doi: 10.1016/j.jseaes.2015.06.028

Carolin, S. A., Cobb, K. M., Lynch-Stieglitz, J., Moerman, J. W., Partin, J. W., Lejau, S., et al. (2016). Northern Borneo stalagmite records reveal West Pacific hydroclimate across MIS 5 and 6. *Earth Planet. Sci. Lett.* 439, 182–193. doi: 10.1016/j.epsl.2016.01.028

Chen, H. F., Yeh, P. Y., Song, S. R., Hsu, S. C., Yang, T. N., Wang, Y., et al. (2013). The Ti/Al molar ratio as a new proxy for tracing sediment transportation processes and its application in Aeolian events and sea level change in East Asia. *J. Asian Earth Sci.* 73, 31–38. doi: 10.1016/j.jseaes.2013.04.017

Clift, P. D., Wan, S., and Blusztajn, J. (2014). Reconstructing chemical weathering, physical erosion and monsoon intensity since 25 Ma in the northern South China Sea: a review of competing proxies. *Earth Sci. Rev.* 130, 86–102. doi: 10.1016/j.earscirev.2014.01.002

Corella, J. P., Stefanova, V., El Anjoumi, A., Rico, E., Giralt, S., Moreno, A., et al. (2013). A 2500-year multi-proxy reconstruction of climate change and human activities in northern Spain: the Lake Arreo record. *Palaeogeogr. Palaeoclimatol. Palaeoecol.* 386, 555–568. doi: 10.1016/j.palaeo.2013.06.022

Dou, Y., Yang, S., Liu, Z., Shi, X., Li, J., Yu, H., et al. (2012). Sr–Nd isotopic constraints on terrigenous sediment provenances and Kuroshio Current variability in the Okinawa Trough during the late Quaternary. *Palaeogeogr. Palaeoclimatol. Palaeoecol.* 365–366:38–47. doi: 10.1016/j.palaeo.2012.09.003

Folk, R. L., Andrews, P. B., and Lewis, D. W. (1970). Detrital sedimentary rock classification and nomenclature for use in New Zealand. *N. Z. J. Geol. Geophys.* 13, 937–968. doi: 10.1080/00288306.1970.10418211

Garzanti, E., Limonta, M., Resentini, A., Bandopadhyay, P. C., Najman, Y., Andò, S., et al. (2013). Sediment recycling at convergent plate margins (Indo-Burman Ranges and Andaman–Nicobar Ridge). *Earth Sci. Rev.* 123, 113–132. doi: 10.1016/j.earscirev.2013.04.008

Hanebuth, T. J. J., Stattegger, K., and Grootes, P. M. (2000). Rapid flooding of the Sunda shelf: a late-glacial sea-level record. *Science* 288, 1033–1035. doi: 10.1126/science.288.5468.1033

Hanebuth, T. J. J., Voris, H. K., Yokoyama, Y., Saito, Y., and Okuno, J. (2011). Formation and fate of sedimentary depocentres on Southeast Asia's Sunda Shelf over the past sea-level cycle and biogeographic implications. *Earth Sci. Rev.* 104, 92–110. doi: 10.1016/j.earscirev.2010.09.006

Horton, B. P., Gibbard, P. L., Mine, G. M., Morley, R. J., Purintavaragul, C., and Stargardt, J. M. (2005). Holocene sea levels and palaeoenvironments, Malay-Thai Peninsula, southeast Asia. *Holocene* 15, 1199–1213.

Hu, D., Clift, P. D., Böning, P., Hannigan, R., Hillier, S., Blusztajn, J., et al. (2013). Holocene evolution in weathering and erosion patterns in the Pearl River delta. *Geochem. Geophys. Geosyst.* 14, 2349–2368. doi: 10.1002/ggge.20166

Hu, S., Zeng, Z., Fang, X., Yin, X., Chen, Z., Li, X., et al. (2020). Increasing terrigenous sediment supply from Taiwan to the southern Okinawa Trough over the last 3000 years evidenced by Sr-Nd isotopes and geochemistry. *Sediment. Geol.* 406, 105725. doi: 10.1016/j.sedgeo.2020.105725

Huang, C., Zeng, T., Ye, F., Xie, L., Wang, Z., Wei, G., et al. (2018). Natural and anthropogenic impacts on environmental changes over the past 7500 years based on the multi-proxy study of shelf sediments in the northern South China Sea. *Quat. Sci. Rev.* 197, 35–48. doi: 10.1016/j.quascirev.2018.08.005

Hutchison, C. S. (1968). Dating tectonism in the Indosinian-Thai-Malayan orogen by thermoluminescence. *Geol. Soc. Am. Bull.* 79, 375–386.

Jiwarungrueangkul, T., Liu, Z., Stattegger, K., and Sang, P. (2019a). Reconstructing chemical weathering intensity in the Mekong River basin since the Last Glacial Maximum. *Paleoceanogr. Paleoclimatol.* 34, 1710–1725. doi: 10.1029/2019PA003608

Jiwarungrueangkul, T., Liu, Z., and Zhao, Y. (2019b). Terrigenous sediment input responding to sea level change and East Asian monsoon evolution since the last deglaciation in the southern South China Sea. *Glob. Planet. Change* 174, 127–137. doi: 10.1016/j.gloplacha.2019.01.011

Joussain, R., Colin, C., Liu, Z., Meynadier, L., Fournier, L., Fauquembergue, K., et al. (2016). Climatic control of sediment transport from the Himalayas to the proximal NE Bengal Fan during the last glacial-interglacial cycle. *Quat. Sci. Rev.* 148, 1–16. doi: 10.1016/j.quascirev.2016.06.016

Kamarudin, M. K. A., Toriman, M. E., Rosli, M. H., Juahir, H., Aziz, N. A. A., Azid, A., et al. (2015). Analysis of meander evolution studies on effect from land use and climate change at the upstream reach of the Pahang River, Malaysia. *Mitig. Adapt. Strateg. Glob. Change* 20, 1319–1334. doi: 10.1007/s11027-014-9547-6

Koopmans, B. N. (1972). Sedimentation in the Kelantan Delta (Malaysia). *Sediment. Geol.* 7, 65–84. doi: 10.1016/0037-0738(72)90054-1

Li, J., Liu, S., Shi, X., Zhang, H., Fang, X., Cao, P., et al. (2019). Sedimentary responses to the sea level and Indian summer monsoon changes in the central Bay of Bengal since 40 ka. *Mar. Geol.* 415:105947. doi: 10.1016/j.margeo.2019.05.006

Li, J., Liu, S., Shi, X., Zhang, H., Fang, X., Chen, M., et al. (2018). Clay minerals and Sr-Nd isotopic composition of the Bay of Bengal sediments: implications for sediment provenance and climate control since 40 ka. *Quat. Int.* 493, 50–58. doi: 10.1016/j.quaint.2018.06.044

Liang, Z., Li, M., and Yang, B. (2011). *A History of Ancient Southeast Asia*. (Beijing: Peking University Press), 254–258.

Liu, S., Li, J., Zhang, H., Cao, P., Mi, B., Khokiattiwongc, S., et al. (2020). Complex response of weathering intensity registered in the Andaman Sea sediments to the Indian Summer Monsoon over the last 40 kyr. *Mar. Geol.* 426:106206. doi: 10.1016/j.margeo.2020.106206

Liu, Z., Colin, C., Huang, W., Le, K., Tong, S., Chen, Z., et al. (2007). Climatic and tectonic controls on weathering in South China and the Indochina Peninsula: clay mineralogical and geochemical investigations from the Pearl, Red, and Mekong drainage basins. *Geochem. Geophys. Geosyst.* 8:Q05005. doi: 10.1029/2006GC001490

Liu, Z., Wang, H., Hantoro, W., Sathiamurthy, E., Colin, C., Zhao, Y., et al. (2012). Climatic and tectonic controls on chemical weathering in tropical Southeast Asia (Malay Peninsula, Borneo, and Sumatra). *Chem. Geol.* 291, 1–12. doi: 10.1016/j.chemgeo.2011.11.015

Liu, Z., Zhao, Y., Colin, C., Stattegger, K., Wiesner, M. G., Huh, C. A., et al. (2016). Source-to-sink transport processes of fluvial sediments in the South China Sea. *Earth Sci. Rev.* 153, 238–273. doi: 10.1016/j.earscirev.2015.08.005

McLennan, S. M. (1993). Weathering and global denudation. *J. Geol.* 101, 295–303. doi: 10.1086/648222

Milliman, J. D., Farnsworth, K. L., and Albertin, C. S. (1999). Flux and fate of fluvial sediments leaving large islands in the East Indies. *J. Sea Res.* 41, 97–107. doi: 10.1016/S1385-1101(98)00040-9

Nesbitt, H. W., and Young, G. M. (1982). Early Proterozoic climates and plate motions inferred from major element chemistry of lutites. *Nature* 299, 715–717. doi: 10.1038/299715a0

Partin, J. W., Cobb, K. M., Adkins, J. F., Clark, B., and Fernandez, D. P. (2007). Millennial-scale trends in west Pacific warm pool hydrology since the Last Glacial Maximum. *Nature* 449, 452–455. doi: 10.1038/nature06164

Pelejero, C., Kienast, M., Wang, L., and Grimalt, J. O. (1999). The flooding of Sundaland during the last deglaciation: imprints in hemipelagic sediments from the southern South China Sea. *Earth Planet. Sci. Lett.* 171, 661–671. doi: 10.1016/S0012-821X(99)00178-8

Raj, J. K., Yusoff, I., and Abdullah, W. H. (2007). Past, present and future coastal changes at the Kuala Kemasin estuary, Kelantan State. *Bull. Geol. Soc. Malaysia* 53, 75–80. doi: 10.7186/bgsm53200712

Raymo, M. E., and Ruddiman, W. F. (1992). Tectonic forcing of late Cenozoic climate. *Nature* 359, 117–122. doi: 10.1038/359117a0

Reimer, P. J., Bard, E., Bayliss, A., Beck, J. W., Blackwell, P. G., Ramsey, C. B., et al. (2013). Selection and treatment of data for radiocarbon calibration: an update to the international calibration (IntCal) criteria. *Radiocarbon* 55, 1923–1945. doi: 10.1017/S003382220004889X

Singh, M., Sharma, M., and Tobschall, H. J. (2005). Weathering of the Ganga alluvial plain, northern India: implications from fluvial geochemistry of the Gomati River. *Appl. Geochem.* 20, 1–21. doi: 10.1016/j.apgeochem.2004.07.005

Southon, J., Kashgarian, M., Fontugne, M., Metivier, B., and Yim, W. W. (2002). Marine reservoir corrections for the Indian Ocean and Southeast Asia. *Radiocarbon* 44, 167–180. doi: 10.1017/S0033822200064778

Steinke, S., Kienast, M., and Hanebuth, T. J. J. (2003). On the significance of sea-level variations and shelf paleo-morphology in governing sedimentation in the southern South China Sea during the last deglaciation. *Mar. Geol.* 201, 179–206. doi: 10.1016/S0025-3227(03)00216-0

Stott, L., Cannariato, K., Thunell, R., Haug, G. H., Koutavas, A., and Lund, S. (2004). Decline of surface temperature and salinity in the western tropical Pacific Ocean in the Holocene epoch. *Nature* 431, 56–59. doi: 10.1038/nature02903

Stuut, J. B. W., and Lamy, F. (2004). Climate variability at the southern boundaries of the Namib (southwestern Africa) and Atacama (northern Chile) coastal deserts during the last 120,000 yr. *Quat. Res.* 62, 301–309. doi: 10.1016/j.yqres.2004.08.001

Tan, L., Shen, C., Löwemark, L., Chawchai, S., Edwards, R. L., Cai, Y., et al. (2019). Rainfall variations in central Indo-Pacific over the past 2,700 y. *Proc. Natl. Acad. Sci. U.S.A.* 116, 17201–17206. doi: 10.1073/pnas.1903167116

Tangang, F. T., Xia, C., Qiao, F., Juneng, L., and Shan, F. (2011). Seasonal circulations in the Malay Peninsula Eastern continental shelf from a wave–tide–circulation coupled model. *Ocean Dyn.* 61, 1317–1328. doi: 10.1007/s10236-011-0432-5

Voris, H. K. (2000). Maps of Pleistocene sea-levels in Southeast Asia: shorelines, river systems and time durations. *J. Biogeogr.* 27, 1153–1167. doi: 10.1046/j.1365-2699.2000.00489.x

Wan, S., Li, A., Clift, P. D., and Stuut, J. B. W. (2007). Development of the East Asian monsoon: mineralogical and sedimentologic records in the northern South China Sea since 20 Ma. *Palaeogeogr. Palaeoclimatol. Palaeoecol.* 254, 561–582. doi: 10.1016/j.palaeo.2007.07.009

Wan, S., Toucanne, S., Clift, P. D., Zhao, D., Bayon, G., Yu, Z., et al. (2015). Human impact overwhelms long-term climate control of weathering and erosion in southwest China. *Geology* 43, 439–442. doi: 10.1130/G36570.1

Wang, A., Bong, C., Xu, Y., Hassan, M. H. A., Xiang, Y., Bakar, A. F. A., et al. (2017). Assessment of heavy metal pollution in surficial sediments from a tropical river-estuary-shelf system: a case study of Kelantan River, Malaysia. *Mar. Pollut. Bull.* 125, 492–500. doi: 10.1016/j.marpolbul.2017.08.010

Wang, A., Wei, B., Xiang, Y., Li, Y., Hassan, M. H. A., Hoe, L. K., et al. (2020). Transport mechanism and fate of terrestrial materials delivered by a small tropical mountainous river: a case study of the Kelantan River, Malaysia. *Mar. Geol.* 430:106344. doi: 10.1016/j.margeo.2020.106344

Wang, H., Liu, Z., Sathiamurthy, E., Colin, C., Li, J., and Zhao, Y. L. (2011). Chemical weathering in Malay Peninsula and North Borneo: clay mineralogy and element geochemistry of river surface sediments. *Sci. China Earth Sci.* 54, 272–282. doi: 10.1007/s11430-010-4158-x

Wang, P., Clemens, S., Beaufort, L., Braconnot, P., Ganssen, G., Jian, Z., et al. (2005). Evolution and variability of the Asian monsoon system: state of the art and outstanding issues. *Quat. Sci. Rev.* 24, 595–629. doi: 10.1016/j.quascirev.2004.10.002

Wei, G., Liu, Y., Li, X., Shao, L., and Fang, D. (2004). Major and trace element variations of the sediments at ODP Site 1144, South China Sea, during the last 230 ka and their paleoclimate implications. *Palaeogeogr.*

Palaeoclimatol. Palaeoecol. 212, 331–342. doi: 10.1016/j.palaeo.2004.06.011

Wei, G., Liu, Y., Ma, J., Xie, L., Chen, J., Deng, W., et al. (2012). Nd, Sr isotopes and elemental geochemistry of surface sediments from the South China Sea: implications for provenance tracing. *Mar. Geol.* 319, 21–34. doi: 10.1016/j.margeo.2012.05.007

West, A. J., Galy, A., and Bickle, M. (2005). Tectonic and climatic controls on silicate weathering. *Earth Planet. Sci. Lett.* 235, 211–228. doi: 10.1016/j.epsl.2005.03.020

White, A. F., and Blum, A. E. (1995). Effects of climate on chemical weathering in watersheds. *Geochim. Cosmochim. Acta* 59, 1729–1747. doi: 10.1016/0016-7037(95)00078-E

Wu, K., Liu, S., Kandasamy, S., Jin, A., Lou, Z., Li, J., et al. (2019). Grain-size effect on rare earth elements in Pahang River and Kelantan River, Peninsular Malaysia: implications for sediment provenance in the southern South China Sea. *Cont. Shelf Res.* 189:103977. doi: 10.1016/j.csr.2019.103977

Wu, K., Liu, S., Shi, X., Lou, Z., Kandasamy, S., Wu, B., et al. (2020). Distribution of rare earth elements in surface sediments of the western Sunda Shelf: constraints from sedimentology and mineralogy. *Cont. Shelf Res.* 206:104198. doi: 10.1016/j.csr.2020.104198

Xue, Z., He, R., Liu, J., and Warner, J. C. (2012). Modeling transport and deposition of the Mekong River sediment. *Cont. Shelf Res.* 37, 66–78. doi: 10.1016/j.csr.2012.02.010

Xue, Z., Liu, J., DeMaster, D., Van Nguyen, L., and Ta, T. K. O. (2010). Late Holocene evolution of the Mekong subaqueous delta, southern Vietnam. *Mar. Geol.* 269, 46–60. doi: 10.1016/j.margeo.2009.12.005

Zong, Y., Huang, K., Yu, F., Zheng, Z., Switzer, A. D., Huang, G., et al. (2012). The role of sea-level rise, monsoonal discharge and the palaeo-landscape in the early Holocene evolution of the Pearl River delta, southern China. *Quat. Sci. Rev.* 54, 77–88. doi: 10.1016/j.quascirev.2012.01.002

Conflict of Interest: The authors declare that the research was conducted in the absence of any commercial or financial relationships that could be construed as a potential conflict of interest.

The handling editor declared a past co-authorship with one of the authors XS.

ORIGINAL RESEARCH
published: 16 April 2021
doi: 10.3389/feart.2021.633713

Applicability and Variability of Chemical Weathering Indicators and Their Monsoon-Controlled Mechanisms in the Bay of Bengal

Jingrui Li[1,2], Shengfa Liu[1,2], Xuefa Shi[1,2]*, Hui Zhang[1,2], Peng Cao[1,2], Xiaoyan Li[1,2], Hui-Juan Pan[3,4], Somkiat Khokiattiwong[5] and Narumol Kornkanitnan[5]

[1] Key Laboratory of Marine Geology and Metallogeny, First Institute of Oceanography, Ministry of Natural Resources, Qingdao, China, [2] Laboratory for Marine Geology, Qingdao National Laboratory for Marine Science and Technology, Qingdao, China, [3] Institute of Earth Sciences, College of Ocean Science and Resource, National Taiwan Ocean University, Keelung, Taiwan, [4] Center of Excellence for Ocean Engineering, College of Engineering, National Taiwan Ocean University, Keelung, Taiwan, [5] Department of Marine and Coastal Resources, Marine and Coastal Resources Research and Development Institute, Bangkok, Thailand

OPEN ACCESS

Edited by:
Gary E. Stinchcomb,
Murray State University, United States

Reviewed by:
William Ellis Lukens,
James Madison University,
United States
Anil Shukla,
Physical Research Laboratory, India
Yongbo Wang,
Capital Normal University, China

***Correspondence:**
Xuefa Shi
xfshi@fio.org.cn

Specialty section:
This article was submitted to Quaternary Science, Geomorphology and Paleoenvironment, a section of the journal Frontiers in Earth Science

Received: 26 November 2020
Accepted: 29 March 2021
Published: 16 April 2021

Citation:
Li J, Liu S, Shi X, Zhang H, Cao P, Li X, Pan H-J, Khokiattiwong S and Kornkanitnan N (2021) Applicability and Variability of Chemical Weathering Indicators and Their Monsoon-Controlled Mechanisms in the Bay of Bengal. Front. Earth Sci. 9:633713. doi: 10.3389/feart.2021.633713

To help understanding the potential relationship between chemical weathering and Indian summer monsoon (ISM) since the last glacial period a gravity core (BoB-56) was retrieved from the central Bay of Bengal (BoB). The data of chemical weathering indexes (CIA, WIP, and α^{Al}Na) used in this study showed general synchronicity with the regional monsoon precipitation and temperature record on precessional scale, indicating existence of control from the ISM on weathering. Corresponding to alteration of warm/cold period during the last deglaciation, obvious simultaneously alteration of higher/lower values of the chemical weathering and terrestrial input proxies' record support our hypothesis that the ISM driving chemical weathering on the millennial scale. However, a contradiction occurred during the Holocene period, when the ISM precipitation and temperature rose to a higher level, while the alternative indexes unanimously reflected a weaker chemical weathering conditions. In this study, we discussed the applicability of chemical weathering indexes in the BoB during the Holocene period. Besides the possible weakened monsoon during 6–3 ka, recorded by the stalagmite δ^{18}O and Sea Surface Temperature (SST) reconstruction results in the northeastern Indian Ocean, other factors were responsible for this phenomenon, including the grain size effect and distinction between the mountain high land and floodplain low land. The chemical weathering records, during the last glaciation, indicated the presence of control from the ISM on weathering at precessional and millennial scales. While, during the Holocene, they failed to reflect the actual chemical weathering dynamics of the source area. Indeed, a mixture of physical erosion and chemical weathering seems to be representative of the chemical weathering dynamics in the area. Our findings emphasized on the tight connections between the chemical weathering evolution and global-regional climate conditions around the BoB, implying possible ISM-controlled mechanisms during different time scales.

Keywords: geochemistry, chemical weathering, Indian summer monsoon, precipitation, Bay of Bengal

INTRODUCTION

Chemical weathering is one of the most important processes of the earth's elemental cycle, especially for the carbon cycle, and is closely related to tectonic, climatic, and environmental factors (Walker et al., 1981; Berner, 1992; Gaillardet et al., 1999; Yang et al., 2004a; Eiriksdottir et al., 2011; Miriyala et al., 2017; He et al., 2020; Liu et al., 2020). During the journey from "source" to "sink," particles carry source chemical weathering signals to the sink area, which are interfered and modified by path signals, and form strata, containing chemical weathering signals. Therefore, deciphering the chemical weathering intensity records in stratigraphic signals can provide us with information on the environmental evolution in source regions at different time scales, helping to understand the different control mechanisms of chemical weathering. From the transportation characteristics of environmental signals in the process of "source-sink," the stronger the signal in the source area, the shorter the transformation time, and the more stable and continuous the strata are, the more conducive to the decoding of environmental signals (Romans et al., 2016). In addition, the obvious tectonic and climatic signals in the source area are likely to be masked, modified, or damaged by other signals during transportation (Jerolmack and Paola, 2010; Romans et al., 2016), such as fluvial-floodplain processes, which are not affected by the original upstream signals. Located back against "the roof of the world," the Tibetan Plateau, the Bay of Bengal (BoB) is considered as the supergiant source of sediment in the Asian continent margin, with a mixture of world-class high mountain terrain and low relief develop in the foreland like flood plain, combined with the developed river systems. In addition to the world-class delta, the BoB has developed a largest submarine fan in the world. Typical Indian monsoon climate affects the whole BoB and surrounding areas. The drilling results show that except for the early Eocene and late Miocene, the remaining strata are relatively continuous (Curray and Moore, 1971), providing us with a good target for deciphering regional chemical weathering evolution and its control mechanism, and recorded in the sediment strata.

Tectonics, climate, and sea level fluctuations have significant control on generating, transportation, and preservation of the chemical weathering signals. Overall, the major tectonics around the BoB remained stable during the last glaciation scale. The sediment in the BoB are mainly transported from the Ganges-Brahmaputra River (hereinafter referred to as "G-B" River), so the influence from tectonic characteristics is mainly reflected in the difference between the composition of the high mountainous terrain in the upper reaches and the low plain terrain in the middle and lower reaches (Joussain et al., 2016; Yu et al., 2020). The sea level mainly controls the relative input between the delta-shelf and the deep sea on a glacial-interglacial scale (Li et al., 2019). Regardless of long or short time scales, climate change seems to be the closest factor, controlling the chemical weathering, with two basic parameters, i.e., the precipitation and temperature (Liu et al., 2020). The "competition" among these factors has been maintained throughout the late Quaternary in the area and preserved in the sediments, transported by rivers into the ocean. In the northeast Indian Ocean, the Indian monsoon climate change, recorded by ocean indexes since the last glaciation, mainly embodied in glacial-interglacial, precessional and millennial scales variations, subjected to the global ice condition, the latitude distribution distinction of solar radiation, caused by the earth parameters, and the millennial climate events in the high latitudes of the northern hemisphere, respectively (Duplessy, 1982; Prell and Kutzbach, 1987; Schulz et al., 1998; Clemens and Prell, 2003; Gupta et al., 2005; Caley et al., 2011; Bolton et al., 2013; Cao et al., 2015; Mohtadi et al., 2016; Raza et al., 2017). These periodic changes are recorded in the marine sedimentary strata and have been subjected to study in several research (Clemens and Prell, 2003; Cao et al., 2015; Li et al., 2018, 2019, 2020; Sebastian et al., 2019; Liu et al., 2020; Yu et al., 2020). If the chemical weathering evolution in the BoB is mainly controlled by the Indian monsoon climate, one or more of the above periodic changes should have occurred in its temporal variation trend. Indian monsoon rainfall is mainly concentrated in the summer monsoon period, accounting for more than 90% of the annual precipitation (Rodolfo, 1969; Singh et al., 2007). Therefore, summer monsoon rainfall can be regarded as a typical alternative index of Indian monsoon intensity and its time-evolution characteristics and control mechanism are stablished in a large number of studies (Prell and Kutzbach, 1987; Schulz et al., 1998; Kudrass et al., 2001; Fleitmann et al., 2003, 2007; Rashid et al., 2007; Bolton et al., 2013), which are used as references for our comparative analysis.

Element molar contents based proxies, e.g., Chemical Index of Alteration (CIA; Nesbitt and Young, 1982), Weathering Index of Parker (1970), and α^{Al}E (Garzanti et al., 2013), have been successfully applied in different sedimentary environments to estimate the chemical weathering intensity (Liu et al., 2013, 2020; Li et al., 2017; Xu et al., 2018). It should be noted that the variation of geochemical element content is controlled not only by the changes in chemical weathering intensity, but also by the mixing process of sediment particles from different sources or various components. Therefore, while applying the above parameters, the influence of provenance factors needs to be taken into account. In this study, these three commonly used chemical weathering index parameters, i.e., CIA, WIP, and α^{Al}E are analyzed to evaluate the chemical weathering dynamics around the BoB and its response to the Indian monsoon climate, since the last glaciation. Meanwhile, the application of geochemical parameters, represented by the CIA are discussed to estimate the chemical weathering dynamics in different stages. The findings from this study can help to build a "climate-weathering-sedimentation" connection in the BoB.

MATERIALS AND METHODS

Materials

Core BoB-56 (location: 16.56°N, 88.55°E; length: 3.41 m; water depth: 2,615 m; **Figure 1**) was collected from the central BoB in 2012, during China-Thailand BoB joint scientific cruise. The general procedures of the Key Laboratory of Marine Geology and Metallogeny, Ministry of Natural Resources, China, was followed as a pre-treatment procedure, including a detailed core

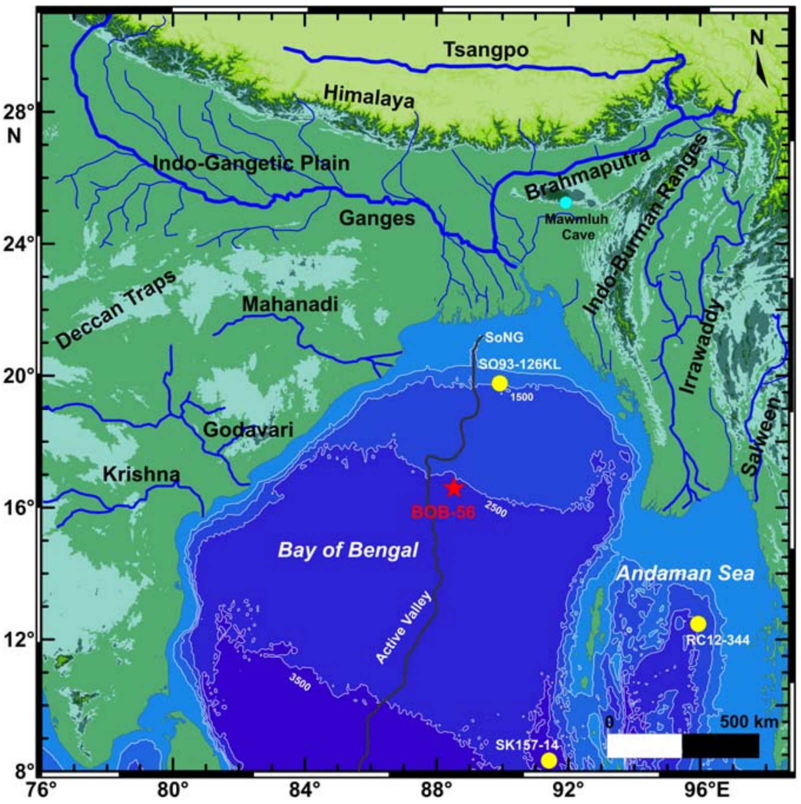

FIGURE 1 | Location of the BoB. The core BoB-56 and referenced cores are marked by red stars and yellow circles, respectively. The cyan color circle in the land show location of the Mawmluh Cave. SoNG: Swatch of No Ground, the largest submarine canyon in the BoB.

description and sub-samples division. Briefly, sediments of core BoB-56 were composed of relatively homogeneous gray clay silt except the upper 30 cm which showed the yellow brown color mainly due to the relative higher sand fraction. Grain size and geochemical analyses were carried out on the 2 cm intervals. AMS ^{14}C age model was constructed based on mixed planktonic foraminifera species (**Figure 2**; Li et al., 2018). Downcore ages were calculated by linear interpolation between dated sediment layers and the bottom age is 40.0 ka BP. Correspondingly, the sedimentation rates during the Holocene period (~3.1 cm/kyr) were lower than those during the last glacial and deglacial periods (~10.9 cm/kyr). The chronology, grain size, and part of element geochemistry (Ti, Ca, Rb, Sr, and Ba) compositions have been reported in our previous work (Li et al., 2018, 2019). In particular, sediment provenance of the core BoB-56 has been identified using Sr and Nd isotope compositions (Li et al., 2018), which confirmed that most of the sediments are from the Himalayas. This could decrease the difficulty of interpretation of weathering signal due to the complex sediment sources, and improve the reliability of the indexes.

Geochemical Analyses

Each frozen and dried sample with a weight of 0.05 g was placed in a polytetrafluoroethylene digestion tank, dissolved twice in HF-HNO_3 (1:1), and dried at 190°C for 48 h. Subsequently, by reacting with 1 mL of HNO_3, the residual HF was removed and the samples were digested with a mixture of 3 mL of 50% HNO_3 and 1 mL of Rh (500 ppb) for 24 h in an oven at 150°C. Then, 50 g of the mixture was prepared for element concentration analyses using Inductively Coupled Plasma Optical Emission Spectrometry. 10% of these samples were analyzed repeatedly, to determine the measurement error. The GSD-9 reference standard was also measured to confirm the accuracy and an approximately 5% measurement error was determined.

Chemical Weathering Indexes Calculation

Three element molar contents based proxies, CIA (Nesbitt and Young, 1982), Weathering Index of Parker (WIP; Parker, 1970) and $\alpha^{Al}E$ (Garzanti et al., 2013) were applied in this study to evaluate the chemical weathering conditions, and the calculation formulas are as follows:

$$\mathrm{CIA} = \mathrm{Al_2O_3}/(\mathrm{Al_2O_3} + \mathrm{CaO}^* + \mathrm{Na_2O} + \mathrm{K_2O}) \times 100 \tag{1}$$

$$\mathrm{WIP} = (2\mathrm{Na_2O}/0.35 + \mathrm{MgO}/0.9 + 2\mathrm{K_2O}/0.25 + \mathrm{CaO}^*/0.7) \times 100 \tag{2}$$

$$\alpha^{\mathrm{Al}}\mathrm{E} = \left(\mathrm{Al/E}\right)_{\mathrm{sediment}} / \left(\mathrm{Al/E}\right)_{\mathrm{UCC}} \tag{3}$$

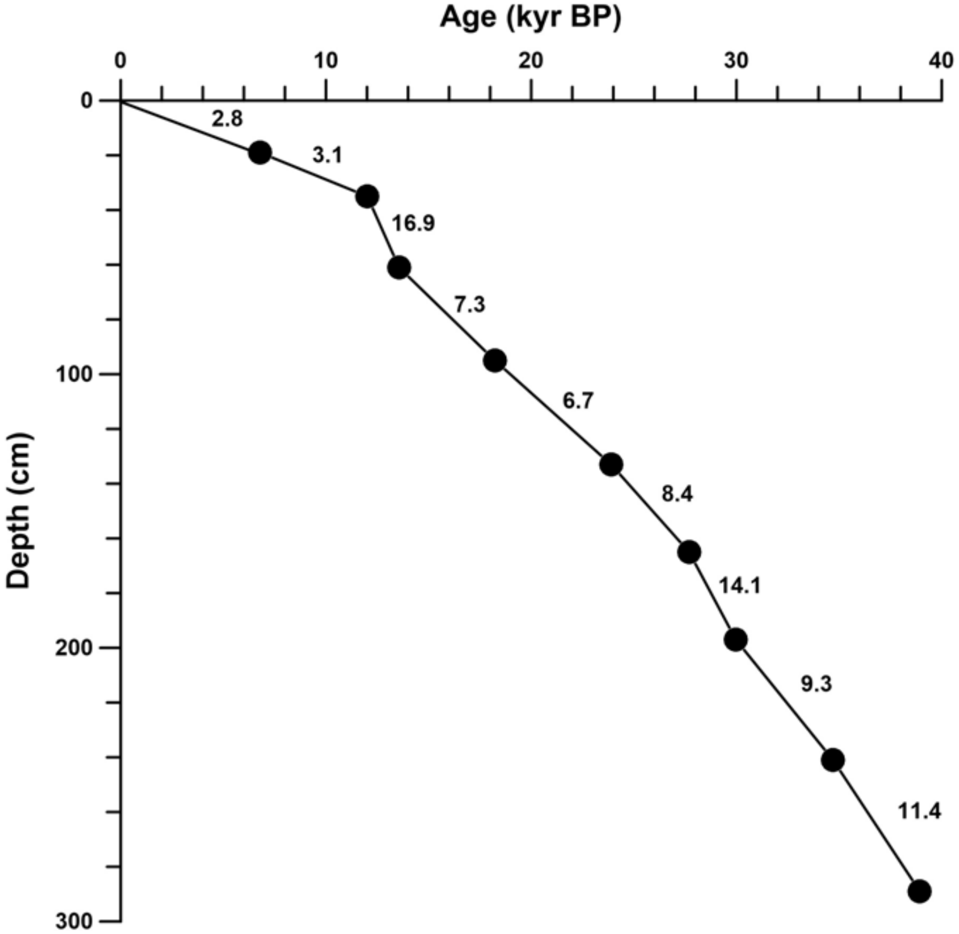

FIGURE 2 | Depth versus calibrated AMS^{14}C age and linear sedimentation rate (LSR) plots of core BoB-56 (Li et al., 2018). The LSR is listed for each interval in cm/kyr.

Where, CaO* refers to CaO contents in the silicate. In this study, the method from Mclennan et al. (1993) was adopted to approximately correct the CaO* content for the presence of Ca in carbonates (calcite and dolomite) and phosphates (apatite). CaO was corrected for phosphate using P_2O_5. If the remaining number of moles is less than that of Na_2O, this CaO value is adopted. Otherwise, CaO* is assumed to be equivalent to Na_2O. In this method, minimum CIA values could be yielded since the Ca lost more rapidly than Na during weathering. UCC refers to the Upper Continental Crust (Taylor and Mclennan, 1985). In this study, E = Na.

Principal Component Analysis

To better extract the inner regularities and further constrain the controlling mechanisms of the chemical weathering indexes, the principal component analysis (PCA) is performed for these chemical weathering dataset (CIA, WIP, and α^{Al}Na), using the IBM SPSS Statistics 19.0 software. Generally, three conditions must be satisfied, including sufficient samples (at least five times the number of variables), a strong correlation between the original data (the Bartlett test of sphericity yields a value under 0.05 or the KMO measure of sampling adequacy is above 0.5), and significant common factors obtained (factor rotation if necessary). In this study, 441 data points are used and the Bartlett test of sphericity/the KMO measure of sampling adequacy yields values 0 and 0.64. Then, controlling factors with eigen value above 1 were extracted and the rotating component matrix was gotten by Maximum-variance Algorithm. Comparing with the climatic proxies, detailed variations and controlling mechanisms of chemical weathering intensity on different timescales were discussed.

RESULTS

Geochemical Composition Variations

The geochemical compositions and downcore variations of core BoB-56 sediments are presented in **Figure 3**. Al_2O_3, K_2O, and TiO_2 appear to vary synchronously, while the CaO contents tend to be a mirror trend. Na_2O shows a roughly similar average contents between the Last Glaciation and the Holocene periods, but a decreased trend since the Holocene period. Overall, higher contents of CaO are observed during the Holocene period and lower contents during the last glaciation. Meanwhile, opposite pattern is identified for other oxides. Alternation of high and low values could be seen during the last deglaciation. The major oxides contents, i.e., Al_2O_3, K_2O, TiO_2, CaO, and Na_2O range between 11.61 and 16.87%, 2.22 and 3.76%, 0.54 and 0.84%, 1.64 and 4 13.84%, and 2.13 and 3.06%, respectively, with average contents of 15.03, 3.00, 0.72, 6.39, and 2.60%, respectively. Similar to the geochemistry variations, sand fractions of core BoB-56 sediment show significantly higher volume contents during the Holocene period (averaged 7.08%), compared to the last glaciation (averaged 0.62%).

Chemical Weathering Intensity Estimation

Three chemical weathering indexes, including CIA, WIP, and α^{Al}Na used in this study are shown in **Figure 4**. All these indexes

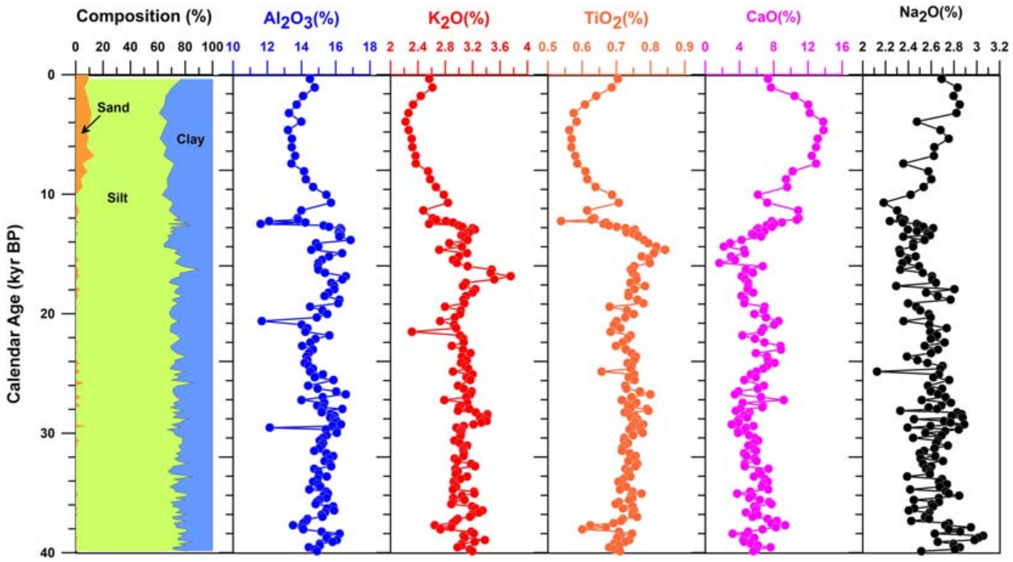

FIGURE 3 | Downcore variations of grain size (Li et al., 2018) and elemental composition in the core BoB-56.

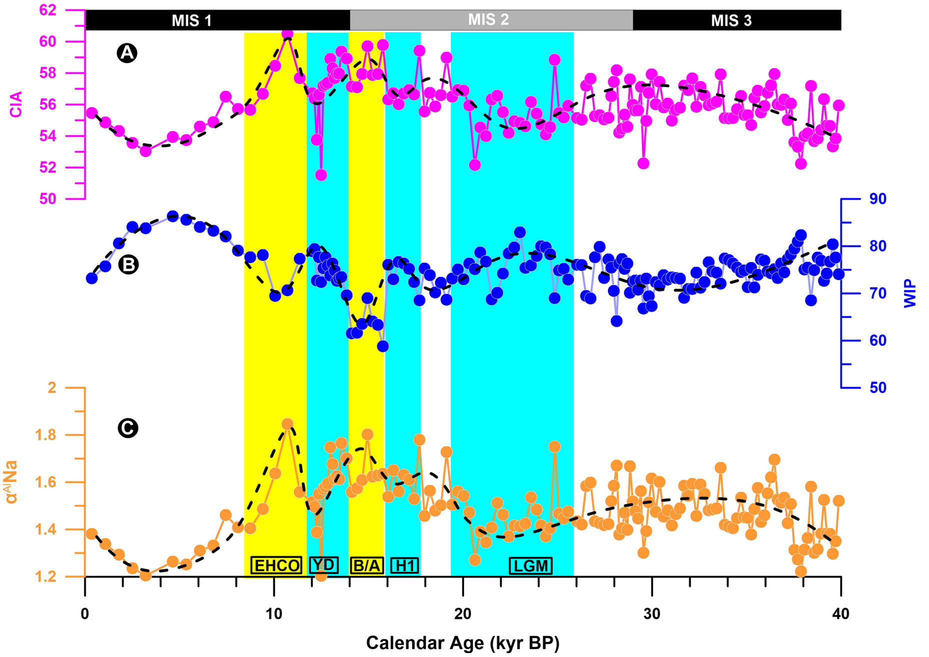

FIGURE 4 | Downcore variations of the chemical weathering indexes. **(A)** CIA; **(B)** WIP; and **(C)** α^{Al}Na.

TABLE 1 | Factor analysis of CIA, WIP, αAlNa, and extraction of three factors with eigen values > 1.

	F1	F2	F3
Eigen value	2.44	0.52	0.04
% variation	81.41	17.22	1.37
CIA	0.94	–0.31	0.14
WIP	-0.28	0.96	–0.06
α^{Al}Na	0.96	–0.26	–0.11

indicate a relatively weak chemical weathering condition on the whole. Within the current chronology frame, two precessional cycles (40–20 ka and 20 ka to present) can be identified through the whole cores. Two obvious low values are associated with the Last Glacial Maximum (LGM) and the Holocene period. However, the latter cycle (20 ka to present) shows a distinct peak with higher frequency oscillation, indicating that the elemental data might more closely follow higher-frequency event [e.g., Heinrich 1 (H1), Bølling/Allerød (B/A), Younger Dryas (YD), and Early Holocene Climate Optimum]. Actually, it reminds us of a millennial scale variation for the chemical weathering intensity. Briefly, the results exhibit that the chemical weathering proxies vary in two different cycles, precessional, and millennial cycles.

Principal Component Analysis of Chemical Weathering Indexes

The PCA results show that three components with eigen value above 1 could be extracted and 81% of common variance could be explained by the first component (F1; **Table 1**), clearly suggesting that the variations of chemical weathering proxies are mainly controlled by the same driving force. Considering the typical monsoon climate around the BoB and close relationship between climate and weathering (Romans et al., 2016; Liu et al., 2020), simultaneously compared downcore variations of F1 with the Indian summer monsoon (ISM) records in and around the BoB (**Figures 5**, **7**; Kudrass et al., 2001; Rashid et al., 2007; Berkelhammer et al., 2012; Raza et al., 2017), we could initially conclude that F1 represents control from the ISM, due to the covariant relationship between chemical weathering indexes (CIA and α^{Al}Na) and F1 (**Table 1** and **Figures 4**, **5**).

However, 20% of the elemental weathering signal is lost to other processes, mainly the F2 which could interpret 19% of the variations, and the main proxy controlled by F2 is the WIP (**Table 1** and **Figure 6A**). Comparing the calculation formulas of three chemical weathering proxies used in this study, the main difference between the WIP and the others is the MgO which is not contained in the CIA and α^{Al}Na. We plot F2 and these three proxies and MgO, CaO, Al_2O_3, K_2O, and Na_2O in the binary scatter diagram (**Figure 6**). It shows significant correlation between F2 and the WIP (R^2 = 0.90), but distinct expression between F2 and oxides during the last glaciation and the Holocene period. Positive correlation occurred between F2 and MgO, CaO during the last glaciation (R^2 = 0.39, 0.55, respectively), and significant positive correlation between F2 and CaO (R^2 = 0.97), negative correlation between F2 and MgO, Al_2O_3, and K_2O (R^2 = 0.89, 0.76, and 0.73, respectively) during the Holocene period could be seen. Na_2O shows nothing to do

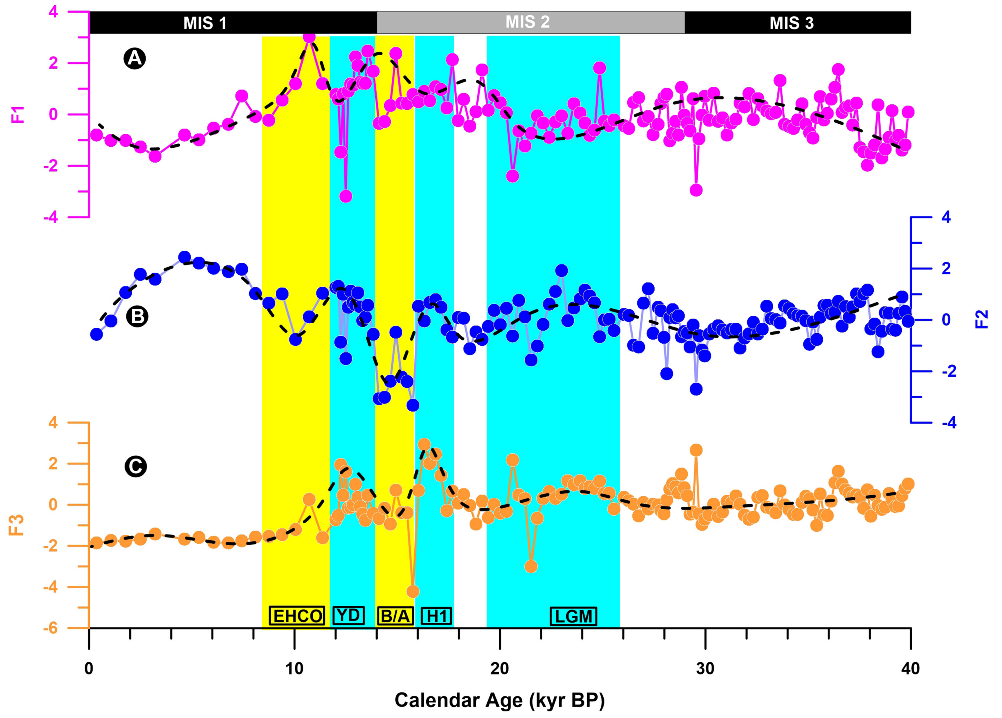

FIGURE 5 | Downcore variations of PCA components scores. **(A)** Curves of F1 scores; **(B)** curves of F2 scores; **(C)** curves of F3 scores.

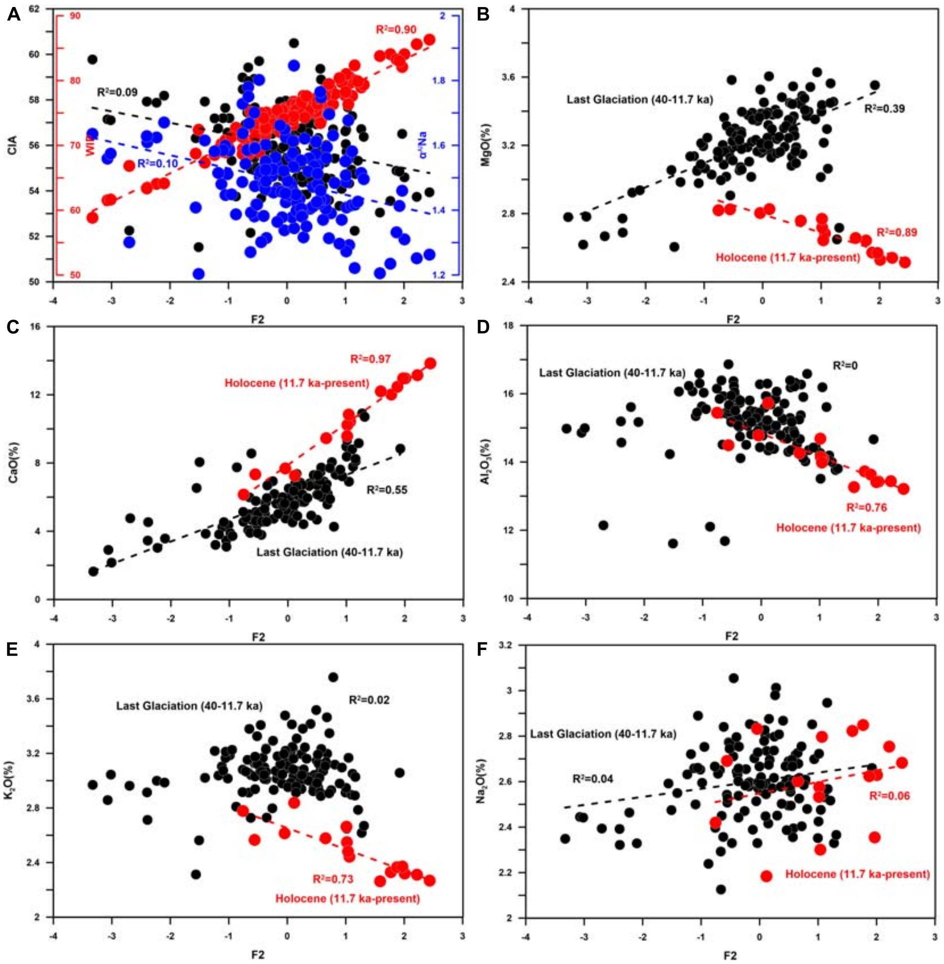

FIGURE 6 | Scatter diagrams between F2 and chemical weathering indexes and oxides. **(A)** Chemical weathering indexes (CIA-black circles, WIP-red circles and αAlNa-blue circles) vs F2 (the second factors extracted by principal component analysis); **(B)** MgO vs F2; **(C)** CaO vs F2; **(D)** Al_2O_3 vs F2; **(E)** K_2O vs F2; **(F)** Na_2O vs F2.

with F2 both in the last glaciation and the Holocene period. We thus suggest the F2 as control from carbonate input, both from the ocean and Ganges River (Garzanti et al., 2010). Dolomite and calcite could be the main carrier.

DISCUSSION

Chemical Weathering Intensity Responses to Monsoon Precipitation on Precessional Scale

Apart from climate, other driving forces including regional tectonic activity (Dixon et al., 2012; Liu et al., 2016a), rock types (Babechuk et al., 2014; Yang et al., 2004b; Liu et al., 2016b), vegetation (Galy et al., 2008; Shen et al., 2018), and geomorphology (Albert Galy, 1999; Yang et al., 2004a; Bouchez et al., 2012) also play important role in chemical weathering. The mountainous areas around the BoB have tectonically been stable during the last 40 ka. Weathering process has sensitive response to the distinctions in the lithology (e.g., ultramafic or granitic rocks) and landform (e.g., mountain or floodplain), mainly through climate change (precipitation/temperature). Long-term vegetation evolution is now suggested to be connected to the climate change (Galy et al., 2008; Shen et al., 2018). Thus, climate is suggested to be the main controlling factor of the chemical weathering intensity, since the last glacial period. Typical monsoon climate around the BoB provides us with abundant climate signatures, which could be carried by sediment particles and stored in the sink basins. Theoretically, our chronology framework has a resolution of 100–200 years and therefore has the ability to provide reliable climate signals above the millennium scale, excluding the negative processes such as signal attenuation and interference. Since the F1 shows co-variation with our indexes and faithfully record the chemical weathering dynamics and forcing mechanisms, we compared it with ISM precipitation, temperature, July solar radiation in 20°N, sea level and sedimentary rate to give a systematical analyses. The Indian monsoon intensity is affected by solar radiation, showing periodic changes on the precession scale, which is widely recorded in the Indian monsoon region (Prell and Kutzbach, 1987; Caley et al., 2011; Mohtadi et al., 2016). Our sedimentary records also show that chemical weathering indicators have roughly changed in two precession cycles simultaneously with the July solar radiation in 20°N and monsoon precipitation over the last 40,000 years (**Figures 4A,C**, **7I**). Here, the Ti/Ca ratio is calculated to estimate the terrestrial input variation, based on the stable feature of Ti in hypergenesis and considerable part of biogenic input CaO (Hu et al., 2012; Chen et al., 2013; Clift et al., 2014; Cao et al., 2015; Li et al., 2017, 2019) and its efficiency has been confirmed by the roughly consistent trend of the sedimentary rate (Li et al., 2019). The results show that the Ti/Ca ratio change simultaneously with the chemical weathering indexes (**Figures 4**, **7D**). Indeed, along the studied core, enhancing the chemical weathering is associated with the increase in the terrestrial input, vice versa. This pattern is similar to the temperature and precipitation patterns in the Asian monsoon regions recorded by stalagmite δ^{18}O values (Wang et al., 2001; Yuan et al., 2004; Berkelhammer et al., 2012; Raza et al., 2017) and planktonic foraminifera *G. ruber* δ^{18}O values in the BoB (Kudrass et al., 2001; **Figures 7A,B,E,F**). Combined with the PCA results and the low sea level (**Figures 7C,H**) which could ensure that the deposition center is located in the Bengal Fan (Curray et al., 2003; Li et al., 2019), this indicates the ISM controlled the weathering/erosion processes on precessional scale. During the oxygen isotope stage III and the last deglaciation, higher temperature (Rashid et al., 2007; Raza et al., 2017), and monsoon precipitation (Prell and Kutzbach, 1987; Kudrass et al., 2001) improved the erosion and weathering intensity in the source area, causing overall higher records of CIA, α^{Al}Na, Ti/Ca values and lower records of WIP values in the BoB (**Figures 4**, **7D**). On the other hand, during the LGM when temperature and monsoon precipitation decreased to the lowest level (Prell and Kutzbach, 1987; Kudrass et al., 2001; Rashid et al., 2007; Raza et al., 2017), both physical erosion and chemical weathering in the source area significantly weakened. Additionally, ice cover in the high mountains expanded, causing decreased exposure area, and erosion production (Owen et al., 2002). Corresponding to this cold and dry climate conditions, sedimentary records in the BoB showed lower CIA, α^{Al}Na, and Ti/Ca values, as well as higher WIP values (**Figures 4**, **7D**). It was also supported by lower CIA* values (∼10 reduction) and decreased Himalayan material contribution (∼30% reduction) in an adjacent core SK187/PC33 (Tripathy et al., 2014). It is worth noting that chemical weathering and terrestrial inputs are not fully synchronized with changes in monsoon rainfall and solar radiation, especially during the second precessional cycle (20 ka to present; **Figure 7**). This is due to the fact that the short-cycle climate changes on the millennial scale break up such long-cycle changes on the orbital scale and special circumstances during the Holocene period, which will be discussed in depth later.

Chemical Weathering Intensity Responses to Temperature and Monsoon Precipitation on Millennial Scale

Corresponding to alteration of warm/cold period during the last deglaciation, the precipitation and temperature in the Indian monsoon regions show a simultaneously alteration of higher/lower values distribution (Kudrass et al., 2001; Rashid et al., 2007; Raza et al., 2017). The obvious simultaneously alteration of higher/lower values in the chemical weathering and terrestrial input proxies records (**Figures 4**, **7D**) provides us with evidences supporting our hypothesis that monsoon climate drives the chemical weathering on millennial scale. In detail, during the cold periods, e.g., H1 and YD, the lower CIA, α^{Al}Na, and Ti/Ca values and the higher WIP values (**Figures 4**, **7D**) indicate the weakened chemical weathering and erosion intensity. In the northeastern Indian Ocean, climate during these two events were characterized by obvious weakened ISM intensity with sharply decreased trends of precipitation and temperature (Kudrass et al., 2001; Rashid et al., 2007; Raza et al., 2017). The lower total organic carbon contents in the Arabian Sea can be considered as additional evidence for a weakened ISM conditions (Schulz et al., 1998). During this period, simultaneously decreased precipitation and temperature improved the ice expansion (Chauhan, 2003) and limited glacial melting process and the water-rock interactions, thus decreased weathering reaction rate. Opposite circumstance occurred during the warm periods, e.g., B/A and Early Holocene Climatic Optimum (EHCO), when the increased ISM intensity was recorded in the Asian monsoon regions, as evidenced by the higher volume of melted ice in the Himalaya mountains (Benn and Owen, 1998), warmer and wetter climate (Weber et al., 1997), the rainfall (Kudrass et al., 2001; Yuan et al., 2004; Fleitmann et al., 2007), and runoff reconstructions from the northeastern Indian Ocean, based on the planktonic foraminifera *G. sacculifer* shell Ba/Ca ratios (Gebregiorgis et al., 2016). The prevailing warm-wet climate conditions improved the weathering rate again, causing the higher CIA, α^{Al}Na, and Ti/Ca values, as well as the lower WIP values in our studied core (**Figures 4**, **7D**). Briefly, it supported our hypothesis that chemical weathering intensity responses to temperature and monsoon precipitation on millennial scale.

Contradiction Between Chemical Weathering and Indian Monsoon Records During the Holocene Period: Reason and Applicability

After a period of co-variation, the chemical weathering indicators, and the monsoon indicators showed opposite paths during the Holocene period: both monsoon rainfall and temperature reconstruction results showed that ISM was significantly stronger during the Holocene period, in comparison with the last glaciation (Kudrass et al., 2001; Rashid et al., 2007; Raza et al., 2017; **Figures 7A,E,F**), while the lower CIA, α^{Al}Na, and Ti/Ca values and the higher WIP values reflected weaker chemical weathering intensity and less terrestrial input (**Figures 4**, **7D**). Although, between 6 and 3 ka both stalagmites δ^{18}O from South Asia and SST reconstruction results in the northeastern Indian Ocean recorded a significant reduction in rainfall and temperature (Berkelhammer et al., 2012; **Figures 7B,F**), more factors were responsible for the low chemical weathering intensity values in the whole middle-late Holocene period on glacial-interglacial scale, especially that chemical weathering intensity started to be decreased after the EHCO, but the rainfall and temperature were still at a high level (**Figures 7A,C,E,F**). Indeed, the chemical weathering intensity,

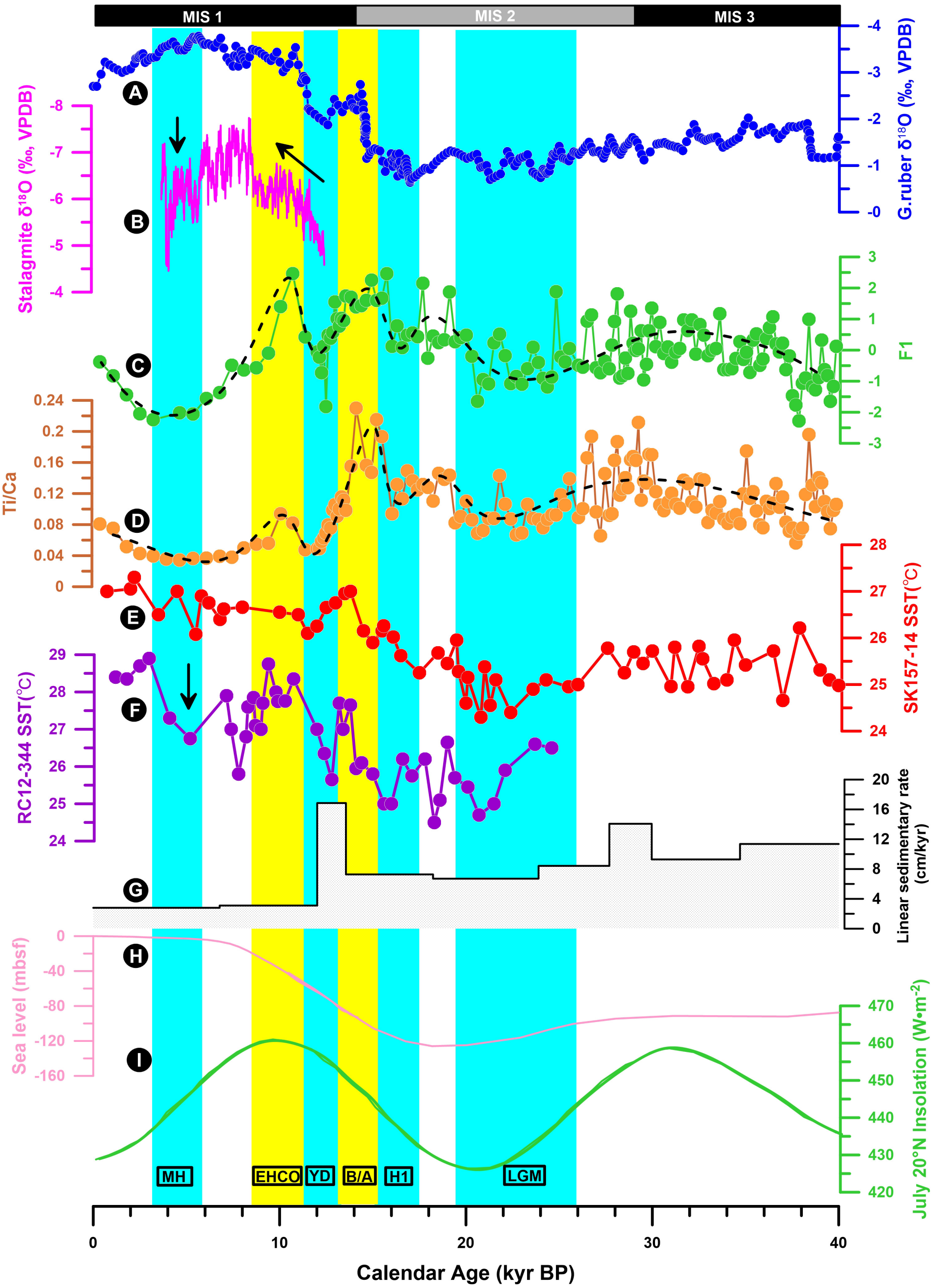

FIGURE 7 | Comparison of curves for chemical weathering intensity and climate proxies. **(A)** *G. ruber* $\delta^{18}O$ data from the core SO-126KL located in the northern BoB (Kudrass et al., 2001); **(B)** Mawmluh Cave stalagmite $\delta^{18}O$ data (Berkelhammer et al., 2012); **(C)** Chemical weathering stack of the core BoB-56; **(D)** Ti/Ca of the core BoB-56; **(E)** SST from the core SK157-14 from northeastern Indian Ocean (Raza et al., 2017); **(F)** SST from the core RC12-344 from northeastern Indian Ocean (Rashid et al., 2007); **(G)** Linear sedimentary rate of core BoB-56 (Li et al., 2019); **(H)** Sea level curve (Arz et al., 2007; Stanford et al., 2011); and **(I)** July insolation at 20°N (Prell and Kutzbach, 1987). The cyan and yellow color bars show the typical millennial scale intervals. LGM, Last Glacial Maximum; H1, Heinrich 1; B/A, Bølling/Allerød; YD, Younger Dryas; EHCO, Early Holocene Climatic Optimum; MH, Middle Holocene; and SST, Sea surface temperature. The dashed lines in **(C,D)** indicate the variation trends of the proxies.

revealed by clay minerals in the BoB, is consistent with that of the ISM intensity: e.g., a stronger intensity is identified in the Holocene, compared to the last glaciation (Li et al., 2018; Liu et al., 2019; Yu et al., 2020). In particular, clay mineral index smectite/(illite + chlorite) ratio and K/Al (molar ratio) in adjacent cores MD12-3417 and MD12-3418CQ also indicate increasing weathering since the Holocene period (Joussain et al., 2017). Moreover, it is widely accepted that the ISM during the Holocene was significantly stronger than the last glaciation (Kudrass et al., 2001; Rashid et al., 2007; Raza et al., 2017). A new question arises: why did the chemical weathering indicators (such as CIA, WIP, and α^{Al}Na) sensitivities reduced during the Holocene? Taking CIA as an example, the reasons may be, as follows:

The CIA is significantly affected by sediment grain size. The Ganges river "bank sediment-surface water suspension-bedload" depth profile CIA results show that the particles with a size of less than 0.1 μm in the bank sediment show the highest CIA value (CIA = 94). The particles with less than 2 μm in the bank sediment and surface water suspension show the similar CIA value (CIA = 82–85), while, the bulk sediments contain the lowest CIA value and the value of the surface suspension bulk CIA (CIA = 71) is higher than that of the bedload (CIA = 58; Garzanti et al., 2010, 2011; **Figure 8A**). Studies on the CIA value of bedload and suspension in G-B River show that the CIA value of suspension (mostly between 60 and 80) is significantly higher than that of bedload (mostly between 50 and 60; Singh and France-Lanord, 2002; Singh, 2009; Garzanti et al., 2010; **Figures 8B–D**). The bulk sediment CIA values of core BoB-56 are between 50 and 60 (**Figure 4A**), which is closer to the CIA of the bedload, with the clay fraction content of below 30% (**Figure 3**). Grain size of sediments in the core BoB-56 show a coarsening upward trend from the last glaciation to the Holocene period, with around 7% increase in the sand fractions (**Figure 3**). This seems to explain why fine particles (<2 μm), represented by clay minerals, indicates significantly stronger chemical weathering during the Holocene period than the last glaciation (Li et al., 2018; Yu et al., 2020), which is the opposite of the circumstance reflected by the bulk sediment geochemistry in this study (**Figure 4**).

The obvious difference of CIA between the two geomorphic units in the source region (high mountain terrain and low plain terrain) can be considered as another possible factor. The high mountain terrain is dominated by physical erosion and has relatively weak chemical weathering intensity, while, the low terrain, represented by the Indo-Gangetic Plain, has relatively

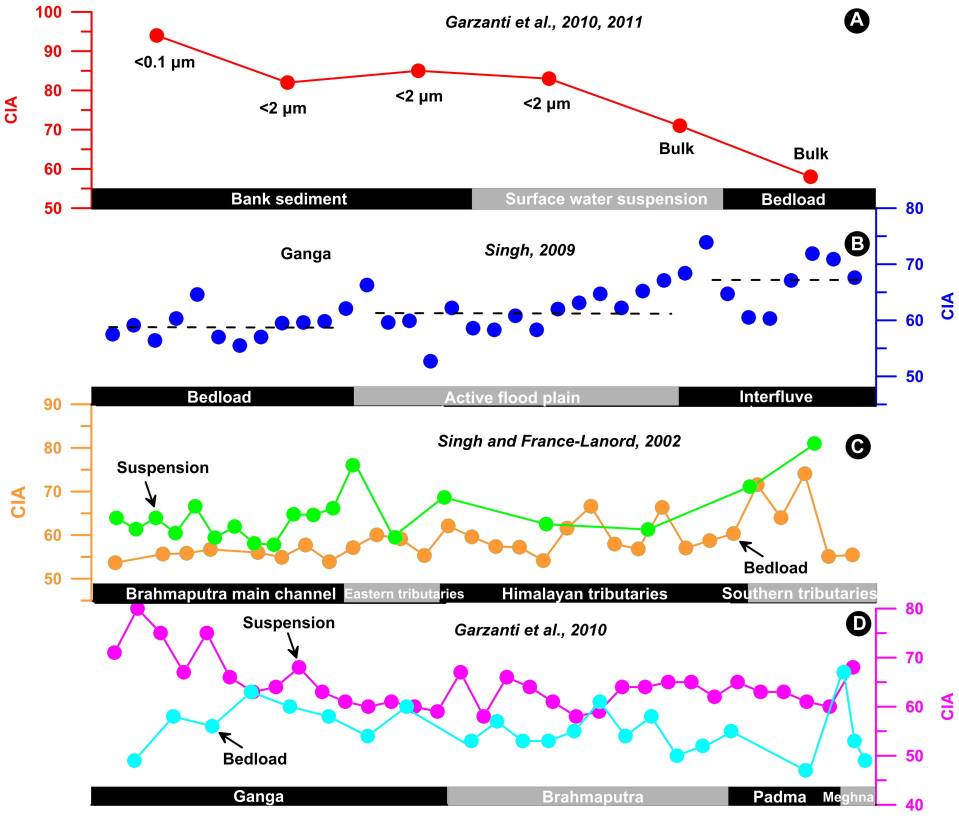

FIGURE 8 | CIA records in the source area (modified from published literature). **(A)** "Bank-suspension-bedload" CIA depth profile in the Ganga River (Garzanti et al., 2010, 2011); **(B)** CIA records in the Ganga River and its flood plain (Singh, 2009); **(C)** Bedload and suspension CIA records in the main channel and different tributaries of the Brahmaputra River (Singh and France-Lanord, 2002); and **(D)** Bedload and suspension CIA records in different rivers passing the Bangladesh (Garzanti et al., 2010).

stronger chemical weathering intensity and the CIA value is significantly higher than that of the mountain (Singh and France-Lanord, 2002; Owen, 2009; Singh, 2009). Under the background of significantly enhanced ISM during the Holocene, the erosion rate accelerated and the erosion yield and flux to the ocean increased significantly in both mountains and flood plains. As a result, the largest delta in the world, the G-B River delta, was constructed and improved. Subsequently, the continental shelf was submerged and the deposition center shifted from the Bengal Fan to the shelf, as a result of about 120–130 m sea level rise during the Holocene (Arz et al., 2007; Stanford et al., 2011), causing deduction in the sediment flux reaching the deep sea, hence, decrease in the Ti/Ca ratio during the Holocene (**Figure 7D**), though the ISM enhanced. Sediment in the floodplain are relatively fine and contribute a lot to the fine fractions, represented by clay minerals in the Bengal Fan. Smectite is originated mainly from the Indo-Gangetic Plain (Sarin et al., 1989; Huyghe et al., 2011). Therefore, the content of smectite in the BoB increased significantly under the background of intensified ISM during the Holocene, revealing strong chemical weathering dynamics (Joussain et al., 2016; Li et al., 2018; Yu et al., 2020). Studies of the adjacent cores MD12-3417 and MD12-3418CQ provide detail evidences of distinct weathering between high mountain terrain and the Indo-Gangetic Plain during the Holocene period (Joussain et al., 2017), which might be a supplement for our data during the Holocene period. Three stages, 9.2–7, 6.0–2.5, and 2.5 ka to present were divided and indicated more input from the mountains, the Indo-Gangetic Plain and plain soils due to anthropogenic activity, respectively. Due to the increase of physical erosion in the high mountain terrain, as the main sediment supplier, together with the grain size effect discussed above, the CIA value of bulk sediment decreased (**Figure 4A**). Therefore, it can be concluded that the bulk sediment geochemical-based weathering indicators, including CIA, WIP, and α^{Al}Na could not accurately reflect the chemical weathering dynamics of the source region and they appear to be a mixture of physical erosion and chemical weathering signals, which should be treated with caution.

CONCLUSION

1. Three geochemistry-based indexes, CIA, WIP, and α^{Al}Na, were extracted to estimate chemical weathering intensity dynamics. Overall, changes in the chemical weathering intensity were coincide with that of 20°N insolation, precipitation, and temperature changes, indicating that the ISM controlled weathering on precessional scales.
2. Obvious response between climate and chemical weathering occurred during the last deglaciation: stronger weathering during the B/A and EHCO periods, weaker weathering during the H1 and YD periods. The higher (lower) precipitation and temperature enhanced (weakened) the chemical weathering intensity during these warm (cold) periods, suggesting presence of control from the ISM on weathering on millennial scales.
3. Chemical weathering indexes showed significantly lower values during the Holocene period, which was inconsistence with the rising ISM precipitation and temperature. Besides the possible weakened monsoon during 6–3 ka, the grain size effect (finer particles are more sensitive than the bulk sediment especially when sand fractions increased), and relative geological location (sediment from the high mountain terrain has significant lower chemical weathering intensity than that from the low plain terrain) were suggested to be comprehensively responsible for this contradiction. Thus, the CIA, WIP, and α^{Al}Na values from bulk sediments cannot be representative of the chemical weathering intensity during the Holocene, as they seem to be a mixture of physical erosion and chemical weathering.

DATA AVAILABILITY STATEMENT

The original contributions presented in the study are included in the article/**Supplementary Material**, further inquiries can be directed to the corresponding author/s.

AUTHOR CONTRIBUTIONS

JL, XS, and SL proposed the topic, and conceived and designed the study. JL wrote the manuscript. HZ, PC, and XL carried out the experimental study and data analyses. H-JP, SK, and NK helped in data interpretation. SL collaborated with the corresponding author, XS, in the construction of the manuscript. All authors read and approved the final manuscript.

FUNDING

This work was supported by the National Program on Global Change and Air-Sea Interaction (GASI-GEOGE-06-03), the National Nature Science Foundation of China (41806081, U1606401, and 41676054), Natural Science Foundation of Shandong Province (ZR2019BD018), China-Thailand cooperation project "Research on Vulnerability of Coastal Zones," and the Taishan Scholar Program of Shandong.

ACKNOWLEDGMENTS

We would like to thank scientists from the First Institute of Oceanography, Ministry of Natural Resources, China, and the Phuket Marine Biological Center, Thailand, for sediment sampling.

SUPPLEMENTARY MATERIAL

The Supplementary Material for this article can be found online at: https://www.frontiersin.org/articles/10.3389/feart.2021.633713/full#supplementary-material

REFERENCES

Albert Galy, C. F.-L. (1999). Weathering processes in the Ganges–Brahmaputra basin and the riverine alkalinity budget. *Chem. Geol.* 159:30.

Arz, H. W., Lamy, F., Ganopolski, A., Nowaczyk, N., and Pätzold, J. (2007). Dominant Northern Hemisphere climate control over millennial-scale glacial sea-level variability. *Quat. Sci. Rev.* 26, 312–321. doi: 10.1016/j.quascirev.2006.07.016

Babechuk, M. G., Widdowson, M., and Kamber, B. S. (2014). Quantifying chemical weathering intensity and trace element release from two contrasting basalt profiles. Deccan Traps, India. *Chem. Geol.* 363, 56–75. doi: 10.1016/j.chemgeo.2013.10.027

Benn, D. I., and Owen, L. A. (1998). The role of the Indian summer monsoon and the mid-latitude westerlies inHimalayan glaciation-review and speculative discussion. *J. Geol. Soc.* 155, 353–363. doi: 10.1144/gsjgs.155.2.0353

Berkelhammer, M., Sinha, A., Stott, L., Cheng, H., Pausata, F. S. R., and Yoshimura, K. (2012). "An abrupt shift in the indian monsoon 4000 years ago," in *Geophysical Monograph Series: Climate Landscapes and Civilization*, eds L. Giosan, D. Q. Fuller, K. Nicoll, R. K. Flad, and P. D. Clift (Washington, D.C: AGU), 75–88. doi: 10.1029/2012gm001207

Berner, R. A. (1992). Weathering, plants, and the long-term carbon cycle. *Geochimica et Cosmochimica Acta* 56, 3225–3231. doi: 10.1016/0016-7037(92)90300-8

Bolton, C. T., Chang, L., Clemens, S. C., Kodama, K., Ikehara, M., Medina-Elizalde, M., et al. (2013). A 500,000 year record of Indian summer monsoon dynamics recorded by eastern equatorial Indian Ocean upper water-column structure. *Quat. Sci. Rev.* 77, 167–180. doi: 10.1016/j.quascirev.2013.07.031

Bouchez, J., Gaillardet, J., Lupker, M., Louvat, P., France-Lanord, C., Maurice, L., et al. (2012). Floodplains of large rivers: weathering reactors or simple silos? *Chem. Geol.* 33, 166–184. doi: 10.1016/j.chemgeo.2012.09.032

Caley, T., Malaizé, B., Zaragosi, S., Rossignol, L., Bourget, J., Eynaud, F., et al. (2011). New Arabian Sea records help decipher orbital timing of Indo-Asian monsoon. *Earth Planetary Sci. Lett.* 308, 433–444.

Cao, P., Shi, X., Li, W., Liu, S., Yao, Z., Hu, L., et al. (2015). Sedimentary responses to the Indian Summer Monsoon variations recorded in the southeastern Andaman Sea slope since 26ka. *J. Asian Earth Sci.* 114, 512–525. doi: 10.1016/j.jseaes.2015.06.028

Chauhan, O. S. (2003). Past 20,000-year history of Himalayan aridity: evidence from oxygen isotope records in the Bay of Bengal. *Curr. Sci.* 84, 90–93.

Chen, H.-F., Yeh, P.-Y., Song, S.-R., Hsu, S.-C., Yang, T.-N., Wang, Y., et al. (2013). The Ti/Al molar ratio as a new proxy for tracing sediment transportation processes and its application in aeolian events and sea level change in East Asia. *J. Asian Earth Sci.* 73, 31–38. doi: 10.1016/j.jseaes.2013.04.017

Clemens, S. C., and Prell, W. L. (2003). A 350,000 year summer-monsoon multi-proxy stack from the Owen Ridge. Northern Arabian Sea. *Mar. Geol.* 201, 35–51. doi: 10.1016/s0025-3227(03)00207-x

Clift, P. D., Wan, S., and Blusztajn, J. (2014). Reconstructing chemical weathering, physical erosion and monsoon intensity since 25Ma in the northern South China Sea: a review of competing proxies. *Earth-Science Rev.* 130, 86–102. doi: 10.1016/j.earscirev.2014.01.002

Curray, J., and Moore, D. (1971). Growth of the bengal deep-sea fan and denudation in the Himalayas. *Geol. Soc. Am. Bull.* 82, 563–572. doi: 10.1130/0016-7606(1971)82[563:gotbdf]2.0.co;2

Curray, J. R., Emmel, F. J., and Moore, D. G. (2003). The Bengal Fan: morphology, geometry, stratigraphy, history and processes. *Mar. Petroleum Geol.* 19, 1191–1223. doi: 10.1016/s0264-8172(03)00035-7

Dixon, J. L., Hartshorn, A. S., Heimsath, A. M., DiBiase, R. A., and Whipple, K. X. (2012). Chemical weathering response to tectonic forcing: a soils perspective from the San Gabriel Mountains. *California. Earth Planetary Sci. Lett.* 32, 40–49. doi: 10.1016/j.epsl.2012.01.010

Duplessy, J. C. (1982). Glacial to interglacial contrasts in the northern Indian Ocean. *Nature* 295, 494–498. doi: 10.1038/295494a0

Eiriksdottir, E. S., Gislason, S. R., and Oelkers, E. H. (2011). Does runoff or temperature control chemical weathering rates? *Appl. Geochem.* 26, S346–S349.

Fleitmann, D., Burns, S. J., Mangini, A., Mudelsee, M., Kramers, J., Villa, I., et al. (2007). Holocene ITCZ and Indian monsoon dynamics recorded in stalagmites from Oman and Yemen (Socotra). *Quat. Sci. Rev.* 26, 170–188. doi: 10.1016/j.quascirev.2006.04.012

Fleitmann, D., Burns, S. J., Mudelsee, M., Neff, U., Kramers, J., Mangini, A., et al. (2003). Holocene forcing of the Indian monsoon recorded in a stalagmite from Southern Oman. *Science* 300, 1737–1739. doi: 10.1126/science.1083130

Gaillardet, J., Dupré, B., and Allègre, C. J. (1999). Geochemistry of large river suspended sediments: silicate weathering or recycling tracer? *Geochimica et Cosmochimica Acta* 63, 4037–4051. doi: 10.1016/s0016-7037(99)00307-5

Galy, V., François, L., France-Lanord, C., Faure, P., Kudrass, H., Palhol, F., et al. (2008). C4 plants decline in the Himalayan basin since the Last Glacial Maximum. *Quat. Sci. Rev.* 27, 1396–1409. doi: 10.1016/j.quascirev.2008.04.005

Garzanti, E., Andó, S., France-Lanord, C., Censi, P., Vignola, P., Galy, V., et al. (2011). Mineralogical and chemical variability of fluvial sediments 2. Suspended-load silt (Ganga–Brahmaputra, Bangladesh). *Earth Planetary Sci. Lett.* 302, 107–120. doi: 10.1016/j.epsl.2010.11.043

Garzanti, E., Andò, S., France-Lanord, C., Vezzoli, G., Censi, P., Galy, V., et al. (2010). Mineralogical and chemical variability of fluvial sediments1. Bedload sand (Ganga–Brahmaputra, Bangladesh). *Earth Planetary Sci. Lett.* 299, 368–381. doi: 10.1016/j.epsl.2010.09.017

Garzanti, E., Limonta, M., Resentini, A., Bandopadhyay, P. C., Najman, Y., Andò, S., et al. (2013). Sediment recycling at convergent plate margins (Indo-Burman Ranges and Andaman–Nicobar Ridge). *Earth-Science Rev.* 123, 113–132. doi: 10.1016/j.earscirev.2013.04.008

Gebregiorgis, D., Hathorne, E. C., Sijinkumar, A. V., Nath, B. N., Nürnberg, D., and Frank, M. (2016). South Asian summer monsoon variability during the last 54 kyrs inferred from surface water salinity and river runoff proxies. *Quat. Sci. Rev.* 138, 6–15. doi: 10.1016/j.quascirev.2016.02.012

Gupta, A. K., Das, M., and Anderson, D. M. (2005). Solar influence on the Indian summer monsoon during the Holocene. *Geophys. Res. Lett.* 32, 1–4.

He, J., Garzanti, E., Dinis, P., Yang, S., and Wang, H. (2020). Provenance versus weathering control on sediment composition in tropical monsoonal climate (South China) - 1. Geochemistry and clay mineralogy. *Chem. Geol.* 558:119860. doi: 10.1016/j.chemgeo.2020.119860

Hu, D., Böning, P., Köhler, C. M., Hillier, S., Pressling, N., Wan, S., et al. (2012). Deep sea records of the continental weathering and erosion response to East Asian monsoon intensification since 14ka in the South China Sea. *Chem. Geol.* 32, 1–18. doi: 10.1016/j.chemgeo.2012.07.024

Huyghe, P., Guilbaud, R., Bernet, M., Galy, A., and Gajurel, A. P. (2011). Significance of the clay mineral distribution in fluvial sediments of the Neogene to Recent Himalayan Foreland Basin (west-central Nepal). *Basin Res.* 23, 332–345. doi: 10.1111/j.1365-2117.2010.00485.x

Jerolmack, D. J., and Paola, C. (2010). Shredding of environmental signals by sediment transport. *Geophys. Res. Lett.* 37, 1–5.

Joussain, R., Colin, C., Liu, Z., Meynadier, L., Fournier, L., Fauquembergue, K., et al. (2016). Climatic control of sediment transport from the Himalayas to the proximal NE Bengal Fan during the last glacial-interglacial cycle. *Quat. Sci. Rev.* 148, 1–16. doi: 10.1016/j.quascirev.2016.06.016

Joussain, R., Liu, Z., Colin, C., Duchamp-Alphonse, S., Yu, Z., Moréno, E., et al. (2017). Link between Indian monsoon rainfall and physical erosion in the Himalayan system during the Holocene. *Geochem. Geophys. Geosystems* 18, 3452–3469. doi: 10.1002/2016gc006762

Kudrass, H. R., Hofmann, A., Doose, H., Emeis, K., and Erlenkeuser, H. (2001). Modulation and amplification of climatic changes in the Northern Hemisphere by the Indian summer monsoon during the past 80 ky. *Geology* 29, 63–66. doi: 10.1130/0091-7613(2001)029<0063:maaocc>2.0.co;2

Li, J., Liu, S., Feng, X., Sun, X., and Shi, X. (2017). Major and trace element geochemistry of the mid-Bay of Bengal surface sediments: implications for provenance. *Acta Oceanol. Sinica* 36, 82–90. doi: 10.1007/s13131-017-1041-z

Li, J., Liu, S., Shi, X., Chen, M.-T., Zhang, H., Zhu, A., et al. (2020). Provenance of terrigenous sediments in the central Bay of Bengal and its relationship to climate changes since 25?ka. *Prog. Earth Planetary Sci.* 7:16.

Li, J., Liu, S., Shi, X., Zhang, H., Fang, X., Cao, P., et al. (2019). Sedimentary responses to the sea level and Indian summer monsoon changes in the central Bay of Bengal since 40?ka. *Mar. Geol.* 415:105947. doi: 10.1016/j.margeo.2019.05.006

Li, J., Liu, S., Shi, X., Zhang, H., Fang, X., Chen, M.-T., et al. (2018). Clay minerals and Sr-Nd isotopic composition of the Bay of Bengal sediments: implications for sediment provenance and climate control since 40 ka. *Quat. Int.* 493, 50–58. doi: 10.1016/j.quaint.2018.06.044

Liu, J., He, W., Cao, L., Zhu, Z., Xiang, R., Li, T., et al. (2019). Staged fine-grained sediment supply from the Himalayas to the Bengal Fan in response to climate change over the past 50,000 years. *Quat. Sci. Rev.* 212, 164–177. doi: 10.1016/j.quascirev.2019.04.008

Liu, J. T., Hsu, R. T., Hung, J.-J., Chang, Y.-P., Wang, Y.-H., Rendle-Bühring, R. H., et al. (2016a). From the highest to the deepest: the Gaoping River–Gaoping Submarine Canyon dispersal system. *Earth-Science Rev.* 153, 274–300. doi: 10.1016/j.earscirev.2015.10.012

Liu, Z., Zhao, Y., Colin, C., Stattegger, K., Wiesner, M. G., Huh, C.-A., et al. (2016b). Source-to-sink transport processes of fluvial sediments in the South China Sea. *Earth-Science Rev.* 153, 238–273. doi: 10.1016/j.earscirev.2015.08.005

Liu, S., Li, J., Zhang, H., Cao, P., Mi, B., Khokiattiwong, S., et al. (2020). Complex response of weathering intensity registered in the Andaman Sea sediments to the Indian Summer Monsoon over the last 40 kyr. *Mar. Geol.* 426:106206. doi: 10.1016/j.margeo.2020.106206

Liu, S., Shi, X., Liu, Y., Wu, Y., Yang, G., and Wang, X. (2013). Holocene paleoclimatic reconstruction based on mud deposits on the inner shelf of the East China Sea. *J. Asian Earth Sci.* 69, 113–120. doi: 10.1016/j.jseaes.2013.01.003

Mclennan, S. M., Hemming, S. R., Mcdaniel, D. K., and Hanson, G. N. (1993). Geochemical approaches to sedimentation, provenance, and tectonics. *Special Paper of the Geological Society of America* 284, 21–40. doi: 10.1130/SPE284-p21

Miriyala, P., Sukumaran, N. P., Nath, B. N., Ramamurty, P. B., Sijinkumar, A. V., Vijayagopal, B., et al. (2017). Increased chemical weathering during the deglacial to mid-Holocene summer monsoon intensification. *Sci. Rep.* 7:44310.

Mohtadi, M., Prange, M., and Steinke, S. (2016). Palaeoclimatic insights into forcing and response of monsoon rainfall. *Nature* 533, 191–199. doi: 10.1038/nature17450

Nesbitt, H. W., and Young, G. M. (1982). Early Proterozoic climates and plate motions inferred from major element chemistry of lutites. *Nature* 299, 715–717. doi: 10.1038/299715a0

Owen, L., Finkel, R., and Caffee, M. (2002). A note on the extent of glaciation throughout the Himalaya during the global Last Glacial Maximum. *Quat. Sci. Rev.* 21, 147–157. doi: 10.1016/s0277-3791(01)00104-4

Owen, L. A. (2009). Latest pleistocene and holocene glacier fluctuations in the Himalaya and tibet. *Quat. Sci. Rev.* 28, 2150–2164. doi: 10.1016/j.quascirev.2008.10.020

Parker, A. (1970). An index of weathering for silicate rocks. *Geol. Magazine* 107, 501–504. doi: 10.1017/s0016756800058581

Prell, W. L., and Kutzbach, J. E. (1987). Monsoon variability over the past 150,000 years. *J. Geophys. Res.* 92, 8411–8425. doi: 10.1029/jd092id07p08411

Rashid, H., Flower, B. P., Poore, R. Z., and Quinn, T. M. (2007). A 25ka Indian Ocean monsoon variability record from the Andaman Sea. *Quat. Sci. Rev.* 26, 2586–2597. doi: 10.1016/j.quascirev.2007.07.002

Raza, T., Ahmad, S. M., Steinke, S., Raza, W., Lone, M. A., Beja, S. K., et al. (2017). Glacial to Holocene changes in sea surface temperature and seawater δ18O in the northern Indian Ocean. *Palaeogeography Palaeoclimatol. Palaeoecol.* 485, 697–705. doi: 10.1016/j.palaeo.2017.07.026

Rodolfo, K. (1969). Sediments of the Andaman Basin, northeastern Indian Ocean. *Mar. Geol.* 7, 371–182. doi: 10.1016/0025-3227(69)90014-0

Romans, B. W., Castelltort, S., Covault, J. A., Fildani, A., and Walsh, J. P. (2016). Environmental signal propagation in sedimentary systems across timescales. *Earth-Science Rev.* 153, 7–29. doi: 10.1016/j.earscirev.2015.07.012

Sarin, M. M., Krishnaswami, S., Dilli, K., Somayajulu, B. L. K., and Moore, W. S. (1989). Major ion chemistry of the Ganga-Brahmaputra river system: weathering processes and fluxes to the Bay of Bengal. *Geochimica et Cosmochimica Acta* 53, 997–1009. doi: 10.1016/0016-7037(89)90205-6

Schulz, H., Rad, U. V., and Erlenkeuser, H. (1998). Correlation between Arabian Sea and Greenland climate oscillations of the past 110,000 years. *Nature* 393, 54–57. doi: 10.1038/31750

Sebastian, T., Nagender Nath, B., Venkateshwarlu, M., Miriyala, P., Prakash, A., Linsy, P., et al. (2019). Impact of the Indian Summer Monsoon variability on the source area weathering in the Indo-Burman ranges during the last 21?kyr: a sediment record from the Andaman Sea. *Palaeogeography Palaeoclimatol. Palaeoecol.* 516, 22–34. doi: 10.1016/j.palaeo.2018.11.035

Shen, X., Wan, S., Colin, C., Tada, R., Shi, X., Pei, W., et al. (2018). Increased seasonality and aridity drove the C4 plant expansion in Central Asia since the Miocene–Pliocene boundary. *Earth Planetary Sci. Lett.* 502, 74–83. doi: 10.1016/j.epsl.2018.08.056

Singh, M., Singh, I. B., and Müller, G. (2007). Sediment characteristics and transportation dynamics of the Ganga River. *Geomorphology* 86, 144–175. doi: 10.1016/j.geomorph.2006.08.011

Singh, P. (2009). Major, trace and REE geochemistry of the Ganga River sediments: influence of provenance and sedimentary processes. *Chem. Geol.* 266, 242–255. doi: 10.1016/j.chemgeo.2009.06.013

Singh, S. K., and France-Lanord, C. (2002). Tracing the distribution of erosion in the Brahmaputra watershed from isotopic compositions of stream sediments. *Earth Planetary Sci. Lett.* 202, 645–662. doi: 10.1016/s0012-821x(02)00822-1

Stanford, J. D., Hemingway, R., Rohling, E. J., Challenor, P. G., Medina-Elizalde, M., and Lester, A. J. (2011). Sea-level probability for the last deglaciation: a statistical analysis of far-field records. *Global Planetary Change* 79, 193–203. doi: 10.1016/j.gloplacha.2010.11.002

Taylor, S. R., and Mclennan, S. M. (1985). The continental crust: its composition and evolution. *J. Geol.* 94, 632–633.

Tripathy, G. R., Singh, S. K., and Ramaswamy, V. (2014). Major and trace element geochemistry of Bay of Bengal sediments: implications to provenances and their controlling factors. *Palaeogeography Palaeoclimatol. Palaeoecol.* 397, 20–30. doi: 10.1016/j.palaeo.2013.04.012

Walker, J. C. G., Hays, P. B., and Kasting, J. F. (1981). A negative feedback mechanism for the long-term stabilization of Earth's surface temperature. *J. Geophys. Res.: Oceans* 86, 9776–9782. doi: 10.1029/jc086ic10p09776

Wang, Y. J., Cheng, H., Edwards, R. L., An, Z. S., Wu, J. Y., Shen, C. C., et al. (2001). A high-resolution absolute-dated late Pleistocene Monsoon record from Hulu Cave. China. *Science* 294, 2345–2348. doi: 10.1126/science.1064618

Weber, M. E., Wiedicke, M. H., Kudrass, H. R., Hübscher, C., and Erlenkeuser, E. (1997). Active growth of the Bengal Fan during sea-level rise and highstand. *Geology* 25, 315–318. doi: 10.1130/0091-7613(1997)025<0315:agotbf>2.3.co;2

Xu, Z., Li, T., Clift, P. D., Wan, S., Qiu, X., and Lim, D. (2018). Bathyal records of enhanced silicate erosion and weathering on the exposed Luzon shelf during glacial lowstands and their significance for atmospheric CO 2 sink. *Chem. Geol.* 476, 302–315. doi: 10.1016/j.chemgeo.2017.11.027

Yang, S. Y., Jung, H. S., and Li, C. X. (2004a). Two unique weathering regimes in the Changjiang and Huanghe drainage basins: geochemical evidence from river sediments. *Sedimentary Geol.* 164, 19–34. doi: 10.1016/j.sedgeo.2003.08.001

Yang, S. Y., Li, C. X., Yang, D. Y., and Li, X. S. (2004b). Chemical weathering of the loess deposits in the lower Changjiang Valley, China, and paleoclimatic implications. *Quat. Int.* 117, 27–34. doi: 10.1016/s1040-6182(03)00113-7

Yu, Z., Colin, C., Bassinot, F., Wan, S., and Bayon, G. (2020). Climate-Driven weathering shifts between highlands and floodplains. *Geochem. Geophys. Geosystems* 21:e2020GC008936.

Yuan, D., Cheng, H., Edwards, R. L., Dykoski, C. A., Kelly, M. J., Zhang, M., et al. (2004). Timing, duration, and transitions of the last interglacial Asian monsoon. *Science* 304, 575–578. doi: 10.1126/science.1091220

Conflict of Interest: The authors declare that the research was conducted in the absence of any commercial or financial relationships that could be construed as a potential conflict of interest.

frontiers in Earth Science

ORIGINAL RESEARCH
published: 30 April 2021
doi: 10.3389/feart.2021.674842

Geochemistry of Surface Sediments From the Emperor Seamount Chain, North Pacific

Jie Chen[1], Jianjun Zou[1,2], Aimei Zhu[1,2], Xuefa Shi[1,2]*, Dirk Nürnberg[3], Lester Lembke-Jene[4], Ralf Tiedemann[4], Kunshan Wang[1,2], Yonghua Wu[1,2], Zhi Dong[1,2], Jianxing Liu[1,2] and Ruxi Dou[1]*

[1] Key Laboratory of Marine Geology and Metallogeny, First Institute of Oceanography, Ministry of Natural Resources, Qingdao, China, [2] Laboratory for Marine Geology and Environment, Pilot National Oceanography Laboratory for Marine Science and Technology, Qingdao, China, [3] GEOMAR Helmholtz Centre for Ocean Research Kiel, Kiel, Germany, [4] Alfred-Wegener-Institute, Helmholtz-Zentrum für Polar- und Meeresforschung, Bremerhaven, Germany

Edited by:
Min-Te Chen,
National Taiwan Ocean University,
Taiwan

Reviewed by:
Huang Huang,
Sun Yat-sen University, China
Yuan-Pin Chang,
National Sun Yat-sen University,
Taiwan

***Correspondence:**
Jianjun Zou
zoujianjun@fio.org.cn
Xuefa Shi
xfshi@fio.org.cn

Specialty section:
This article was submitted to
Quaternary Science, Geomorphology
and Paleoenvironment,
a section of the journal
Frontiers in Earth Science

Received: *02 March 2021*
Accepted: *07 April 2021*
Published: *30 April 2021*

Citation:
Chen J, Zou J, Zhu A, Shi X, Nürnberg D, Lembke-Jene L, Tiedemann R, Wang K, Wu Y, Dong Z, Liu J and Dou R (2021) Geochemistry of Surface Sediments From the Emperor Seamount Chain, North Pacific. Front. Earth Sci. 9:674842. doi: 10.3389/feart.2021.674842

Investigating the composition and distribution of pelagic marine sediments is fundamental in the field of marine sedimentology. The spatial distributions of surface sediment are unclear due to limited investigation along the Emperor Seamount Chain of the North Pacific. In this study, a suite of sedimentological and geochemical proxies were analyzed, including the sediment grain size, organic carbon, $CaCO_3$, major and rare earth elements of 50 surface sediment samples from the Emperor Seamount Chain, spanning from ∼33°N to ∼52°N. On the basis of sedimentary components, we divide them into three Zones (I, II, and III) spatially with distinct features. Sediments in Zone I (∼33°N–44°N) and Zone III (49.8°N–53°N) are dominated by clayey silt, and mainly consist of sand and silty sand in Zone II. The mean grain size of the sortable silt shows that the hydrodynamic condition in the study area is significantly stronger than that of the abyssal plain, especially at the water depth of 1,000–2,500 m. The $CaCO_3$ contents in sediments above 4,000 m range from 20 to 84% but decrease sharply to less than 1.5% below 4,000 m, confirming that the water depth of 4,000 m is the carbonate compensation depth of the study area. Strong positive correlations between Al_2O_3 and Fe_2O_3, TiO_2, MgO, and K_2O ($R > 0.9$) in the bulk sediments indicate pronounced contributions of terrigenous materials from surrounding continent mass to the study area. Furthermore, the eolian dust makes contributions to the composition of bulk sediments as confirmed by rare earth elements. There is no significant correlation between grain size and major and minor elements, which indicates that the sedimentary grain size does not exert important effects on terrigenous components. There is significant negative δCe and positive δEu anomalies at all stations. The negative Ce anomaly mainly exists in carbonate-rich sediments, inheriting the signal of seawater. The positive Eu anomaly indicates widespread volcanism contributions to the study area from active volcanic islands arcs around the North Pacific. The relative contributions of terrestrial, volcanic, and biogenic materials vary with latitude and water depth in the study area.

Keywords: sediment grain size, spatial distribution of sediment, Ce negative anomaly, sediment provenance, Emperor Seamount Chain

INTRODUCTION

The geochemical composition of marine sediments, including the contributions of terrestrial, volcanic and biogenic materials, reveals abundant information about ocean current circulation, ecosystem community structure, tectonic movement, and climate change, etc. (Ding et al., 1994; Liu et al., 2009; Hu et al., 2012; Franzese and Hemming, 2013). Determining the composition and distribution of pelagic sediments is fundamental to marine sedimentology, as well as the basis for studying marine ecological assessment, resource exploitation, the reconstruction of past oceanic environment and climatic evolution, etc.

The seamounts are widespread and prominent features of the world's underwater topography. More and more studies suggest that their biological communities, benthic biodiversity, marine biogeography, marine fisheries, hydrodynamic conditions, mineral resources, and climate change are all vital (Clark et al., 2010). In recent years, some studies have greatly improved our understanding of seamount ecology (Mcclain, 2007), especially the vulnerability of seamount communities to human impacts. With progresses in seamount research, it is necessary to reveal some basic characteristics of seamounts, including the composition of sediments deposited on seamount evolution of ecosystems and the development of resources (Mcclain, 2007).

The Emperor Seamount Chain is located in the North Pacific Ocean, extending from ∼20°N to ∼50°N, with a length of more than 6,000 km, which varies greatly in topography. It extends from the point of junction between the Aleutian Trench and the Kuril Trench to Hawaii Island (Jiang et al., 2019). The formation mechanism of the Emperor Seamount Chain is related to hot

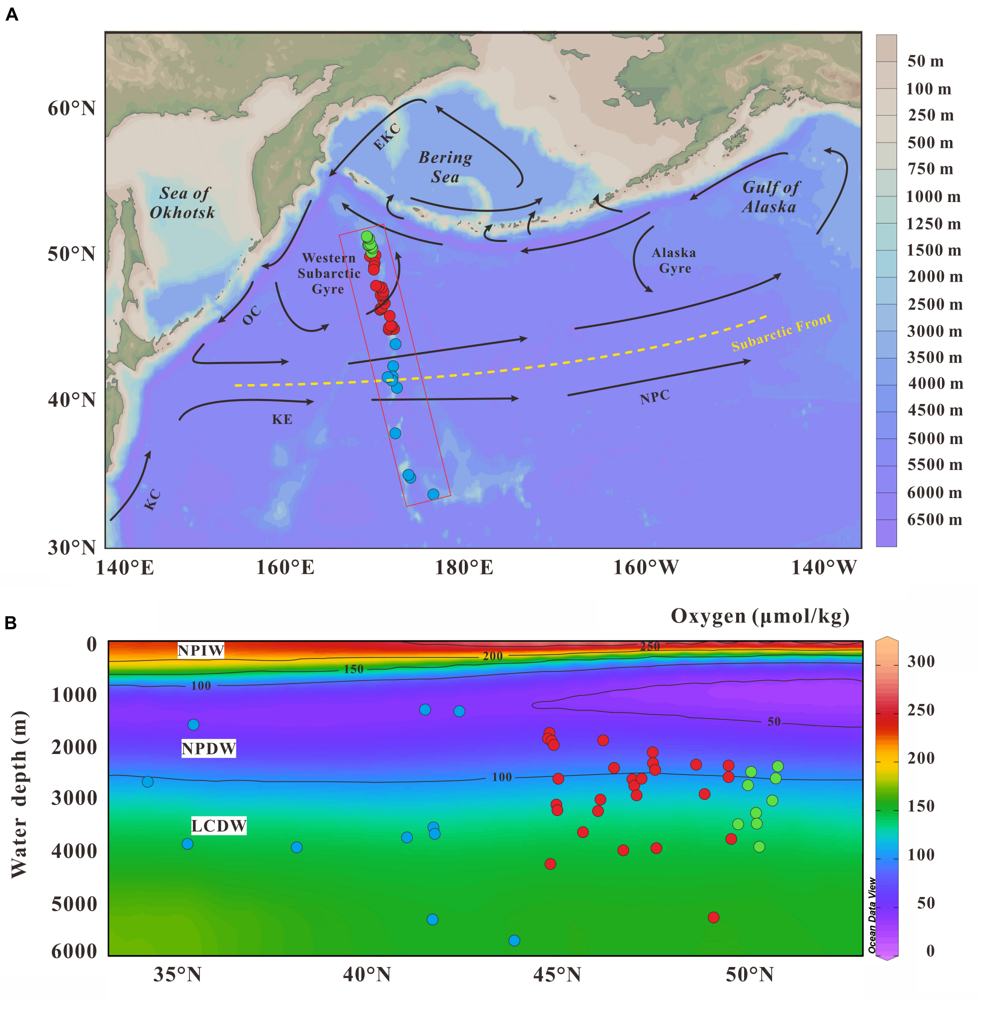

FIGURE 1 | The map of sites locations, schematic of ocean circulation **(A)** (Wang et al., 2016) and the sectional view of dissolved oxygen concentration **(B)** of SO264 surface sediments from the Emperor Seamount Chain in North Pacific Ocean. The study sites are marked with red, blue, and green dots in panels **(A,B)**. Blue dots, red dots and green dots represent samples in zone I, II, and III, respectively. Black arrows and yellow dashed lines denote surface ocean circulation and Subarctic Front (Aydin et al., 2004), respectively. EKC = East Kamchatka Current, KC = Kuroshio Current, KE = Kuroshio Extension, NPC = North Pacific Current, OC = Oyashio Current. Map drawn with Ocean Data View (Schlitzer, 2002). NPIW = North Pacific Intermediate Water, NPDW = North Pacific Deep Water, LCDW = Lower Circumpolar Deep Water.

spot, and the tectonic plate beneath most parts of the Pacific Ocean are constantly moving to the northwest, while hot spot remains stationary, forming a chain slowly (Wilson, 1973). Due to the existence of seamounts, atolls, shoals, ridges, and submerged reefs, the study area is a hot area for geophysicists to investigate plate tectonics and models (Moore, 1970; Suzanne and David, 2000). However, there is little research on the sedimentology, paleoclimate, and paleoenvironment in this area.

To reveal the spatial distributions of sediment compositions, here a suite of proxies were measured on 50 surface sediments from the Emperor Seamount Chain, including the grain size, major elements, rare earth elements, and $CaCO_3$.

OCEANOGRAPHY BACKGROUND

The North Pacific Ocean is divided into the Subarctic Gyre and the Subtropical Gyre by the Subarctic Front (Qiu, 2002; Wang et al., 2016). The surface circulation to the south of the Subarctic Front includes the North Pacific Current, the Kuroshio Current, and the Kuroshio Extension. The Subarctic Gyre contains the Alaska Gyre in the east and the Western Subarctic Gyre in the west respectively (Ren et al., 2014). The ventilation of the Western Subarctic Gyre flows into the subtropical sea along the western boundary, which may be created by the invasion of Oyashio Current. Along the west subarctic region, the southward Oyashio Current deflects eastward at about 40°N and enters the open North Pacific Ocean. In the Aleutian forearc area, the surface circulation is mainly composed by the Alaskan Current, and the part extending northward to the Bering Sea (**Figure 1A**).

There is no formation of deep water in the modern Pacific Ocean, but the North Pacific Intermediate Water (NPIW) is developed (Warner et al., 1996), mainly from the Sea of Okhotsk (Talley, 1993) and the Gulf of Alaska (Van Scoy and Druffel, 1993; You, 2003). The NPIW is mainly transported to 150°W in the east of about 40°N, then to ∼20°N in the south, and partially returns to the west, forming a clockwise cycle. At present, the NPIW is characterized by low salt, rich oxygen, and low density (water depth of 300–800 m, salinity of 33.3–33.4, content of dissolved oxygen is 50–150 μmol/kg and density is 26.6–27.0 $\sigma\theta$) (Talley, 1993). There is also much debate about the formation of deep water masses in the North Pacific Ocean. The water mass with a depth of more than 3,500 m is mainly transported northward by the lower circumpolar deep water (LCDW), which is characterized by higher salinity and lower silicate (Kawabe and Fujio, 2010), and deep water in the North Pacific is developed between NPIW and LCDW and transported southward.

The open Subarctic Pacific is mainly fed by two types of terrestrial sediments: aeolian dust and clastic deposits carried by ocean currents (Wang et al., 2016). Eolian dust accounts for 90% of the open Subarctic Pacific sediments, but the volcanic contribution increased significantly and the eolian dust contribution decreased in the Kuril Islands and the Aleutian Arc region (Serno et al., 2014). Up to now, we have not paid enough attention to the geochemical composition and sediments provenance in the Emperor Seamount Chain of North Pacific.

TABLE 1 | All samples of surface sediment information are mentioned in this article.

Sample ID ID	Latitude (°N)	Longitude (°E)	Water depth (m)	Area
SO264-8-1	33.65	174.75	2,682	E' of Kimmei Seamount
SO264-9-1	34.767	172.333	3,866	Koko Seamount
SO264-10-1	34.917	172.133	1,599	Koko Seamount
SO264-13-1	37.783	170.717	3,933	Ojin and Jingu Seamount
SO264-14-2	40.833	170.9	3,739	Nintoku Seamount
SO264-15-1	41.6	170.417	3,668	E' of Ninigi Seamount
SO264-16-1	41.567	170.417	3,570	E' of Ninigi Seamount
SO264-18-1	41.333	170.367	1,313	Nintoku Seamount
SO264-19-1	41.533	169.917	5,304	W' of Nintoku Seamount
SO264-21-1	42.283	170.5	1,329	Yomei Seamount
SO264-22-1	43.8	170.767	5,709	near Soga Seamount
SO264-23-1	44.8	170.6	4,248	Suiko Seamount
SO264-25-1	44.767	170.117	1,819	Suiko Seamount
SO264-26-1	44.767	170.167	1,772	Suiko Seamount
SO264-28-1	44.85	170.05	1,935	Suiko Seamount
SO264-29-2	44.867	170.05	1,966	Suiko Seamount
SO264-30-1	44.767	170.017	1,857	Suiko Seamount
SO264-31-2	44.85	170.117	1,941	Suiko Seamount
SO264-32-1	44.983	170.4	3,203	Suiko Seamount
SO264-33-1	44.967	170.35	3,141	Suiko Seamount
SO264-34-1	45.017	170.217	2,622	Suiko Seamount
SO264-41-1	45.683	170.15	3,641	Suiko Seamount
SO264-42-1	46.167	169.167	3,024	Jimmu Seamount
SO264-43-1	46.1	169.117	3,242	Jimmu Seamount
SO264-44-1	46.25	169.333	1,892	Jimmu Seamount
SO264-45-1	46.55	169.6	2,423	Minnetonka Seamount
SO264-46-4	46.8	169.4	3,992	Minnetonka Seamount
SO264-47-1	47.067	169.35	2,644	Minnetonka Seamount
SO264-49-1	47.667	169.017	2,433	Minnetonka Seamount
SO264-50-1	47.317	169.483	2,622	Minnetonka Seamount
SO264-51-1	47.167	169.417	2,933	Minnetonka Seamount
SO264-52-1	47.117	169.15	2,754	Minnetonka Seamount
SO264-53-1	47.633	169.333	2,325	Minnetonka Seamount
SO264-54-1	47.617	169.233	2,127	Minnetonka Seamount
SO264-56-1	47.733	168.667	3,946	Minnetonka Seamount
SO264-57-1	48.833	168.467	2,355	Tenji Seamount
SO264-59-1	49.067	168.5	2,916	Tenji Seamount
SO264-60-14	49.3	168.55	5,270	Tenji Seamount
SO264-61-01	49.717	168.033	2,590	N' of Tenji Seamount
SO264-62-01	49.717	168.3	2,378	N' of Tenji Seamount
SO264-63-01	49.8	168.633	3,772	Tenji Seamount
SO264-64-02	49.983	168.217	3,492	S' of Detroit Seamount
SO264-65-01	50.35	168.217	2,496	S' of Detroit Seamount
SO264-66-01	50.25	168.283	2,747	S' of Detroit Seamount
SO264-68-01	50.483	167.85	3,285	Detroit Seamount
SO264-69-01	50.5	167.917	3,478	Detroit Seamount
SO264-70-02	50.567	168.067	3,916	Detroit Seamount
SO264-71-01	51.083	167.7	2,394	Detroit Seamount
SO264-72-01	51.017	167.75	2,615	Detroit Seamount
SO264-73-01	50.933	167.917	3,039	Detroit Seamount

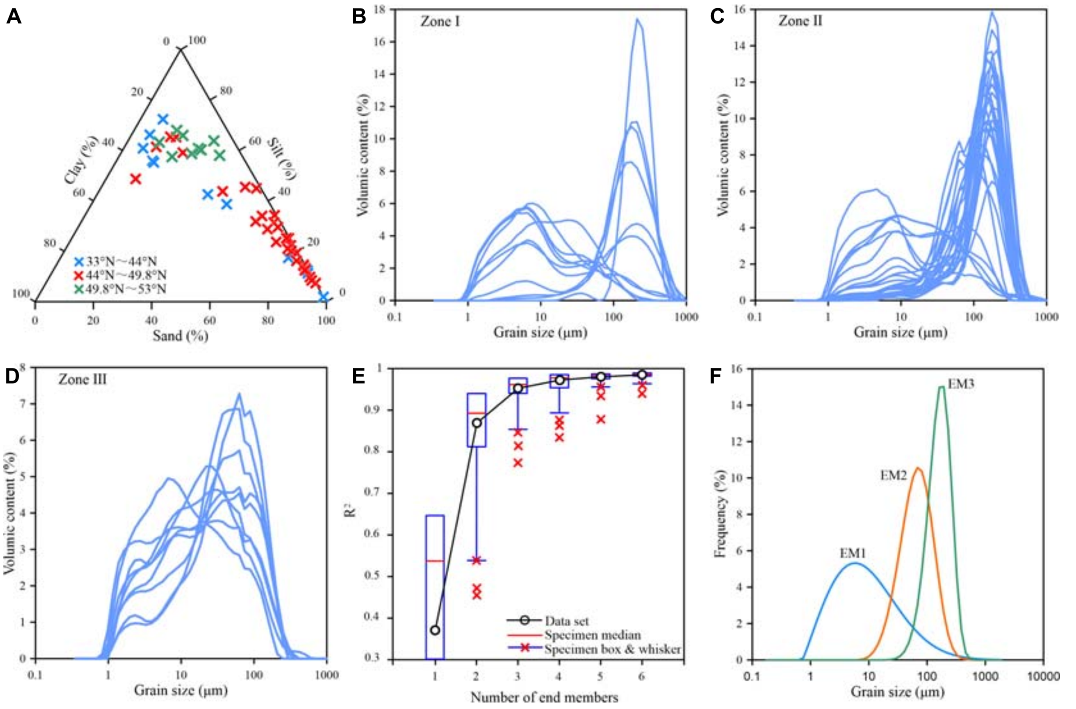

FIGURE 2 | The distribution diagrams of parameters related to grain size of surface sediments. The triangular diagram of grain size **(A)**, the distribution curves of grain size-volumic content **(B–D)**, the graph of linear correlation of end members **(E)**, and the distribution curves of grain size-frequency of modeled end members **(F)**.

Studies of sediments on core ODP 882A in Detroit Seamount, which is located in the northernmost part of ESC, show that terrestrial sediments of core ODP 882A mainly consist of ice raft debris in the high latitude regions and Asian eolian dust brought by westerly jet (Jiang and Liu, 2011). The environment magnetism index recognizes that the degree of drought in the source region of terrigenous clastic material increases obviously, which is consistent with the change record of the aggravation of drought in the Inner Asian and the prevalence of monsoon in East Asia recorded by the loess in East Asia (Jiang and Liu, 2011).

MATERIALS AND METHODS

Sediments Samples

Surface multicorers (MUC) sediments were investigated, which were collected during SO264 Expedition in 2018 (Nürnberg, 2018), and all stations information are reported in **Table 1**. These cores were sampled in 1 cm slice at the onboard laboratory, and then stored in the sample cabin at 4℃. The sampling stations are located along the Emperor Seamount Chain shown in **Figure 1A**, between ~167°E–175°E and 33.5°N–52°N. The water depth ranges from 1,313 to 5,709 m, covering with intermediate water (200–1,500 m), deep water (1,500–4,000 m) and bottom water (>4,000 m) in the North Pacific Ocean. And all the surface sediment samples are collected from the multicores, which has been dated on the basis of planktic foraminiferal AMS ^{14}C. The dating results support that the age of surface sediments belonged to the Holocene interval.

TABLE 2 | The grain-size modeled end members of SO264 surface sediments from the Emperor Seamount Chain in the North Pacific Ocean.

End member	Grain size (μm)	Sort coefficient (σ)	Skewness	Peakedness
EM1	9.12	3.60	0.57	3.08
EM2	64.95	1.90	–0.18	2.81
EM3	157.67	1.59	–0.44	3.15

The surface sediments (0–1 cm) from 50 stations were used to determine grain size, major elements, and rare earth elements. The contents of organic carbon, total carbon (TC), and total nitrogen (TN) of the bulk samples were analyzed. All experiment processing and analysis tests were done at the Key Laboratory of Marine Geology and Metallogeny, First Institute of Oceanography, Ministry of Natural Resources, China.

Sediment Grain Size Analysis

The organic matter, carbonate fractions and biogenic silica of all samples were removed with 5 mL H_2O_2 (30%), 5 mL HCl (10%), and excessive NaOH (0.2 M), respectively. After adding different reagents, the water bath was heated in the above three steps for 1, 1, and 2 h, respectively. Then they were rinsed with deionized water for three times, and the pH value of supernatant was neutral. Grain-size measurements were conducted by laser diffraction particle size analysis using a Malvern Mastersizer 3000. The grain-size range of measurement by the Malvern Mastersizer 3000 is 0.01–3,500 μm, and the relative error of

TABLE 3 | Statistical results of elemental concentrations of surface sediments in the study area.

33°N–53°N elements	Minimum	Maximum	Mean	Standard	Variable coefficient (%)	33°N–44°N elements	Minimum	Maximum	Mean	Standard	Variable coefficient (%)
Al_2O_3 (%)	1.16	12.39	6.08	3.29	54.05	Al_2O_3 (%)	1.16	11.84	5.49	3.37	61.28
CaO (%)	1.47	44.72	25.77	12.63	49.02	CaO (%)	1.47	44.72	27.23	13.3	48.86
Fe_2O_3 (%)	0.57	6.02	2.9	1.43	49.33	Fe_2O_3 (%)	0.57	6.02	3	1.47	49.08
K_2O (%)	0.22	2.21	0.88	0.47	53.86	K_2O (%)	0.29	2.21	1.01	0.53	52.6
MgO (%)	0.54	2.98	1.49	0.67	44.79	MgO (%)	0.54	2.9	1.48	0.67	45.36
MnO (%)	0.05	0.8	0.19	0.14	72.46	MnO (%)	0.05	0.8	0.27	0.22	80.35
Na_2O (%)	2.1	6.29	3.51	1.15	32.77	Na_2O (%)	2.1	6.29	3.52	1.46	41.57
P_2O_5 (%)	0.05	0.15	0.1	0.03	27.68	P_2O_5 (%)	0.07	0.14	0.12	0.02	18.88
TiO_2 (%)	0.06	0.58	0.3	0.14	48.17	TiO_2 (%)	0.06	0.58 135.71	0.29	0.14 31.83	48.79
Σ*P*EE(ππμ)	31.03	135.71	61.1	22.43	36.7	Σ*P*EE(ππμ)	35.72	119.73	78.72	28.35	40.44
ΣΛ*P*EE(ππμ)	25.49	119.73	51.25	19.88	38.79	ΣΛ*P*EE(ππμ)	29.21	15.98	66.98	3.62	42.32
ΣH*P*EE(ππμ)	5.54	15.98	9.86	2.64	26.76	ΣH*P*EE(ππμ)	6.35	7.49	11.74	0.86	30.81
Λ*P*EE/H*P*EE						Λ*P*EE/H*P*EE					
δEυ	3.9	7.49	5.07	0.64	12.52	δEυ	4.35	4.24	5.5	0.43	15.61
δXε	2.04	4.24	3.33	0.49	14.83	δXε	2.78	0.9	3.56	0.12	12.07
$CaCO_3$ (%)	0.47	1.1	0.74	0.13	17.15	$CaCO_3$ (%)	0.47	83.78	0.8	25.49	15.4
TOC (%)	0.04	83.78	47.19	25.09	53.18	TOC (%)	0.86	1.36	50.69	0.35	50.29
	0.07	1.36	0.32	0.21	67.33		0.17		0.53		67.28
44°N–49.8°N elements						49.8°N–53°N elements					
Al_2O_3 (%)	1.55	12.39	5.17	2.87	55.52	Al_2O_3 (%)	7.85	11.85	9.84	1.18	12.02
CaO (%)	2.18	44.18	29.38	11.21	38.17	CaO (%)	3.62	17.02	11.95	3.77	31.52
Fe_2O_3 (%)	0.78	6	2.46	1.33	54.04	Fe_2O_3 (%)	3.39	5.3	4.27	0.57	13.35
K_2O (%)	0.22	1.85	0.71	0.42	58.96	K_2O (%)	1.11	1.64	1.3	0.16	12.33
MgO (%)	0.58	2.98	1.28	0.61	47.34	MgO (%)	1.88	2.77	2.17	0.27	12.44
MnO (%)	0.06	0.49	0.16	0.1	63.17	MnO (%)	0.11	0.25	0.19	0.05	24.49
Na_2O (%)	2.23	6.19	3.19	0.96	30.02	Na_2O (%)	3.94	5.68	4.57	0.48	10.47
P_2O_5 (%)	0.05	0.15	0.09	0.03	29.79	P_2O_5 (%)	0.1	0.13	0.12	0.01	7.05
TiO_2 (%)	0.08	0.58	0.25	0.13	50.99	TiO_2 (%)	0.37	0.55	0.45	0.05	11.34
Σ*P*EE(ππμ)	31.03	94.85	53.09	16.47	31.03	Σ*P*EE(ππμ)	58.99	75.38	66.27	5.63	8.49
ΣΛ*P*EE(ππμ)	25.49	81.34	44.21	14.51	32.83	ΣΛ*P*EE(ππμ)	48.93	63.62	55.49	5.01	9.02
ΣH*P*EE(ππμ)	5.54	14.07	8.89	2.04	23.01	ΣH*P*EE(ππμ)	9.96	11.77	10.78	0.62	5.79
Λ*P*EE/H*P*EE						Λ*P*EE/H*P*EE					
δEυ	3.9	6.21	4.9	0.54	11.12	δEυ	4.86	5.41	5.14	0.17	3.35
δXε	2.31	4.13	3.34	0.44	13.16	δXε	2.04	3.91	3.05	0.59	19.28
$CaCO_3$ (%)	0.57	0.96	0.72	0.1	14.29	$CaCO_3$ (%)	0.58	1.1	0.76	0.17	22.76
TOC (%)	0.04	81.73	54.36	22.35	41.11	TOC (%)	2.43	29.87	18.99	7.62	40.1
	0.07	0.53	0.26	0.09	34.42		0.16	0.31	0.26	0.04	16.29

repeated measurement is less than 3%. According to Weltje (1997) and Weltje and Prins (2003), sediments are composed of components from different provenance or dynamic processes, and different end members (EM) can be separated by multi-peak morphology of grain size data. Therefore, the end-member analysis model is proposed to distinguish different provenance or transport mechanisms (Weltje, 1997; Weltje and Prins, 2003). Paterson and Heslop (2015) improved the analysis model of ***EM*** based on ***MATLAB*** (Paterson and Heslop, 2015), and we utilize the modeling algorithm to analyze grain size end-member of surface sediments, with using the mean ***EM*** of sediment was fitted by Gen.Webibull function.

Total Organic Carbon, TN, and $CaCO_3$ Analysis

About 50.00 mg of sample was weighted, freeze-dried and ground to less than 200 mesh by agate mortar, which was directly used for determination of the content of TC and TN. The manually powdered samples of ∼1 g were placed in the centrifuge tube, dissolved by HCl (1M) to remove carbonate, and then they were dried to determine the contents of total organic carbon (TOC). Acetailide (ACET) was used as the standard sample and GSD-9 was used as the quality control standard reference materials during the measurement. The contents of TOC, TC, TN were tested by Elemental Vario EL III (Bai et al., 2013).

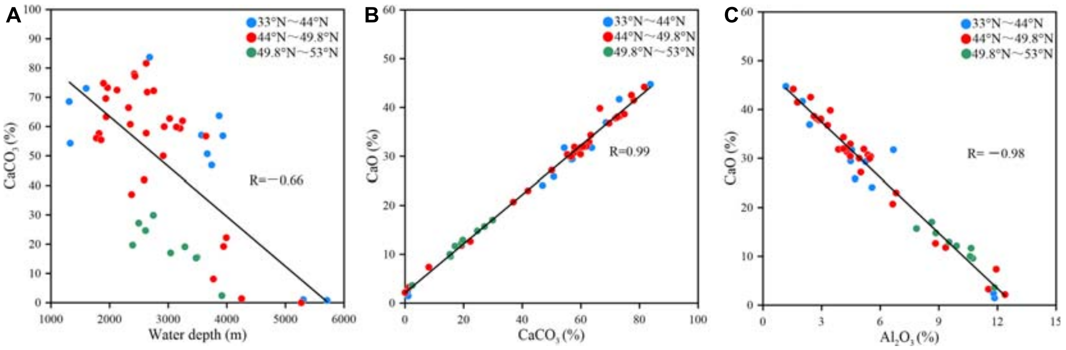

FIGURE 3 | The scatter plots between $CaCO_3$ and water depth **(A)** and between CaO and $CaCO_3$ **(B)** and between CaO and Al_2O_3 **(C)**.

The content of $CaCO_3$ is calculated according to the following formula:

$$CaCO_3 = (TC–TOC) \times 8.33$$

Major and Minor Elements

About 50.00 mg of powdered sample was placed in the centrifuge tube. And high-purity HNO_3, HF and concentrated HCl were used to completely digest sediments. Major elements (Al_2O_3, Fe_2O_3, K_2O, MgO, MnO, P_2O_5, CaO, and TiO_2) were analyzed on Thermal iCAP 6300 ICP-OES. Rare earth elements were analyzed on a Thermal series II ICP-MS. GSD-9, duplicate samples and blank samples were used for quality control during the measurement. The analytical results of blank samples were all below the detection limit. The results show that relative standard deviation of major elements is less than 2.2%, and that of rare earth elements is less than 5.1%.

RESULTS

The Grain-Size Distribution

The grain size and sorting coefficient of sediments in the study area range from 7.74 to 192.71 μm and 0.64 to 2.61, with an average value of 42.91 μm and 1.66, respectively. The frequency distribution curves of sediments grain size have different modes (**Figures 2B–D**), and these curves show the left trailing of some stations, indicating that they are affected by various factors. According to distinct features of grain size-related parameters, including the sediment types and grain size characteristics, the study area was divided into three areas: Zone I (33°N–44°N), Zone II (44°N–49.8°N), and Zone III (49.8°N–53°N) (**Figure 2A**). Sediments in Zone I and in Zone III are dominated by clayey silt with higher value of sorting coefficient (>1.66). The grain size-frequency distribution curves are characterized by usually double peaks, which are concentrated between 5 and 8 μm and 140–150 μm in Zone I, respectively (**Figure 2B**). This indicates that the sediments may have different provenance or poor sorting coefficient. In zone III, the curves are dominated by single peaks, with the peak value between 7 and 64 μm (**Figure 2D**). In Zone II (44°N–49.8°N), the sediments are mainly composed of sand and silty sand, with lower sorting coefficient. The stations with grain size of less than 42.91 μm are mainly located in this zone, and curves consist of single and double peaks. Most of curves are single peaks, and vary between 120 and 170 μm, indicating that the sediment has a single provenance or is well sorted.

The calculation results of grain size data shows that when the end-member number is 1–6, the R^2 is 0.6517, 0.9485, 0.9875, 0.9925, 0.9960, and 0.9979 (**Figure 2E**), respectively. From the point of view of the degree of data fitting, three end-member numbers are selected to analyze the grain size in this paper because it can well represent the overall characteristics of the grain size. End-member analysis of sediment grain-size distribution has an optimal model with three EM, all of which are single peaks and close to Gaussian distribution (**Figure 2F** and **Table 2**). These peaks appear at 2.54–17.1, 48.40–96.75, and 136.85–230.1 μm, with mean grain size of 9.12 μm, 64.95 μm and 157.67 μm, respectively. The abundance of EM is 0–100, 0–75.33, and 0–100%, with average abundances of 37.85, 24.73, and 37.42% respectively.

Contents of $CaCO_3$ and TOC

The content of calcium carbonate in surface sediments in the study area ranges between 0.04 and 83.78%, with a mean value of about ∼47.19% (**Table 3**). The calcium carbonate content in marine sediments is mainly affected by production, dissolution and dilution effect. Generally, the content of $CaCO_3$ is less than 2% at stations with water depth of more than 4,000 m (**Figure 3A**). According to Farrell and Warren (1989), 10% calcium carbonate in the Pacific Ocean is defined as the carbonate compensation depth (Farrell and Warren, 1989). Therefore, the calcium carbonate content in this area indicates that the water depth of 4,000 m is the carbonate compensation depth of this area. There is no significant relationship between the content of $CaCO_3$ and water depth of above 4,000 m. At similar water depth to the north of 49.8°N, the content of $CaCO_3$ is obviously lower than that to the south of 49.8°N in the study area. In the range of 33°N–49.8°N, the content of $CaCO_3$ in most stations is more than 30%. The mean content of $CaCO_3$ in the zone of 33°N–44°N is about 50.69%, and which decreases gradually from south to north on the whole.

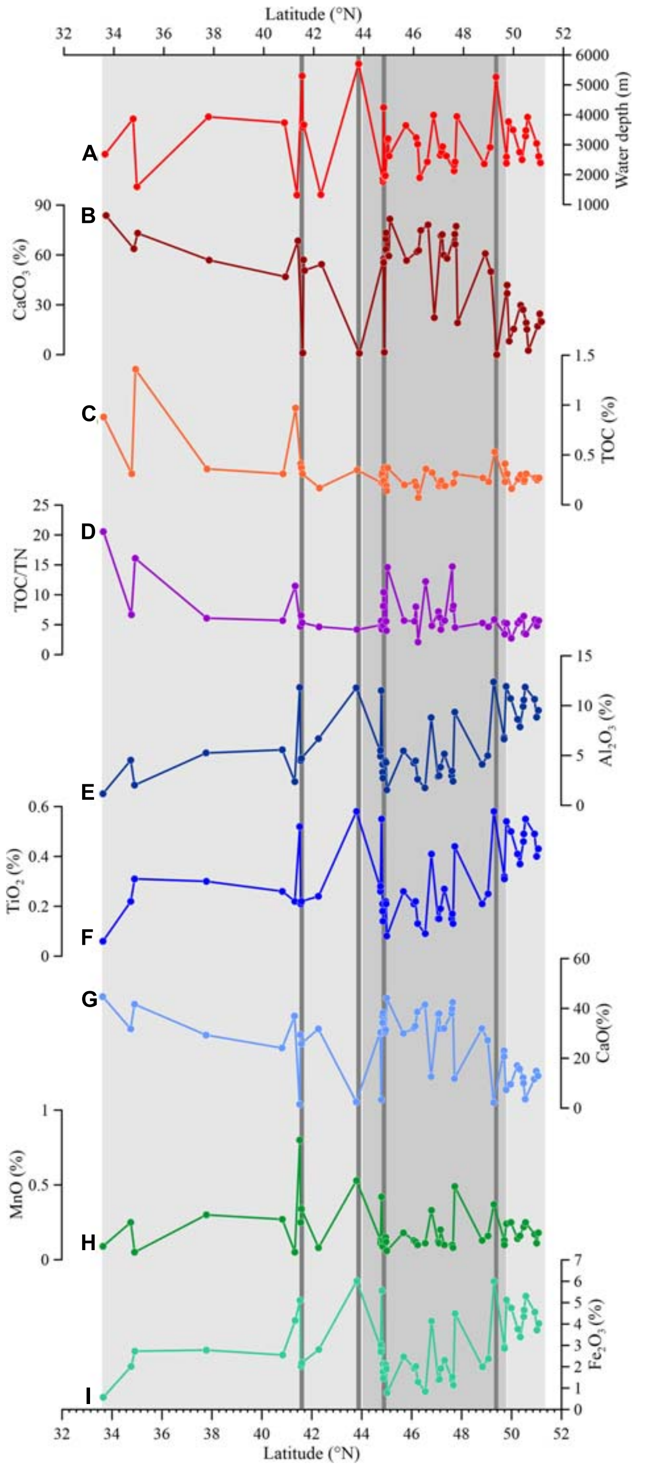

FIGURE 4 | Spatial variations in the contents of major elements in the study area. The dark black vertical lines indicate stations with water depth greater than 4,000 m. The spatial variation of water depth **(A)**, spatial variation in the content of $CaCO_3$ **(B)**, spatial variation in the content of TOC **(C)**, spatial variation in the content of TOC/TN **(D)**, spatial variation in the content of Al_2O_3 **(E)**, spatial variation in the content of TiO_2 **(F)**, spatial variation in the content of CaO **(G)**, spatial variation in the content of MnO **(H)** and spatial variation in the content of Fe_2O_3 **(I)**.

The content of TOC in sediments varies between 0.07 and 1.36%, averaging about 0.32% (**Table 3**). In general, the stations with higher contents of TOC mainly are located between 33°N–44°N (**Figure 4**). The correlation coefficient between TOC and TN is insignificant (R = 0.48). The ratio of TOC/TN varies between 2.45 and 24.0, with a mean value of 7.68. Besides the supply from surface primary productivity, the content of organic matter is also affected by aerobic respiration and denitrification (Wang et al., 2018). The ratio of TOC/TN of terrestrial organic matter is generally greater than 15, as well as between 5 and 7 for marine organic matter (Fry and Sherr, 1984; Meyers, 1997). We noted that the ratio of TOC/TN of 6 stations is more than 12, although the study area is far from land, indicating a potential supply of terrestrial organic matter to the study area, or that nitrogen loss caused by early diagenesis, leading to an increase of TOC/TN ratio.

Major Elements

The content of CaO in surface sediments is dominant with a range of 1.47–44.72% and a mean value of 25.77% (**Table 3**). There is a strong positive correlation between CaO and $CaCO_3$ on the whole (R = 0.99) (**Figure 3B**), thus mainly reflects the contribution of biogenic materials. Within the latitudinal range of 33°N–44°N, 44°N–49.8°N, and 49.8°N–53°N, the mean content of CaO is 27.23, 29.38 and 11.95%, respectively. The lower values mainly appears between around 44°N and 49.8°N, and the highest value is found around 33.65°N (**Figure 3**).

The content of Al_2O_3 ranges between 1.16 and 12.39% with an average value of 6.08% (**Table 3**). As a whole the variation of Al_2O_3 with latitude is opposite to that of CaO, the high value of Al_2O_3 in the northern region of 49.8°N and deeper than 4,000 m. The mean content of Fe_2O_3, K_2O, MgO and TiO_2 is 2.95, 0.89, 1.51, and 0.30%, respectively, which is similar to the spatial distribution pattern of Al_2O_3. Correlation analysis shows that there are significant positive correlations among Al-Fe, Al-K, Al-Mg and Al-Ti, with correlation coefficients of 0.93, 0.93, 0.98, and 0.97, respectively (**Figure 6**). There is positive correlations between Al_2O_3–MnO and Al_2O_3–P_2O_5, and the correlation coefficient is 0.65 and 0.82, respectively (**Figure 6**).

Rare Earth Elements

The content of rare earth elements (ΣREE) of surface sediments varies between ∼31 and 136 μg/g, with a mean value of ∼61 μg/g, and the coefficient of variation is 36.70% (**Table 3**), indicating that there are significant differences in content of different stations. The contents of light rare earth elements (ΣLREE: La, Ce, Pr, Nd, Sm, and Eu) and heavy rare earth elements (ΣHREE: Gd, Tb, Td, Dy, Ho, Er, Tm, Yb, and Lu) range between 25.49–119.73 and 5.54–15.98 μg/g, with a mean value of 51.25 μg/g and 9.86 μg/g, respectively. LREE/HREE ranges from 4.60 to 7.50, with an average value of 5.20. There is a significant positive correlation between rare elements with correlation coefficient of more than 0.98. Also significant positive correlation is observed between Al_2O_3 and ΣREE (R = 0.65). Overall, the patterns of ΣREE, ΣLREE, and ΣHREE are similar along the latitudinal zone, with higher values at around 44°N and 49.8°N (**Figure 7**).

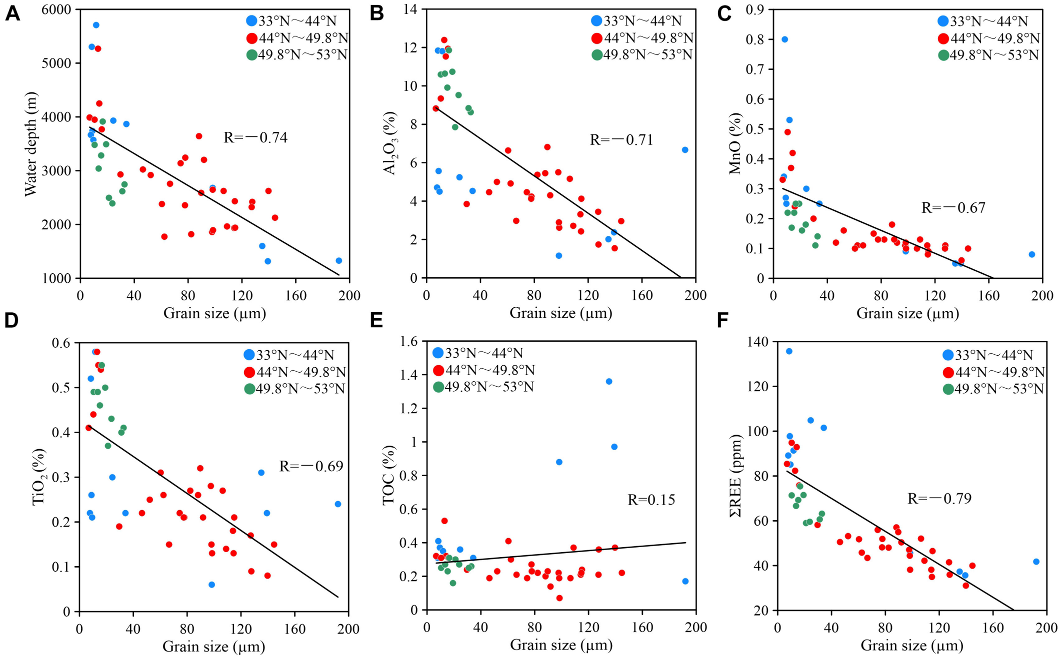

FIGURE 5 | The scatter plots between grain size and contents of major elements. The correlation between water depth and grain size (*R* = −0.74, **A**), the correlation between Al_2O_3 and grain size (*R* = −0.71, **B**), the correlation between MnO and grain size (*R* = −0.67, **C**), the correlation between TiO_2 and grain size (*R* = −0.69, **D**), the correlation between TOC and grain size (*R* = 0.15, **E**) and the correlation between ΣREE and grain size (*R* = −0.79, **F**).

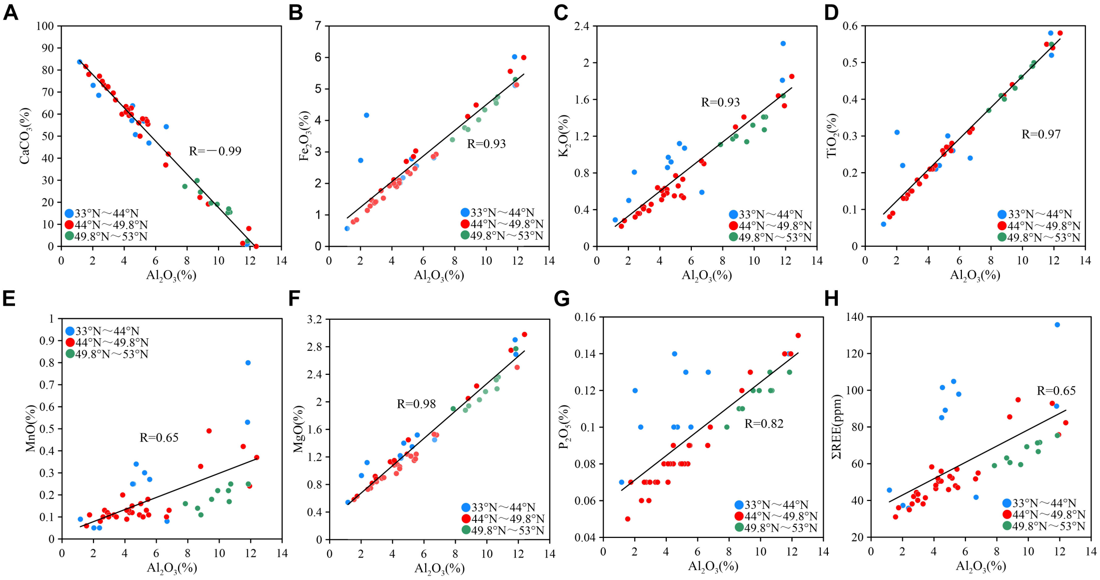

FIGURE 6 | The scatter plots between Al_2O_3 and other elements. The correlation between $CaCO_3$ and Al_2O_3 (*R* = −0.99, **A**), the correlation between Fe_2O_3 and Al_2O_3 (*R* = 0.93, **B**), the correlation between K_2O and Al_2O_3 (*R* = 0.93, **C**), the correlation between TiO_2 and Al_2O_3 (*R* = 0.97, **D**), the correlation between MnO and Al_2O_3 (*R* = 0.65, **E**), the correlation between MgO and Al_2O_3 (*R* = 0.98, **F**), the correlation between P_2O_5 and Al_2O_3 (*R* = 0.82, **G**) and the correlation between ΣREE and Al_2O_3 (*R* = 0.65, **H**).

We used the Post-Archean Average Shale (PAAS) to normalize the rare earth elements in the study area as shown in **Figure 8**. The distribution patterns of curves show obvious characteristics of enrichment of HREE. The analysis shows that both Ce and Eu range between 0.47–1.10 and 2.04–4.24, with average values of 0.74 and 3.33, respectively. Although the contents of ΣREE at different stations in the study area are quite variable, the distribution patterns of REE in surface sediments are roughly

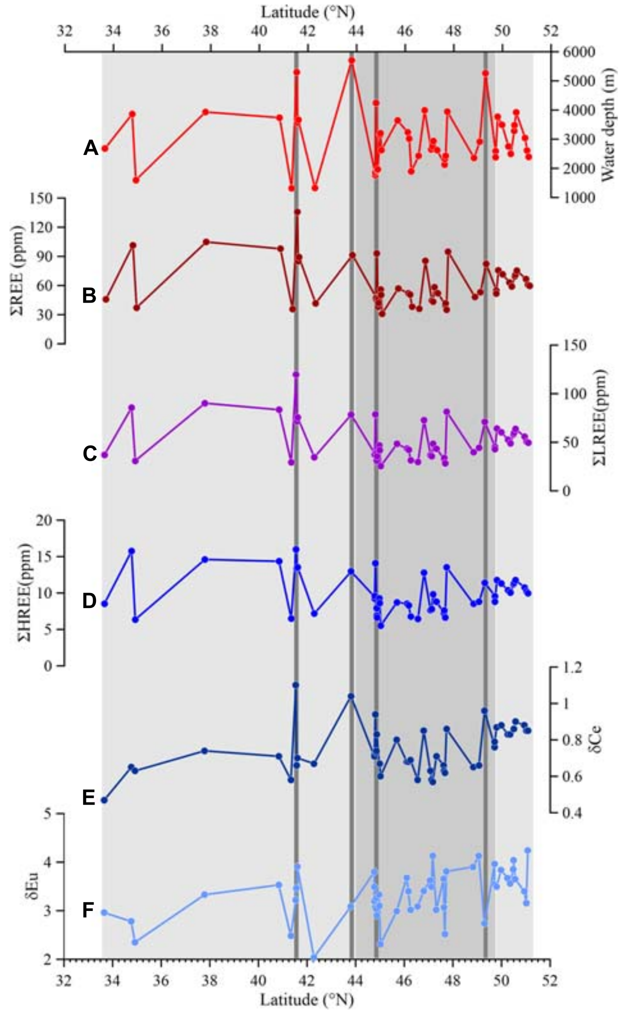

FIGURE 7 | Spatial trends of rare earth elements and related proxies. The spatial variation of water depth **(A)**, spatial variation in the content of ΣREE **(B)**, spatial variation in the content of ΣLREE **(C)**, spatial variation in the content of ΣHREE **(D)**, spatial variation of δCe **(E)** and spatial variation of δEu **(F)**.

identical, and the sediments totally appear Ce negative anomaly and Eu positive anomaly (**Figure 7**).

DISCUSSION

Sediment Dynamics in the Emperor Seamount Chain

The grain size of sediments is affected by mineral composition, process of weathering transport and sedimentary dynamic conditions, and the grain size and morphology of sediments in different regions are obviously different. Negative correlation between water depth and grain size ($R = -0.74$, **Figure 5A**) in the study area suggests that the deeper the water depth is, the finer the grain size of sediments is. In order to further reveal the relationship between hydrodynamic condition and water depth, we calculated the mean grain size of the sortable silt, a proxy for deep current intensity (Mccave et al., 1995). Mean grain size of sortable silt shows strong positive correlation with the contents of sortable silt in the study area, suggesting that it can be used to indicate the relative change of bottom current strength (Mccave et al., 2020). As shown in **Figure 9**, there is a negative correlation between grain size of sortable silt and water depth ($R = -0.73$), and grain size of sortable silt increases significantly, indicating strong hydrodynamic conditions. Modern observations have shown that there are strong hydrodynamic conditions at the water depth of ∼2,000 m in the study area (Ueno, 2003), and the results of grain size further confirmed the observation results of deep flow field. It can be seen from **Figures 5A**, 9 that the range of water depth in different zones is discrepant, the water depth of all sediment collected in zone II is no deeper than 4,000 m. Therefore, the water depth could affect the geochemical proxies variation in the study area. And we only discuss the relationship between the overall water depth and the grain size and the mean grain size of the sortable silt due to the lack of samples in different water depth of discussion section, such as the lack of samples in the 1,500–3,000 m of zone I.

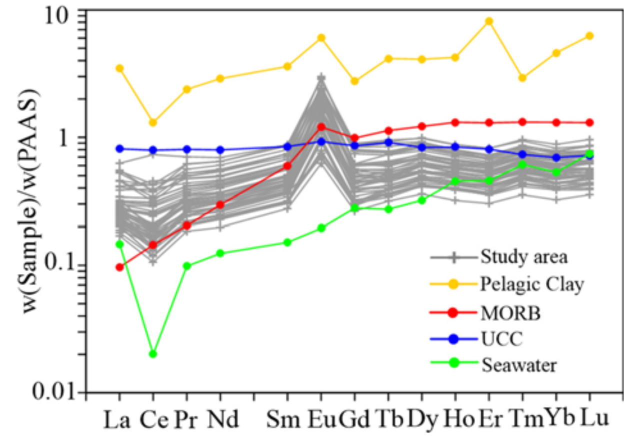

FIGURE 8 | Comparisons of PAAS-normalized rare earth elements patterns of surface sediments of the Emperor Seamount Chain, the content of REE of pelagic clay (Kato et al., 2011), MORB (Klein, 2003), UCC (Taylor and Mclennan, 1995), and seawater (Zhang and Nozaki, 1998).

Also, we conducted the sediment grain size end-member simulations using MATLAB (Paterson and Heslop, 2015). According to the grain size analysis of simulated EM, there are three EM with mean grain size of 9.12 μm (EM1), 64.95 μm (EM2), and 157.67 μm (EM3), representing fine silt, fine sand and medium sand, respectively. Furthermore, using the same simulation method of EM analysis, we compared our data with the results of the SO202 Expedition from the open subarctic Pacific Ocean (Serno et al., 2014), and found that mean grain size was about 5.33 μm. This indicates that there are great differences in hydrodynamic conditions between seamounts and deep plain of the open subarctic Pacific Ocean. It has previously been observed that vortex is easily to occur around seamount under the combined influence of

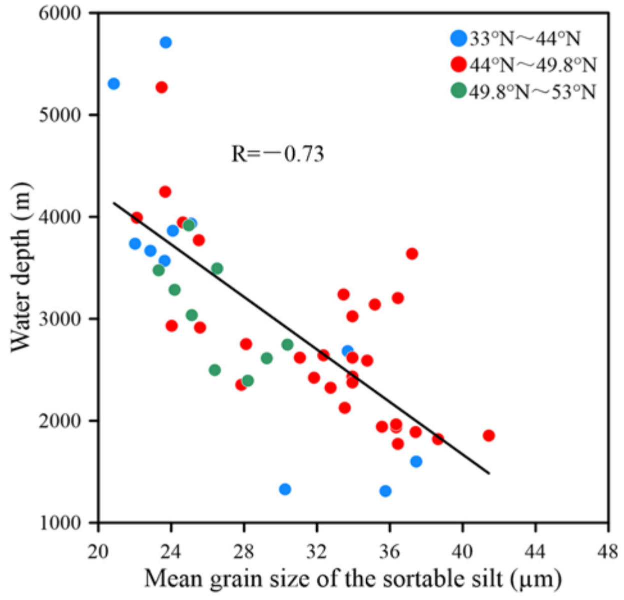

FIGURE 9 | The correlation plot between grain size of sortable silt and water depth.

tide and topography (Oka and Niwa, 2013), and hydrodynamic condition is significantly enhanced, causing the sediment being severely winnowed.

The higher contents of EM1 mainly appear at stations of 33°N–44°N and deeper than 4,000 m (**Figure 10**), which may represent the input of terrestrial and volcanic sources by wind, and also correspond to the westerly path of the modern Northern Hemisphere. In this context, it is reasonable to speculate that EM1 mainly reflects the contribution of eolian dust, including dust of Central Asia and volcanic materials by wind-transported. The grain sizes of EM2 and EM3 are coarser and cannot be transported by wind over long distances, so they cannot be explained by dust input. The content of EM3 decreases to the north of 49.8°N and increases to the south of 49.8°N, which may reflect that sediments in the study area are reworked after deposition by strong hydrodynamic conditions.

As shown in **Figure 5A** and end member analysis, coarser sediment grain size can be seen in Zone II, relative to Zone I and III, we argue that this is mainly related to strong mid-depth and deep-depth circulation in Zone II as mentioned above. And the mean grain size of sortable silt (**Figure 9**), which shows higher SS values, corroborating our interference. Some coarser sediment grain size in zone II at the water depth of 3,000–4,000 m in comparison with those of zone I and III also can be observed in **Figure 9**, which may be caused by additional factors, such as the input of volcanic materials, proximal erosion of seamount, etc.

There is significant relationship between composition of sediment and grain size, which is especially obvious in the coastal sediments (Zhao et al., 2002; Gao et al., 2003; Jiang et al., 2008; Miao et al., 2008). Through the correlation analysis, we find the grain size in the study area is negatively correlated with Al_2O_3 (R = −0.71, **Figure 5B**) and TiO_2 (R = −0.69, **Figure 5D**), indicating that the finer the grain size is, the higher the contents of Al_2O_3 and TiO_2 are. Rare earth elements are negatively correlated with grain size (R = −0.79, **Figure 5F**), arguing that rare earth elements are mainly enriches in fine-grained sediments and depleted in coarse-grained sediments. There is no significant correlation between grain size and MnO and TOC (**Figures 5C,E**), and the coefficient of variation is higher, reaching 67.33 and 72.46%, respectively, which demonstrates that the grain size is not the main factor controlling the composition and distribution of MnO and TOC in surface sediments.

Negative Ce Anomaly

The δCe of surface sediments in the study area ranges from 0.5 to 1.1, with a significant negative Ce anomaly. The factors causing Ce anomaly are very complex, involving sedimentary environment, diagenesis, content of oxygen of bottom water and other factors (Pattan et al., 2005). Therefore, the interpretation and application of index of Ce anomaly must be careful. REE analysis of different types of sediments in the Indian Ocean reveals that there are positive Ce anomaly in siliceous ooze and negative Ce anomaly in calcareous sediments (Nath et al., 1992). The rare earth elements in different types of sediments in the open Pacific Ocean showed that there is clear negative Ce anomaly in sediments enrich in calcareous ooze. Toyoda et al. (1990) suggested that the negative Ce anomaly in calcareous ooze mainly is related to the enrichment of phosphorus. No Ce anomaly was observed in the bulk sediments mainly composed of silicate (Zou et al., 2010; Zhu et al., 2012). The analysis of leaching experiment found that the positive Ce anomaly mainly occurred in Fe-Mn phase of sediments (Toyoda and Masuda, 1991), which indicated that the enrichment of Ce was closely related to Fe-Mn oxide. In general, it is believed that Ce is easily adsorbed on the surface of Fe-Mn oxide and subsequently result in Ce enrichment in Fe-Mn oxides. Under anoxic condition, Ce can be removed from the Fe-Mn oxides due to the desorption along with the dissolution of particulate Fe-Mn oxides, leading to negative Ce anomaly in sediments (Tachikawa et al., 1999).

Our REE data shows that there is strong positive correlation between $CaCO_3$ and δCe (R = −0.90), which suggests that higher the content of $CaCO_3$, the greater the depletion of Ce (**Figure11A**). The pattern of negative Ce anomaly is consistent with distribution pattern of REE in seawater (**Figure 8**), suggesting that the negative Ce anomaly in sediments in the study area mainly inherits the signal from seawater. No negative Ce anomaly is observed at the depth of more than 4,000 m, which proves that the contribution of calcareous materials decreases significantly and is mainly composed of terrigenous materials.

As mentioned above, the change of oxidation-reduction in sediments also has potential effects on δCe. The Mn/Fe ratio could be used to indicate the sedimentary redox condition changes. The main reason is that both these two elements have contrasting geochemical behaviors under changing redox conditions. The lower correlation coefficient between bulk sedimentary Fe_2O_3 and MnO (R = 0.65, **Figure 11C**) further corroborates this inference. The correlation analysis of MnO/Fe_2O_3 and δCe reveals that there is no obvious positive correlation (R = −0.10) (**Figure 11B**). Hence, we argue that the

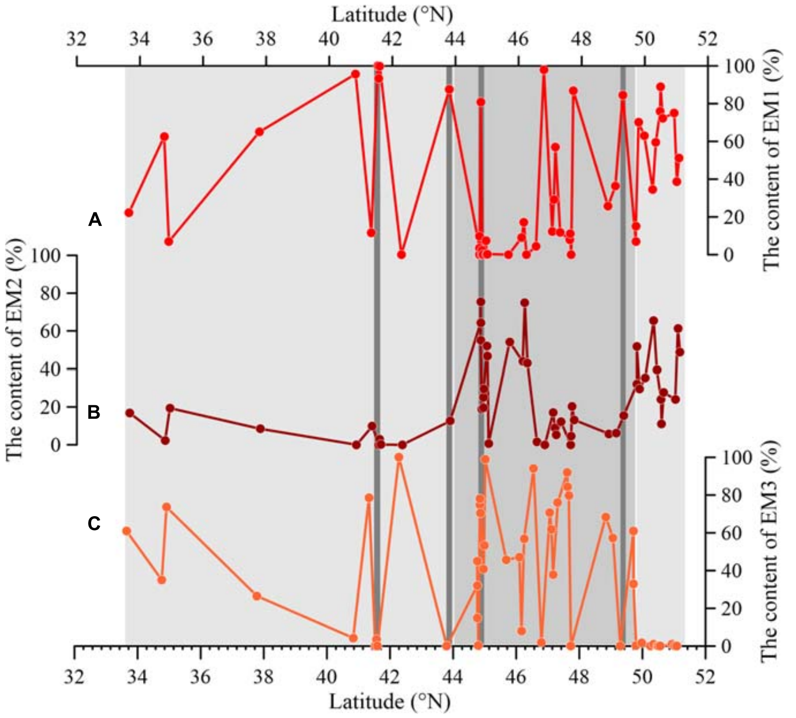

FIGURE 10 | The changing trend graph of content of three modeled grain-size end members. The spatial variation in the content of EM1 **(A)**, spatial variation in the content of EM2 **(B)** and spatial variation in the content of EM3 **(C)**.

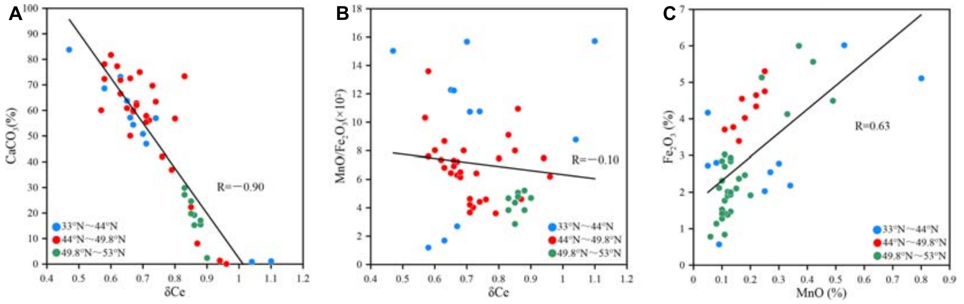

FIGURE 11 | The scatter plots between $CaCO_3$ and δCe **(A)** and between MnO/Fe_2O_3 ratio of Fe-Mn phase and δCe of bulk sediments **(B)** and between Fe_2O_3 and MnO **(C)**.

oxidation-reduction changes in surface sediments in the study area have no distinct effects on δCe.

Provenance of Sediments

The study area is far away from surrounding continents, therefore lots of terrigenous materials deposited in the open northwest Pacific Ocean mainly are delivered by eolian dust, volcanic materials, ice raft debris, and debris carried by ocean currents. The eolian dust mainly comes from Central Asia, and the volcanism materials are mainly sourced from the surrounding island arcs, including the Kuril Islands, the Aleutian Islands, the Kamchatka Peninsula, and the volcanic arc of Alaska and Japan. The clastic components transported by sea ice and ocean currents may also have potential contributions to the sediments in the study area.

In general, the provenance and composition of surface sediments are closely related to the characteristics of parent rocks. The large ion lithophile elements such as Al, Fe, Ti, K, and Mg are rock forming elements, and rare earth elements are also enriched in silicate minerals. These elements are mainly concentrated in the upper crust with good symbiotic relationships, similar geochemical behavior and active geochemical properties (Wang, 2014), and as shown in **Figure 6**, the correlation analysis shows that there is strong positive correlation between Al_2O_3 and Fe_2O_3, TiO_2, MgO, K_2O, and REE (R = 0.93, 0.97, 0.98, and 0.93), respectively, which suggests that sediments in the study area contribute significantly to terrigenous detritus.

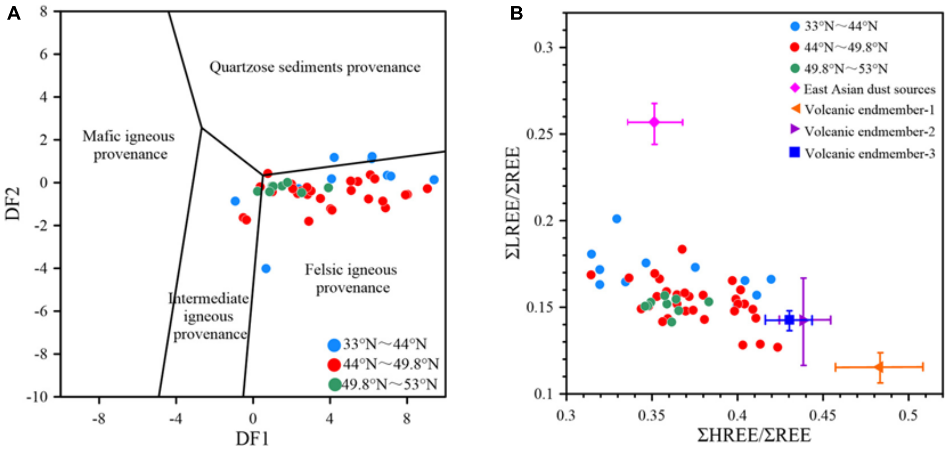

FIGURE 12 | Discrimination plot of the nature of parental rock of sediment provenance **(A)** and the scatter plot of (LREE/REE)$_N$ and (HREE/REE)$_N$ **(B)**, east Asian dust sources and volcanic sources refer to Serno et al. (2014).

There are multiple sources for Ca, such as aeolian dust, volcanic and biogenic contributions in bulk sediments. The content of $CaCO_3$ in the surface sediments of study area is about 47.2%, which is negatively correlated with the representative element Al ($R = -0.99$, **Figure 6A**) of terrigenous detritus, indicating that it is mainly contributed by biogenic material. As shown in **Figure 3B**, there is strong positive correlation between CaO and $CaCO_3$ ($R = 0.99$, **Figure 3B**), indicating potential biogenic input. Also a strong negative correlation ($R = -0.98$, **Figure 3C**) can be observed between CaO and Al_2O_3, a lithogenic element, indicating little contributions of detrital materials. In terms of spatial distribution, the content of $CaCO_3$ is less than 2% at water depth of deeper than 4,000 m, and with similar water depth, the content of $CaCO_3$ in sediments to the north of 49.8°N is significantly lower than that to the south of 49.8°N. This implies that the conditions to the south of 49.8°N are more conducive to the preservation of calcareous organisms.

The sources of P_2O_5 in sediments are various, mainly consisting of rivers, atmospheric deposition and volcanic activities (Paytan and McLaughlin, 2007). Studies over the past years have suggested that the contribution of volcanic materials to phosphorus is much higher than that of input of atmospheric precipitation (Wang, 2014). Meanwhile, phosphorus from seawater is also absorbed by organisms in seawater and related to biogenic carbonate (Wang and Chen, 2011). There is a positive correlation between P_2O_5 and Al_2O_3 ($R = 0.64$, **Figure 6G**), but lower than the correlation between Fe_2O_3 and TiO_2 and Al_2O_3, while the negative correlation between $CaCO_3$ and P_2O_5 indicates that the contribution of biogenic phosphorus may be small, mainly clastic phosphorus.

The content of MnO in sediments is affected by both redox conditions and terrestrial input. Correlation analysis of MnO and Al_2O_3 shows positive correlation ($R = 0.67$, **Figure 6E**), which indicates that MnO has significant terrestrial contributions in surface sediments of study area. There is also a significant positive correlation between MnO and water depth ($R = 0.83$), and the lower content of stations is mainly located in which is affected by the NPIW. Modern observations have shown that the dissolved oxygen at this depth is low (**Figure 1B**), and therefore a part of manganese oxide may be dissolved due to lower oxygenation.

In the study area, Eu generally has significant positive anomaly with range of 1.5–4, confirming that there are significant volcanic input. The clastic surface sediments near the Emperor Seamount Chain is characterized by sediment with more radiogenic εNd values (averaging -4.4 ± 4.3) that reflect inputs from volcanic ash (Jones et al., 2000). The content of smectite at stations near the Emperor Seamount Chain increased significantly, indicating large input of volcanic materials (Wang et al., 2016). Positive Eu anomaly occurred not only in the open Northwest Pacific Ocean, but also in the Sea of Okhotsk and the Bering Sea (Wang et al., 2016; Zhu et al., 2019). Therefore volcanic debris makes a significant contribution for marine sediments in the northwestern Pacific Ocean and its marginal seas.

The geochemical behavior of major elements can be used to trace the characteristics of parent rocks of the sediment provenance, which has been widely used in the study of determined provenance signatures (Zhu et al., 2015, 2019). In this paper, we employ the sediments source discriminant function proposed by Roser and Korsch (1988) to identify the characteristics of provenance (**Figure 12A**) (Roser and Korsch, 1988). The formulation is as follows, and DF1 and DF2 mainly represent the component of felsic igneous rock source and mafic igneous rock source, respectively:

$$DF1 = 30.638w(TiO_2)/w(Al_2O_3) - 12.541w(Fe_2O_3)/w(Al_2O_3)$$
$$+7.329w(MgO)/w(Al_2O_3) + 12.031w(Na_2O)/w(Al_2O_3)$$
$$+35.402w(K_2O)/w(Al_2O_3) - 6.382$$

$$DF2 = 56.500w(TiO_2)/w(Al_2O_3) - 10.879w(TFe_2O_3)/ w(Al_2O_3) + 30.875w(MgO)/w(Al_2O_3) - 5.404w(Na_2O)/ w(Al_2O_3) + 11.112w(K_2O)/w(Al_2O_3) - 3.89$$

The results suggest that the clastic materials in the study area are mainly volcanic materials and small amount of quartzose sediments, while the magma composition is mainly felsic magma, which is consistent with the results based on positive Eu anomaly. On the other hand, rare earth elements have been also widely used as proxies for tracing sediment provenance, especially in the open North Pacific Ocean, where rare earth elements are considered as an effective indicator for tracing changes of eolian dust (Serno et al., 2014). Serno et al. (2014) confirmed the effectiveness of rare earth elements in tracing the dust contribution in the Subarctic Pacific Ocean based on the three independent indexes of ^{4}He, ^{230}Th$_{xs}$ and rare earth elements. The scatter plot of (LREE/REE)$_N$ and (HREE/REE)$_N$ (**Figure 12B**) shows that the composition of the surface sediments of the Emperor Seamount Chain falls into the range of two EM: volcanic and terrigenous dust, which can be regarded as a mixture of two EM. Our data further reveals that the eolian dust contribution is higher between 33°N and 44°N, while the volcanic materials contribution is relatively higher between 44°N and 49.8°N, as shown in **Figure 12B**.

IMPLICATIONS

At present, the main challenge in the study of paleoclimate in the Subarctic Pacific is to establish a reliable and accurate age model, which is mainly due to the lack of calcareous biogenic shells in relation with dissolution in the sediments. Our data shows that the depth of carbonate compensation is ∼4,000 m in the northwestern Pacific Ocean, and the content of $CaCO_3$ increases significantly in the sea area south of 49.8°N. These information provides a useful reference for sampling implementation in the subarctic open Pacific Ocean.

For one thing, understanding the evolution of climate and desertification in the Asian interior and verifying the hypothesis of eolian dust and iron fertilization have been a matter of debate in paleoceanography and paleoclimate. The Emperor Seamount Chain is far away from the land, and it receives continuous deposition of large amount of eolian dust, which is a key area for reconstructing the climate and environment of Asian interior. Our research discovered that the current contribution of eolian dust to Zone I is relative higher, consistent with the present pathway of the northern westerly. For another thing, significant input of volcanic material is also prevalent in the study area. Effectively discriminating the sources from eolian dust and volcanic detrital is crucial for above research. Here, we find that some parameters related to rare earth elements are reliable proxies for distinguishing eolian dust and volcanic materials, which provides a useful tool for tracing environment and climate changes in the Asian interior.

CONCLUSION

In this study, we investigate the compositions and spatial distribution of surface sediments along the Emperor Seamount Chain with a suite of proxies, including the grain size, organic matter, $CaCO_3$, major and rare earth elements. The main findings can be drawn as follows:

The sediment composition varies with latitude and there are significant differences in the types and composition of sediments between 33°N–44°N (Zone I), 44°N–49.8°N (Zone II), and 49.8°N–53°N (Zone III) in study area. Sediments are dominated by clayey silt in Zone I and Zone III and mainly consist of sand and silty sand in Zone II. The mean grain size of sortable silt shows that the hydrodynamic condition in sea mountain area is significantly stronger than that of the abyssal plain, especially at the water depth of 1,000–2,500 m in study area. The sediments in the study area mainly include three components: terrestrial, volcanic and biogenic materials. There are evident positive correlation between Al_2O_3 and Fe_2O_3, TiO_2, MgO, K_2O, MnO, and REE, indicating that sediments in the study area have significant contribution of terrigenous debris. Obvious negative correlations between the content of $CaCO_3$ and Al_2O_3 and positive Eu anomaly indicate contribution of biogenic and volcanic materials, respectively. The index of rare earth elements further shows that the contribution of eolian dust is higher between 33°N and 44°N, while the contribution of volcanic materials is higher between 44°N and 49.8°N. The relative contributions of terrestrial, biogenic and volcanic sources vary with latitude and water depth.

There are visible negative Ce anomalies in surface sediments of the study area, which mainly occur in areas where calcareous ooze develops. The distribution pattern of negative Ce anomaly is the same as that of REE in seawater, and has weak negative correlation with Mn/Fe. Therefore, we conclude that the negative Ce anomaly in the study area mainly inherits signal of seawater, and redox change of sediments has weak influence on negative Ce anomaly.

DATA AVAILABILITY STATEMENT

The original contributions presented in the study are included in the article/supplementary material, further inquiries can be directed to the corresponding authors.

AUTHOR CONTRIBUTIONS

XS and JZ conceived the study. JZ, ZD, KW, YW, JL, DN, and LL-J collected the samples. JC and AZ completed the experiments. JC and JZ analyzed the data and wrote the manuscript with contribution from all co-authors. All authors contributed to the article and approved the submitted version.

FUNDING

This work was supported by the National Natural Science Foundation of China (Grant Nos. 41876065 and 41476056), the National Program on Global Change and Air-Sea Interaction (GASI-GEOGE-04), and the Taishan Scholars Program of Shandong (TSQN20182117).

ACKNOWLEDGMENTS

We would like to thank the captain, crews and participants of RV SONNE cruise SO264 for their support during sampling. We also particularly thank the German Federal Ministry of Education and Research for providing the fund for the SO264 cruise. We are also thankful to the Key Laboratory of Marine Geology and Metallogeny, First Institute of Oceanography, Ministry of Natural Resources, China for providing experimental support for the analysis and testing of the samples in this article.

REFERENCES

Aydin, M., Top, Z., and Olson, D. B. (2004). Exchange processes and watermass modifications along the subarctic front in the North Pacific: oxygen consumption rates and net carbon flux. *J. Mar. Res.* 62, 153–167. doi: 10.1357/002224004774201672

Bai, Y., Liu, J., Zhang, H., Gao, J., and Cui, J. (2013). The analysis of organic carbon and total nitrogen in marine sediments. *Mar. Environ. Sci.* 32, 444–459.

Clark, M. R., Rowden, A. A., Schlacher, T., Williams, A., Consalvey, M., and Stocks, K. I. (2010). The ecology of seamounts: structure, function, and human impacts. *Annu. Rev. Mar. Sci.* 2, 253–278. doi: 10.1146/annurev-marine-120308-081109

Ding, Z., Yu, Z., and Rutter, N. W. (1994). Towards an orbital time scale for chinese loess deposits. *Quantern. Sci. Rev.* 13, 39–70. doi: 10.1016/0277-3791(94)90124-4

Farrell, J. W., and Warren, L. P. (1989). Climatic change and CaCO3 Preservation: an 800000 year bathymetric reconstruction from the Central Equatorial Pacific Ocean. *Paleoceanography* 4, 447–466. doi: 10.1029/PA004i004p00447

Franzese, A. M., and Hemming, S. R. (2013). "Terrigenous sediments," in *Encyclopedia of Quaternary Science (Second Edition)*, eds S. A. Elias and C. J. Mock (Amsterdam: Elsevier), 941–945.

Fry, B., and Sherr, E. B. (1984). 13C measurements as indicators of carbon flow in marine and freshwater ecosystems. *Stable Isotopes Ecol. Res.* 27, 13–47. doi: 10.1007/978-1-4612-3498-2-12

Gao, A., Chen, Z., Liu, Y., Sun, H., and Yang, S. (2003). Geochemical characteristics of rare earth elements in the surface sediments of the Chukchi Sea. *Sci. China Ser. D Earth Sci.* 33, 148–154. doi: 10.3321/j.issn:1006-9267.2003.02.007

Hu, D. K., Böning, P., Köhler, C. M., Hillier, S., Pressling, N., and Wan, S. (2012). Deep sea records of the continental weathering and erosion response to East Asian monsoon intensification since 14ka in the South China Sea. *Chem. Geol.* 326-327, 1–18. doi: 10.1016/j.chemgeo.2012.07.024

Jiang, F., Zhou, X., Li, A., and Li, T. (2008). δEuN-σREEs graphically and quantitatively distinguish the sediments of the Yangtze River and the Yellow River. *Sci. China Ser. D Earth Sci.* 38, 1460–1468.

Jiang, Z., Li, S., Liu, Q., Zhang, J., and Zhang, Y. (2019). The kinematic mechanism study of Hawaii-Emperor seamount chain: evidence from paleomagnetic records. *Mar. Geol. Quatern. Geol.* 39, 104–114.

Jiang, Z., and Liu, Q. (2011). Magnetic characteristics of the sediments from the ODP882A hole in the Northwest Pacific from the late Pliocene to the early Pleistocene and their paleoclimatic significance. *Sci. Sin.* 41, 1242–1252. doi: 10.1007/s11769-011-0446-4

Jones, C. E., Halliday, A. N., Rea, D. K., and Owen, R. M. (2000). Eolian inputs of lead to the North Pacific. *Geochim. Cosmochim. Acta* 64, 1405–1416. doi: 10.1016/s0016-7037(99)00439-1

Kato, Y., Fujinaga, K., Nakamura, K., Takaya, Y., Kitamura, K., and Ohta, J. (2011). Deep-sea mud in the Pacific Ocean as a potential resource for rare-earth elements. *Nat. Geosci.* 4, 535–539. doi: 10.1038/ngeo1185

Kawabe, M., and Fujio, S. (2010). Pacific ocean circulation based on observation. *J. Oceanogr.* 66, 389–403. doi: 10.1007/s10872-010-0034-8

Klein, E. M. (2003). "Geochemistry of the igneous oceanic crust," in *Treatise on Geochemistry*, eds H. D. Holland and K. K. Turekian (Amsterdam: Elsevier).

Liu, J. P., Xue, Z., Ross, K., Wang, H. J., Yang, Z. S., and Li, A. C. (2009). Fate of sediments delivered to the sea by Asian large rivers: long-distance transport and formation of remote alongshore clinothems. *Sediment. Rec.* 7, 4–9. doi: 10.2110/sedred.2009.4.4

Mccave, I. N., Andrews, J., Smik, L., and Belt, S. T. (2020). Ocean surface and bottom water conditions, iceberg drift and sediment transport on the North Iceland margin during MIS 3 and MIS 2. *Quatern. Sci. Rev.* 252:106722. doi: 10.1016/j.quascirev.2020.106722

Mccave, I. N., Manighetti, B., and Robinson, S. G. (1995). Sortable silt and fine sediment size/composition slicing: parameters for palaeocurrent speed and palaeoceanography. *Paleoceanography* 10, 593–610. doi: 10.1029/94pa03039

Mcclain, C. R. (2007). Seamounts: identity crisis or split personality? *J. Biogeogr.* 34, 2001–2008. doi: 10.1111/j.1365-2699.2007.01783.x

Meyers, P. A. (1997). Organic geochemical proxies of paleoceanographic, paleolimnologic, and paleoclimatic processes. *Organ. Geochem.* 27, 213–250. doi: 10.1016/S0146-6380(97)00049-1

Miao, W., Shao, L., Pang, X., Lei, Y., Qiao, P., and Li, A. (2008). Ree geochemical characteristics in the Northern South China Sea since the oligocene. *Mar. Geol. Quatern. Geol.* 28, 71–78.

Moore, J. G. (1970). Relationship between subsidence and volcanic load, Hawaii. *Bull. Volcanol.* 34, 562–576. doi: 10.1007/BF02596771

Nath, B. N., Roelanclts, I., Sudhakar, M., and Pluger, W. L. (1992). Rare earth elements patterns of the central Indian basin sediments related to their lithology. *Geophys. Res. Lett.* 19, 1197–1200. doi: 10.1029/92GL01243

Nürnberg, D. (ed.) (2018). *RV SONNE Fahrtbericht/Cruise Report SO264-SONNE-EMPEROR: The Plio/Pleistocene to Holocene Development of the Pelagic North Pacific from Surface to Depth -Assessing its Role for the Global Carbon Budget and Earth's Climate, Suva (Fiji)-Yokohama (Japan), 30.6 - 24.8.2018*. GEOMAR Report, N. Ser. 046. Kiel: GEOMAR Helmholtz-Zenturm für Ozeanforschung.

Oka, A., and Niwa, Y. (2013). Pacific deep circulation and ventilation controlled by tidal mixing away from the sea bottom. *Nat. Commun.* 4:2419. doi: 10.1038/ncomms3419

Paterson, G. A., and Heslop, D. (2015). New methods for unmixing sediment grain size data. *Geochem. Geophys. Geosyst.* 16, 4494–4506. doi: 10.1002/2015GC006070

Pattan, J. N., Pearce, N. J. G., and Mislankar, P. G. (2005). Constraints in using Cerium-anomaly of bulk sediments as an indicator of paleo bottom water redox environment: a case study from the Central Indian Ocean Basin. *Chem. Geol.* 221, 260–278. doi: 10.1016/j.chemgeo.2005.06.009

Paytan, A., and McLaughlin, K. (2007). The oceanic phosphorus cycle. *Chem. Rev.* 107, 563–576. doi: 10.1021/cr0503613

Qiu, B. (2002). The kuroshio extension system: its large-scale variability and role in the midlatitude Ocean-Atmosphere interaction. *J. Oceanogr.* 58, 57–75. doi: 10.1023/A:1015824717293

Ren, J., Gersonde, R., Esper, O., and Sancetta, C. (2014). Diatom distributions in northern North Pacific surface sediments and their relationship to modern environmental variables. *Palaeogeogr. Palaeoclimatol. Palaeoecol.* 402, 81–103. doi: 10.1016/j.palaeo.2014.03.008

Roser, B. P., and Korsch, R. J. (1988). Provenance signatures of sandstone-mudstone suites determined using discriminant function analysis of major-element data. *Chem. Geol.* 67, 119–139. doi: 10.1016/0009-2541(88)90010-1

Schlitzer, R. (2002). Interactive analysis and visualization of geoscience data with Ocean data view. *Comput. Geosci.* 28, 1211–1218. doi: 10.1016/s0098-3004(02)00040-7

Serno, S., Winckler, G., Anderson, R. F., Hayes, C. T., McGee, D., Machalett, B., et al. (2014). Eolian dust input to the Subarctic North Pacific. *Earth Planet. Sci. Lett.* 387, 252–263. doi: 10.1016/j.epsl.2013.11.008

Suzanne, N. L., and David, T. S. (2000). Three-dimensional estimation of elastic thickness under the Louisville Ridge. *J. Geophys. Res.* 105, 13239–13252. doi: 10.1029/2000JB900065

Tachikawa, K., Jeandel, C., Vangriesheim, A., and Dupre, B. (1999). Distribution of rare earth elements and neodymium isotopes in suspended particles of the tropical Atlantic Ocean (EUMELI site). *Deep Sea Res. I* 46, 733–755. doi: 10.1016/S0967-0637(98)00089-2

Talley, L. D. (1993). Distribution and formation of North Pacific intermediate water. *J. Phys. Oceanoraphy* 23, 517–537. doi: 10.1175/1520-048519930232.0.CO;2

Taylor, S. B., and Mclennan, S. M. (1995). The geochemical evolution of the continental crust. *Rev. Geophys.* 33, 241–265. doi: 10.1029/95RG00262

Toyoda, K., and Masuda, A. (1991). Chemical leaching of pelagic sediments : identification of the carrier of Ce anomaly. *Geochem. J.* 25, 95–119. doi: 10.2343/geochemj.25.95

Toyoda, K., Nakamura, Y., and Masuda, A. (1990). Rare earth elements of Pacific pelagic sediments. *Geochim. Cosmochim. Acta* 54, 1093–1103. doi: 10.1016/0016-7037(90)90441-M

Ueno, H. (2003). Intermediate water circulation in the North Pacific subarctic and northern subtropical regions. *J. Geophys. Res.* 108:JC001372. doi: 10.1029/2002JC001372

Van Scoy, K. A., and Druffel, E. R. M. (1993). Ventilation and transport of thermocline and intermediate waters in the Northeast Pacific during recent E1 Ninos. *J. Geophys. Res.* 98, 18083–18088. doi: 10.1029/93JC01797

Wang, R., Biskaborn, B. K., Ramisch, A., Ren, J., Zhang, Y., and Gersonde, R. (2016). Modern modes of provenance and dispersal of terrigenous sediments in the North Pacific and Bering Sea: implications and perspectives for palaeoenvironmental reconstructions. *Geo Mar. Lett.* 36, 259–270. doi: 10.1007/s00367-016-0445-7

Wang, W. (2014). *Late Paleozoic tectonic evolution of the central-northern margin of the North China Craton: Constraints from zircon U-Pb Ages and geochemistry of igneous rocks in Ondor Sum-Jining area*. Changchun: Jinlin University of China.

Wang, W., and Chen, J. (2011). Distribution characters of major elemental composition contents and the influence factors in sediments of the late Pleistocene in central South China Sea. *J. Oceanogr. Taiwan Strait* 30, 449–457. doi: 10.3969/J.ISSN.1000-8160.2011.04.001

Wang, Y., Dou, Y., Xu, J., Chen, X., Li, J., and Cai, F. (2018). Organic matter source in the middle southern Okinawa Trough and its response to paleoenvironmental evolution since 16 ka. *Quatern. Sci.* 38, 769–781.

Warner, M. J., Bullister, J. L., Wisegarver, D. P., Gammon, R. H., and Weiss, R. F. (1996). Baisn-wide distributions of chlorofluorocarbons CFC-11 and CFC-12 in the North Pacific: 1985-1989. *J. Geophys. Res.* 101, 20525–20542. doi: 10.1029/96JC01849

Weltje, G. J. (1997). End-member modeling of compositional data: numerical-statistical algorithms for solving the explicit mixing problem. *Math. Geol.* 29, 503–549. doi: 10.1007/BF02775085

Weltje, G. J., and Prins, M. A. (2003). Muddled or mixed? Inferring palaeoclimate from size distributions of deep-sea clastics. *Sedimen. Geol.* 162, 39–62. doi: 10.1016/S0037-0738(03)00235-5

Wilson, J. T. (1973). Mantle plumes and plate motions. *Tectonophysics* 19, 149–164. doi: 10.1016/0040-1951(73)90037-1

You, Y. Z. (2003). The pathway and circulation of North Pacific Intermediate Water. *Geophys. Res. Lett.* 30:GL018561. doi: 10.1029/2003GL018561

Zhang, J., and Nozaki, Y. (1998). Behavior of rare earth elements in seawater at the ocean margin: a study along the slopes of the Sagami and Nankai troughs near Japan. *Geochim. Cosmochim. Acta* 62, 1307–1317. doi: 10.1016/s0016-7037(98)00073-8

Zhao, Y., Yan, M., Li, A., Gao, S., and Jia, J. (2002). Geochemistry of muds along the coast of China and their significance. *Geol. China* 29, 181–185. doi: 10.3969/j.issn.1000-3657.2002.02.014

Zhu, A., Liu, J., Zhang, H., Bai, Y., Cui, J., and Liu, S. (2012). Distribution pattern of REEs in the inner-shelf mud area of east China Sea. *Mar. Geol. Quatern. Geol.* 32, 1–10. doi: 10.3724/SP.J.1140.2012.01001

Zhu, A., Liu, J., Zou, J., Sergey, G., Li, C., and Liu, Y. (2019). Characteristics of sedimentary geochemistry of surface sediments in the subarctic Pacific Marginal Seas. *Adv. Mar. Sci.* 37, 601–612. doi: 10.3969/j.issn.1671-6647.2019.04.007

Zhu, A., Shi, X., Zou, J., Zhang, H., Wu, Y., and Liu, Y. (2015). Paleoenvironment changes in the northern Okinawa trough since 88 ka: evidences from element geochemistry. *Acta Oceanol. Sin.* 37, 58–69.

Zou, J., Shi, X., Liu, Y., and Liu, J. (2010). Geochemical record of terrigenous sediments from the Sea of Japan since last glacial and its response to sea level and climate change. *Mar. Geol. Quatern. Geol.* 30, 75–86. doi: 10.3724/SP.J.1140.2010.02075

Conflict of Interest: The authors declare that the research was conducted in the absence of any commercial or financial relationships that could be construed as a potential conflict of interest.

ORIGINAL RESEARCH
published: 25 May 2021
doi: 10.3389/feart.2021.678189

Response of Mangrove Development to Air Temperature Variation Over the Past 3000 Years in Qinzhou Bay, Tropical China

Yao Zhang[1,2], Xianwei Meng[2,3]*, Peng Xia[2]* and Zhen Li[4†]

[1]College of Marine Geosciences, Ocean University of China, Qingdao, China, [2]Key Laboratory of Marine Geology and Metallogeny, First Institute of Oceanography, Ministry of Natural Resources, Qingdao, China, [3]Laboratory for Marine Geology and Environment, Qingdao National Laboratory for Marine Science and Technology, Qingdao, China, [4]School of Earth and Ocean Sciences, University of Victoria, Victoria, BC, Canada

Edited by:
Min-Te Chen,
National Taiwan Ocean University,
Taiwan

Reviewed by:
Lejun Liu,
Ministry of Natural Resources, China
Chuanxiu Luo,
Chinese Academy of Sciences (CAS),
China
Hasrizal Shaari,
University of Malaysia Terengganu,
Malaysia

***Correspondence:**
Xianwei Meng
mxw@fio.org.cn
Peng Xia
pengxia@fio.org.cn

†Present address:
Zhen Li,
Department of Earth, Ocean and
Atmospheric Sciences, University of
British Columbia, Vancouver, BC,
Canada

Specialty section:
This article was submitted to
Quaternary Science, Geomorphology
and Paleoenvironment,
a section of the journal
Frontiers in Earth Science

Received: 09 March 2021
Accepted: 05 May 2021
Published: 25 May 2021

Citation:
Zhang Y, Meng X, Xia P and Li Z (2021)
Response of Mangrove Development
to Air Temperature Variation Over the
Past 3000 Years in Qinzhou Bay,
Tropical China.
Front. Earth Sci. 9:678189.
doi: 10.3389/feart.2021.678189

Mangroves, a blue carbon ecosystem between land and ocean in the (sub)tropics, are sensitive to changes in climate and the sea level. It is imperative to reconstruct the historical dynamics of their development to predict the fate of mangrove ecosystems in the backdrop of rapid global changes. This study analyzes records of the sources of organic matter from sediment core Q43 of Qinzhou Bay in tropical China by using the endmember mixing model based on stable organic carbon isotopes and C/N ratio. Mangrove-derived organic matter (MOM) is regarded as a reliable indicator for reconstructing the historical development of mangroves. The variations in MOM in Qinzhou Bay over the past ~3,000 cal yr BP indicate that mangrove forests underwent two periods of flourishment: ~2,200–1,750 cal yr BP and ~1,370–600 cal yr BP, as well as three periods of deterioration: ~3,000–2,200 cal yr BP, ~1,750–1,370 cal yr BP, and ~600–0 cal yr BP. Of factors that might have been influential, changes in the relative sea level and the regional hydrological environment (e.g., seawater temperature, salinity, and hydrodynamic conditions) did not appear to have notable effects on mangrove flourishing/degradation. However, climate change, especially the variation in air temperature, formed the primary factor controlling mangrove development. The stages of mangrove flourishing/deterioration corresponded to the warm/cold periods of the climate, respectively. Noteworthy is that the rapid rise in air temperature during the Anthropocene warm period should have promoted mangrove development, but the increasing intensity of human activity has reversed this tendency leading to the degradation of mangroves.

Keywords: organic matter source, mangrove-derived organic matter, mangrove development, air temperature, anthropogenic activity, late Holocene

INTRODUCTION

Mangroves inhabit intertidal zones in tropical and subtropical regions, and control exchanges of materials at the interfaces of the land, marine, and atmosphere ecosystems (Woodroffe et al., 2016; Hatje et al., 2020). They provide multiple ecosystem services, such as mitigating coastal erosion from waves and wind, guaranteeing fishery resources and food security for coastal inhabitants, and aiding

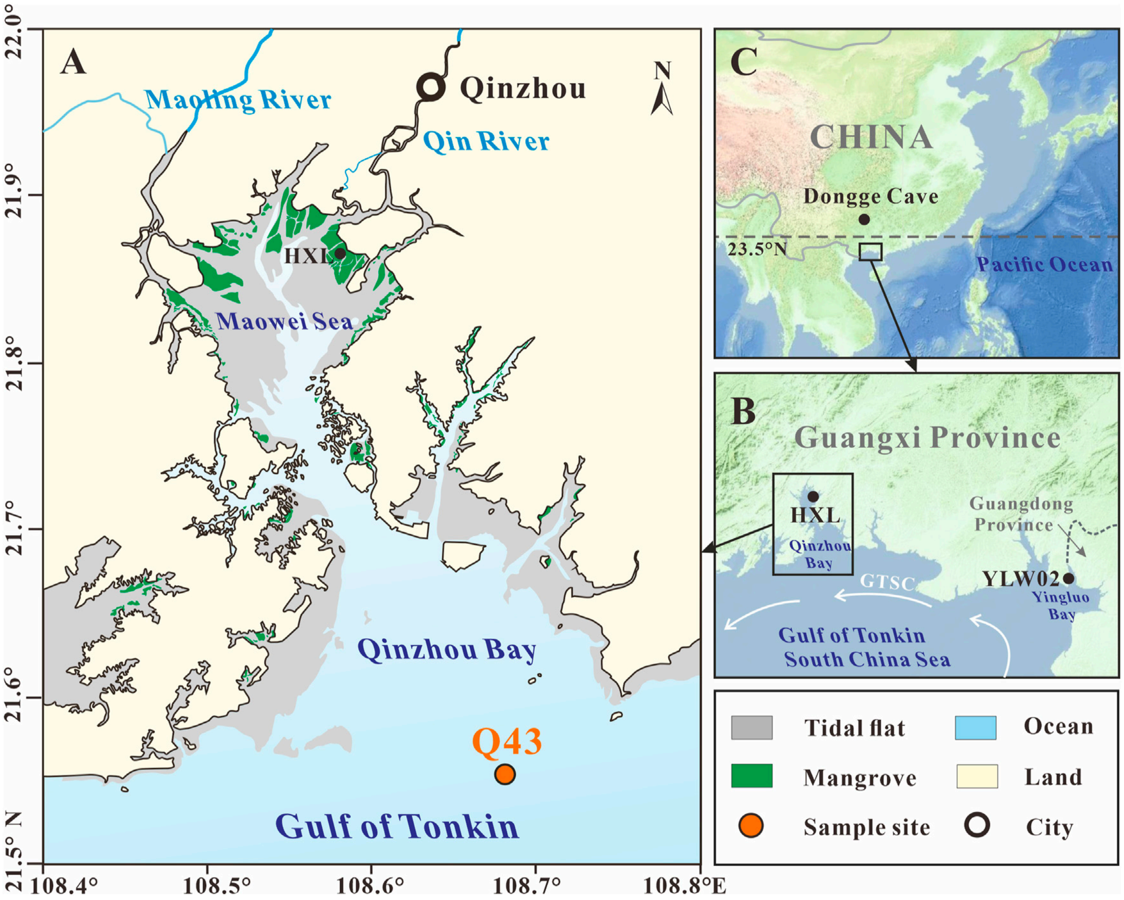

FIGURE 1 | Locations of the **(A)** sediment core Q43 in Qinzhou Bay, **(B)** northern Gulf of Tonkin, **(C)** tropical China. The referenced sites contain HXL in Qinzhou Bay (Xia et al., 2019), YLW02 in Yingluo Bay (Meng et al., 2017), and Dongge Cave in SW China (Wang et al., 2005). GTSC: Gulf of Tonkin Surface Current (Liu et al., 2016).

in the protection of adjacent seagrass and coral reef ecosystems (Duke et al., 2007; Nellemann et al., 2009; Lee et al., 2014; Himes-Cornell et al., 2018; Hatje et al., 2020). More importantly, mangrove forests are efficient producers, capturers, and sinks of carbon (Jennerjahn and Ittekot, 2002; Duarte et al., 2005; Alongi, 2014; Jennerjahn, 2021). Hence, they play a disproportionately important role in global carbon cycling, and are key blue carbon sinks that can contribute to climate change mitigation (Duke et al., 2007; Duarte et al., 2013; Duarte and Arabia, 2017; Alongi, 2020; Sasmito et al., 2020).

However, mangrove forests are sensitive and vulnerable to environmental changes, e.g., climate change and fluctuations in the sea level (Ellison and Stoddart, 1991; Alongi, 2008; Ellison, 2008; Jennerjahn, 2012; Ellison, 2014; Lovelock et al., 2015; Woodroffe et al., 2016). Mangroves can migrate to landward/seaward regions with the rise/fall in the relative sea level (RSL) (Ellison and Stoddart, 1991; Woodroffe et al., 2016). A rapid change in the RSL can result in the decline or even the disappearance of mangrove habitats. Low-intensity rainfall can also lead to mangrove degradation through reductions in freshwater runoff, fluvial sediment, and nutrient inputs (Alongi, 2008; Gilman et al., 2008). High-frequency winter cooling events induced by variations in the intensity of the monsoon can also prevent mangrove development (Meng et al., 2016a). Likewise, high-temperature events can result in hypersaline conditions with high evaporation rates (Gilman et al., 2008), which lead to mangrove degradation. In addition, anthropogenic threats, such as pollution, overexploitation, and the conversion of patterns of land use (Bao et al., 2013; Friess et al., 2019; Veettil et al., 2019), have vastly impacted mangrove dynamics, especially since the Anthropocene.

The world at present is characterized by a rapid sea level rise, rapid warming, frequent extreme climate events, and an increasing population. Therefore, to predict the fate of mangrove ecosystems under this rapidly changing environment, it is imperative to understand how they have changed or disappeared in the past (Valiela et al., 2001), by reconstructing historical mangrove dynamics through useful indicators recorded in sediments (Gonneea et al., 2004; Ellison, 2008; França et al., 2013; Cohen et al., 2016; Meng et al., 2017; Xia et al., 2019; Vaughn et al., 2021).

Tropical or subtropical Asia, a region that features a unique climate system (Asian monsoon) and a long history of human civilization, holds most of the world's mangrove forests along its winding and long coastline (Giri et al., 2011). Hence, it is an ideal selection to study the mangrove development and its responses to natural and anthropogenic factors. In this study, we use records of organic matter (OM) sources from sediment core Q43 of Qinzhou Bay (**Figure 1**) in tropical China to reconstruct the history of mangrove development over the past 3,000 years. The aim is to answer the question of how mangrove forests respond to changes in the sea level, climate (air temperature and rainfall), hydrological environment (seawater temperature, salinity, and hydrodynamic conditions), and anthropogenic activities.

MATERIALS AND METHODS

Study Area and Sampling Site

Qinzhou Bay is located in the northern Gulf of Tonkin (**Figure 1B**) in tropical China (**Figure 1C**), and is divided into an inner zone (Maowei Sea) and an outer zone by a narrow channel (**Figure 1A**). Two small tropical rivers, the Maoling River and the Qin River, debouching into the Qinzhou Bay. Most of the intertidal zone of the Maowei Sea and adjacent coasts are occupied by mangrove forests. The Maowei Sea Mangrove Nature Reserve was established by the local government in 2005. The mangrove forests are generally 1–4 m high and exhibit a zonal distribution from the upper (*Bruguiera gymnorrhiza* and *Rhizophora stylosa*), middle (*Kandelia candel* and *Egiceras corniculatum*), and lower (*Avicennia marina*) tidal flats (Li et al., 2008).

The study area is characterized by tropical monsoonal climate. The mean annual air temperature is 22.4°C, and ranges from 0.8 to 37.4°C. The average annual rainfall is 2,150 mm, 80–85% of which falls during the summer rainy season (April–September). The region experiences an irregular diurnal tide with a mean tidal range of 2.5 m (Meng and Zhang, 2014). The features of the seawater, which are affected only by monsoonal rainfall, are relatively stable, with a mean temperature of 23.5°C, salinity of 20–23‰, and pH of 7.6–7.8 (Fan et al., 2005). The anticlockwise Gulf of Tonkin Surface Current (GTSC) controls the regional hydrologic system (Liu et al., 2016).

The sediment core Q43 (108°40.49′E, 21°32.73′N), which is 150 cm long, was collected from Qinzhou Bay at a depth of 9 m in May 2009 using a gravity piston corer (**Figure 1A**). The core is located in the center of the outer zone of Qinzhou Bay, and thus its sedimentary records best reflect the history of mangrove development for the entire Qinzhou Bay. According to the sedimentary features, the core can be visually divided into two sections: the lower section (150–100 cm) is characterized by dark yellowish-brown sandy sediments and lower water concentration, and the upper section (150–0 cm) is mainly composed of finer dark gray sand-silt-clay and contains many fragmentized shells at 5–6, 56–57, and 86–88 cm. There is no clear hiatus between the upper and lower sections. The sediment core was sectioned by stainless steel cutters at intervals of 2 cm within 24 h of collection. All sediment subsamples were freeze-dried for 72 h at −55°C, and were then packed in sealed polyethylene bags and stored in a desiccator at room temperature for subsequent analyses.

Laboratory Analyses

Shells from six horizons were selected for accelerator mass spectrometry (AMS) ^{14}C dating measurement at the Beta Analyses Company in FL, United States (**Table 1**). The conventional radiocarbon ages were corrected by a regional carbon reservoir age of 10 ± 50 years (Southon et al., 2002) and converted into calibrated calendar years by the program Calib 7.1 with Marine 13 calibration curves (Reimer et al., 2013). All calibrated ages were reported in years before 1950 CE (yr BP) and in cal yr BP with a precision of 2σ.

The grain size distribution was measured by using a Malvern Mastersizer 2000 laser particle analyzer (Malvern, Inc., United Kingdom), at a measurement range of 0.02–2,000 μm and a size resolution of 0.01 φ after removing the OM and carbonate fractions by adding 15 ml 3% H_2O_2 and 5 ml 10% hydrochloric acid (HCl), respectively. All sample preparation and measurements were completed at the Key Laboratory of Marine Geology and Metallogeny of the First Institute of Oceanography, China Ministry of Natural Resources.

The freeze-dried sediment samples were treated with 1 N of HCl for 24 h at room temperature (25°C) to remove inorganic carbon. Then, they were rinsed by ultra-pure water several times until pH 7, and left to dry at 50°C for 72 h. Approximately 30–40 mg of homogenized dry sediments were carefully placed in tin capsules and crimp-sealed for analysis. The contents of stable organic carbon isotope ($^{13}C_{org}$), total organic carbon (TOC), and total nitrogen (TN) were determined for all subsamples by a Delta Plus XP mass spectrometer (Thermo Scientific, Bremen, Germany), and by a Vario EL-III Elemental Analyzer (Elementar, Hanau, Germany) in continuous flow mode at the Stable Isotope Laboratory of College of Resources and Environmental Sciences of the China Agricultural University (Beijing). The results are reported in standard delta notation (δ) using permitted units (‰):

$$\delta\,(‰) = \frac{\left(R_{\text{sample}} - R_{\text{standard}}\right)}{R_{\text{standard}}} \times 1000 \qquad (1)$$

where δ (‰) represents the stable isotope value of organic carbon and R is the $^{13}C/^{12}C$ ratio. The reference standard used for carbon is the Vienna PeeDee Belemnite (VPDB) standard. The analytical precisions of $^{13}C_{org}$, TOC, and TN were ±0.2‰, ±0.02 wt. %, and ±0.005 wt. %, respectively. The C/N ratio was calculated by the atomic (molar) ratio of TOC to TN.

Endmember Mixing Models for Discriminating Organic Matter Sources

The endmember mixing model is a classical method by which the proportional contributions of different sources to a mixture OM can be quantified (Dittmar et al., 2001; Gonneea et al., 2004). Models based on $\delta^{13}C$ and/or C/N have been widely used to identify the sources of OM in the sediments or suspended solids of different ecosystems, such as rivers (Liu et al., 2019; Zhang et al., 2021), lakes (Dong et al., 2020), and ocean (Gonneea et al., 2004; Xia et al., 2015; Meng et al., 2016b, 2017). The formulae for the ternary mixing model based on $\delta^{13}C$ and C/N are as follows:

TABLE 1 | List of AMS ^{14}C ages from core Q43.

Depth (cm)	Material	Conventional age (yr BP)	Calibrated age range (cal yr BP, 2σ)	Mean calibrated age (cal yr BP)
6	Shell	660 ± 30	138–431	285
27	Shell	1,340 ± 30	729–995	862
57	Shell	1,850 ± 30	1,278–1,517	1,398
81	Shell	2,160 ± 30	1,582–1,879	1,731
101	Shell	2,500 ± 30	1,994–2,300	2,147
149	Shell	3,330 ± 30	2,933–3,331	3,162

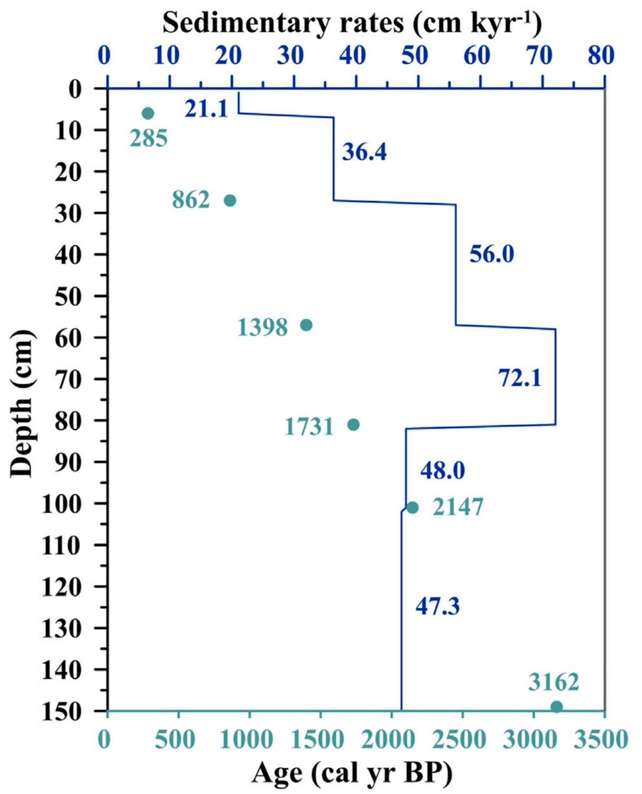

FIGURE 2 | Plots of Depth vs. Age and Sedimentary rates from core Q43.

$$\delta^{13}\mathrm{C}_{\mathrm{sample}} = \left[f_{\mathrm{A}} \times \delta^{13}\mathrm{C}_{\mathrm{A}}\right] + \left[f_{\mathrm{B}} \times \delta^{13}\mathrm{C}_{\mathrm{B}}\right] + \left[f_{\mathrm{C}} \times \delta^{13}\mathrm{C}_{\mathrm{C}}\right] \quad (2)$$

$$\frac{\mathrm{C}}{\mathrm{N}_{\mathrm{sample}}} = \left[f_{\mathrm{A}} \times \frac{\mathrm{C}}{\mathrm{N}_{\mathrm{A}}}\right] + \left[f_{\mathrm{B}} \times \frac{\mathrm{C}}{\mathrm{N}_{\mathrm{B}}}\right] + \left[f_{\mathrm{C}} \times \frac{\mathrm{C}}{\mathrm{N}_{\mathrm{C}}}\right] \quad (3)$$

$$f_{\mathrm{A}} + f_{\mathrm{B}} + f_{\mathrm{C}} = 1 \quad (4)$$

where A, B, and C are the potential OM endmembers, and f represents the percentage of contribution of each endmember. The values of δ^{13}C and C/N of the endmembers are discussed in *Potential Sources of Organic Matter and Their Endmember Values*. When the OM in a sample is a mixture of two sources, it should be explained by using a binary mixing model with δ^{13}C:

$$\delta^{13}\mathrm{C}_{\mathrm{sample}} = \left[f_{\mathrm{A}} \times \delta^{13}\mathrm{C}_{\mathrm{A}}\right] + \left[f_{\mathrm{B}} \times \delta^{13}\mathrm{C}_{\mathrm{B}}\right] \quad (5)$$

$$f_{\mathrm{A}} + f_{\mathrm{B}} = 1 \quad (6)$$

RESULTS

Chronological Results and Sedimentary Rates

Calibrated radiocarbon ages at depths of 6, 27, 57, 81, 101, and 122 cm produced ages of 285, 862, 1,398, 1,731, 2,147, and 3,162 cal yr BP, respectively, and no age inversion was observed (**Table 1**). Downcore ages were calculated by linear interpolation between the dated sediment layers. Based on the ratio of the depth intervals to the time spans, the sedimentation rates of the core sections 0–6, 6–27, 27–57, 57–81, 81–101, and 101–149 cm were about 21.1, 36.4, 56.0, 72.1, 48.0, and 47.3 cm kyr^{-1}, respectively (**Figure 2**), with a mean value of 47.12 cm kyr^{-1}. The sedimentation rates in core Q43 are similar to the vertical accretion of mangrove forests reported by other researchers in tropical China (Meng et al., 2017; Xia et al., 2019), Puerto Rico (Cohen et al., 2016), and the Amazon Region (França et al., 2013).

Features of Grain Size, Total Organic Carbon, Total Nitrogen, C/N Ratio, and δ^{13}C$_{\mathrm{org}}$

The values of and variations in the grain size, TOC, TN, C/N ratio, and δ^{13}C$_{\mathrm{org}}$ are shown in **Figures 3A–F**. The proportions of sand, silt, and clay in the entire core were 58.6 ± 14.9%, 24.1 ± 8.1%, and 17.3 ± 7.6%, respectively. The mean grain size (Mz) varied from 0.5 to 6.1 φ, with an average of 4.0 ± 1.6 φ. The TOC and TN contents were 0.67 ± 0.27% and 0.04 ± 0.02%, ranging between 0.16–1.3% and 0.01–0.08%, respectively. TOC was significantly and positively correlated with TN (TOC = 9.06 × TN + 0.25, $R^2 = 0.52$, $p < 0.01$), and the short intercept implies that the impact of inorganic nitrogen could be neglected (Goñi et al., 1998). The C/N value varied from 9.9 to 43.0 with a mean value of 19.0 ± 7.8. The average δ^{13}C$_{\mathrm{org}}$ value was −24.7 ± 0.6‰, ranging from −26.0 to −23.1‰. On the whole, the grain size and δ^{13}C$_{\mathrm{org}}$ showed a finer trend and an increasing tendency since ~3,000 cal yr BP, respectively, while the TOC, TN, and C/N collectively exhibited an abrupt change during 1,370–600 cal yr BP. Based on these vertical variations in the sediment core, it can be divided into three sections: the upper

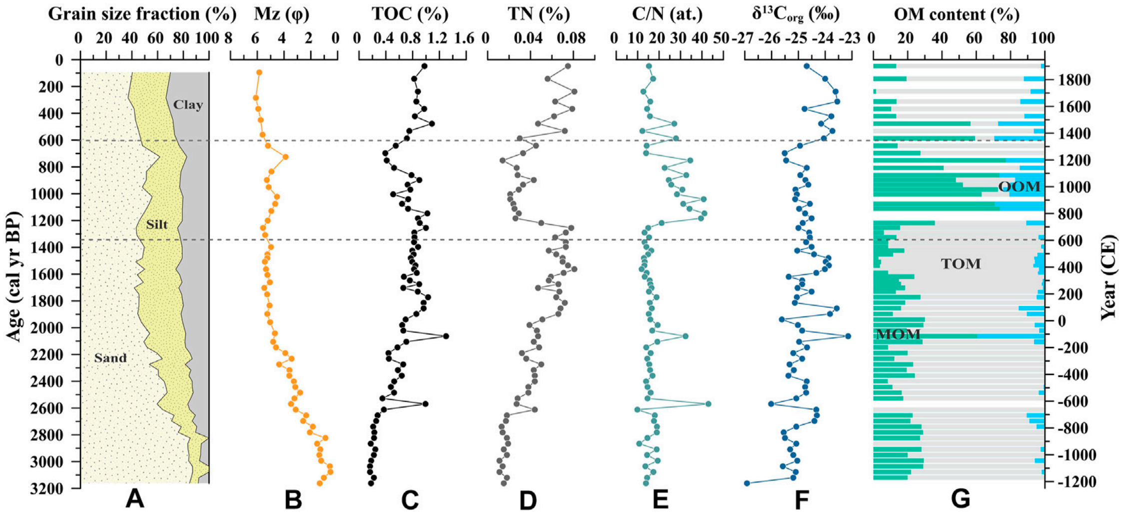

FIGURE 3 | Variations in the **(A)** grain size fraction, **(B)** mean grain size (Mz), **(C)** total organic carbon (TOC) and **(D)** total nitrogen contents (TN), **(E)** C/N ratio, **(F)** stable organic carbon isotope ($\delta^{13}C_{org}$), and **(G)** composition of organic matter (OM) source in sediment core Q43. TOM, MOM, and OOM represent terrestrial organic matter, mangrove-derived organic matter, and oceanic organic matter, respectively.

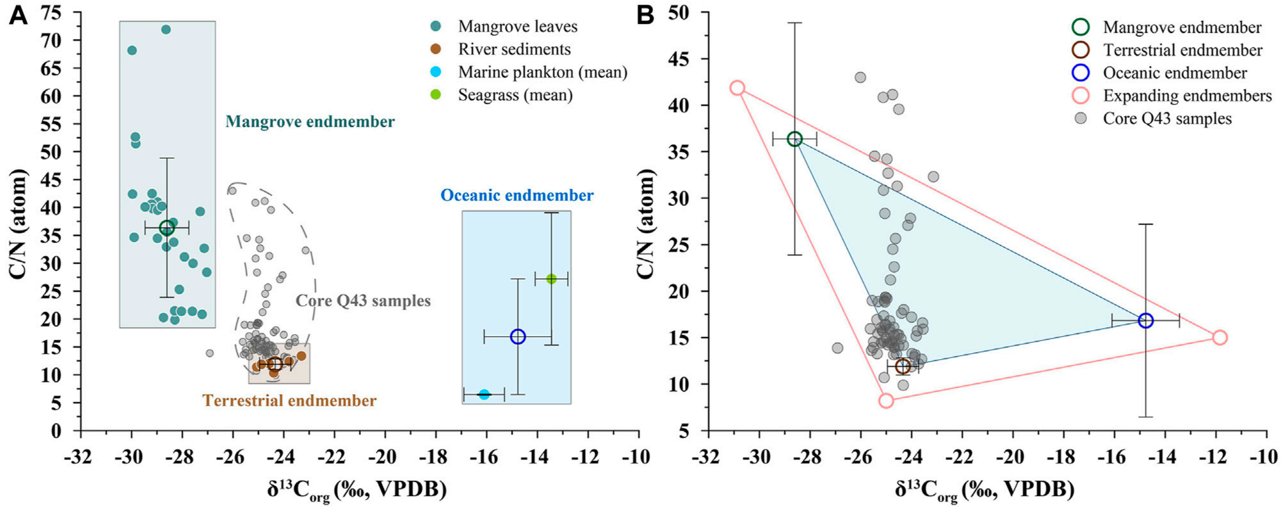

FIGURE 4 | Scatter diagrams of $\delta^{13}C_{org}$ vs. C/N for **(A)** endmembers of organic matter (OM) sources and **(B)** core Q43 samples with the ternary mixing model. The shadow areas in **(A)** represent the ranges of mangrove, terrestrial (Xia et al., 2015; Meng et al., 2016b), and oceanic endmembers (Xue et al., 2009; Xia et al., 2015; Qiu, unpublished data). The error bars show the standard deviation of the endmember values. The pink empty circles in **(B)** are endmember values with the tolerance interval expanded by 25%.

section (600–0 cal yr BP), middle section (1,370–600 cal yr BP), and lower section (3,000–1,370 cal yr BP).

In the upper section, all of the indices were relatively stable. The minimum grain size and the highest positive $\delta^{13}C_{org}$ appeared in this section, with mean values of −24.0 ± 0.4‰, and 5.8 ± 0.2 φ, respectively. However, most of the indicators, especially TOC, TN, and the C/N ratio, were abnormal in the middle section. The C/N ratio was as high as 27.3 ± 9. In the lower section, TOC, TN, and $\delta^{13}C_{org}$ showed an increasing trend, whereas the grain size became finer and the C/N ratio was relatively stable. The maximum grain size and lowest TOC content occurred in this section, with mean values of 3.4 ± 1.6 φ and 0.61 ± 0.28%, respectively.

Potential Sources of Organic Matter and Their Endmember Values

In general, the OM stored in marine sediments originates from autochthonous (i.e., marine production) and allochthonous contributions (i.e., terrestrial input). However, mangrove forests are also a significant contributor to the OM in mangrove coasts and adjacent seas. For example, a previous study in Qinzhou Bay reported that ~27% of the sedimentary OM derived from mangroves (Meng et al., 2016a). Therefore, mangrove forests, terrestrial matter, and marine production can be considered the potential endmembers of the sources of sedimentary OM in Qinzhou Bay (**Figure 4A**).

Mangrove roots and leaf litter are important contributors to carbon stocks in mangrove sediments (Duarte et al., 2005; Bouillon et al., 2008; Alongi, 2014). However, recent studies have shown that the values of $\delta^{13}C_{org}$ and C/N of the roots are generally within the range of, or overlap, those of leaf litter (Kusumaningtyas et al., 2019; Sasmito et al., 2020). Therefore, the values of $\delta^{13}C_{org}$ and C/N of mangrove leaves can be regarded as endmember values of mangrove production. The average $\delta^{13}C_{org}$ and C/N values of the leaves of different mangrove species (n = 30) collected along the Guangxi coasts were −28.6 ± 0.9‰ and 36.4 ± 12.5 (Xia et al., 2015; Meng et al., 2016b), respectively, and are consistent with those from Hainan Island in tropical China (Herbeck et al., 2011). They can thus be reasonably regarded as the endmember in this study.

Riverine inputs, especially in small tropical catchments, contribute a large amount of terrestrial OM flux that reaches the ocean (Moyer et al., 2013; Hernes et al., 2017). In the study region, there are two small tropical rivers, i.e., the Maoling River and the Qin River, debouching into the Qinzhou Bay. Thus, their riverine sediments (n = 6) can represent the terrestrial endmember of OM sources in this study with average values of −24.3 ± 0.6‰ for $\delta^{13}C_{org}$ and 11.9 ± 0.9 for C/N (Xia et al., 2015; Meng et al., 2016b).

Seagrass is widely distributed in the coastal waters of Guangxi, China (Meng and Zhang, 2014), and should be considered an important part of marine production. According to previous studies, seagrass collected from Guangxi coasts (n = 19) has an average $\delta^{13}C_{org}$ of −13.5 ± 0.6‰ and C/N of 27.2 ± 11.9 (Qiu, unpublished data), while marine plankton collected from the northern South China Sea (Xue et al., 2009; Xia et al., 2015) has an average $\delta^{13}C_{org}$ of −16.1 ± 0.8‰ and C/N of 6.5 ± 0.1. The oceanic endmember values ($\delta^{13}C_{org}$, −14.8 ± 1.3‰; C/N, 16.8 ± 10.4) of OM sources can be reasonably determined from these values.

Quantitative Estimation for Organic Matter Sources

Considering the indeterminacy of endmember values and isotopic fractionation effects in the endmember mixing model, a tolerance interval is introduced to the model, and it can be determined by the standard deviations and mean values of each endmember (Dittmar et al., 2001; Gonneea et al., 2004). When the original ternary plot was expanded by a tolerance interval of 25%, more than 90% of the samples could be explained in terms of the endmember mixing model (**Figure 4B**), which confirms the feasibility of using this method to discriminate among the sources of OM. Notably, samples that fell outside the strict validity (i.e., original triangle in blue) of the model, but were within the expanded area (in pink), should be treated with their corresponding binary mixing model based on $\delta^{13}C_{org}$.

According to the above methods, the contributions of terrestrial organic matter (TOM), mangrove-derived organic matter (MOM), and oceanic organic matter (OOM) to OM sources of sediment core Q43 were determined (**Figure 3G**). TOM was the largest OM contributor with a mean value of 68.6 ± 27.6%, followed by MOM with a mean value of 24.3 ± 19.7%, and OOM with a mean value of 7.1 ± 9.3%. Like the other indicators, the compositions of the OM sources can be roughly divided into three sections: the upper section (600–0 cal yr BP), middle section (1,370–600 cal yr BP), and lower section (3,000–1,370 cal yr BP). The MOM occupied the largest proportion of OM in the middle section with mean value of 48.7 ± 23.4%.

DISCUSSION

Effectiveness of Mangrove-Derived Organic Matter for Tracing Mangrove Development

Traditionally, the pollen content of mangroves is one of the most direct and effective proxies for tracing mangrove evaluation (Gonneea et al., 2004; Ellison, 2008; Li et al., 2008). However, the MOM has been used to successfully reconstruct the histories of mangrove development at different time scales (from the Anthropocene to the Holocene) in different regions around the world, e.g., the western coast of peninsular India (Caratini et al., 1994), Flamenco Lagoon in Puerto Rico (França et al., 2013), Gulf of Tonkin in tropical China (Meng et al., 2016b), and the Amazon estuary of northern Brazil (Cohen et al., 2016). A recent study has shown a relatively consistent tendency of variation and significant positive correlations (0.68–0.89, p < 0.01) between the MOM and mangrove pollen from mangrove sediment cores in different regions (Xia et al., 2021). Consequently, MOM is a reliable proxy for reconstructing regional mangrove development. This index has a more significant potential to recover high-resolution mangrove development, owing to its easily fine-cut sampling and cheaper cost of equipment, than pollen and biomarkers (Xia et al., 2021).

Mangrove Development Over the Past 3,000 Years

According to the variations in MOM, mangrove development in the Qinzhou Bay since ~3,000 cal yr BP can be detailedly divided into five stages (**Figures 2G**, **5A**). The MOM contributions were higher during the periods ~2,200–1,750 and ~1,370–600 cal yr BP, which indicates that the mangrove forest was flourishing. However, MOM contributions were lower in the periods ~3,000–2,200, ~1,750–1,370, and ~600–0 cal yr BP, indicating that the forest had been deteriorating in these periods. To sum up, mangrove forests in Qinzhou Bay underwent two periods of flourishing and three periods of degradation over the last ~3,000 years. Notably, the period of the greatest flourishing was ~1,370–600 cal yr BP, with the highest MOM content of 48.7 ± 23.4%.

Factors Affecting Mangrove Development

From the Holocene to the Anthropocene, mangrove development (i.e., flourishing or degradation) was mainly impacted by two aspects. One is the so-called natural agents such as the sea level, climate (air temperature and rainfall), and the hydrological environment (seawater temperature, salinity, hydrodynamic conditions). Another facet is anthropogenic activities. In this section, we analyzed the factors affecting mangrove development

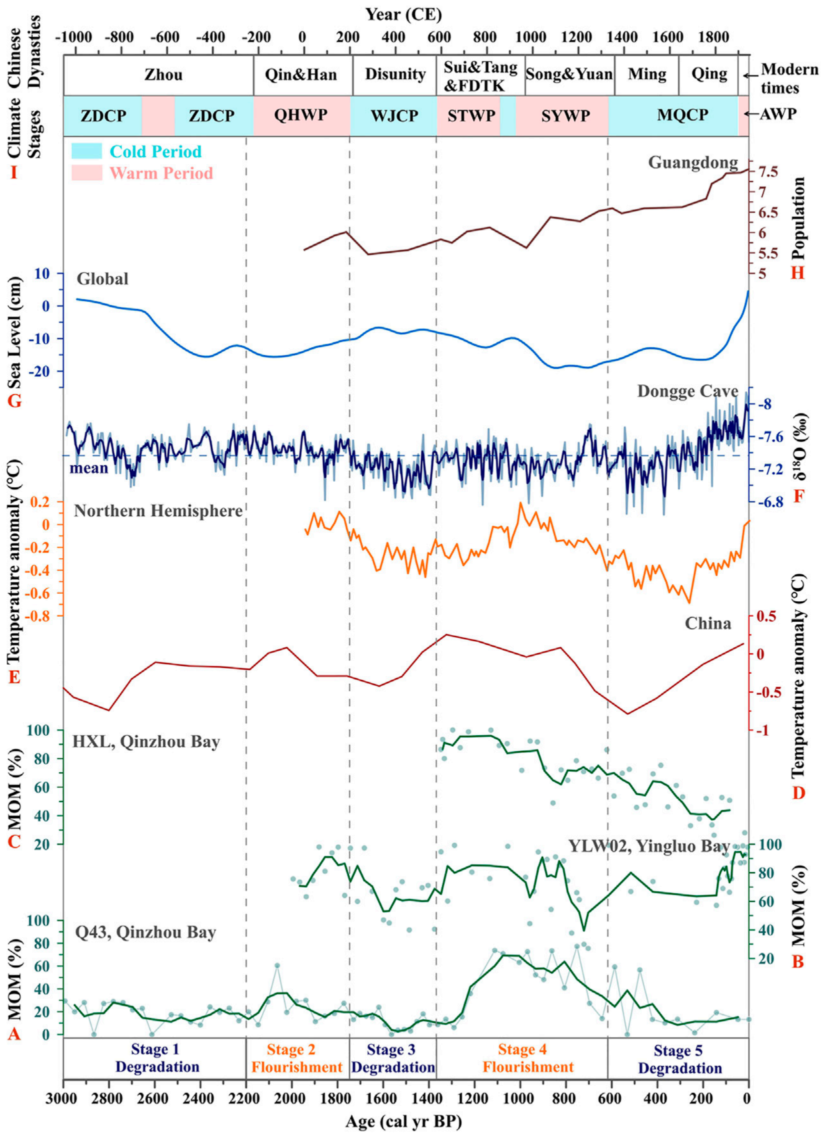

FIGURE 5 | Comparisons between changes in mangrove-derived organic matter (MOM) and natural and anthropogenic records: **(A–C)** variations in MOM from the Q43 (this study), YLW02 (Meng et al., 2017), and HXL (Xia et al., 2019) cores, respectively, in Guangxi coasts; **(D–E)** temperature anomaly in China (Hou and Fang, 2011) and the Northern Hemispheric (Ljungqvist, 2010); **(F)** stalagmite $\delta^{18}O$ records from Dongge Cave, SW China (Wang et al., 2005); **(G)** variation in the global sea level over the past 3,000 cal yr BP (Kemp et al., 2018; Miller et al., 2020) **(H)** population changes in Guangdong Province (logarithmic (base 10) scale (Zhao and Xie, 1988; Huang et al., 2018)); **(I)** Chinese dynasties and climatic stages (Zhu, 1973; Ge et al., 2014). The latter includes the Zhou Dynasty cold period (ZDCP), Qin-Han warm period (QHWP), Wei-Jin cold period (WJCP), Sui-Tang warm period (STWP), Song-Yuan warm period (SYWP), Ming-Qing cold period (MQCP), and Anthropocene warm period (AWP). The stages (Stage 1–Stage 5) of mangrove development in Qinzhou Bay are divided by vertical broken lines.

through the comparisons between changes in MOM and natural and anthropogenic records (**Figure 5**). Meanwhile, a visualized model of mangrove development in Qinzhou Bay, tropical China, over the past 3,000 years has been provided (**Figure 6**).

Relative Sea Level

Mangrove habitats occur on intertidal shorelines in the tropics and subtropics, and are sensitive to changes in the RSL, i.e., they can migrate to landward/seaward regions with RSL rise/fall (Ellison and Stoddart, 1991; Woodroffe et al., 2016). These consequences primarily depend on the balance between changes in the relative sea level and the state of the mangrove substrate (sedimentation/erosion rate) (Ellison 2008; Soares, 2009; Cohen et al., 2016). However, rapid changes in the RSL can upset this balance, leading to a decline in or even the disappearance of mangrove habitats. Previous studies on worldwide mangrove development during the entire Holocene have shown that the landward migration and communities succession of mangrove forests occurred from the Early to Middle Holocene, the period in which the RSL rose quickly

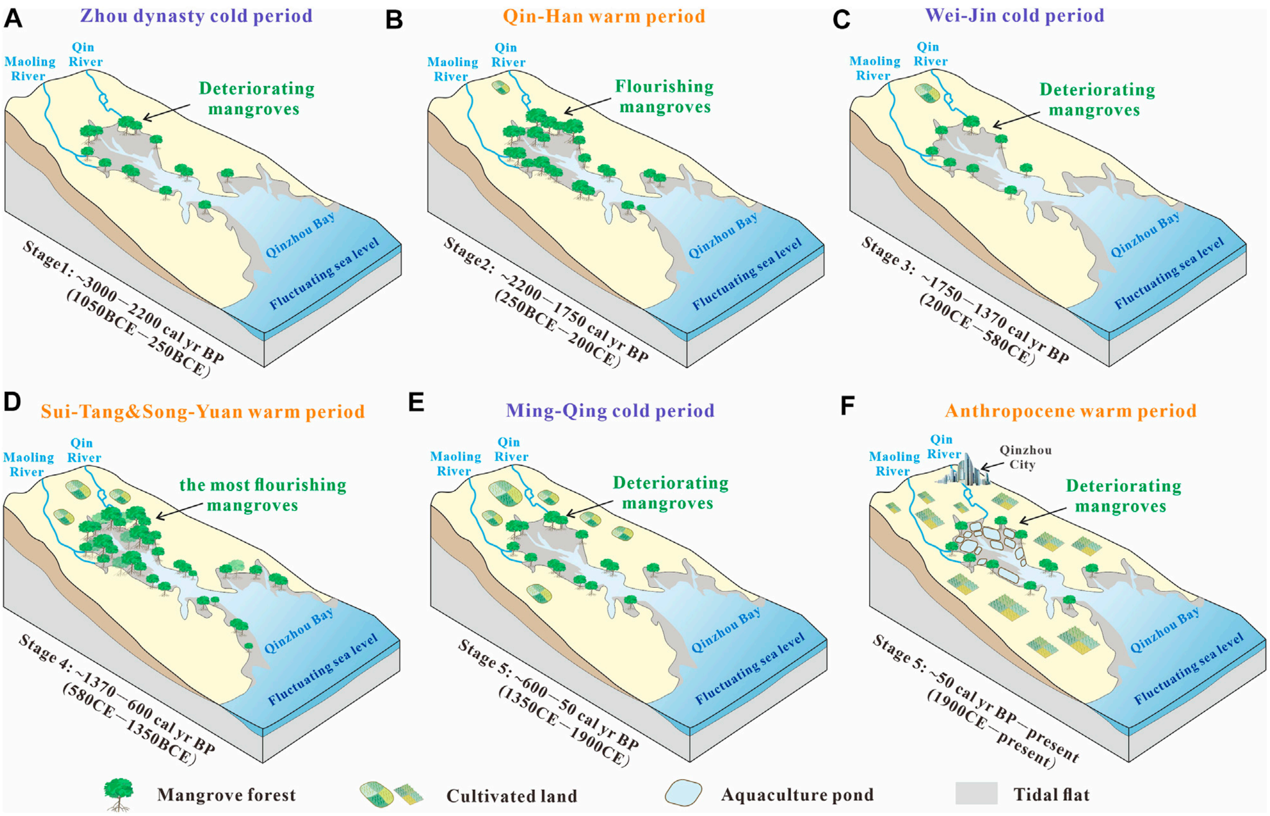

FIGURE 6 | Model of mangrove development in **(A–F)** different stages in Qinzhou Bay, tropical China, over the past 3000 years.

(Parkinson et al., 1994; Gilman et al., 2007; Gilman et al., 2008; Li et al., 2012), while most mangrove forests developed *in situ* over the Late Holocene with a relatively stable RSL (Urrego et al., 2013; Cohen et al., 2016). According to the variation in sea level over the past 3,000 cal yr BP (Kemp et al., 2018; Miller et al., 2020), the sea level in each stage of mangrove development in Qinzhou Bay varied from 0.004 to 0.37 mm yr^{-1} (**Figure 5G**). Compared with the vast fluctuation in the RSL in the Early Holocene or even the Last Glacial Period, the changes in RSL have been relatively flat since 3,000 cal yr BP, which implies that mangroves had sufficient capacity to adapt to these changes. Notably, in the Late Holocene, the sea level rose rapidly in the last 200 years. In this case, the mangrove forests still had the ability to keep pace with the RSL rise and avoid inundation via the vertical accumulation of sediments (Lovelock et al., 2015). A previous study on Yingluo Bay in tropical China showed that mangroves had not been impacted by RSL over the last 150 years (Xia et al., 2015; Meng et al., 2017). The persistence of most worldwide mangroves also implies an ability to cope with high rates of rises in the RSL. Further research suggests that mangrove forests in sites with low sedimentary supply and tidal range may be submerged as early as 2,070 (Lovelock et al., 2015). Consequently, the changes in RSL should not have been the primary factor influencing mangrove development in Qinzhou Bay over the last 3,000 cal yr BP.

Hydrological Environment

Mangrove development can be impacted by the regional hydrological environment, such as the hydrodynamic conditions, surface seawater temperature (SST), and salinity. Variations in hydrodynamic conditions are mainly impacted by changes in the climate, RSL, and terrain. However, mangrove forests have the capacity to resist changes in hydrodynamic conditions (e.g., increased wave energy) owing to their dense and complex aerial root systems (e.g., such as prop roots and pneumatophores) (Duke et al., 2007). Previous studies on the Qinzhou and Yingluo bays collectively indicate that mangrove development was little influenced by the hydrodynamic conditions during the Late Holocene (Meng et al., 2017; Xia et al., 2019). Thus, this factor does not require excessive consideration in this study.

The SST is dominated by air temperature through air-sea interactions. Similar to the air temperature, an increased SST is beneficial for mangrove growth provided the temperature does not exceed its thresholds (Ellison, 2008; Gilman et al., 2008). The study area is located in Qinzhou Bay (**Figure 1**), and its seawater salinity is primarily diluted by freshwater input from the Maoling and Qin rivers. Decreased precipitation can result in a decrease in groundwater discharge and surface freshwater water input (Duke et al., 1998), and can cause an increase in seawater salinity. Increased salinity is likely to cause a conversion of upper tidal zones to hypersaline flats, which poses a significant threat to the mangrove habitats

(Gilman et al., 2008). On the whole, the effects of the SST and salinity on mangrove development ultimately depend on air temperature and rainfall, owing to the coupling relationship between them.

Air Temperature and Rainfall

As observed in most global locations, mangroves are prone to inhabit lower latitudes with higher temperature and precipitation (Duke et al., 1998; Giri et al., 2011). For instance, the same mangrove species (e.g., *Rhizophora* sp.) can reach up to 30 m in the Amazon region (0.7°S; Matos et al., 2020), whereas its average height in Guangxi (~21°N) is merely about 3 m. Therefore, air temperature and rainfall are expected to control mangrove development by impacting their diversity, productivity, and area (Ellison, 2008; Gilman et al., 2008; Friess et al., 2019).

In Guangxi Province, SW China, rainfall is controlled by the East Asian summer monsoon (EASM), changes in which during the Holocene can be reconstructed by high-resolution stalagmite $\delta^{18}O$ records from the Dongge Cave in SW China (**Figures 1C**, **5F**; Wang et al., 2005). The negative excursion of $\delta^{18}O$ value indicates a general increase in the strength of the EASM and rainfall, and vice versa. If rainfall is the main factor controlling the development of local mangroves, sections of the negative excursion of the $\delta^{18}O$ value should correspond to periods of mangroves flourishing. Our results show that stages of relatively negative excursion of $\delta^{18}O$ (~2,200–1,750 and ~1,370–600 cal yr BP) correspond to the periods of mangrove flourishing (Stage 2 and Stage 4), while sections with positive $\delta^{18}O$ (~1,750–1,370 and ~600–200 cal yr BP) correspond to the periods of mangrove deterioration (Stage 3 and early Stage 5). However, these corresponding relationships are not prominent, and the stages of negative excursion of $\delta^{18}O$ (~3,000–2,200 and ~200–0 cal yr BP) unconventionally correspond to the periods of deterioration of mangroves (Stage 1 and late Stage 5). Therefore, rainfall induced by the EASM may not have been the dominant factor in mangrove development since 3,000 cal yr BP. In other words, mangrove development can, but only in part, be ascribed to changes in rainfall.

Previous study has reconstructed Holocene temperature anomaly in China (**Figure 5D**; Hou and Fang, 2011), and have found that its tendency is consistent with temperature variation in the Northern Hemisphere over the last two millennia (**Figure 5E**; Ljungqvist, 2010). Based on the reconstructed temperature changes and historical records, the China's climate can be roughly divided into three cold periods and four warm periods (**Figure 5I**; Zhu, 1973; Ge et al., 2014). The cold periods mainly include the Zhou Dynasty cold period (ZDCP), Wei-Jin cold period (WJCP, i.e., Dark Ages Cold Period), and Ming-Qing cold period (MQCP, i.e., Little Ice Age), while the warm periods mainly contain the Qin-Han warm period (QHWP), Sui-Tang warm period (STWP), Song-Yuan warm period (SYWP, i.e., Medieval Warm Period), and Anthropocene warm period (AWP). If air temperature is the main factor controlling mangrove development, these cold/warm climate periods ought to correspond to the stages of mangrove deterioration/flourishing, respectively. Our results show that the three periods of mangrove deterioration (stages 1, 3, and 5) approximately correspond to the ZDCP, WJCP, and MQCP, whereas the two periods of mangrove flourishing (stages 2 and 4) approximately correspond to the QHWP and STWP-SYWP, respectively (**Figure 5**). Notably, the STWP is one of the warmest period in Chinese climate history (Ge et al., 2014), which promoted the appearances of two famous flourishing ages (i.e., the Zhen Guan and Kai Yuan periods) in Chinese history. Owing to the collective occurrences of the STWP and SYWP in Stage 4 (~1,370–600 cal yr BP), this stage featured the greatest flourishing of mangroves since 3,000 cal yr BP, although a transitory cold period occurred in the middle. Overall, the variation in air temperature is undoubtedly the dominant factor controlling mangrove development in Qinzhou Bay over the last 3,000 cal yr BP (**Figures 6A–E**). Corresponding relationships between the stages of mangrove development and temperature periods in Qinzhou Bay (**Figures 1A,B**, **5C**; Xia et al., 2019) and Yingluo Bay (**Figures 1B**, **5B**; Meng et al., 2017), tropical China, were very similar to our results, which further proves the controlling role of temperature in mangrove development.

However, another problem worth discussing is that the last warm period (AWP) corresponds to a stage of mangrove deterioration (late Stage 5), which implies that other factors might have influenced mangrove development.

Human Activities

Preindustrial mangrove utilization likely did not alter the extent and habitat quality of mangrove forests to a substantial degree, but the effects of human beings on mangrove resources have increased in the past few centuries and peaked in the 20th century (Friess et al., 2019). As much as 35% of the world's mangrove areas had been lost by the 1980s and 1990s (Valiela et al., 2001). Human threats on mangrove dynamics include pollution, overexploitation, and conversion to aquaculture and agriculture (Bao et al., 2013; Friess et al., 2019; Veettil et al., 2019). In Guangxi, the population has rapidly risen over the last two centuries, similar to that in an adjacent province, Guangdong (**Figure 5H**; Zhao and Xie, 1988). With the population growth, the mangroves area abruptly decreased from 23,904 to 9,351 ha by 1955 (Fan, 1995), of which 97.6% was converted into aquaculture ponds (Chen et al., 2009). These realities explain the persistent mangrove degradation in late Stage 5 (~50 cal yr BP to present), i.e., the rapid temperature rise should have promoted mangroves flourishment during the AWP just as in other warm periods in history, but this was reversed by the increase in the intensity of human activities, especially the expansion of aquaculture ponds (**Figure 6F**). Likewise, mangrove degradation occurred at a site (HXL) located in mangrove interior of the Qinzhou Bay during the AWP (**Figures 1A,B**, **5C**; Xia et al., 2019). Interestingly, the records of core YLW02 showed that mangroves were flourishing in Yingluo Bay during the AWP (**Figures 1B**, **5B**; Meng et al., 2017). Yingluo Bay is located far from industrial areas, city centers, and river basins, such that population-related negative disturbances can be ignored

(Xia et al., 2015). Therefore, mangrove development in Yingluo Bay has continued to be controlled by temperature rather than human activities since the Anthropocene.

CONCLUSION

The contributions of terrestrial organic matter, MOM, and oceanic organic matter to OM sources of sediment core Q43 were quantified here by using endmember mixing models based on δ^{13}C and C/N. The MOM is considered a reliable proxy for reconstructing regional mangrove development. The variations in MOM in Qinzhou Bay over the past ~3,000 cal yr BP indicate that the mangrove forests underwent two periods of flourishing: ~2,200–1,750 cal yr BP (Stage 2) and ~1,370–600 cal yr BP (Stage 4), and three periods of deterioration: ~3,000–2,200 cal yr BP (Stage 1), ~1,750–1,370 cal yr BP (Stage 3), and ~600–0 cal yr BP (Stage 5). Of the potential factors that impact mangrove development, the RSL changes and the regional hydrological environment (e.g., seawater temperature, salinity, and hydrodynamic conditions) did not have notable effects on mangrove flourishing/degradation. However, climate change, especially variations in the air temperature variations, was the primary factor controlling mangrove development. The stages of mangrove flourishing/deterioration corresponded to warm/cold periods of the Chinese climate, respectively. Notably, the rapid air temperature rise should have promoted mangrove development during the AWP, just as in other warm periods in history, but this trend was reversed by the increase in the intensity of human activities, especially the expansion of aquaculture ponds.

DATA AVAILABILITY STATEMENT

The raw data supporting the conclusion of this article will be made available by the authors, without undue reservation.

AUTHOR CONTRIBUTIONS

YZ contributed to laboratory analysis, data analysis, and manuscript writing; XM contributed to project design and method establishment; PX and ZL contributed to field investigation and laboratory analysis; All authors have reviewed the manuscript.

FUNDING

This work was supported by the National Natural Science Foundation of China (Grant Nos. 41976068 and 41576061).

ACKNOWLEDGMENTS

We are grateful to Guanglong Qiu from the Guangxi Mangrove Research Center for providing raw data of seagrass.

REFERENCES

Alongi, D. M. (2014). Carbon Cycling and Storage in Mangrove Forests. *Annu. Rev. Mar. Sci.* 6, 195–219. doi:10.1146/annurev-marine-010213-135020

Alongi, D. M. (2020). Global Significance of Mangrove Blue Carbon in Climate Change Mitigation (Version 1). *Sci* 2, 57. doi:10.3390/sci2030057

Alongi, D. M. (2008). Mangrove Forests: Resilience, Protection From Tsunamis, and Responses to Global Climate Change. *Estuar. Coast. Shelf Sci.* 76, 1–13. doi:10.1016/j.ecss.2007.08.024

Bao, H., Wu, Y., Unger, D., Du, J., Herbeck, L. S., and Zhang, J. (2013). Impact of the Conversion of Mangroves Into Aquaculture Ponds on the Sedimentary Organic Matter Composition in a Tidal Flat Estuary (Hainan Island, China). *Cont. Shelf Res.* 57, 82–91. doi:10.1016/j.csr.2012.06.016

Bouillon, S., Boregs, A. V., Castañda-Moya, E., Diele, K., Dittmar, T., Duke, N. C., et al. (2008). Mangrove Production and Carbon Sinks: A Revision of Global Budget Estimates. *Glob. Biogeochem. Cycles* 22, 1–12. doi:10.1029/2007gb003052

Caratini, C., Bentaleb, I., Fontugne, M., Morzadec-Kerfourn, M. T., Pascal, J. P., and Tissot, C. (1994). A Less Humid Climate Since ca. 3500 yr B.P. from Marine Cores Off Karwar, Western India. *Palaeogeogr. Palaeoclimatol. Palaeoecol.* 109 (2–4), 371–384. doi:10.1016/0031-0182(94)90186-4

Chen, L., Wang, W., Zhang, Y., and Lin, G. (2009). Recent Progresses in Mangrove Conservation, Restoration and Research in China. *J. Plant Ecol.* 2 (2), 45–54. doi:10.1093/jpe/rtp009

Cohen, M. C. L., Lara, R. J., Cuevas, E., Oliveras, E. M., and Da Silveira Sternberg, L. (2016). Effects of Sea-Level Rise and Climatic Changes on Mangroves from Southwestern Littoral of Puerto Rico During the Middle and Late Holocene. *Catena* 143, 187–200. doi:10.1016/j.catena.2016.03.041

Dittmar, T., Lara, R. J., and Kattner, G. (2001). River or Mangrove? Tracing Major Organic Matter Sources in Tropical Brazilian Coastal Waters. *Mar. Chem.* 73 (3–4), 253–271. doi:10.1016/s0304-4203(00)00110-9

Dong, Y., Li, Y., Kong, F., Zhang, J., and Xi, M. (2020). Source, Structural Characteristics and Ecological Indication of Dissolved Organic Matter Extracted From Sediments in the Primary Tributaries of the Dagu River. *Ecol. Indic.* 109, 105776. doi:10.1016/j.ecolind.2019.105776

Duarte, C. M., and Arabia, S. (2017). Reviews and Syntheses: Hidden Forests, the Role of Vegetated Coastal Habitats in the Ocean Carbon Budget. *Biogeosciences* 14, 301–310. doi:10.5194/bg-14-301-2017

Duarte, C. M., Losada, I. J., Hendriks, I. E., Mazarrasa, I., and Marbà, N. (2013). The Role of Coastal Plant Communities for Climate Change Mitigation and Adaptation. *Nat. Clim. Change* 3, 961–968. doi:10.1038/nclimate1970

Duarte, C. M., Middelburg, J. J., and Caraco, N. (2005). Major Role of Marine Vegetation on the Oceanic Carbon Cycle. *Biogeosciences* 2, 1–8. doi:10.5194/bg-2-1-2005

Duke, N. C., Ball, M. C., and Ellison, J. C. (1998). Factors Influencing Biodiversity and Distributional Gradients in Mangroves. *Glob. Ecol. Biogeogr. Lett.* 7 (1), 27–47. doi:10.2307/2997695

Duke, N. C., Meynecke, J.-O., Dittmann, S., Ellison, A. M., Anger, K., Berger, U., et al. (2007). A World Without Mangroves? *Science* 317, 41b–42b. doi:10.1126/science.317.5834.41b

Ellison, J. C. (2008). Long-Term Retrospection on Mangrove Development Using Sediment Cores and Pollen Analysis: A Review. *Aquat. Bot.* 89, 93–104. doi:10.1016/j.aquabot.2008.02.007

Ellison, J. C., and Stoddart, D. R. (1991). Mangrove Ecosystem Collapse During Predicted Sea-Level Rise: Holocene Analogues and Implications. *J. Coast. Res.* 7 (1), 151–165. doi:10.2307/4297812

Ellison, J. C. (2014). Vulnerability Assessment of Mangroves to Climate Change and Sea-Level Rise Impacts. *Wet. Ecol. Manag.* 23, 115–137. doi:10.1007/s11273-014-9397-8

Fan, H. Q. (1995). Mangrove Resources, Human Disturbance and Rehabilitation Action in China. *Chin. Biodiv.* 3 (Suppl. 1), 49–54.

França, M. C., Francisquini, M. I., Cohen, M. C. L., and Pessenda, L. C. R. (2013). Inter-Proxy Evidence for the Development of the Amazonian Mangroves During the Holocene. *Veg. Hist. Archaeobot.* 23 (5), 527–542. doi:10.1007/s00334-013-0420-4

Friess, D. A., Rogers, K., Lovelock, C. E., Krauss, K. W., Hamilton, S. E., Lee, S. Y., et al. (2019). The State of the World's Mangrove Forests: Past, Present, and Future. *Annu. Rev. Environ. Resour.* 44, 89–115. doi:10.1146/annurev-environ-101718-033302

Ge, Q., Fang, X., and Zheng, J. (2014). Learning From the Historical Impacts of Climatic Change in China. *Adv. Earth Sci.* 29, 23–29. doi:10.11867/j.issn.1001-8166.2014.01.0023

Gilman, E., Ellison, J., and Coleman, R. (2007). Assessment of Mangrove Response to Projected Relative Sea-Level Rise and Recent Historical Reconstruction of Shoreline Position. *Environ. Monit. Assess.* 124, 105–130. doi:10.1007/s10661-006-9212-y

Gilman, E. L., Ellison, J., Duke, N. C., and Field, C. (2008). Threats to Mangroves From Climate Change and Adaptation Options: A Review. *Aquat. Bot.* 89, 237–250. doi:10.1016/j.aquabot.2007.12.009

Giri, C., Ochieng, E., Tieszen, L. L., Zhu, Z., Singh, A., Loveland, T., et al. (2011). Status and Distribution of Mangrove Forests of the World Using Earth Observation Satellite Data. *Glob. Ecol. Biogeogr.* 20, 154–159. doi:10.1111/j.1466-8238.2010.00584.x

Goñi, M. A., Ruttenberg, K. C., and Eglinton, T. I. (1998). A Reassessment of the Sources and Importance of Land-Derived Organic Matter in Surface Sediments from the Gulf of Mexico. *Geochim. Cosmochim. Acta* 62 (18), 3055–3075. doi:10.1016/s0016-7037(98)00217-8

Gonneea, M. E., Paytan, A., and Herrera-Silveira, J. A. (2004). Tracing Organic Matter Sources and Carbon Burial in Mangrove Sediments Over the Past 160 Years. *Estuar. Coast. Shelf Sci.* 61, 211–227. doi:10.1016/j.ecss.2004.04.015

Hatje, V., Masqué, P., Patire, V. F., Dórea, A., and Barros, F. (2020). Blue Carbon Stocks, Accumulation Rates, and Associated Spatial Variability in Brazilian Mangroves. *Limnol. Oceanogr.* 1, 1–14. doi:10.1002/lno.11607

Herbeck, L. S., Unger, D., Krumme, U., Liu, S. M., and Jennerjahn, T. C. (2011). Typhoon-Induced Precipitation Impact on Nutrient and Suspended Matter Dynamics of a Tropical Estuary Affected by Human Activities in Hainan, China. *Estuar. Coast. Shelf Sci.* 93, 375–388. doi:10.1016/j.ecss.2011.05.004

Hernes, P. J., Dyda, R. Y., and McDowell, W. H. (2017). Connecting Tropical River DOM and POM to the Landscape With Lignin. *Geochim. Cosmochim. Acta* 219, 143–159. doi:10.1016/j.gca.2017.09.028

Himes-Cornell, A., Grose, S. O., and Pendleton, L. (2018). Mangrove Ecosystem Service Values and Methodological Approaches to Valuation: Where Do We Stand?. *Front. Mar. Sci.* 5, 376. doi:10.3389/fmars.2018.00376

Hou, G. L., and Fang, X. Q. (2011). Characteristics of Holocene Temperature Change in China *Prog. Geogr.* 30 (9), 1075–1080. [in Chinese with English abstract]. doi:10.11820/dlkxjz.2011.09.001

Fan, H. Q., Chen, G. H., He, B. Y., and Mo, Z. C. (Editors) (2005). *Coastal Wetland and Management of Shankou Mangroves*. (Beijing, China: China Ocean Press), 35–89.

Huang, C., Zeng, T., Ye, F., Xie, L., Wang, Z., Wei, G., et al. (2018). Natural and Anthropogenic Impacts on Environmental Changes Over the Past 7500 Years Based on the Multi-Proxy Study of Shelf Sediments in the Northern South China Sea. *Quat. Sci. Rev.* 197, 35–48. doi:10.1016/j.quascirev.2018.08.005

Jennerjahn, T. C. (2012). Biogeochemical Response of Tropical Coastal Systems to Present and Past Environmental Change. *Earth Sci. Rev.* 114, 19–41. doi:10.1016/j.earscirev.2012.04.005

Jennerjahn, T. C., and Ittekkot, V. (2002). Relevance of Mangroves for the Production and Deposition of Organic Matter Along Tropical Continental Margins. *Sci. Nat.* 89, 23–30. doi:10.1007/s00114-001-0283-x

Jennerjahn, T. C. (2021). Relevance and Magnitude of 'Blue Carbon' Storage in Mangrove Sediments: Carbon Accumulation Rates vs. Stocks, Sources vs. Sinks. *Estuar. Coast. Shelf Sci.* 248, 107156. doi:10.1016/j.ecss.2020.107156

Kemp, A. C., Wright, A. J., Edwards, R. J., Barnett, R. L., Brain, M. J., Kopp, R. E., et al. (2018). Relative Sea-Level Change in Newfoundland, Canada During the Past ~3000 Years. *Quat. Sci. Rev.* 201, 89–110. doi:10.1016/j.quascirev.2018.10.012

Kusumaningtyas, M. A., Hutahaean, A. A., Fischer, H. W., Pérez-Mayo, M., Ransby, D., and Jennerjahn, T. C. (2019). Variability in the Organic Carbon Stocks, Sources, and Accumulation Rates of Indonesian Mangrove Ecosystems. *Estuar. Coast. Shelf Sci.* 218, 310–323. doi:10.1016/j.ecss.2018.12.007

Lee, S. Y., Primavera, J. H., Dahdouh-Guebas, F., McKee, K., Bosire, J. O., Cannicci, S., et al. (2014). Ecological Role and Services of Tropical Mangrove Ecosystems: a Reassessment. *Glob. Ecol. Biogeogr.* 23, 726–743. doi:10.1111/geb.12155

Li, Z., Saito, Y., Mao, L., Tamura, T., Li, Z., Song, B., et al. (2012). Mid-Holocene Mangrove Succession and its Response to Sea-Level Change in the Upper Mekong River Delta, Cambodia. *Quat. Res.* 78, 386–399. doi:10.1016/j.yqres.2012.07.001

Li, Z., Zhang, Z., Li, J., Zhang, Y., Li, Z., Liu, L., et al. (2008). Pollen Distribution in Surface Sediments of a Mangrove System, Yingluo Bay, Guangxi, China. *Rev. Palaeobot. Palynol.* 152, 21–31. doi:10.1016/j.revpalbo.2008.04.001

Liu, Y., Wang, X., Wen, Q., and Zhu, N. (2019). Identifying Sources and Variations of Organic Matter in an Urban River in Beijing, China Using Stable Isotope Analysis. *Ecol. Indic.* 102, 783–790. doi:10.1016/j.ecolind.2019.03.023

Liu, Z., Zhao, Y., Colin, C., Stattegger, K., Wiesner, M. G., Huh, C.-A., et al. (2016). Source-to-Sink Transport Processes of Fluvial Sediments in the South China Sea. *Earth Sci. Rev.* 153, 238–273. doi:10.1016/j.earscirev.2015.08.005

Ljungqvist, F. C. (2010). A New Reconstruction of Temperature Variability in the Extra-Tropical Northern Hemisphere during the Last Two Millennia. *Geogr. Ann. Ser. A. Phys. Geogr.* 92 (3), 339–351. doi:10.1111/j.1468-0459.2010.00399.x

Lovelock, C. E., Cahoon, D. R., Friess, D. A., Guntenspergen, G. R., Krauss, K. W., Reef, R., et al. (2015). The Vulnerability of Indo-Pacific Mangrove Forests to Sea-Level Rise. *Nature* 526, 559–563. doi:10.1038/nature15538

Matos, C. R. L., Berrêdo, J. F., Machado, W., Sanders, C. J., Metzger, E., and Cohen, M. C. L. (2020). Carbon and Nutrient Accumulation in Tropical Mangrove Creeks, Amazon Region. *Mar. Geol.* 429, 106317. doi:10.1016/j.margeo.2020.106317

Meng, X., Xia, P., Li, Z., and Liu, L. (2016a). Mangrove Forest Degradation Indicated by Mangrove-Derived Organic Matter in the Qinzhou Bay, Guangxi, China, and its Response to the Asian Monsoon During the Holocene Climatic Optimum. *Acta Oceanol. Sin.* 35, 95–100. doi:10.1007/s13131-015-0778-5

Meng, X., Xia, P., Li, Z., and Meng, D. (2016b). Mangrove Degradation and Response to Anthropogenic Disturbance in the Maowei Sea (SW China) Since 1926 AD: Mangrove-Derived OM and Pollen. *Org. Geochem.* 98, 166–175. doi:10.1016/j.orggeochem.2016.06.001

Meng, X., Xia, P., Li, Z., and Meng, D. (2017). Mangrove Development and its Response to Asian Monsoon in the Yingluo Bay (SW China) Over the Last 2000 Years. *Estuar. Coasts* 40, 540–552. doi:10.1007/s12237-016-0156-3

Meng, X. W., and Zhang, C. Z. (2014). Basic Situations of Marine Environment and Resources in Guangxi. (Beijing, China: China Ocean Press), 5–22.

Miller, K. G., Schmelz, W. J., Browning, J. V., Kopp, R. E., Mountain, G. S., and Wright, J. D. (2020). Ancient Sea Level as Key to the Future. *Oceanography* 33, 32–41. doi:10.5670/oceanog.2020.224

Moyer, R. P., Bauer, J. E., and Grottoli, A. G. (2013). Carbon Isotope Biogeochemistry of Tropical Small Mountainous River, Estuarine, and Coastal Systems of Puerto Rico. *Biogeochemistry* 112 (13), 589–612. doi:10.1007/s10533-012-9751-y

Nellemann, C., Corcoran, E., Duarte, C., Valdes, L., Young, C. D., Fonseca, L., et al. (2009). Blue Carbon: The Role of Healthy Oceans in Binding Carbon. (Arendal, Norway: United Nations Environment Programme), 11–65.

Parkinson, R. W., Delaune, R. D., and White, J. R. (1994). Holocene Sea-Level Rise and the Fate of Mangrove Forests Within the Wider Caribbean Region. *J. Coast. Res.* 10, 1077–1086. doi:10.2307/4298297

Reimer, P. J., Bard, E., Bayliss, A., Beck, J. W., Blackwell, P. G., Ramsey, C. B., et al. (2013). IntCal13 and Marine13 Radiocarbon Age Calibration Curves 0-50,000 Years Cal BP. *Radiocarbon* 55, 1869–1887. doi:10.2458/azu_js_rc.55.16947

Sasmito, S. D., Kuzyakov, Y., Lubis, A. A., Murdiyarso, D., Hutley, L. B., Bachri, S., et al. (2020). Organic Carbon Burial and Sources in Soils of Coastal Mudflat and Mangrove Ecosystems. *Catena* 187, 104414. doi:10.1016/j.catena.2019.104414

Soares, M. L. G. (2009). A Conceptual Model for the Responses of Mangrove Forests to Sea Level Rise. *J. Coast. Res.* 56, 267–271. doi:10.2307/25737579

Southon, J., Kashgarian, M., Fontugne, M., Metivier, B., and W-S Yim, W. (2002). Marine Reservoir Corrections for the Indian Ocean and Southeast Asia. *Radiocarbon* 44, 167–180. doi:10.1017/s0033822200064778

Urrego, L. E., Correa-Metrio, A., González, C., Castaño, A. R., and Yokoyama, Y. (2013). Contrasting Responses of Two Caribbean Mangroves to Sea-Level Rise in the Guajira Peninsula (Colombian Caribbean). *Palaeogeogr. Palaeoclimatol. Palaeoecol.* 370, 92–102. doi:10.1016/j.palaeo.2012.11.023

Valiela, I., Bowen, J. L., and York, J. K. (2001). Mangrove Forests: One of the World's Threatened Major Tropical Environments. *BioScience* 51 (10), 807–815. doi:10.1641/0006-3568(2001)051[0807:mfootw]2.0.co;2

Vaughn, D. R., Bianchi, T. S., Shields, M. R., Kenney, W. F., and Osborne, T. Z. (2021). Blue Carbon Soil Stock Development and Estimates Within Northern Florida Wetlands. *Front. Earth Sci.* 9, 552721. doi:10.3389/feart.2021.552721

Veettil, B. K., Ward, R. D., Quang, N. X., Trang, N. T. T., and Giang, T. H. (2019). Mangroves of Vietnam: Historical Development, Current State of Research and Future Threats. *Estuar. Coast. Shelf Sci.* 218, 212–236. doi:10.1016/j.ecss.2018.12.021

Wang, Y., Cheng, H., Edwards, R. L., He, Y., Kong, X., An, Z., et al. (2005). The Holocene Asian Monsoon: Links to Solar Changes and North Atlantic Climate. *Science* 308, 854–857. doi:10.1126/science.1106296

Woodroffe, C. D., Rogers, K., McKee, K. L., Lovelock, C. E., Mendelssohn, I. A., and Saintilan, N. (2016). Mangrove Sedimentation and Response to Relative Sea-Level Rise. *Annu. Rev. Mar. Sci.* 8, 243–266. doi:10.1146/annurev-marine-122414-034025

Xia, P., Meng, X., Li, Z., Feng, A., Yin, P., and Zhang, Y. (2015). Mangrove Development and its Response to Environmental Change in Yingluo Bay (SW China) During the Last 150 years: Stable Carbon Isotopes and Mangrove Pollen. *Org. Geochem.* 85, 32–41. doi:10.1016/j.orggeochem.2015.04.003

Xia, P., Meng, X., Li, Z., Zhi, P., Zhao, M., and Wang, E. (2019). Late Holocene Mangrove Development and Response to Sea Level Change in the Northwestern South China Sea. *Acta Oceanol. Sin.* 38, 111–120. doi:10.1007/s13131-019-1359-9

Xia, P., Meng, X., Zhang, Y., Zhang, J., Li, Z., and Wang, W. (2021). The Potential of Mangrove-Derived Organic Matter in Sediments for Tracing Mangrove Development During the Holocene. *Estuar. Coast.* 44, 1020–1035. doi:10.1007/s12237-020-00826-w

Xue, B., Yan, C., Lu, H., and Bai, Y. (2009). Mangrove-Derived Organic Carbon in Sediment from Zhangjiang Estuary (China) Mangrove Wetland. *J. Coast. Res.* 254, 949–956. doi:10.2112/08-1047.1

Zhang, Y., Meng, X., Bai, Y., Wang, X., Xia, P., Yang, G., et al. (2021). Sources and Features of Particulate Organic Matter in Tropical Small Mountainous Rivers (SW China) Under the Effects of Anthropogenic Activities. *Ecol. Indic.* 125, 107471. doi:10.1016/j.ecolind.2021.107471

Zhao, W., and Xie, S. (1988). *Population History of China*. Beijing, China: People's Press

Zhu, K. Z. (1973). A Preliminary Study on the Climatic Change during the Last 5000 Years in China. *Sci. Sin. (B)* 16, 226–256. [in Chinese with English abstract].

Conflict of Interest: The authors declare that the research was conducted in the absence of any commercial or financial relationships that could be construed as a potential conflict of interest.

The reviewer (LL) declared a shared affiliation with several of the authors, (XM, PX, ZL), to the handling editor at time of review.

frontiers in Earth Science

ORIGINAL RESEARCH
published: 14 June 2021
doi: 10.3389/feart.2021.663634

Multi—Proxy Reconstructions of Climate Change and Human Impacts Over the Past 7000 Years From an Archive of Continental Shelf Sediments off Eastern Hainan Island, China

Chao Huang [1,2], ***Deming Kong*** [1], ***Fajin Chen*** [1]*, ***Jianfang Hu*** [3], ***Peng Wang*** [1] ***and Junchuan Lin*** [1]

[1]Key Laboratory of Climate, Resources and Environment in Continental Shelf Sea and Deep Sea of Department of Education of Guangdong Province, Guangdong Ocean University, Zhanjiang, China, [2]State Key Laboratory of Loess and Quaternary Geology, Institute of Earth Environment, Chinese Academy of Sciences, Xi'an, China, [3]State Key Laboratory of Organic Geochemistry, Guangzhou Institute of Geochemistry, Chinese Academy of Sciences, Guangzhou, China

OPEN ACCESS

Edited by:
Min-Te Chen,
National Taiwan Ocean University,
Taiwan

Reviewed by:
Yu Li,
Lanzhou University, China
Asif Ali,
Anna University, Chennai, India

****Correspondence:***
Fajin Chen
fjchen@gdou.edu.cn

Specialty section:
This article was submitted to Quaternary Science, Geomorphology and Paleoenvironment, a section of the journal Frontiers in Earth Science

Received: *03 February 2021*
Accepted: *31 May 2021*
Published: *14 June 2021*

Citation:
Huang C, Kong D, Chen F, Hu J, Wang P and Lin J (2021) Multi—Proxy Reconstructions of Climate Change and Human Impacts Over the Past 7000 Years From an Archive of Continental Shelf Sediments off Eastern Hainan Island, China. Front. Earth Sci. 9:663634. doi: 10.3389/feart.2021.663634

Abrupt climatic events and the history of human activities on Hainan Island are poorly understood, due to the lack of high-resolution records. We present high-resolution multiproxy records from the coastal shelf off eastern Hainan Island in China to investigate abrupt climate change and regional human–environment interaction over the last 7,000 years. A prominent climatic anomaly occurred during 5,400–4,900 cal yr BP. This abrupt monsoon failure has been detected in various paleoclimatic records from monsoonal regions. Anomalous summer monsoon intensity during 5,400–4,900 cal yr BP is probably driven by solar variability, ENSO activity and ice-rafting events in the North Atlantic. Over the past 1,500 years, with the growing population and progress in production technology, human activity has increasingly become the dominant factor controlling the natural environment of Hainan Island.

Keywords: Asian summer monsoon, holocene, human activity, abrupt climate change, chemical weathering, terrigenous influx

INTRODUCTION

Extreme weather events are becoming more frequent owing to global warming, and people are increasingly concerned about climate change and its impacts on their lives. Over recent Earth history, several abrupt global climatic anomalies occurred during the Holocene (Bond et al., 2001; Mayewski et al., 2004; Wanner et al., 2011). For example, the 4200 BP climate event and the Little Ice Age, these events had disastrous consequences for humans, and seriously influenced the development of agriculture and the prehistoric advancement of human society (Cullen et al., 2000; DeMenocal, 2001; Douglas et al., 2016; Sinha et al., 2019). Climatic anomaly around 5,500 cal yr BP have recently received attention as a result of the close linkage between climate change and the evolution of prehistoric culture (Shuman, 2012; Bai et al., 2017; Wu et al., 2018; Hou and Wu, 2021; Tan et al., 2020). A detailed understanding of abrupt climatic events in the past is therefore critical for exploring their underlying forcing mechanisms and dealing with abrupt changes in the climate system in the future.

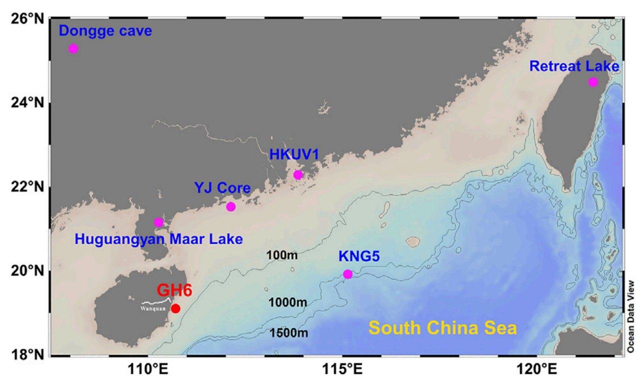

FIGURE 1 | Location map for the GH6 sediment core retrieved from the continental shelf off eastern Hainan Island (red dot) and related study sites in the region (purple dots).

In recent years, studies have suggested that human activities play an important role in controlling ecosystems and soil erosion in monsoonal China. Increases in χ_{lf} and χ_{fd} over the last 2000 years in sediments from the Yangtze delta in eastern China, Lake Xiaolongwan in northeast China, and lakes Erhai and Xingyun in southwest China reflect an increase in soil erosion attributed to enhanced human activity (Dearing et al., 2008; Wang et al., 2010; Su et al., 2015; Wu et al., 2015). Numerous studies likewise found that increasing contents of various metals, including Cu, Pb, and Zn, could be closely linked to mining and metalworking activities, reflecting a progressive intensification of human activities (Zong et al., 2010; Hu et al., 2013; Hillman et al., 2014; Wan et al., 2015; Xu et al., 2017; Huang et al., 2018). Additionally, pollen and black carbon results indicate significantly accelerated deforestation in monsoonal China since 2000 cal yr BP (Zhao et al., 2010; Ma et al., 2016a; Cheng et al., 2018; Lu et al., 2019; Pei et al., 2020).

As human populations grew and progress in production technology increased, human influences on the natural environment became increasingly important during the late Holocene, and often obscure the detection of climatic fluctuations in the archives investigated. Human activities can mediate the terrestrial ecosystems and soil erosion, generating unavailability of the relevant proxy indicators to reconstruct climate change. It is therefore essential to understand climate and human activities, as well as their impacts upon terrestrial ecosystems on longer timescales, in order to reconstruct each of them accurately. However, previous studies to determine human—environment interactions were mainly dependent on sediment cores from lakes (Dearing et al., 2008; Hillman et al., 2014; Su et al., 2015) and river deltas (Wang et al., 2010; Zong et al., 2010; Strong et al., 2013). High-resolution records from continental shelves are relatively scarce. Well dated and high-resolution data of various geologic archives from wide regions are crucial for better understanding the complex interplays between humans and the Earth. Sediment cores from continental shelves would therefore provide an excellent opportunity to understand human–environment interactions at regional scales.

Hainan Island, the second largest island in the northern South China Sea (SCS), is sensitive to climatic fluctuations. Previous studies have confirmed that continental shelf sediments off eastern Hainan provide valuable information on paleoclimate variation and human activity (Liu et al., 2013; Wu et al., 2017; Xu et al., 2017; Ji et al., 2020). However, most previous studies have focused on short timescales during the past 200 years (Liu et al., 2013; Wu et al., 2017). Accurate timing and intensity of human activity have not been well constrained. This study presents a high-resolution multi-proxy record with a robust chronology spanning the last 7,000 years collected from the continental shelf off eastern Hainan. The main aims are to investigate the interaction between Holocene climate variability, human activity and environmental changes, and to determine the timing and intensity of human activity on Hainan Island during the last 1,500 years.

MATERIALS AND METHODS

Materials

Hainan Island is the second largest island in the northern SCS and has an area of ~33.9 × 10^3 km^2 (**Figure 1**). The Wanquan River is the third largest river on the island and originates from the Wuzhishan Mountains. It drains southeast Hainan and eventually discharges into the northwestern SCS at Boao Township in Qionghai City. The river's total length is ~157 km and its drainage area covers 3,693 km^2 (Yang et al., 2013). The study region is dominated by a tropical monsoon climate (Zeng and Zeng, 1989). The annual mean temperature is 22.8–25.8°C. Annual precipitation ranges 961–2,439 mm yr^{-1}, with about 80% occurring during the wet season from April to September (Zhang et al., 2013).

The GH6 core (19°06′N, 110°42.85′E; 2.4 m in length) was collected using a gravity corer from approximately 50 m water

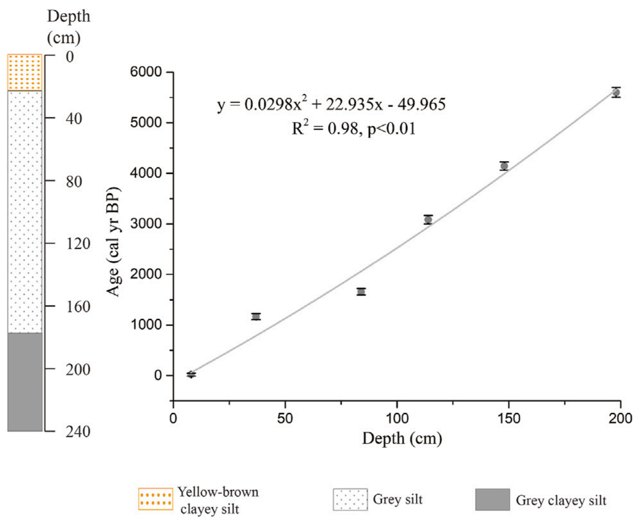

FIGURE 2 | Simplified lithological units and profiles of AMS ^{14}C age for sediment core GH6 (after Kong et al., 2021).

TABLE 1 | Details of 6 AMS ^{14}C dates from the GH6 core (after Kong et al., 2021).

Sample Code	Beta Lab Code	Depth (cm)	Material	Conventional age (years, BP)	Error (2σ)	Calibrated Age (years, BP)	Error (2σ)
GH6-F10	530613	8	Foraminifera	460	30	20	30
GH6-F17	530614	37	Foraminifera	1,760	30	1,165.5	60
GH6-F84	530615	84	Foraminifera	2,240	30	1,656.5	65
GH6-F114	545408	114	Foraminifera	2,980	30	3,085	84.5
GH6-F148	532199	148	Foraminifera	4,230	30	4,142	81.5
GH6-F198	532200	198	Foraminifera	5,420	30	5,599.5	96.5

depth on the continental shelf off eastern Hainan Island (**Figure 1**). The sediment core was cut longitudinally and samples were stored at 4°C prior to analysis. As shown in **Figure 2**, GH6 core can be divided into three lithological units: Unit 1 (0–20 cm) consists of yellow-brown clayey silt; Unit 2 (20–176 cm) consists of grey silt containing occasional shells; and Unit 3 (176–240 cm) consists of grey clayey silt.

Age Model

The chronology for the GH6 core was based on six AMS ^{14}C dates from mixed species of planktonic foraminifera (**Table. 1**; **Figure 2**). 10 mg of complete and clean planktonic foraminifera were selected hand-picked under a binocular dissecting microscope at 40 × magnification and cleaned by sonication in deionized water in order to remove surface adhesions. AMS ^{14}C dates were measured at the BETA Laboratory in the United States. All radiocarbon dates were calibrated to calendar ages with Calib 8.1.0 software using the marine20 program (Reimer et al., 2020). The age models of each sample are established by Polynomial ($n = 2$) fitting between these calibrated ages. The average temporal resolution is ~58 years, and the average sedimentation rate is 0.03 cm/yr. For further details of the dating method and modelling approach, see Kong et al. (2021).

Major and Trace Element Compositions

Bulk sediment samples were freeze-dried and ground, then heated at 650°C for 4 h to remove organic matter. The samples were digested in an HNO_3 + HF acid mixture and the solutions then used for major and trace-element analyses at 2-cm intervals. Major element concentrations were measured on a Varian 720 ES inductively coupled plasma—atomic emission spectrometer (ICP–AES). Trace element concentrations were measured on a Varian 820 inductively coupled plasma–mass spectrometer (ICP–MS). Precision and accuracy were monitored by analysing several United States Geological Survey (USGS) and Chinese certified reference standards (BHVO-2, BCR-2, GBW07314, GBW07315, GBW07316), yielding values that were generally within ± 10% (RSD) of the certified values.

The chemical index of alteration (CIA), defined as $Al_2O_3/(Al_2O_3 + CaO + Na_2O + K_2O) \times 100$, using molecular proportions, has been widely used as an indicator of chemical weathering intensity (Nesbitt and Young, 1982). In this study, it was difficult to evaluate the CaO content of the silicate fraction. The CIA was therefore calculated using the following formula, excluding CaO: molar $Al_2O_3/(Al_2O_3 + Na_2O + K_2O) \times 100$ (Arnaud et al., 2012; Liu et al., 2014). This amendment does not have a significant effect on the results because only relative variations in chemical weathering are considered (Arnaud et al., 2012).

Environmental Magnetic Measurements

Magnetic susceptibility was determined at about 1–6 cm intervals. The low-field magnetic susceptibility (χ) for all discrete samples was measured using a Kappabridge MFK1-FA (AGICO) magnetic susceptibility meter at low (976 Hz) and high (15,616 Hz) frequencies (defined as χ_{lf} and χ_{hf}, respectively). Frequency-dependent magnetic susceptibility (χ_{fd}%) was calculated using the formula $\chi_{fd}\% = 100 \times (\chi_{lf}—\chi_{hf})/\chi_{lf}$.

Particle Size Analysis

The samples used for the particle-size analysis were collected at about 1–7 cm intervals. All samples were pre-treated with 10% H_2O_2, followed by treatment with 10% HCl, to remove organic matter and carbonates, respectively. They were then rinsed with deionized water and dispersed with 10 ml of 0.05 mol L^{-1} $(NaPO_3)_6$ on an ultrasonic vibrator for 10 min. The grain-size distribution was measured using a Malvern 3,000 laser diffraction instrument. Mean grain size was calculated according to Folk and Ward (1957).

RESULTS

As shown in **Figure 3**, the Al/K, CIA, Al, Fe, Ti, Cu and Pb values share very similar trends through time. Generally, the variations in multi-proxies of GH6 core can be divided into four stages. During the interval 7,000–5,400 cal yr BP, CIA values and Al/K ratios are relatively high, and contents of Al, Fe, Ti, Cu, and Pb are also relatively high; both χ_{lf} and χ_{fd} values remain relatively high, but the mean grain size has relatively low values. During the interval 5,400–4,900 cal yr BP, all of proxies in GH6 core show an abrupt shift; a sharp decrease in CIA and Al/K raios is observed, and contents of Al, Fe, Ti, Cu, and Pb exhibit clear decreasing trends; both χ_{lf} and χ_{fd} values show a rapid decrease, but the mean grain size exhibits a rapid increase. During the interval 4,900–1,500 cal yr BP, CIA and Al/K ratios are relatively low, and contents of Al, Fe, Ti, Cu, and Pb remain fairly constant and relatively low values; both χ_{lf} and χ_{fd} values are relatively low except the period of 4,000–3,200 cal yr BP, and prominent peaks

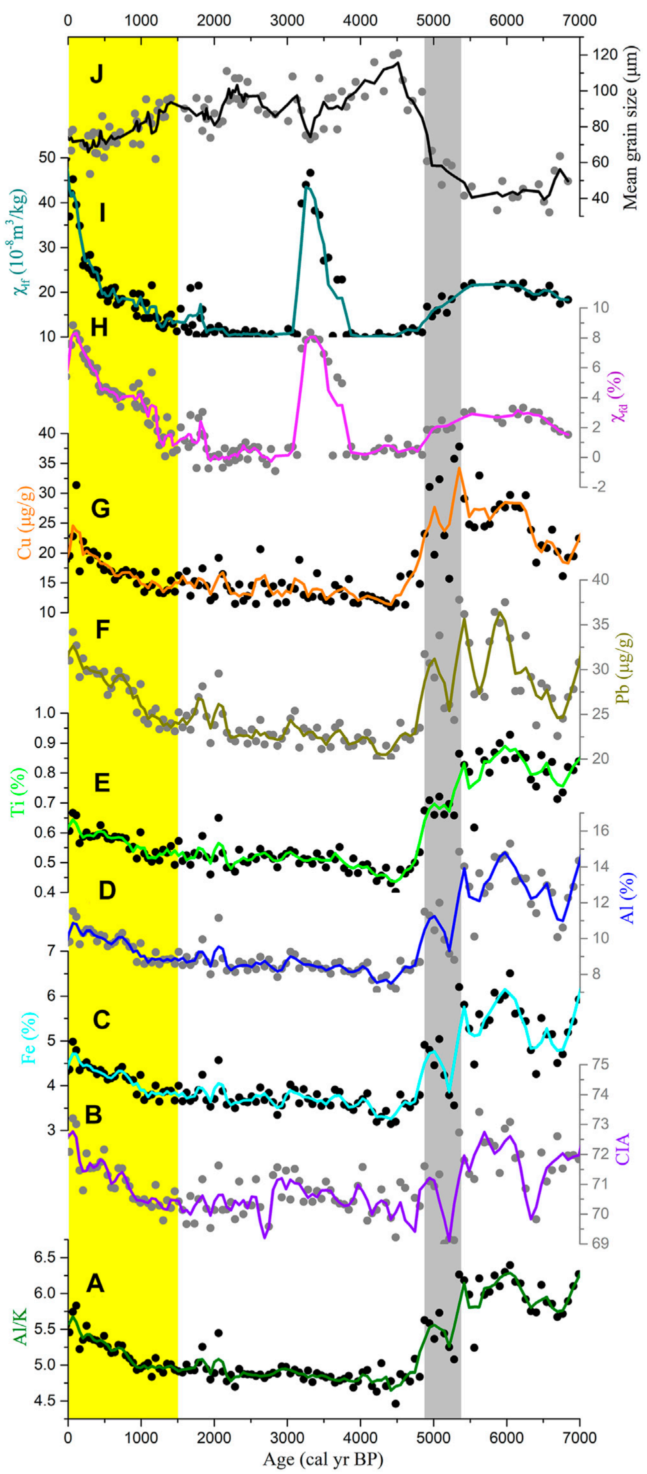

FIGURE 3 | Time series for multiple proxies measured in core GH6. The dots indicate the raw data, and the lines represent 3-point moving average. The grey bar indicates the recorded episode of abrupt climate change. The yellow bar represents the recent time period dominated by human activity.

of them would be attributed the pedogenic process; the mean grain size show a rapid increase. After 1,500 cal yr BP, CIA, and Al/K exhibit clear increasing trends, and contents of Al, Fe, Ti, Cu, and Pb show an overall increasing trend; both χ_{lf} and χ_{fd} values show an overall increase, and the mean grain size exhibits an overall decreasing trend.

DISCUSSION

Palaeoclimatic Significance of Proxy Indicators

Different elements behave differently during chemical weathering processes. Elemental ratios can therefore be applied to indicate variations in chemical weathering intensity. K tends to be enriched in weathering products after moderate chemical weathering, but depleted after extreme chemical weathering (Nesbitt et al., 1980; Condie et al., 1995), whereas Al tends to be retained and enriched in weathering products (Nesbitt and Markovics, 1997; Nesbitt et al., 1980). Thus, Al/K ratios can be used to reflect the intensity of chemical weathering, with higher Al/K ratios indicating stronger chemical weathering. In our core GH6, Al/K ratios exhibit similar variations to CIA values (**Figures 3A,B**). The latter have been widely used to trace the intensity of chemical weathering; e.g., core KNG5 from the northern SCS slope (Huang et al., 2015), core YJ from the northern SCS inner shelf (Huang et al., 2018), and core 337 PC from the Qiongdongnan Basin (Wan et al., 2015). In addition, Al/K ratios have been successfully used to indicate variations in chemical weathering intensity in the northern SCS and the Pearl River delta (Wei et al., 2006; Hu et al., 2012; Hu et al., 2013; Clift et al., 2014). This provides further evidence that Al/K ratios can be employed as an indicator of chemical weathering intensity.

Climate is believed to be the dominant factor controlling the degree of chemical weathering under specific environmental conditions (White and Blum, 1995). Warm and humid conditions favour intense chemical weathering, with humidity playing the more important role (White and Blum, 1995; West et al., 2005; Gabet et al., 2006). Previous studies have confirmed that sediments on the continental shelf off Hainan in the northern SCS were primarily derived from the island itself (Tian et al., 2013; Hu et al., 2014; Yan et al., 2016; Xu et al., 2017). Hainan currently experiences a humid tropical climate that is strongly influenced by the Asian summer monsoon (Liu et al., 1999). The proxies for chemical weathering (CIA and Al/K) in core GH6 can therefore be used to trace the strength of the summer monsoon.

In marine sediments, concentrations of Al, Ti, and Fe are primarily derived from terrigenous detrital materials (Latimer and Filippelli, 2001; Ishfaq et al., 2013). Thus, these elements are widely employed as a tracer of terrigenous influx in marine sediments (Haug et al., 2001; Peterson and Haug, 2006; Revel et al., 2010). Al, Ti, and Fe variations in core YJ from the northern inner shelf of the SCS have been successfully used to indicate changes in terrigenous influx (Huang et al., 2019). This provides further evidence that Al, Ti, and Fe concentrations in our GH6 core can be used to trace changes in terrigenous sediment input. In southern China, numerous studies have confirmed that continental erosion is primarily associated with monsoon precipitation, with heavier monsoon precipitation causing

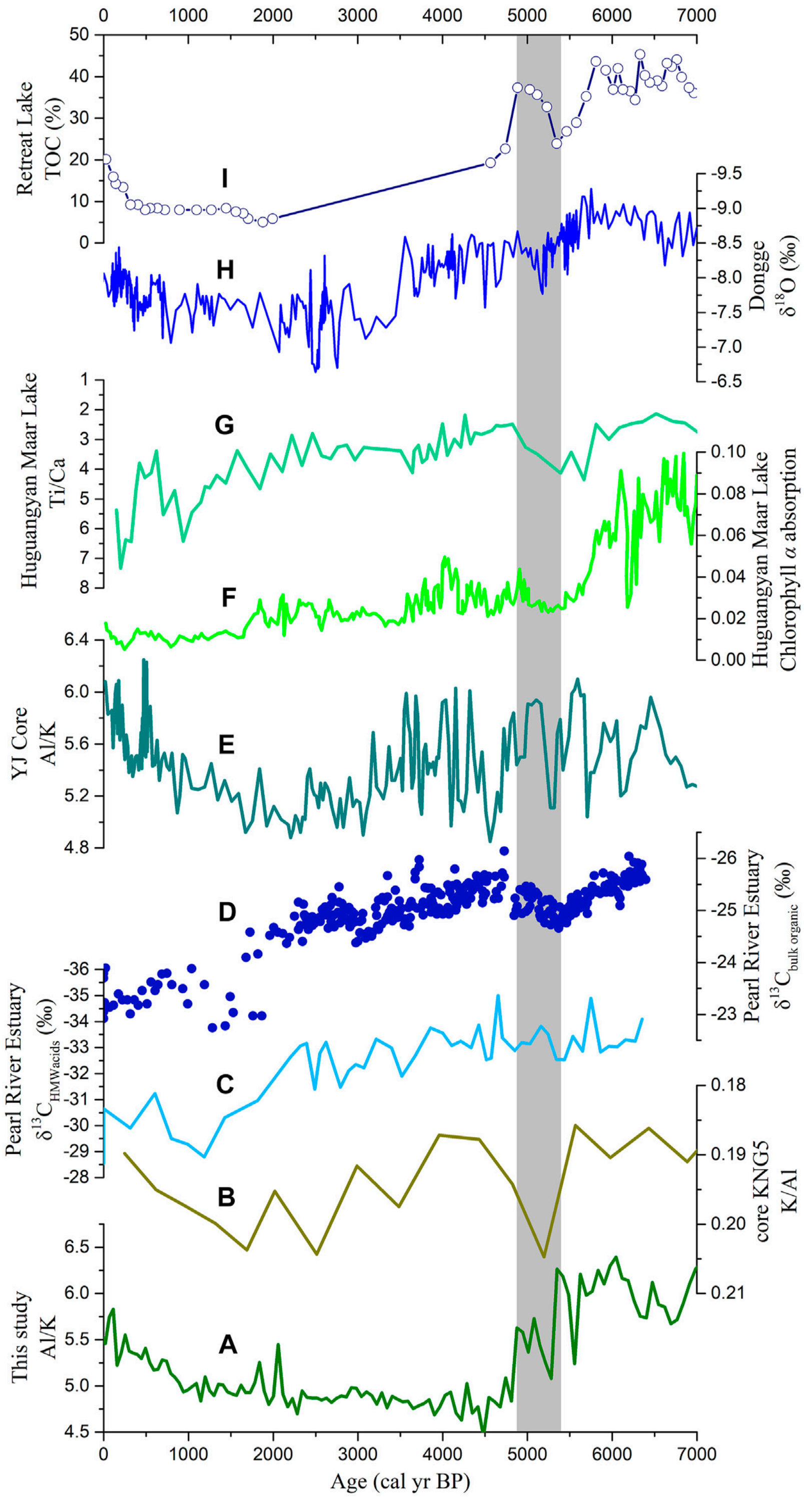

FIGURE 4 | Comparisons between related records: **(A)** Al/K ratios from our GH6 core; **(B)** K/Al record from the northern South China Sea slope (Huang et al., 2016); **(C)** compound-specific δ^{13}C record from the Pearl River Estuary (Strong et al., 2013); **(D)** $\delta^{13}C_{org}$ record from the Pearl River Estuary (Yu et al., 2012); **(E)** Al/K ratios from the northern inner shelf of the South China Sea (Huang et al., 2019); **(F)** chlorophyll-α record from Huguangyan Maar Lake (Wu et al., 2012); **(G)** Ti/Ca record from Huguangyan Maar Lake (Shen et al., 2013); **(H)** stalagmite δ^{18}O record from Dongge Cave (Dykoski et al., 2005); and **(I)** TOC data from Retreat Lake in northeastern Taiwan (Selvaraj et al., 2007).

greater terrigenous influx (Hu et al., 2012; Clift et al., 2014; Wan et al., 2015; Huang et al., 2019). Furthermore, Al, Ti, and Fe variations in our GH6 core, as proxies for terrigenous influx, show similar temporal patterns to CIA and Al/K ratios throughout the core. Consequently, we can reasonably speculate that stronger monsoon precipitation generates greater chemical weathering and associated volumes of terrigenous inputs.

Abrupt Changes in Summer Monsoon Strength 5,400–4,900 cal yr BP and Forcing Mechanisms

During the period 5,400–4,900 cal yr BP, the intensity of chemical weathering decreased rapidly, as inferred from the profiles of CIA and Al/K in our GH6 core. The terrigenous influx decreased rapidly during the same interval, as indicated by concentrations of Al, Ti, and Fe. Simultaneously, the mean sediment grain size increased sharply. The distinct variations in these records suggest a rapid climatic deterioration, which was likely associated with abrupt changes in the Asian summer monsoon. This abrupt climatic event generally coincides with a dramatic weakening of the summer monsoon at 5,400–4,900 cal yr BP, as inferred from various paleoclimate records from monsoonal regions elsewhere (Dykoski et al., 2005; Strong et al., 2013; Huang et al., 2019; Shah et al., 2020).

Chemical weathering interpreted from core KNG5, retrieved from the northern SCS slope, shows an abrupt decrease, reflecting reduced monsoon rainfall (**Figure 4B**; Huang et al., 2016). In the Pearl River estuary, abrupt summer monsoon failure can be detected in bulk-sedimentary $\delta^{13}C_{org}$ and compound-specific $\delta^{13}C$ records (**Figures 4C,D**; Yu et al., 2012; Strong et al., 2013). In the northern inner shelf of the SCS, Al/K ratios, used as an indicator of chemical weathering, exhibit a rapid decrease in response to the weakening monsoon (**Figure 4E**; Huang et al., 2019). This sudden climate shift is also documented in terrestrial sediment records in southern China. In Huguangyan Maar Lake, the weak summer monsoon during this period is detected from multiple climatic indices, including records of chlorophyll α and TOC (**Figure 4F**; Wu et al., 2012), Ti/Ca ratios (**Figure 4G**; Shen et al., 2013), and magnetic properties (Duan et al., 2014). Similarly, a positive shift in the stalagmite $\delta^{18}O$ record from Dongge Cave implies a weakening of the summer monsoon (**Figure 4H**; Dykoski et al., 2005). The development of stagnant swampy environments in the northern Wuyi Mountains is also attributed to a decline in the summer monsoon (Ma et al., 2016b). Within age uncertainty, the subalpine Retreat Lake in Taiwan also experienced an abrupt weak monsoon event, as indicated by low TOC (**Figure 4I**; Selvaraj et al., 2007). Taken together, these multiple proxy records from various geological archives in southern China capture this abrupt climatic shift (**Figure 4**). In addition, the event can similarly be detected across different monsoonal regions of China (An et al., 2012; Li et al., 2017a; Bai et al., 2017; Goldsmith et al., 2017; Tan et al., 2020).

As shown in **Figure 5**, the weak monsoon between 5,400 and 4,900 cal yr BP, recorded in our GH6 core, shows good correspondence within dating uncertainty with an interval of weak solar activity as inferred from residual atmospheric ^{14}C ($\Delta^{14}C$) (Stuiver, et al., 1998) and ice core ^{10}Be data (Steinhilber et al., 2009). This synchroneity suggests a causal linkage between solar activity and summer monsoon variability. In fact, previous studies have linked weak monsoon events to solar activity (Huang et al., 2019). The solar–monsoon link can be explained by a direct influence: solar forcing may control monsoon precipitation by regulating the land—sea thermal contrast (Liu et al., 2009; Xu et al., 2015). A decline in solar output would decrease the land–sea thermal contrast, subsequently leading to southward movement of the Intertropical Convergence Zone (ITCZ). Reduced transportation of water vapour from the ocean to the continents thereby causes less rainfall over monsoonal Asia (Fleitmann et al., 2003; Dykoski et al., 2005; Li et al., 2017b).

In addition, solar activity may influence variability in the summer monsoon indirectly, perhaps amplified by North Atlantic teleconnection and El Niño-Southern Oscillation (ENSO) activity (Wang et al., 2005; 2016; Marchitto et al., 2010). During the period 5,400–4,900 cal yr BP, the weaker monsoon inferred from our GH6 core coincides with higher percentages of hematite-stained grains in the North Atlantic, which can be taken as an indication of ice-rafted debris (IRD) (**Figure 5D**; Bond et al., 2001). Reduced solar activity may trigger IRD events in the North Atlantic (Bond et al., 2001) and a slowdown of North Atlantic meridional overturning circulation (AMOC) (Oppo et al., 2003), eventually weakening the summer monsoon. Likewise, the abrupt summer monsoon failure during this period is also consistent with strong ENSO activity, indicated by sea surface temperature (SST) records from the Western Pacific Warm Pool (**Figure 5E**; Stott et al., 2004). Previous studies have confirmed that ENSO may act as a mediator between solar energy input and the Asian summer monsoon (Asmerom et al., 2007; Emile-Geay et al., 2007; Marchitto et al., 2010). These results suggest a link between East Asia, the tropical Pacific and the North Atlantic: a potential forcing mechanism for abrupt climate change is that solar variability can affect the Asian summer monsoon via the North Atlantic and the ENSO system.

Human Disturbance Over the Past 1,500 Years

AS shown in **Figure 6**, some decoupling have been observed between records of climate, chemical weathering and fluvial discharge over the past 1,500 years. Temperature reconstructions for the Northern hemisphere and the whole of China exhibit an overall cooling trend (**Figures 6A,B**; Yang et al., 2002; PAGES 2k Consortium, 2013). There is a general decrease in the intensity of monsoonal precipitation during this period, as inferred from pollen-reconstructed annual rainfalls from Gonghai Lake and annual mean precipitation reconstructions in northern China (**Figures 6C,D**; Chen et al., 2015; Li et al., 2017b). Similarly, a long-term decrease in monsoon precipitation can be found in high-resolution stalagmite $\delta^{18}O$ records from Dongge and Heshang caves in southern China (Wang et al., 2005; Hu et al., 2008).

However, values of CIA and Al/K ratios in our GH6 core show an overall increasing trend during the last 1,500 years

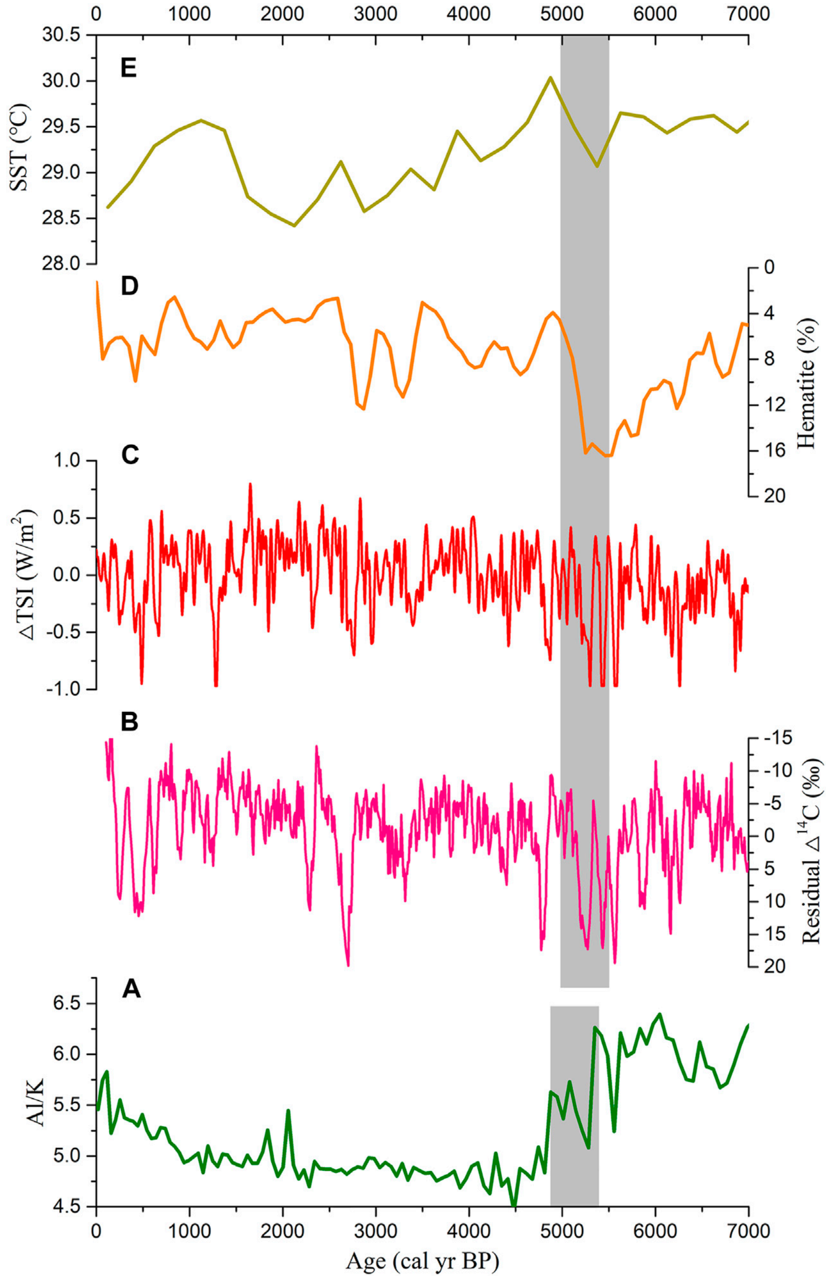

FIGURE 5 | Comparison between various paleoclimate records: **(A)** Al/K ratios from core GH6; **(B)** atmospheric residual $\Delta^{14}C$ record (Stuiver et al., 1998); **(C)** reconstructed total solar irradiance (TSI) from ice-core ^{10}Be data (Steinhilber et al., 2009); **(D)** hematite-stained grains from the subpolar North Atlantic (Bond et al., 2001); and **(E)** sea surface temperature (SST) in the Western Pacific Warm Pool (Stott et al., 2004). The grey bar indicates the abrupt climate change recorded in core GH6.

(**Figure 6E**), reflecting enhanced chemical weathering. An overall increasing trend of terrigenous supply can be also seen, as indicated by concentrations of Al, Ti, and Fe (**Figure 6F**). These trends suggest that climate alone cannot be responsible for changes in chemical weathering and fluvial influx. The concentrations of Cu and Pb in the GH6 core increase dramatically over the past 1,500 years (**Figures 6G,H**). Previous studies have confirmed that increasing metal contents (Cu, Pb, and Zn) appear to be associated with mining and smelting activities (Hu et al., 2013; Hillman et al., 2014; Wan et al., 2015; Huang et al., 2018). Moreover, χ_{lf} and χ_{fd} values in core GH6 exhibit a striking increase over the same period. Mounting evidence suggests that such increases in χ_{lf} and χ_{fd} can be attributed to human-induced soil erosion (Dearing et al., 2008; Wang et al., 2010; Wu et al., 2015; Huang et al., 2018).

More importantly, all of the proxies in our GH6 core are generally consistent with the historical exploitation of Hainan Island (**Figure 7**; Situ, 1987). This provides further evidence for

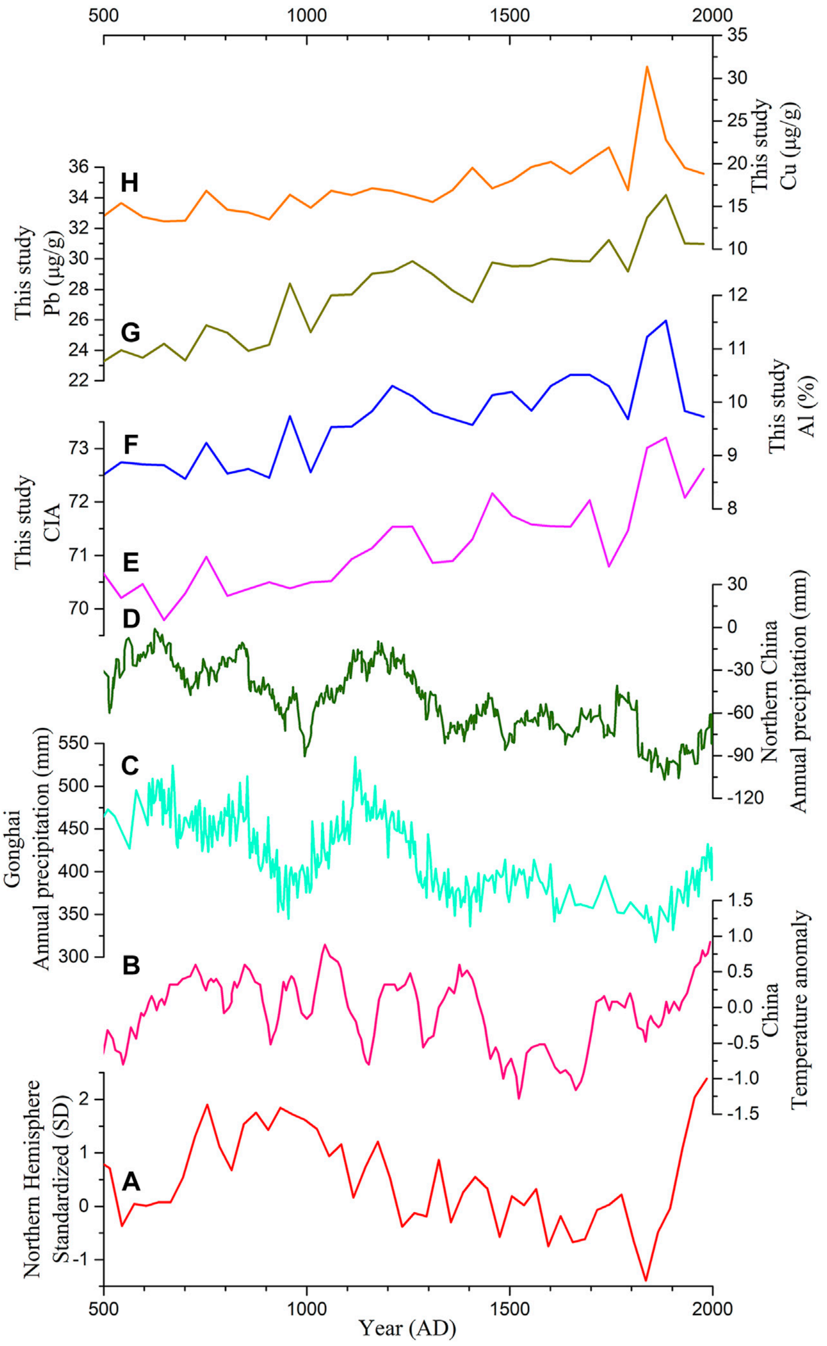

FIGURE 6 | Comparison between GH6 core records and temperature and precipitation data: **(A)** standardized 30-years-mean temperature record averaged over the whole Northern Hemisphere (PAGES 2k Consortium, 2013); **(B)** temperature reconstructions for the whole of China (Yang et al., 2002); **(C)** pollen-inferred annual precipitation data from Gonghai Lake (Chen et al., 2015); **(D)** KCM-based annual precipitation record for northern China (Li et al., 2017b); **(E–H)** multiple proxies from GH6 core.

increasing influence of human activities over the last 1,500 years. According to historical documents, the first large-scale immigration from mainland China took place during the Sui and Tang Dynasty (581–907 AD), with the majority of migrants settling in eastern coastal areas of Hainan (**Figure 7**; Situ, 1987). Migrant numbers increase dramatically during the Song Dynasty. These migrants brought advanced tools and cultivation techniques, such as metalworking and Champa rice (Situ, 1987). The advent of metal tools and metalworking activities may be responsible for the increasing concentrations of Cu and Pb in core GH6 during the past 1,500 years. Population expansion and advanced cultivation techniques would have accelerated

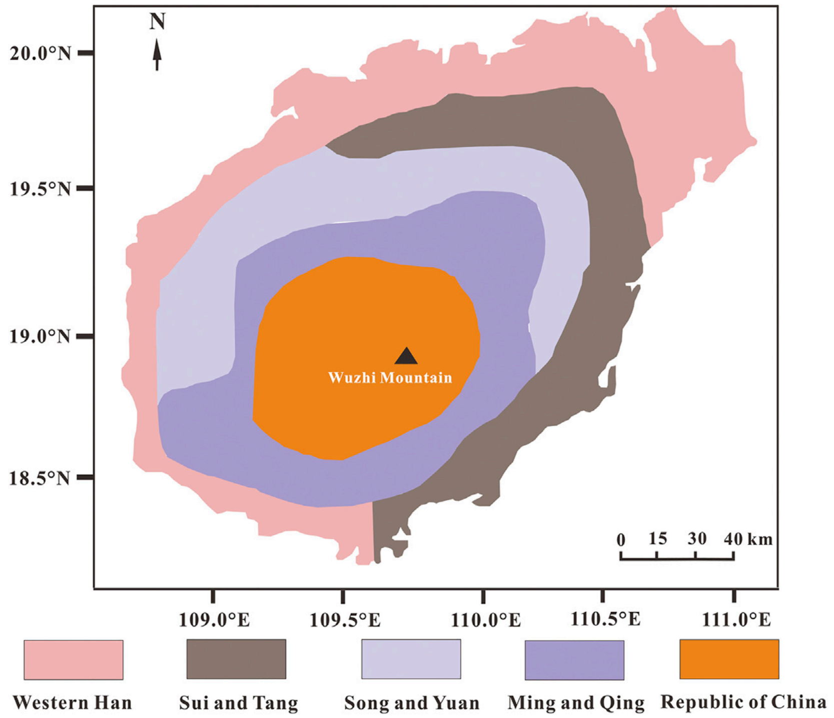

FIGURE 7 | Map depicting the historical exploitation of Hainan Island over past dynasties (redrawn from Situ. (1987) with minor modifications).

deforestation for farming and caused reworking of older highly-weathered materials. This probably enhanced the input of terrestrial material, sourced more deeply and from a wider area. These effects correspond to the increase of proxy indicators in our GH6 core (i.e., CIA, Al/K, χ_{lf}, χ_{fd}, Al, Ti, Fe, Cu, and Pb). Consequently, we can reasonably conclude that human activities have had a growing influence on the natural environment and landscape in eastern Hainan over the past 1,500 years.

CONCLUSION

This study presents high-resolution multi-proxy analyses incorporating chronological, environmental-magnetic, geochemical and grain-size evidence from the coastal shelf off eastern Hainan Island, China. The prominent climatic anomaly during 5,400–4,900 cal yr BP is observed, which is coincides with a dramatic weakening of the summer monsoon. This abrupt event is synchronous with a period of weak solar activity, strong El Niño-Southern Oscillation (ENSO) activity and North Atlantic ice-rafting. These results suggest a climatic link between East Asia, the tropical Pacific and the North Atlantic. The possible forcing mechanism for abrupt climate change is solar variability affecting the Asian summer monsoon via the North Atlantic and ENSO system. There are some decoupling between records of climate, chemical weathering and fluvial discharge over the past 1,500 years. Moreover, enhanced chemical weathering and terrigenous influx during the past 1,500 years are consistent with increasing metal contents (Cu and Pb), and increases in magnetic susceptibility (χ_{lf}) and frequency-dependent magnetic susceptibility (χ_{fd}). All of these proxies are generally consistent with the historical exploitation of Hainan Island. We therefore suggest that enhanced human activity (deforestation, cultivation and mining) over the past 1,500 years has overwhelmed the natural climatic controls on the environment and landscape of Hainan Island.

DATA AVAILABILITY STATEMENT

The original contributions presented in the study are included in the article/**Supplementary Material**, further inquiries can be directed to the corresponding author.

AUTHOR CONTRIBUTIONS

FC and CH designed the study; CH, DK, JH, PW, and JL performed research; CH analyzed data and contributed to data interpretation and paper writing. All authors contributed to the discussion and interpretation of the results and to the writing of the manuscript.

FUNDING

This work was financially supported by National Natural Science Foundation of China (Nos. 42001078, U1901213, 41876058, 41991252), Guangdong Natural Science Foundation of China (No. 2020A1515010500), Open Fund of the State Key Laboratory of Loess and Quaternary Geology, Institute of Earth Environment, CAS (SKLLQG 1908), and Marine Science Research Team Project of Guangdong Ocean University (No. 002026002004).

SUPPLEMENTARY MATERIAL

The Supplementary Material for this article can be found online at: https://www.frontiersin.org/articles/10.3389/feart.2021.663634/full#supplementary-material

REFERENCES

An, Z., Colman, S. M., Zhou, W., Li, X., Brown, E. T., Jull, A. J. T., et al. (2012). Interplay between the Westerlies and Asian Monsoon Recorded in lake Qinghai Sediments since 32 Ka. *Sci. Rep.* 2, 619. doi:10.1038/srep00619

Arnaud, F., Révillon, S., Debret, M., Revel, M., Chapron, E., Jacob, J., et al. (2012). Lake Bourget Regional Erosion Patterns Reconstruction Reveals Holocene NW European Alps Soil Evolution and Paleohydrology. *Quat. Sci. Rev.* 51, 81–92. doi:10.1016/j.quascirev.2012.07.025

Asmerom, Y., Polyak, V., Burns, S., and Rassmussen, J. (2007). Solar Forcing of Holocene Climate: New Insights from a Speleothem Record, Southwestern United States. *Geol.* 35, 1–4. doi:10.1130/g22865a.1

Bai, Y., Zhang, P., Gao, T., Yu, R., Zhou, P., and Cheng, H. (2017). The 5400 a BP Extreme Weakening Event of the Asian Summer Monsoon and Cultural Evolution. *Sci. China Earth Sci.* 60, 1171–1182. doi:10.1007/s11430-016-9017-3

Bond, G., Kromer, B., Beer, J., Muscheler, R., Evans, M. N., Showers, W., et al. (2001). Persistent Solar Influence on North Atlantic Climate during the Holocene. *Science* 294, 2130–2136. doi:10.1126/science.1065680

Chen, F., Xu, Q., Chen, J., Birks, H. J., Liu, J., Zhang, S., et al. (2015). East Asian Summer Monsoon Precipitation Variability since the Last Deglaciation. *Sci. Rep.* 5, 11186. doi:10.1038/srep11186

Cheng, Z., Weng, C., Steinke, S., and Mohtadi, M. (2018). Anthropogenic Modification of Vegetated Landscapes in Southern China from 6,000 Years Ago. *Nat. Geosci.* 11, 939–943. doi:10.1038/s41561-018-0250-1

Clift, P. D., Wan, S., and Blusztajn, J. (2014). Reconstructing Chemical Weathering, Physical Erosion and Monsoon Intensity since 25Ma in the Northern South China Sea: A Review of Competing Proxies. *Earth-Science Rev.* 130, 86–102. doi:10.1016/j.earscirev.2014.01.002

Condie, K. C., Dengate, J., and Cullers, R. L. (1995). Behavior of Rare Earth Elements in a Paleoweathering Profile on Granodiorite in the Front Range, Colorado, USA. *Geochimica et Cosmochimica Acta* 59, 279–294. doi:10.1016/0016-7037(94)00280-y

Cullen, H. M., deMenocal, P. B., Hemming, S., Hemming, G., Brown, F. H., Guilderson, T., et al. (2000). Climate Change and the Collapse of the Akkadian empire: Evidence from the Deep Sea. *Geology* 28, 379–382. doi:10.1130/0091-7613(2000)028<0379:ccatco>2.3.co;2

Dearing, J. A., Jones, R. T., Shen, J., Yang, X., Boyle, J. F., Foster, G. C., et al. (2008). Using Multiple Archives to Understand Past and Present Climate-Human-Environment Interactions: the lake Erhai Catchment, Yunnan Province, China. *J. Paleolimnol.* 40, 3–31. doi:10.1007/s10933-007-9182-2

DeMenocal, P. B. (2001). Cultural Responses to Climate Change during the Late Holocene. *Science (New York, N.Y.)* 292, 667–673. doi:10.1126/science.1059827

Douglas, P. M. J., Demarest, A. A., Brenner, M., and Canuto, M. A. (2016). Impacts of Climate Change on the Collapse of lowland Maya Civilization. *Annu. Rev. Earth Planet. Sci.* 44, 613–645. doi:10.1146/annurev-earth-060115-012512

Duan, Z., Liu, Q., Yang, X., Gao, X., Su, Y., and Su, Y. (2014). Magnetism of the Huguangyan Maar Lake Sediments, Southeast China and its Paleoenvironmental Implications. *Palaeogeogr. Palaeoclimatol. Palaeoecol.* 395, 158–167. doi:10.1016/j.palaeo.2013.12.033

Dykoski, C., Edwards, R., Cheng, H., Yuan, D., Cai, Y., Zhang, M., et al. (2005). A High-Resolution, Absolute-Dated Holocene and Deglacial Asian Monsoon Record from Dongge Cave, China. *Earth Planet. Sci. Lett.* 233, 71–86. doi:10.1016/j.epsl.2005.01.036

Emile-Geay, J., Cane, M., Seager, R., Kaplan, A., and Almasi, P. (2007). El Niño as a Mediator of the Solar Influence on Climate. *Paleoceanography* 22. doi:10.1029/2006pa001304

Fleitmann, D., Burns, S. J., Mudelsee, M., Neff, U., Kramers, J., Mangini, A., et al. (2003). Holocene Forcing of the Indian Monsoon Recorded in a Stalagmite from Southern Oman. *Science* 300, 1737–1739. doi:10.1126/science.1083130

Folk, R. L., and Ward, W. C. (1957). Brazos River Bar [Texas]; a Study in the Significance of Grain Size Parameters. *J. Sediment. Res.* 27, 3–26. doi:10.1306/74d70646-2b21-11d7-8648000102c1865d

Goldsmith, Y., Broecker, W. S., Xu, H., Polissar, P. J., deMenocal, P. B., Porat, N., et al. (2017). Northward Extent of East Asian Monsoon Covaries with Intensity on Orbital and Millennial Timescales. *Proc. Natl. Acad. Sci. USA*. 114, 1817–1821. doi:10.1073/pnas.1616708114

Haug, G. H., Hughen, K. A., Sigman, D. M., Peterson, L. C., and Röhl, U. (2001). Southward Migration of the Intertropical Convergence Zone through the Holocene. *Science* 293, 1304–1308. doi:10.1126/science.1059725

Hillman, A. L., Yu, J., Abbott, M. B., Cooke, C. A., Bain, D. J., and Steinman, B. A. (2014). Rapid Environmental Change during Dynastic Transitions in Yunnan Province, China. *Quat. Sci. Rev.* 98, 24–32. doi:10.1016/j.quascirev.2014.05.019

Hou, M., and Wu, W. X. (2021). A Review of 6000-5000 Cal BP Climatic Anomalies in China. *Quat. Int.* 571, 58–72. doi:10.1016/j.quaint.2020.12.004

Hu, B., Li, J., Cui, R., Wei, H., Zhao, J., Li, G., et al. (2014). Clay Mineralogy of the Riverine Sediments of Hainan Island, South China Sea: Implications for Weathering and Provenance. *J. Asian Earth Sci.* 96, 84–92. doi:10.1016/j.jseaes.2014.08.036

Hu, C., Henderson, G. M., Huang, J., Xie, S., Sun, Y., and Johnson, K. R. (2008). Quantification of Holocene Asian Monsoon Rainfall from Spatially Separated Cave Records. *Earth Planet. Sci. Lett.* 266, 221–232. doi:10.1016/j.epsl.2007.10.015

Hu, D., Böning, P., Köhler, C. M., Hillier, S., Pressling, N., Wan, S., et al. (2012). Deep Sea Records of the continental Weathering and Erosion Response to East Asian Monsoon Intensification since 14ka in the South China Sea. *Chem. Geology.* 326-327, 1–18. doi:10.1016/j.chemgeo.2012.07.024

Hu, D., Clift, P. D., Böning, P., Hannigan, R., Hillier, S., Blusztajn, J., et al. (2013). Holocene Evolution in Weathering and Erosion Patterns in the Pearl River delta. *Geochem. Geophys. Geosyst.* 14, 2349–2368. doi:10.1002/ggge.20166

Huang, C., Zeng, T., Ye, F., and Wei, G. (2019). Solar-forcing-induced Spatial Synchronisation of the East Asian Summer Monsoon on Centennial Timescales. *Palaeogeogr. Palaeoclimatol. Palaeoecol.* 514, 536–549. doi:10.1016/j.palaeo.2018.11.002

Huang, C., Zeng, T., Ye, F., Xie, L., Wang, Z., Wei, G., et al. (2018). Natural and Anthropogenic Impacts on Environmental Changes over the Past 7500 Years Based on the Multi-Proxy Study of Shelf Sediments in the Northern South China Sea. *Quat. Sci. Rev.* 197, 35–48. doi:10.1016/j.quascirev.2018.08.005

Huang, J., Wan, S., Xiong, Z., Zhao, D., Liu, X., Li, A., et al. (2016). Geochemical Records of Taiwan-Sourced Sediments in the South China Sea Linked to Holocene Climate Changes. *Palaeogeogr. Palaeoclimatol. Palaeoecol.* 441, 871–881. doi:10.1016/j.palaeo.2015.10.036

Ishfaq, A. M., Pattan, J. N., Matta, V. M., and Banakar, V. K. (2013). Variation of Paleo-Productivity and Terrigenous Input in the Eastern Arabian Sea during the Past 100 Ka. *J. Geol. Soc. India* 81, 647–654. doi:10.1007/s12594-013-0086-7

Ji, C., Xu, L., Zhang, Y., Guo, M., and Kong, D. (2020). A 1900-year Record of Mercury (Hg) from the East continental Shelf of Hainan Island, South China Sea. *Geol. J.* 55, 4469–4478. doi:10.1002/gj.3678

Kong, D. M., Chen, G. S., Feng, W., J., Liu, Z. H., Chen, M. T., and Xu, L. Q. (2021). Alkenone-derived SST and Implication for Upwelling Changes off the Eastern Hainan Island over the Last 5000 Years. *Front. Earth Sci.* (submitted for publication).

Latimer, J. C., and Filippelli, G. M. (2001). Terrigenous Input and Paleoproductivity in the Southern Ocean. *Paleoceanography* 16, 627–643. doi:10.1029/2000pa000586

Li, J., Dodson, J., Yan, H., Cheng, B., Zhang, X., Xu, Q., et al. (2017a). Quantitative Precipitation Estimates for the Northeastern Qinghai-Tibetan Plateau over the

Last 18,000 Years. *J. Geophys. Res. Atmos.* 122, 5132–5143. doi:10.1002/2016jd026333

Li, J., Dodson, J., Yan, H., Zhang, D. D., Zhang, X., Xu, Q., et al. (2017b). Quantifying Climatic Variability in Monsoonal Northern China over the Last 2200 Years and its Role in Driving Chinese Dynastic Changes. *Quat. Sci. Rev.* 159, 35–46. doi:10.1016/j.quascirev.2017.01.009

Liu, J., Chen, J., Selvaraj, K., Xu, Q., Wang, Z., and Chen, F. (2014). Chemical Weathering over the Last 1200 Years Recorded in the Sediments of Gonghai Lake, Lvliang Mountains, North China: a High-Resolution Proxy of Past Climate. *Boreas* 43, 914–923. doi:10.1111/bor.12072

Liu, W. T., and Xie, X. (1999). Spacebased Observations of the Seasonal Changes of South Asian Monsoons and Oceanic responses. *Geophys. Res. Lett.* 26, 1473–1476. doi:10.1029/1999gl900289

Liu, X., Dong, H., Yang, X., Herzschuh, U., Zhang, E., Stuut, J., et al. (2009). Late Holocene Forcing of the Asian winter and Summer Monsoon as Evidenced by Proxy Records from the Northern Qinghai-Tibetan Plateau. *Earth Planet Sci. Lett.* 280, 276–284. doi:10.1016/j.epsl.2009.01.041

Liu, Y., Peng, Z., Shen, C.-C., Zhou, R., Song, S., Shi, Z., et al. (2013). Recent 121-year Variability of Western Boundary Upwelling in the Northern South China Sea. *Geophys. Res. Lett.* 40, 3180–3183. doi:10.1002/grl.50381

Lu, F., Dodson, J., Zhang, W., and Yan, H. (2019). Mid to Late Holocene Environmental Change and Human Impact: A View from Central China. *Quat. Sci. Rev.* 223, 105953. doi:10.1016/j.quascirev.2019.105953

Ma, T., Zheng, Z., Rolett, B. V., Lin, G., Zhang, G., and Yue, Y. (2016a). New Evidence for Neolithic rice Cultivation and Holocene Environmental Change in the Fuzhou Basin, Southeast China. *Veget Hist. Archaeobot* 25, 375–386. doi:10.1007/s00334-016-0556-0

Ma, T., Tarasov, P. E., Zheng, Z., Han, A., and Huang, K. (2016b). Pollen- and Charcoal-Based Evidence for Climatic and Human Impact on Vegetation in the Northern Edge of Wuyi Mountains, China, during the Last 8200 Years. *The Holocene* 26, 1616–1626. doi:10.1177/0959683616641744

Marchitto, T. M., Muscheler, R., Ortiz, J. D., Carriquiry, J. D., and van Geen, A. (2010). Dynamical Response of the Tropical Pacific Ocean to Solar Forcing during the Early Holocene. *Science* 330, 1378–1381. doi:10.1126/science.1194887

Mayewski, P. A., Rohling, E. E., Curt Stager, J., Karlén, W., Maasch, K. A., Meeker, L. D., et al. (2004). Holocene Climate Variability. *Quat. Res.* 62, 243–255. doi:10.1016/j.yqres.2004.07.001

Nesbitt, H., and Markovics, G. (1997). Weathering of Granodioritic Crust, Long-Term Storage of Elements in Weathering Profiles, and Petrogenesis of Siliciclastic Sediments. *Geochim. Cosmochim. Acta* 61, 1653–1670.

Nesbitt, H. W., Markovics, G., and Price, R. C. (1980). Chemical Processes Affecting Alkalis and Alkaline Earths during continental Weathering. *Geochimica et Cosmochimica Acta* 44, 1659–1666. doi:10.1016/0016-7037(80)90218-5

Nesbitt, H. W., and Young, G. M. (1982). Early Proterozoic Climates and Plate Motions Inferred from Major Element Chemistry of Lutites. *Nature* 299, 715–717. doi:10.1038/299715a0

Oppo, D. W., Mcmanus, J. F., and Cullen, J. L. (2003). Deepwater Variability in the Holocene Epoch. *Nature* 422, 277. doi:10.1038/422277b

PAGES 2k Consortium (2013). Continental-scale Temperature Variability during the Past Two Millennia. *Nat. Geosci.* 6, 339–346. doi:10.1038/ngeo1797

Pei, W., Wan, S., Clift, P. D., Dong, J., Liu, X., Lu, J., et al. (2020). Human Impact Overwhelms Long-Term Climate Control of Fire in the Yangtze River Basin since 3.0 Ka BP. *Quat. Sci. Rev.* 230, 106165. doi:10.1016/j.quascirev.2020.106165

Peterson, L. C., and Haug, G. H. (2006). Variability in the Mean Latitude of the Atlantic Intertropical Convergence Zone as Recorded by Riverine Input of Sediments to the Cariaco Basin (Venezuela). *Palaeogeogr. Palaeoclimatol. Palaeoecol.* 234, 97–113. doi:10.1016/j.palaeo.2005.10.021

Reimer, P. J., Austin, W., Bard, E., Bayliss, A., Blackwell, P., Ramsey, C., et al. (2020). The Intcal20 Northern Hemisphere Radiocarbon Age Calibration Curve (0-55 Cal kBP). *Radiocarbon* 100, 1–33.

Revel, M., Ducassou, E., Grousset, F. E., Bernasconi, S. M., Migeon, S., Revillon, S., et al. (2010). 100,000 Years of African Monsoon Variability Recorded in Sediments of the Nile Margin. *Quat. Sci. Rev.* 29, 1342–1362. doi:10.1016/j.quascirev.2010.02.006

Shah, R. A., Achyuthan, H., Lone, A. M., Kumar, S., Kumar, P., Sharma, R., et al. (2020). Holocene Palaeoenvironmental Records from the High-Altitude Wular Lake, Western Himalayas. *Holocene* 30, 733–743. doi:10.1177/0959683619895592journals.sagepub

Shen, J., Wu, X., Zhang, Z., Gong, W., and Dong, H. (2013). Ti Content in Huguangyan Maar lake Sediment as a Proxy for Monsoon-Induced Vegetation Density in the Holocene. *Geophys. Res. Lett.* 40, 1–7. doi:10.1002/grl.50740

Shuman, B. (2012). Patterns, Processes, and Impacts of Abrupt Climate Change in a Warm World: the Past 11,700 Years. *Wires Clim. Change* 3, 19–43. doi:10.1002/wcc.152

Sinha, A., Kathayat, G., Weiss, H., Li, H., Cheng, H., Reuter, J., et al. (2019). Role of Climate in the Rise and Fall of the Neo-Assyrian Empire. *Sci. Adv.* 5, eaax6656. doi:10.1126/sciadv.aax6656

Situ, S. (1987). *The Development Research of the Land on the History of Hainan Island [M]*. Haikou: Hainan People's Publishing House, 58. (in Chinese).

Steinhilber, F., Beer, J., and Fröhlich, C. (2009). Total Solar Irradiance during the Holocene. *Geophys. Res. Lett.* 36, L19704. doi:10.1029/2009gl040142

Strong, D., Flecker, R., Valdes, P. J., Wilkinson, I. P., Rees, J. G., Michaelides, K., et al. (2013). A New Regional, Mid-holocene Palaeoprecipitation Signal of the Asian Summer Monsoon. *Quat. Sci. Rev.* 78, 65–76. doi:10.1016/j.quascirev.2013.07.034

Stuiver, M., Reimer, P. J., Bard, E., Beck, J. W., Burr, G. S., Hughen, K. A., et al. (1998). INTCAL98 Radiocarbon Age Calibration, 24,000-0 Cal BP. *Radiocarbon* 40, 1041–1083. doi:10.1017/s0033822200019123

Su, Y., Chu, G., Liu, Q., Jiang, Z., Gao, X., and Haberzettl, T. (2015). A 1400 Year Environmental Magnetic Record from Varved Sediments of Lake Xiaolongwan (Northeast China) Reflecting Natural and Anthropogenic Soil Erosion. *Geochem. Geophys. Geosyst.* 16, 3053–3060. doi:10.1002/2015gc005880

Tan, L., Li, Y., Wang, X., Cai, Y., Lin, F., Lin, F., et al. (2020). Holocene Monsoon Change and Abrupt Events on the Western Chinese Loess Plateau as Revealed by Accurately Dated Stalagmites. *Geophys. Res. Lett.* 46, e2020GL090273. doi:10.1029/2020GL090273

Tian, C. J., Ouyang, T. P., Zhu, Z. Y., Qiu, Y., Peng, X. C., and Li, M. K. (2013). Spatial Distribution of Magnetic Susceptibility and its Provenance Implication of Surface Sediments in the Sea Areas Around the Hainan Island. *Trop. Geogr.* 33, 666–673. (in Chinese with English abstract).

Wan, S., Toucanne, S., Clift, P. D., Zhao, D., Bayon, G., Yu, Z., et al. (2015). Human Impact Overwhelms Long-Term Climate Control of Weathering and Erosion in Southwest China. *Geology* 43, 439–442. doi:10.1130/g36570.1

Wang, Y., Cheng, H., Edwards, R. L., He, Y., Kong, X., An, Z., et al. (2005). The Holocene Asian Monsoon: Links to Solar Changes and North Atlantic Climate. *Science* 308, 854–857. doi:10.1126/science.1106296

Wang, Z., Maotian, L., Ruihu, Z., Chencheng, Z., Yan, L., Saito, Y., et al. (2010). Impacts of Human Activity on the Late-Holocene Development of the Subaqueous Yangtze delta, China, as Shown by Magnetic Properties and Sediment Accumulation Rates. *Holocene* 21, 393–407. doi:10.1177/0959683610378885

Wanner, H., Solomina, O., Grosjean, M., Ritz, S. P., and Jetel, M. (2011). Structure and Origin of Holocene Cold Events. *Quat. Sci. Rev.* 30, 3109–3123. doi:10.1016/j.quascirev.2011.07.010

Wei, G., Li, X. H., Liu, Y., Shao, L., and Liang, X. (2006). Geochemical Record of Chemical Weathering and Monsoon Climate Change since the Early Miocene in the South China Sea. *Paleoceanography* 21, PA4214. doi:10.1029/2006pa001300

White, A. F., and Blum, A. E. (1995). Effects of Climate on Chemical_ Weathering in Watersheds. *Geochimica et Cosmochimica Acta* 59, 1729–1747. doi:10.1016/0016-7037(95)00078-e

Wu, D., Zhou, A., Liu, J., Chen, X., Wei, H., Sun, H., et al. (2015). Changing Intensity of Human Activity over the Last 2,000 Years Recorded by the Magnetic Characteristics of Sediments from Xingyun Lake, Yunnan, China. *J. Paleolimnol.* 53, 47–60. doi:10.1007/s10933-014-9806-2

Wu, L., Fu, P., Xu, L., Wei, Y., Zhou, X., Li, Y., et al. (2017). Changes in the Source of Sedimentary Organic Matter in the Marginal Sea Sediments of Eastern Hainan Island in Response to Human Activities during the Past 200 Years. *Quat. Int.* 440, 150–159. doi:10.1016/j.quaint.2016.07.007

Wu, W., Zheng, H., Hou, M., and Ge, Q. (2018). The 5.5 Cal Ka BP Climate Event, Population Growth, Circumscription and the Emergence of the Earliest

Complex Societies in China. *Sci. China Earth Sci.* 61, 134–148. doi:10.1007/s11430-017-9157-1

Wu, X., Zhang, Z., Xu, X., and Shen, J. (2012). Asian Summer Monsoonal Variations during the Holocene Revealed by Huguangyan Maar lake Sediment Record. *Palaeogeogr. Palaeoclimatol. Palaeoecol.* 323-325, 13–21. doi:10.1016/j.palaeo.2012.01.020

Xu, F., Hu, B., Dou, Y., Song, Z., Yuan, S., et al. (2017). Prehistoric Heavy Metal Pollution on the continental Shelf off Hainan Island, South China Sea: from Natural to Anthropogenic Impacts Around 4.0 Kyr BP. *The Holocene* 28, 455–463. doi:10.1177/0959683617729445

Xu, H., Yeager, K. M., Lan, J., Liu, B., Sheng, E., and Zhou, X. (2015). Abrupt Holocene Indian Summer Monsoon Failures: A Primary Response to Solar Activity? *The Holocene* 25, 677–685. doi:10.1177/0959683614566252

Yan, H. M., Tian, X., Xu, F. J., Hu, B. Q., Yang, Y. M., Feng, J. W., et al. (2016). Sediment Provenance of Offshore Mud Area of the Eastern Hainan Island in South China Sea since the Mid-holocene. *Haiyang Xuebao* 38, 97–106. (in Chinese with English abstract).

Yang, B., Braeuning, A., Johnson, K. R., and Yafeng, S. (2002). General Characteristics of Temperature Variation in China during the Last Two Millennia. *Geophys. Res. Lett.* 29, 381–384. doi:10.1029/2001gl014485

Yang, Z. H., Jia, J. J., Wang, X. K., and Gao, J. H. (2013). Characteristics and Variations of Water and Sediment Fluxes into the Sea of the Top three rivers of Hainan in Recent 50 Years. *Mar. Sci. Bull.* 1, 015. (in Chinese with English abstract).

Zeng, Z. X., and Zeng, X. Z. (1989). *Physicogeography of the Hainan Island*. Beijing, China: Science Press. (in Chinese).

Zhang, J., Wang, D. R., Jennerjahn, T., and Dsikowitzky, L. (2013). Land-sea Interactions at the East Coast of Hainan Island, South China Sea: a Synthesis. *Continental Shelf Res.* 57, 132–142. doi:10.1016/j.csr.2013.01.004

Zhao, Y., Chen, F., Zhou, A., Yu, Z., and Zhang, K. (2010). Vegetation History, Climate Change and Human Activities over the Last 6200years on the Liupan Mountains in the Southwestern Loess Plateau in central China. *Palaeogeogr. Palaeoclimatol. Palaeoecol.* 293, 197–205. doi:10.1016/j.palaeo.2010.05.020

Zong, Y., Yu, F., Huang, G., Lloyd, J. M., and Yim, W. W.-S. (2010). Sedimentary Evidence of Late Holocene Human Activity in the Pearl River delta, China. *Earth Surf. Process. Landforms* 35, 1095–1102. doi:10.1002/esp.1970

Conflict of Interest: The authors declare that the research was conducted in the absence of any commercial or financial relationships that could be construed as a potential conflict of interest.

frontiers in Earth Science

ORIGINAL RESEARCH
published: 14 June 2021
doi: 10.3389/feart.2021.704332

A Lacustrine Biomarker Record From Rebun Island Reveals a Warm Summer Climate in Northern Japan During the Early Middle Holocene Due to a Stronger North Pacific High

Masanobu Yamamoto[1,2]*, Fangxian Wang[2], Tomohisa Irino[1,2], Kenta Suzuki[1], Kazuyoshi Yamada[3], Tsuyoshi Haraguchi[4], Katsuya Gotanda[5], Hitoshi Yonenobu[6], Xuan-Yu Chen[7,8] and Pavel Tarasov[9]

[1]Faculty of Environmental Earth Science, Hokkaido University, Sapporo, Japan, [2]Graduate School of Environmental Science, Hokkaido University, Sapporo, Japan, [3]School of Human Science, Waseda University, Tokorozawa, Japan, [4]Department of Geosciences, Osaka City University, Osaka, Japan, [5]Faculty of Global Studies, Chiba University of Commerce, Ichikawa, Japan, [6]Graduate School of Education, Naruto University of Education, Naruto, Japan, [7]State Key Laboratory of Isotope Geochemistry, Guangzhou Institute of Geochemistry, Chinese Academy of Sciences, Guangzhou, China, [8]CAS Center for Excellence in Deep Earth Science, Guangzhou, China, [9]Institute of Geological Sciences, Freie Universität Berlin, Berlin, Germany

OPEN ACCESS

Edited by:
Min-Te Chen,
National Taiwan Ocean University,
Taiwan

Reviewed by:
Deming Kong,
Guangdong Ocean University, China
Liang-Chi Wang,
National Chung Cheng University,
Taiwan

***Correspondence:**
Masanobu Yamamoto
myama@ees.hokudai.ac.jp

Specialty section:
This article was submitted to
Quaternary Science, Geomorphology
and Paleoenvironment,
a section of the journal
Frontiers in Earth Science

Received: 02 May 2021
Accepted: 28 May 2021
Published: 14 June 2021

Citation:
Yamamoto M, Wang F, Irino T,
Suzuki K, Yamada K, Haraguchi T,
Gotanda K, Yonenobu H, Chen X-Y
and Tarasov P (2021) A Lacustrine
Biomarker Record From Rebun Island
Reveals a Warm Summer Climate in
Northern Japan During the Early
Middle Holocene Due to a Stronger
North Pacific High.
Front. Earth Sci. 9:704332.
doi: 10.3389/feart.2021.704332

The summer climate of northern Japan since the last glacial period has likely been determined by atmospheric and oceanic dynamics, such as changes in the North Pacific High, the position of the westerlies, the Kuroshio Current, the Tsushima Warm Current (TWC), and the East Asian summer monsoon. However, it is unclear which factor has been most important. In this study, we analyzed leaf wax δ^{13}C and δD and glycerol dialkyl glycerol tetraethers (GDGTs) in sediments from Lake Kushu, Rebun Island, northern Japan, and discuss changes in climate over the past 17,000 years. The GDGT-based temperature, the averaged chain length, δ^{13}C and δD of long-chain n-fatty acids indicated that the climate was cold during the Oldest Dryas period ~16 ka and warm in the early Middle Holocene from ~9 to 6 ka. This climate change is consistent with the sea surface temperature in the Kuroshio–Oyashio transition, but inconsistent with changes in the TWC in the Sea of Japan. The results imply that the summer climate of northern Japan was controlled mainly by changes in the development of the North Pacific High *via* changes in the position of the westerly jet and East Asian summer monsoon rainfall, whereas the influence of the TWC was limited over a millennial timescale.

Keywords: climate change, Northern Japan, holocene, lateglacial, Biomarkers, rebun, RK12

INTRODUCTION

The summer climate of northern Japan is influenced by the summer position of the westerly winds and the strength of the Tsushima Warm Current (TWC). The position of the westerly winds is linked to the oceanic subarctic boundary between the subtropical Kuroshio and subarctic Oyashio currents in the Pacific (**Figure 1**) (*e.g.*, Yamamoto et al., 2004; Yamamoto et al., 2005; Isono et al., 2009; Yamamoto, 2009). Yamamoto et al. (2005) and Isono et al. (2009) identified the southern summer position of the Kuroshio–Oyashio transition (KOT) in the Oldest Dryas and Younger Dryas periods

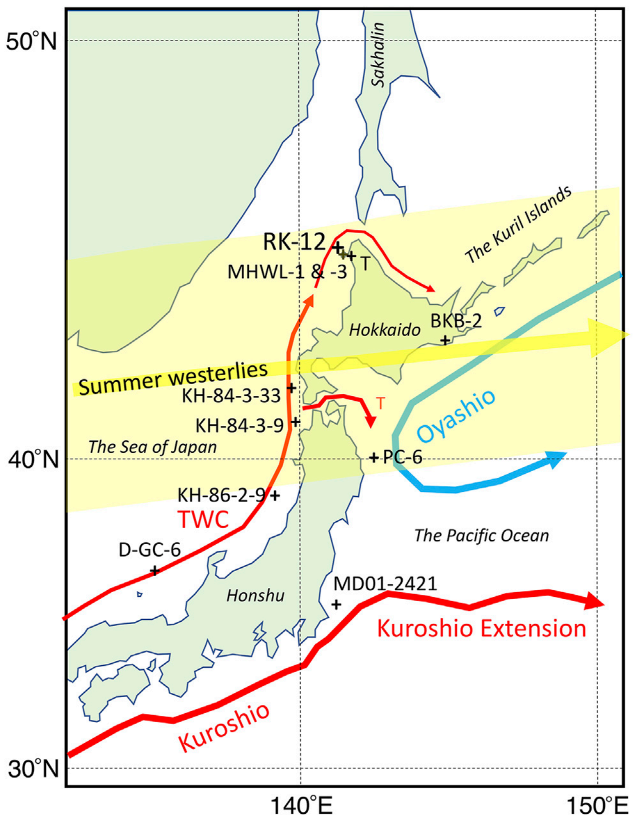

FIGURE 1 | Map showing study site RK12-2 and the reference site locations, *i.e.*, MHWL-1 and 3 (Yamamoto and Seki, in preparation), BKB-2 (Sakurai et al., 2021), PC-6 (Minoshima et al., 2007), MD01-2421 (Yamamoto et al., 2004), KH-84-3-9, KH-84-3-33, KH-86-2-9, and D-GC-6 (Koizumi et al., 2006), and D-GC-9 (Koizumi et al., 2006), as well as the mean positions of the summer (June to August) westerly wind axis with the range of variation for 30 years from 1988 to 2017 (yellow shading) of summer westerlies, the Kuroshio, Kuroshio Extension, Oyashio, Tsushima Warm Current (TWC), and Tsugaru Warm Current (T). T indicates the meteorological station at Teshio.

due to the weaker North Pacific High, a northward shift of the KOT at the end of the Younger Dryas period, the northernmost position at 8 ka and the gradual southward shift during the Middle and Late Holocene. The TWC flows northwards as a branch of the Kuroshio Current along the eastern margin of the Sea of Japan (**Figure 1**). The TWC promotes moisture uptake by the predominant winter monsoon winds and carries heat to northern Japan. Diatom records from four offshore sites along the Sea of Japan coast showed that TWC species appeared after 7 ka and fluctuated in abundance on a millennial timescale (Koizumi et al., 2006).

Pollen records from Hokkaido (Igarashi, 2013 and references therein) and Lake Kushu (Müller et al., 2016; Leipe et al., 2018) on Rebun Island showed that the vegetation of northern Japan changed from a boreal forest in the Late Glacial to a cool-temperate forest in the Early Holocene due to deglacial warming. Temperate deciduous oak trees were more widely spread during the Middle Holocene, while forests containing more *Abies* and Pinaceae trees spread during the Late Holocene due to gradual cooling.

Other proxies such as *Sphagnum* and vascular plant cellulose δ^{18}O in peat are more sensitive to summer hydrological conditions. They showed remarkable changes in the high moors in Rishiri (Sites MHWL-1 and -3) and Hokkaido (Site BKB-2) during the Late Holocene, which corresponded to changes in the summer sea surface temperature (SST) in the KOT and the TWC strength (Sakurai et al., 2021; Yamamoto and Seki, unpublished data).

The summer westerly wind axis, moisture content, temperature, precipitation, and precipitated water δD and d-excess seasonally covaried at the study site (**Figure 2**), indicating a close relationship between the position of the summer westerly wind axis, the East Asian summer monsoon, and precipitated water δD and d-excess (**Figure 2**). In summer, the westerly wind axis shifts north, a warm and moist air mass occupies the study site (45°N), the δD of precipitated water is heavier, and the d-excess is lower. In winter, the westerly wind axis shifts south, a cold and dry air mass occupies the study site, the δD of precipitated water is lighter, and the d-excess is higher. The higher d-excess in winter is attributed to kinetic fractionation during the evaporation process in the Sea of Japan under a large humidity deficit and a strong temperature contrast in the air-sea surface interface (Sugimoto et al., 1988; Li et al., 2017).

In this study, we analyzed leaf wax δ^{13}C and δD and glycerol dialkyl glycerol tetraethers (GDGTs) in sediments from Lake Kushu, Rebun Island, northern Japan, and discuss changes in the summer climate and the atmospheric and ocean dynamics that affected the climate of northern Japan over the past 17 ka.

SAMPLES AND METHODS

Sediment and Chronology

Lake Kushu is located in the northern part of Rebun Island (45°25′58″N, 141°02′05″E) (**Figure 1**), 230–400 m from the modern sea coast. The bean-shaped lake has a maximum length of ~1,100 m. The maximum water depth is ~6 m in the eastern part of the lake, with average depths of 3–5 m. In February 2012, when a thick ice layer covered the lake, Dokon (Sapporo, Japan) performed coring in the central part of the lake. Composite core RK12 was recovered from two boreholes (RK12-1 and RK12-2) located within a few meters of each other.

The composite core revealed a continuous, partly laminated, organic-rich 20.3 m-long sediment column. The lithology is described in Müller et al. (2016). In brief, the basal unit contains sandy clay with pebbles, suggesting a stronger river influence. Peat (1,925–1,935 and 1,905–1,915 cm) and organic-rich clay (1,915–1,925 and 1,895–1,905 cm) layers appear in the lower part of the core, suggesting shallow water or marshy environments. The interval within 1,895–1,390 cm is characterized by homogeneous, relatively organic-poor clay, which is interrupted only by two sand seams (1,790–1,815 and 1,765–1,780 cm). Within 1,390–850 cm, the clay is mostly finely

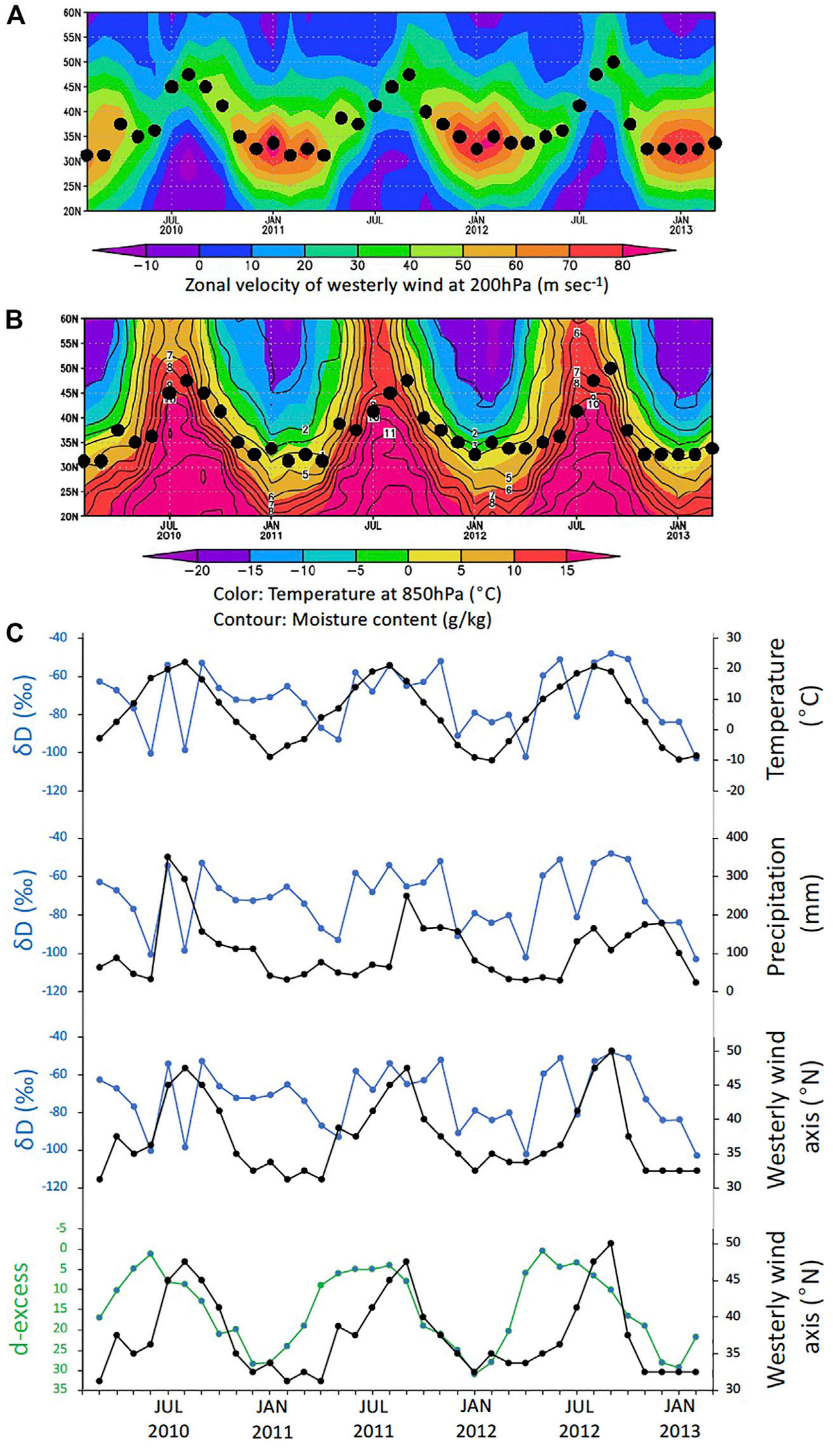

FIGURE 2 | (A) Zonal wind velocity at 200 hPa (positive westward) along 145°E, **(B)** Temperature and moisture content at 850 hPa along 145°E (Sakurai et al., 2021), **(C)** Precipitated water δD, d-excess, temperature and precipitation at the site of Teshio Town (2010–2013; Li et al., 2017) 80 km southeast of the study site, and the position of the westerly wind axis. Black solid dots indicate the positions of the westerly wind axis.

laminated with sections of relatively low to high organic matter concentrations. The upper 850 cm of the sediment column consists of homogeneous organic-rich clay.

An age–depth model of the RK12 core was established based on 57 accelerated mass spectrometry (AMS) radiocarbon dates (Müller et al., 2016), showing continued sedimentation beginning ~17 ka

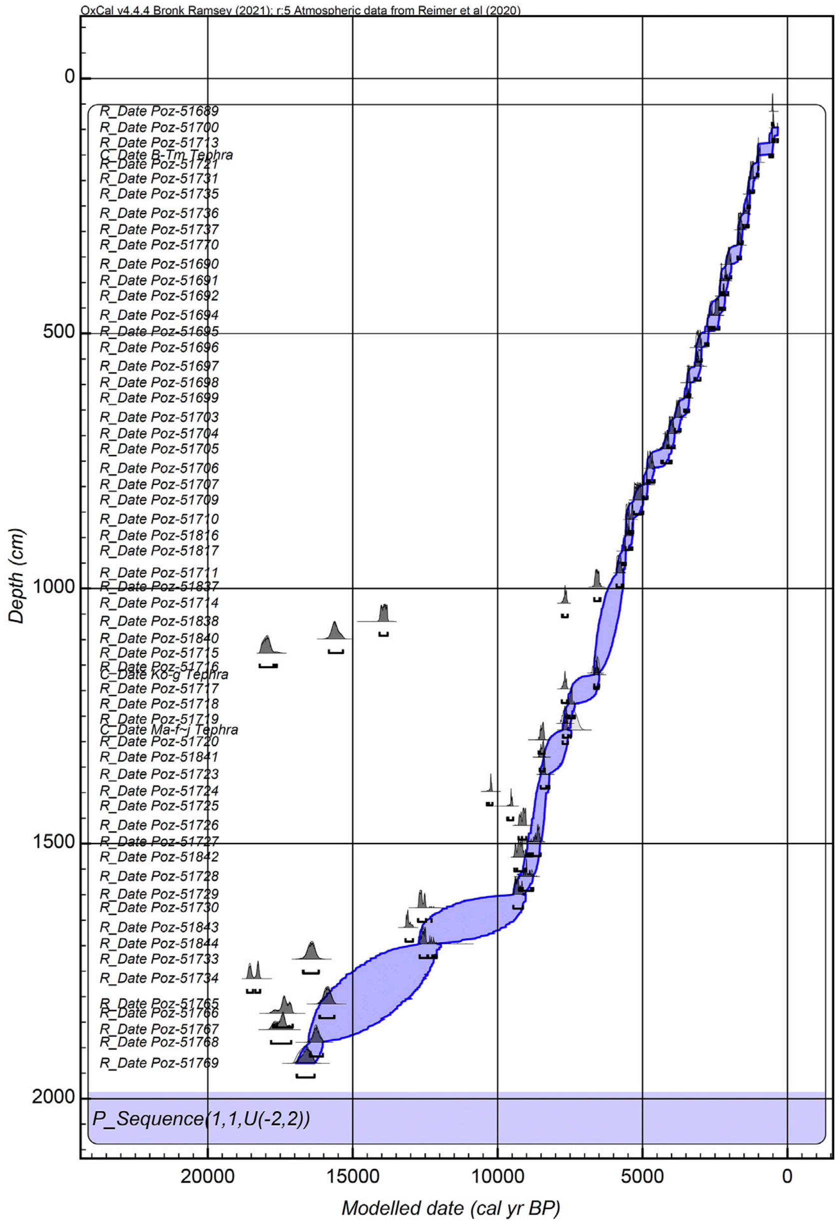

FIGURE 3 | Distribution of 57 calibrated AMS radiocarbon and three tephra dates used to construct Bayesian *P_sequence* depositional age–depth model for the RK12 sediment core from Lake Kushu (**Supplementary Table S1**).

(**Supplementary Table S1**). All available AMS dates were converted into calendar ages using Oxcal v4.4 (Bronk Ramsey, 2021) and the latest IntCal20 calibration curve (Reimer et al., 2020). The 95.4% probability ranges obtained in this study (**Supplementary Table S1**) show very minor differences from the data published in Müller et al. (2016), thus indicating general robustness of the published age model. For the current study, an updated Bayesian age model for the Kushu sequence has been constructed using Oxcal v4.4 (Bronk Ramsey, 2021) based on the 57 AMS ^{14}C dates (Müller et al., 2016) and three tephra ages using Oxcal v4.4 (Bronk Ramsey, 2021). The model utilizes a *P_Sequence* deposition model (Bronk Ramsey, 2008), with a variable *k* parameter (Bronk Ramsey and Lee, 2013) and a "General" *Outlier_Model* (Bronk Ramsey, 2009), applying the latest IntCal20 calibration curve (Reimer et al., 2020). The ^{14}C dates regarded as outliers (see Müller et al., 2016 and **Supplementary Table S1**) have been removed from the model. Three precise tephra ages have been incorporated into the model for providing additional chronological constraints, given the identification of these tephra layers in the RK12 sediment core of Lake Kushu (Chen et al., 2016; Chen et al., 2019). These include B-Tm tephra (composite core depth—150.5 cm; 1,004 cal yr BP; Oppenheimer et al., 2017), Ko-g tephra (core depth—1,169 cm; 95.4% probability range—6,651–6,446 cal yr BP; Chen et al., 2021) and Ma-f~j tephra (core depth—1,277 cm; 95.4% probability range—7,550–7,128 cal yr BP; Chen et al., 2021). The 95.4% Highest Probability Density (HPD) range for the deposition model is illustrated in **Figure 3**.

In the upper half of the core, representing the past ~6 ka, the linear sedimentation rate is very high (*i.e.*, about 1 cm every 6 years). In the bottom half of the core, the age–depth model shows greater variation in the sedimentation rates and substantially slower sedimentation (*i.e.*, about 1 cm every 20 years) before ~9.5 ka. Based on a multi-proxy approach (diatoms, aquatic pollen, algae, geochemistry), Schmidt et al. (2019) reconstructed three phases of lake basin development, including a marshy phase between 16.6 and 9.4 cal ka BP, a lagoon phase between 9.4 and 5.9 cal ka BP, and a freshwater lake phase after 5.9 cal ka BP, as the sand bar separating the Kushu lagoon from the sea formed.

Analytical Methods

Lipids were extracted (×3) from ~1 g of dried sediment using a Dionex ASE 200 Accelerated Solvent Extractor (Dionex, Sunnyvale, CA, United States) with dichloromethane:methanol (6:4). The extract was separated into neutral and acid fractions *via* aminopropyl silica gel column chromatography (Gao et al., 2015). The acid fraction was methylated with methanol:acetyl chloride (95:5) and purified with SiO_2 column chromatography.

The concentration of n-fatty acids in the acid fraction was analyzed using gas chromatography (GC) with an Agilent 6890 series gas chromatograph with on-column injection and electronic pressure control systems, and a flame ionization detector (Agilent, Santa Clara, CA, United States). Samples were dissolved in toluene. Helium was the carrier gas and the flow velocity was maintained at 30 cm/s. An Agilent J&W CP-Sil 5 CB column was used (length 50 m; i.d. 0.25 mm; thickness 0.25 μm). The oven temperature was programmed from 100 to 130°C at 20°C/min and from 130 to 310°C at 4°C/min, and then maintained at 310°C for 30 min. The average chain length (ACL) of n-fatty acids in this study is defined as:

$$\mathrm{ACL} = \frac{(26\mathrm{C}_{26} + 28\mathrm{C}_{28} + 30\mathrm{C}_{30} + 32\mathrm{C}_{32})}{(\mathrm{C}_{26}. + \mathrm{C}_{28} + \mathrm{C}_{30} + \mathrm{C}_{32})}.$$

The $\delta^{13}C$ (‰ Vienna Pee Dee Belemnite [VPDB]) of the methylated n-fatty acids in the acid fraction was analyzed using a Thermo Fisher Scientific (Waltham, MA, United States) GC IsoLink II with a capillary column coated with a TG-5MS column (30 m length; i.d. 0.25 mm; 0.25 μm film thickness) combined with a Delta V mass spectrometer through a combustion furnace at 1,000°C. The sample was dissolved in toluene. The oven temperature was programmed from 100 to 230°C at 30°C/min and from 230 to 310°C at 4°C/min and then maintained at 310°C for 15 min. As an internal isotopic standard, n-$C_{36}H_{74}$ was used to check the measurement conditions. Data were converted into values relative to VPDB using standard delta notation by comparison with CO_2 standard gas. The $\delta^{13}C$ values of fatty acids were obtained from the measured values of fatty acid–methyl esters by correcting for methyl carbon (−34.1‰). The reproducibility of the measurement based on repeated analyses was better than ±0.1‰.

The neutral fraction was separated into four fractions using SiO_2 column chromatography: F1, 3 ml hexane; F2, 3 ml hexane:toluene (3:1); F3, 4 ml toluene; and F4, 3 ml toluene:CH_3OH (3:1). An aliquot of F4 was dissolved in hexane-2-propanol (99:1), spiked with an internal standard (500 ng of C_{46} glycerol trialkyl glycerol tetraether [GTGT]; Patwardhan and Thompson, 1999), and filtered through a short bed of Na_2SO_4. GDGTs were analyzed using high-performance liquid chromatography-mass spectrometry (HPLC-MS) with an Agilent 1260 HPLC system coupled to an Agilent 6130 Series quadrupole mass spectrometer. Separation was achieved on two ultra-HPLC silica columns (ACQUITY BEH HILIC columns, 2.1 × 150 mm, 1.7 μm; Waters, Milford, MA, United States) in series, fitted with a 2.1 × 5 m pre-column of the same material (Waters) and maintained at 30°C. GDGTs were eluted isocratically for 25 min with 18% B, followed by a linear gradient to 35% B in 25 min, then a linear gradient to 100% B in 30 min, where A was hexane and B was hexane:isopropanol (9:1, v/v). The flow rate was 0.2 ml/min. The total run time was 90 min with a 20 min re-equilibration. Ionization was achieved using atmospheric pressure, positive ion chemical ionization-MS. The spectrometer was run in selected ion monitoring mode (m/z 743.8, 1,018, 1,020, 1,022, 1,032, 1,034, 1,036, 1,046, 1,048, 1,050, 1,292.3, 1,296.3, 1,298.3, 1,300.3, and 1,302.3). Compounds were identified by comparing mass spectra and retention times with those in the literature (Hopmans et al., 2000; De Jonge et al., 2014). Quantification was achieved by integrating the peak area in the $(M+H)^+$ chromatogram and comparing these with the peak area of an internal standard (C_{46} GTGT) in the $(M+H)^+$ chromatogram according to the method of Huguet et al. (2006). The correction value of ionization efficiency between GDGTs and the internal standard was obtained in our laboratory by comparing the peak areas of isolated crenarchaeol and branched GDGTs I and II (Schouten et al., 2013) and C_{46} GTGT in known amounts. In the routine analysis, a working standard that was a mixture of C_{46} GTGT and the GDGTs extracted and purified from East China Sea sediment was inserted every 20 samples to monitor ionization efficiency changes.

To estimate the terrestrial/*in-situ* production ratio of branched GDGTs, the weighted average number of cyclopentane moieties of tetramethylated branched GDGTs ($\#\mathrm{Rings}_{\mathrm{tetra}}$) was calculated (Sinninghe Damsté, 2016):

$$\#\mathrm{Rings}_{\mathrm{tetra}} = \frac{([\mathrm{Ib}] + 2[\mathrm{Ic}])}{([\mathrm{Ia}] + [\mathrm{Ib}] + [\mathrm{Ic}])}.$$

To estimate the mean annual temperature (MAT), the following parameters were calculated with the following equations based on a global soil dataset obtained using different calibration strategies (De Jonge et al., 2014):

$$\mathrm{MB}T'_{5\mathrm{ME}} = \frac{([\mathrm{Ia}] + [\mathrm{Ib}] + [\mathrm{Ic}])}{([\mathrm{Ia}] + [\mathrm{Ib}] + [\mathrm{Ic}] + [\mathrm{IIa}] + [\mathrm{IIb}] + [\mathrm{IIc}] + [\mathrm{IIIa}])},$$
$$\mathrm{MAT} = -8.57 + 31.45\,\mathrm{MB}T'_{5\mathrm{ME}}$$
$$(\mathrm{RMSE} = 4.8°\mathrm{C}) \tag{1}$$

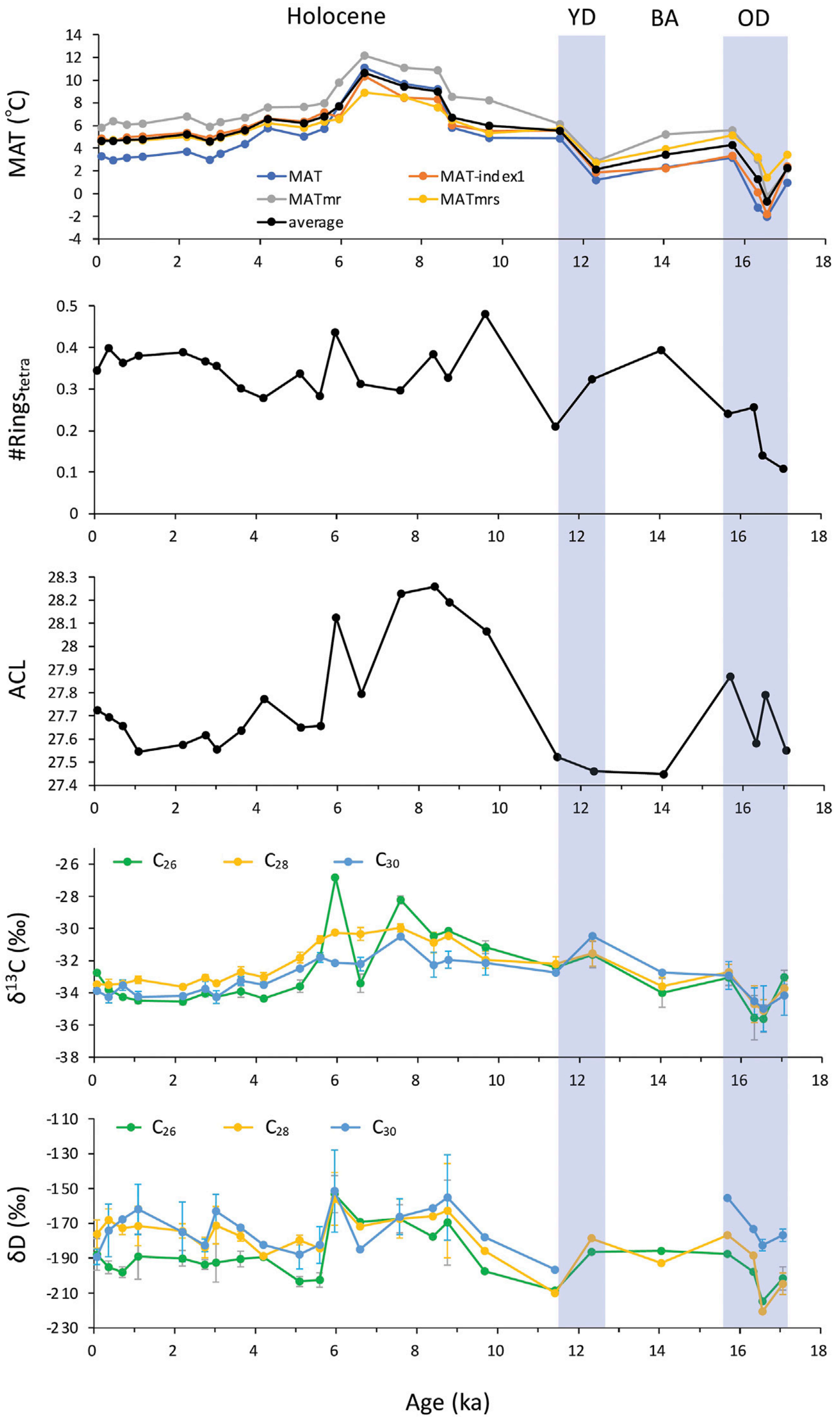

FIGURE 4 | Changes in the glycerol dialkyl glycerol tetraether (GDGT)-based mean annual temperatures (MATs) obtained using different calibrations (**Equations 1–4**), weighted average number of cyclopentane moieties of tetramethylated branched GDGTs (#Rings$_{tetra}$), average chain length (ACL), and δ^{13}C and δD of long-chain n-fatty acids in sediments from core RK12-2, Kushu Lake, Rebun Island, over the last 17 ka. The vertical bar of the sample value indicates 1σ. OD, Oldest Dryas period; BA, Bølling–Allerød period; and YD, Younger Dryas period.

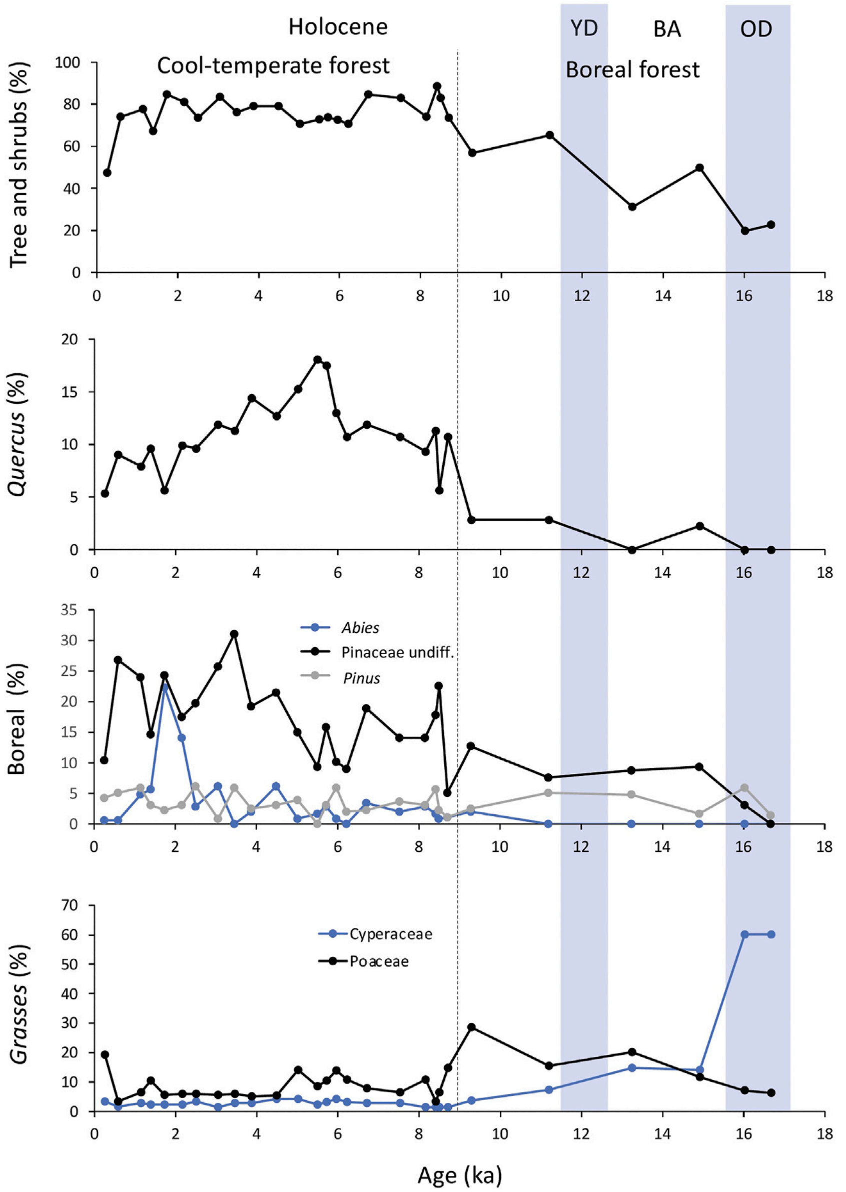

FIGURE 5 | Abundance of pollen in sediments from the RK12 core during the last 17 ka (Müller et al., 2016).

$$\text{Index 1} = \log\frac{([\text{Ia}] + [\text{Ib}] + [\text{Ic}] + [\text{IIa}'] + [\text{IIIa}'])}{([\text{Ic}] + [\text{IIa}] + [\text{IIc}] + [\text{IIIa}] + [\text{IIIa}'])},$$

$$\text{MAT} = 5.05 + 14.86\,\text{Index 1} \quad (2)$$

$$(\text{RMSE} = 4.7°\text{C})$$

$$\text{MATmr} = 7.71 + 17.1\,[\text{Ia}] + 25.9\,[\text{Ib}] + 34.4\,[\text{Ic}] - 28.6\,[\text{IIa}],\ \text{RMSE} = 4.6°\text{C}. \quad (3)$$

$$\text{MATmrs} = 5.58 + 17.91\,[\text{Ia}] - 18.77\,[\text{IIa}]\ (\text{RMSE} = 5.0°\text{C}) \quad (4)$$

where [Ia] to [IIIc′] are the GDGTs defined in De Jonge et al. (2014).

RESULTS AND DISCUSSION

GDGT-Based Temperature

The MAT reconstruction based on the four different calibrations yielded similar variation within the calibration error of 4.6–5.0°C (**Figure 4**). The average value of the reconstructed temperature varied between −0.7 and 10.6°C and was low at ~17 ka and high between 9 and 6 ka (**Figure 4**). The core-top temperature (3.3–5.8°C) was consistent with the current mean annual air temperature ~83 km southeast of the study site (6.4°C at Teshio; Japan Meteorological Agency, https://weather.time-j.net/Stations/JP/teshio) within the calibration error. Because branched GDGTs are produced in both terrestrial and lacustrine environments (*e.g.*, Schouten et al., 2012), the reconstructed temperature may reflect both terrestrial and lake water temperatures. The $\#Rings_{tetra}$ index varied between 0.1 and 0.5, but was mainly 0.3–0.4 after 16 ka (**Figure 4**), corresponding to the range of dominant terrestrial branched GDGTs (Sinninghe Damsté, 2016). This indicated that the branched GDGTs were mainly of terrestrial soil origin, with a small lacustrine contribution after 16 ka. We assume that the GDGT-derived MAT reflects the terrestrial air temperature rather than the lake water temperature. The record shows a colder climate in the Late Glacial and a warmer climate in the early Middle Holocene (**Figure 4**).

The pollen assemblage in sediments from the RK12 core was described and the paleovegetation discussed in Müller et al. (2016) and Leipe et al. (2018) is as follows. From 16 to 11 ka, the vegetation shifted from herbaceous (predominantly Cyperaceae) to trees and shrubs (*Pinaceae*, *Alnus*, and *Betula*) (**Figure 5**). The spread of woody vegetation was interrupted during the Younger Dryas period, although the reversal was not prominent. In the Middle Holocene between 8 and 4 ka, there was a major spread of deciduous *Quercus* trees, with the highest percentages of *Quercus* pollen (17–27%) between 6 and 5 ka (**Figure 5**) (Müller et al., 2016; Leipe et al., 2018). This is in line with a major spread of cool mixed and cool conifer forests in the Hokkaido Region (Igarashi, 2013). The Late Holocene section of the RK12 record showed the highest percentages of *Abies* and Pinaceae pollen by ~2 ka (**Figure 5**), suggesting an increase in coniferous tree cover in the regional forest vegetation. This pollen record in Lake Kushu is consistent with the result of our MAT reconstruction. The culmination of *Quercus* pollen was delayed behind the MAT maximum by ~1 ka, presumably reflecting the time required for vegetation transition.

Distribution of n-Fatty Acids

All of the samples showed a bimodal homologous distribution of n-fatty acids with maxima at C_{16} and C_{26} or C_{28}. The n-fatty acids around C_{16} are ubiquitous in eukaryotes and bacteria, while the long-chain n-fatty acids ($>C_{26}$) are derived from vascular plants (Eglinton and Hamilton, 1967). The long-chain n-fatty acids ($>C_{26}$) were more abundant than the shorter homologs. The even carbon number preference ranged from 5 to 18, typical fresh leaf wax.

The ACL varied between 27.5 and 28.2 and was higher in the period between 10 and 6 ka than in other periods (**Figure 4**). In modern plants, the ACL of plant leaf wax (long-chain n-alkanes) is higher in warmer climates (Tipple and Pagani, 2013). It is also sensitive to relative humidity, but the response is opposite in different species (Hoffmann et al., 2013). The ACL is higher in grasses than trees in the temperate climate zone (Bush McInerney, 2013). The abundance variation in Poaceae and Cyperaceae pollen was not consistent with the ACL (**Figure 5**; Müller et al., 2016), suggesting that the higher ACL between 10 and 6 ka does not reflect grass abundance and aridity but rather a warm climate, as indicated by the GDGT indices.

Relatively high ACL was also found in the Oldest Dryas period (**Figure 4**). The pollen record indicated that Cyperaceae pollen was abundant in this period (**Figure 5**; Müller et al., 2016), suggesting that the high ACL reflected an abundance of sedge.

Leaf Wax $\delta^{13}C$

The $\delta^{13}C$ of long-chain (C_{26}, C_{28}, and C_{30}) n-fatty acids varied between −35.6 and −26.8‰ (**Figure 4**). The values were higher in the period between 9 and 5 ka (**Figure 4**). The $\delta^{13}C$ of long-chain n-fatty acids of C_3 and C_4 plants sampled in the early 2000s (CO_2 concentration ~370 ppm) averaged −37.1 ± 2.0‰ ($n = 13$) and −19.5 ± 1.8‰ ($n = 9$), respectively (Chikaraishi et al., 2004). However, these end-member values have varied in the past. Contemporary $\delta^{13}C$ values for both C_3 and C_4 plants have been affected by the Suess effect (decreasing by ~2‰ over the past 250 years; Keeling et al., 2017). The $\delta^{13}C$ values of C_3 plants have been reduced further by increasing isotopic fractionation, which is governed by the atmospheric CO_2 concentration (Schubert and Jahren, 2015). Considering these effects, the calculated fatty acid $\delta^{13}C$ of C_3 plants at a CO_2 of 280 ppm is −33.7‰. In comparison, the $\delta^{13}C$ value for C_4 plants is independent of the atmospheric CO_2 concentration. The fatty acid $\delta^{13}C$ of C_4 plants before 1750 CE was −17.5‰. The $\delta^{13}C$ of long-chain n-fatty acids in the study samples varied around the end-member values of C_3 plants. If the variation in $\delta^{13}C$ reflected the mixing ratio of C_3 and C_4 plants, the higher $\delta^{13}C$ between 10 and 5 ka would indicate the contribution of C_4 plants. However, the pollen record from the study core did not show evidence of a greater contribution of C_4 plants in this period, suggesting that another factor was responsible for the reconstructed shift in the $\delta^{13}C$ values.

The $\delta^{13}C$ of C_3 plants is affected by photosynthetic activity (Farquhar and Richards, 1984; Evans et al., 1986), where greater activity induces higher $\delta^{13}C$. In the RK12 core, higher $\delta^{13}C$ appeared in a warm period (**Figure 4**). Therefore, we postulate that a warm climate enhanced C_3 plant photosynthesis, which increased $\delta^{13}C$.

Leaf Wax δD

The δD of long-chain (C_{26}, C_{28}, and C_{30}) n-fatty acids varied between −220.6 and −151.5‰ (**Figure 4**). The δD was lower at ~17, 11, and 5 ka and higher at 9–6 ka (**Figure 4**). The variation in δD was similar to that in the GDGT-based MATs (**Figure 4**). Dansgaard (1964) and Jouzel et al. (1994) showed that the $\delta^{18}O$ of global precipitation is related to the MAT. Jouzel et al. (1994) also found that areas with a MAT below 15°C had a linear relationship between MAT and the mean annual $\delta^{18}O$ of precipitation ($\delta^{18}O = 0.64\ MAT—12.8$). This is equivalent to the formula $\delta D = 5.12\ MAT—92.4$. The MAT at the study site is 6.4°C (1981–2010; Japan Meteorological Agency, https://weather.time-j.net/Stations/JP/teshio) and the mean annual δD at Teshio 80 km southeast of the sampling site is −69.6‰ (2010–2014; Li et al., 2017). These values are consistent with the relationship described above.

The maximum range of long-chain fatty acid δD variation was 69.1‰ (**Figure 4**). If this variation was caused only by a process following the above MAT–δD relationship, a 69.1‰ variation in δD would correspond to a 13.5°C variation in MAT. Our MAT estimates based on the GDGT compositions indicated that the temperature variation over the last 17 ka was 11.3°C. Summer SST records from the northern Japan margin over the past 17 ka show a variation of ~8°C (Site PC-6 in Minoshima et al., 2007; Site

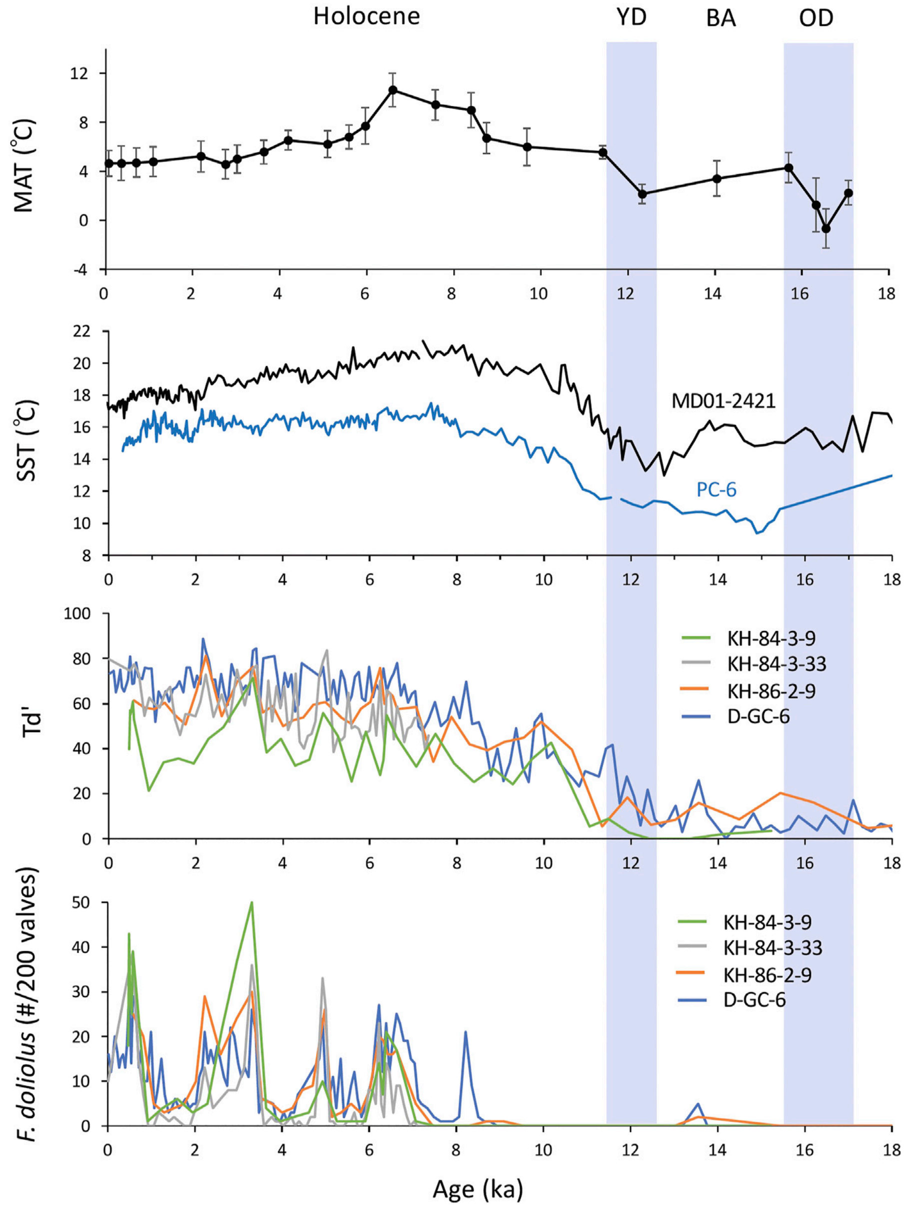

FIGURE 6 | Changes in the glycerol dialkyl glycerol tetraether-based mean annual temperatures (MATs) obtained using different calibrations (averages and 1σ range), $U^{K'}_{37}$-based sea surface temperature (SST) at sites MD01-2421 (Yamamoto et al., 2004; Yamamoto et al., 2005; Isono et al., 2009; Yamamoto, 2009) and PC-6 (Minoshima et al., 2007) in the Kuroshio–Oyashio transition zone, temperature index of diatoms (Td') and relative abundance of *Fragilariopsis doliola*, and Tsushima Warm Current species in cores KH-84-3-9, KH-84-3-33, KH-86-2-9, and D-GC-6 (Koizumi et al., 2006) over the last 17 ka.

GH02-1030 in Inagaki et al., 2009). This implies that the temperature effect explains a large part of the variation observed in C_{26} and C_{28} fatty acid δD.

Two other potential factors control long-chain fatty acid δD *via* the mean annual δD of precipitation. The first factor is the seasonal variation in the δD of precipitation. Water precipitated in autumn has ~30‰ higher δD values than that precipitated in winter and spring (**Figure 2**) (Li et al., 2017). Thus, a large amount of autumn precipitation or a lower amount of winter and spring precipitation would shift the mean annual δD values in a positive direction.

The position of the westerly wind axis is the second factor controlling long-chain fatty acid δD *via* the mean annual δD of precipitation (Li et al., 2017). Precipitation occurs in Hokkaido when a low-pressure system migrates from west to east along with the westerly jet. The δD values of precipitated water were 24–32‰ higher when the migration path of the low-pressure system was located to the north of the study location relative to times when the migration path was located to the south (Li et al., 2017). When the westerly jet is located north of the study site, southerly winds bring moisture from the south, inducing more precipitation at the study site (**Figure 2**). Thus, a

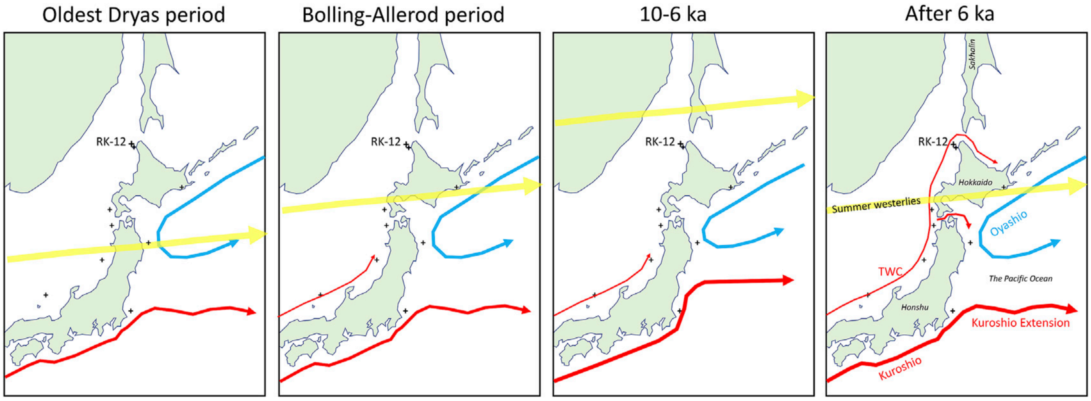

FIGURE 7 | Schematic maps show the postulated positions of the summer westerly jet, the Kuroshio Extension (Yamamoto, 2009) and the Tsushima Warm Current (TWC; Koizumi et al., 2006) in different climate regimes.

northward shift in the position of the westerly jet increases the δD of precipitated water, and the associated higher fraction of summer-to-annual precipitation further increases the δD. These results suggest that the position of the westerly jet controls the amount of precipitation, as well as the δD of precipitated water over a long timescale. Higher long-chain fatty acid δD reflects a northerly position of the summer westerly jet and the resultant increase in summer and autumn precipitation.

One may speculate that the strengthening of the TWC increased winter precipitation and decreased the fatty acid δD from the Middle to Late Holocene because, in winter, the East Asian winter monsoon influences all of Hokkaido and brings heavy snowfall to mountainous areas. Plants might partly use the water supplied by winter precipitation. Even if winter precipitation was higher, the δD should be lower. However, the precipitation from January to April is only one third that from June to October at present (Japan Meteorological Agency, https://weather.time-j.net/Stations/JP/teshio). If winter precipitation was lower in the Middle Holocene than in the Late Holocene, the effect on the δD of annual precipitation should be small. Therefore, this case can likely be neglected on a millennial timescale.

Evapotranspiration induces the enrichment of deuterium in the plant body water. The evapotranspiration rate depends on the relative humidity. When the relative humidity is low, evapotranspiration is expected to be more active, resulting in higher leaf wax δD. However, the low abundance of Poaceae and Cyperaceae pollen does not indicate a dry environment during 9–6 ka (**Figure 5**; Müller et al., 2016) and was not consistent with the high δD during 9–6 ka, suggesting that the higher high δD does not reflect a dry environment.

The above discussion summarizes that the leaf wax δD at the study site reflects the global distribution of precipitated water δD and temperature. The latitudinal gradient of precipitated water δD is enhanced north and south of the westerly jet (Li et al., 2017). We thus conclude that the higher leaf wax δD during 9–6 ka likely reflected a warmer climate and the northern position of the westerlies.

Factors Controlling Summer Climate in Northern Japan Over the Past 17 ka

The Hokkaido region is located at the mean position of the modern summer westerly jet (**Figure 1**) and at the northern margin of the East Asian summer monsoon, which brings a warm, moist air mass from the Pacific Ocean to this area. When the westerly jet is located in the north, the southerly winds (*i.e.*, the East Asian summer monsoon) reach Hokkaido, resulting in a warm, wet climate (Nitta, 1987; Kawamura et al., 1998).

The GDGT-based MATs, the ACL, and the δ^{13}C and δD of long-chain n-fatty acids indicated that climate was cold in the Oldest Dryas period and warm during 10–6 ka (**Figure 4**). This climate change is consistent with the SST changes in the KOT (**Figure 6**) (Site PC-6 in Minoshima et al. (2007); Site MD01-2421 in Yamamoto et al. (2004), Yamamoto et al. (2005), Isono et al. (2009), Yamamoto, (2009)). The summer position of the westerly wind axis in the study region is related to the strength of the North Pacific High (Nitta, 1987; Kawamura et al., 1998), with a stronger (weaker) North Pacific High shifting the westerly wind axis northward (southward) (**Figure 7**). The development of the North Pacific High drives the oceanic subtropical gyre circulation in the North Pacific. The Pacific SST in the KOT is a good indicator of the strength of the Kuroshio and its extension, which form part of the subtropical gyre circulation. Thus, the correspondence between the climate of Rebun Island and the SST in the KOT suggests that the summer position of the westerly wind axis is linked to the oceanic subtropical gyre circulation in the North Pacific via regional atmospheric dynamics in the northwestern Pacific region. The postglacial climate of Rebun Island reflects changes in the atmospheric conditions, *i.e.*, the northward-shifted position of the westerly jet, stronger influence of the

East Asian summer monsoon, and development of the North Pacific High, and *vice versa* (Sakurai et al., 2021).

However, the climate change during the Holocene is not consistent with changes in the TWC in the Sea of Japan indicated by the temperature index of diatoms [Td' = warm/(warm + cold) water diatom species] or the abundance of *Fragilariopsis doliola*, a marker diatom species of the TWC, in core D-GC-6 from the southern Sea of Japan (**Figure 6**) (Koizumi et al., 2006). On Rishiri Island, 40 km south of Rebun Island, cellulose $\delta^{18}O$ in peat cores from site MHWL showed that the influence of the TWC on the $\delta^{18}O$ of precipitated water appeared after 2.8–1.3 ka (Yamamoto and Seki, unpublished data). However, the relationship between the fatty acid δD and the strength of the TWC on a millennial timescale during the Holocene is not clear.

The above considerations imply that the climate of northern Japan was controlled mainly by changes in the development of the North Pacific High *via* changes in the position of the westerly jet and the East Asian summer monsoon rainfall, while the influence of the TWC was limited on a millennial timescale.

CONCLUSION

The GDGT-based MAT, ACL, $\delta^{13}C$ and δD of long-chain n-fatty acids indicated that the climate in northern Japan was cold in the Oldest Dryas period and warm during 9–6 ka. This climate change is consistent with the SST in the KOT, but inconsistent with changes in the TWC in the Sea of Japan. The results imply that the climate of northern Japan was controlled mainly by changes in the development of the North Pacific High *via* changes in the position of the westerly jet and the East Asian summer monsoon rainfall, whereas the influence of the TWC was limited on a millennial timescale.

DATA AVAILABILITY STATEMENT

The original contributions presented in the study are included in the article/**Supplementary Material**, further inquiries can be directed to the corresponding author.

AUTHOR CONTRIBUTIONS

MY conceived the research idea, contributed biomarker data and prepared the manuscript. FW and KS contributed biomarker data. KY and TH conducted the field work. KG, HY and PT managed the drilling project. PT and HYC updated the age model. All authors discussed the data and improved the manuscript.

FUNDING

This study was supported by the Japan Society for the Promotion of Science (25610146, JPMXS05R2900001, and 19H05595 to MY and 26101002, 21101002 to HY).

ACKNOWLEDGMENTS

We also thank Dokon Co. Ltd., Taku Ajioka, Ke Wang, Yoshie Nakai, Eriko Noma, and Keiko Ohnishi for help in the sampling, core description, and subsampling, and Stefanie Müller for discussion.

SUPPLEMENTARY MATERIAL

The Supplementary Material for this article can be found online at: https://www.frontiersin.org/articles/10.3389/feart.2021.704332/full#supplementary-material

REFERENCES

Bronk Ramsey, B. (2008). Deposition Models for Chronological Records. *Quat. Sci. Rev.* 27 (1–2), 42–60. doi:10.1016/j.quascirev.2007.01.019

Bronk Ramsey, C. (2009). Dealing With Outliers and Offsets in Radiocarbon Dating. *Radiocarbon* 51 (3), 1023–1045. doi:10.1017/s0033822200034093

Bronk Ramsey, C. (2021). OxCal 4.4. Available at: http://c14.arch.ox.ac.uk/oxcal (Accessed May 20, 2021).

Bronk Ramsey, C., and Lee, S. (2013). Recent and Planned Developments of the Program OxCal. *Radiocarbon* 55 (2), 720–730. doi:10.1017/s0033822200057878

Bush, R. T., and McInerney, F. A. (2013). Leaf Wax n-Alkane Distributions in and Across Modern Plants: Implications for Paleoecology and Chemotaxonomy. *Geochim. Cosmochim. Acta* 117, 161–179. doi:10.1016/j.gca.2013.04.016

Chen, X.-Y., Blockley, S. P. E., Staff, R. A., Xu, Y.-G., and Menzies, M. A. (2021). Improved Age Estimates for Holocene Ko-g and Ma-f~j Tephras in Northern Japan Using Bayesian Statistical Modelling. *Quat. Geochronol.* [Epub ahead of print].

Chen, X.-Y., Blockley, S. P. E., Tarasov, P. E., Xu, Y.-G., McLean, D., Tomlinson, E. L., et al. (2016). Clarifying the Distal to Proximal Tephrochronology of the Millennium (B-Tm) Eruption, Changbaishan Volcano, Northeast China. *Quat. Geochronol.* 33, 61–75. doi:10.1016/j.quageo.2016.02.003

Chen, X.-Y., McLean, D., Blockley, S. P. E., Tarasov, P. E., Xu, Y.-G., and Menzies, M. A. (2019). Developing a Holocene Tephrostratigraphy for Northern Japan Using the Sedimentary Record From Lake Kushu, Rebun Island. *Quat. Sci. Rev.* 215, 272–292. doi:10.1016/j.quascirev.2019.05.017

Chikaraishi, Y., Naraoka, H., and Poulson, S. R. (2004). Hydrogen and Carbon Isotopic Fractionations of Lipid Biosynthesis Among Terrestrial (C3, C4 and CAM) and Aquatic Plants. *Phytochemistry* 65, 1369–1381. doi:10.1016/j.phytochem.2004.03.036

Dansgaard, W. (1964). Stable Isotopes in Precipitation. *Tellus* 16, 436–468. doi:10.3402/tellusa.v16i4.8993

De Jonge, C., Hopmans, E. C., Zell, C. I., Kim, J.-H., Schouten, S., and Sinninghe Damsté, J. S. (2014). Occurrence and Abundance of 6-Methyl Branched Glycerol Dialkyl Glycerol Tetraethers in Soils: Implications for Palaeoclimate Reconstruction. *Geochim. Cosmochim. Acta* 141, 97–112. doi:10.1016/j.gca.2014.06.013

Eglinton, G., and Hamilton, R. J. (1967). Leaf Epicuticular Waxes. *Science* 156, 1322–1335. doi:10.1126/science.156.3780.1322

Evans, J., Sharkey, T., Berry, J., and Farquhar, G. (1986). Carbon Isotope Discrimination Measured Concurrently With Gas Exchange to Investigate CO2 Diffusion in Leaves of Higher Plants. *Funct. Plant Biol.* 13, 281–292. doi:10.1071/pp9860281

Farquhar, G., and Richards, R. (1984). Isotopic Composition of Plant Carbon Correlates With Water-Use Efficiency of Wheat Genotypes. *Funct. Plant Biol.* 11, 539–552. doi:10.1071/pp9840539

Gao, L., Guimond, J., Thomas, E., and Huang, Y. (2015). Major Trends in Leaf Wax Abundance, δ2H and δ13C Values Along Leaf Venation in Five Species of C3

Plants: Physiological and Geochemical Implications. *Org. Geochem.* 78, 144–152. doi:10.1016/j.orggeochem.2014.11.005

Hoffmann, B., Kahmen, A., Cernusak, L. A., Arndt, S. K., and Sachse, D. (2013). Abundance and Distribution of Leaf Wax n-Alkanes in Leaves of Acacia and Eucalyptus Trees Along a Strong Humidity Gradient in Northern Australia. *Org. Geochem.* 62, 62–67. doi:10.1016/j.orggeochem.2013.07.003

Hopmans, E. C., Schouten, S., Pancost, R. D., van der Meer, M. T. J., and Sinninghe Damsté, J. S. (2000). Analysis of Intact Tetraether Lipids in Archaeal Cell Material and Sediments by High Performance Liquid Chromatography/atmospheric Pressure Chemical Ionization Mass Spectrometry. *Rapid Commun. Mass Spectrom.* 14, 585–589. doi:10.1002/(sici)1097-0231(20000415)14:7<585::aid-rcm913>3.0.co;2-n

Huguet, C., Hopmans, E. C., Febo-Ayala, W., Thompson, D. H., Sinninghe Damsté, J. S., and Schouten, S. (2006). An Improved Method to Determine the Absolute Abundance of Glycerol Dibiphytanyl Glycerol Tetraether Lipids. *Org. Geochem.* 37, 1036–1041. doi:10.1016/j.orggeochem.2006.05.008

Igarashi, Y. (2013). Holocene Vegetation and Climate on Hokkaido Island, Northern Japan. *Quat. Int.* 290-291, 139–150.

Inagaki, M., Yamamoto, M., Igarashi, Y., and Ikehara, K. (2009). Biomarker Records From Core GH02-1030 Off Tokachi in the Northwestern Pacific Over the Last 23,000 Years: Environmental Changes during the Last Deglaciation. *J. Oceanogr.* 65, 847–858. doi:10.1007/s10872-009-0070-4

Isono, D., Yamamoto, M., Irino, T., Oba, T., Murayama, M., Nakamura, T., et al. (2009). The 1500-year Climate Oscillation in the Midlatitude North Pacific During the Holocene. *Geology* 37, 591–594. doi:10.1130/g25667a.1

Jouzel, J., Koster, R. D., Suozzo, R. J., and Russell, G. L. (1994). Stable Water Isotope Behavior during the Last Glacial Maximum: A General Circulation Model Analysis. *J. Geophys. Res.* 99 (D12), 25791–25801. doi:10.1029/94jd01819

Kawamura, R., Sugi, M., Kayahara, T., and Sato, N. (1998). Recent Extraordinary Cool and Hot Summers in East Asia Simulated by an Ensemble Climate Experiment. *J. Meteorol. Soc. Japan* 76, 597–617. doi:10.2151/jmsj1965.76.4_597

Keeling, R. F., Graven, H. D., Welp, L. R., Resplandy, L., Bi, J., Piper, S. C., et al. (2017). Atmospheric Evidence for a Global Secular Increase in Carbon Isotopic Discrimination of Land Photosynthesis. *Proc. Natl. Acad. Sci. U.S.A.* 114, 10361–10366. doi:10.1073/pnas.1619240114

Koizumi, I., Tada, R., Narita, H., Irino, T., Aramaki, T., Oba, T., et al. (2006). Paleoceanographic History Around the Tsugaru Strait Between the Japan Sea and the Northwest Pacific Ocean since 30 cal kyr BP. *Palaeogeogr. Palaeoclimatol. Palaeoecol.* 232, 36–52. doi:10.1016/j.palaeo.2005.09.003

Leipe, C., Müller, S., Hille, K., Kato, H., Kobe, F., Schmidt, M., et al. (2018). Vegetation Change and Human Impacts on Rebun Island (Northwest Pacific) over the Last 6000 Years. *Quat. Sci. Rev.* 193, 129–144. doi:10.1016/j.quascirev.2018.06.011

Li, X., Sugimoto, A., and Ueta, A. (2017). Spatial and Temporal Variations of Stable Isotopes in Precipitation in Midlatitude Coastal Regions. *Hydrol. Process.* 31, 3029–3044. doi:10.1002/hyp.11222

Minoshima, K., Kawahata, H., and Ikehara, K. (2007). Changes in Biological Production in the Mixed Water Region (MWR) of the Northwestern North Pacific during the Last 27 Kyr. *Palaeogeogr. Palaeoclimatol. Palaeoecol.* 254, 430–447. doi:10.1016/j.palaeo.2007.06.022

Müller, S., Schmidt, M., Kossler, A., Leipe, C., Irino, T., Yamamoto, M., et al. (2016). Palaeobotanical Records From Rebun Island and Their Potential for Improving the Chronological Control and Understanding Human-Environment Interactions in the Hokkaido Region, Japan. *The Holocene* 26, 1646–1660. doi:10.1177/0959683616641738

Nitta, T. (1987). Convective Activities in the Tropical Western Pacific and Their Impact on the Northern Hemisphere Summer Circulation. *J. Meteorol. Soc. Japan* 65, 373–390. doi:10.2151/jmsj1965.65.3_373

Oppenheimer, C., Wacker, L., Xu, J., Galván, J. D., Stoffel, M., Guillet, S., et al. (2017). Multi-proxy Dating the 'Millennium Eruption' of Changbaishan to Late 946 CE. *Quat. Sci. Rev.* 158, 164–171. doi:10.1016/j.quascirev.2016.12.024

Patwardhan, A. P., and Thompson, D. H. (1999). Efficient Synthesis of 40- and 48-membered Tetraether Macrocyclic Bisphosphocholines. *Org. Lett.* 1, 241–244. doi:10.1021/ol990567o

Reimer, P. J., Austin, W. E. N., Bard, E., Bayliss, A., Blackwell, P. G., Bronk Ramsey, C., et al. (2020). The IntCal20 Northern Hemisphere Radiocarbon Age Calibration Curve 0–55 CAL kBP). *Radiocarbon* 62, 725–757.

Sakurai, H., Yamamoto, M., Seki, O., Omori, T., and Sato, T. (2021). Cellulose Oxygen Isotopes of *Sphagnum* and Vascular Plants in a Peat Core Reveal Climate Change in Northern Japan over the Past 2,000 Years. *Geochem. Geophys. Geosyst.* [Epub ahead of print].

Schmidt, M., Leipe, C., Becker, F., Goslar, T., Hoelzmann, P., Mingram, J., et al. (2019). A Multi-Proxy Palaeolimnological Record of the Last 16,600 Years from Coastal Lake Kushu in Northern Japan. *Palaeogeogr. Palaeoclimatol. Palaeoecol.* 514, 613–626. doi:10.1016/j.palaeo.2018.11.010

Schouten, S., Hopmans, E. C., Rosell-Melé, A., Pearson, A., Adam, P., Bauersachs, T., et al. (2013). An Interlaboratory Study of TEX86and BIT Analysis of Sediments, Extracts, and Standard Mixtures. *Geochem. Geophys. Geosyst.* 14, 5263–5285. doi:10.1002/2013gc004904

Schouten, S., Hopmans, E. C., and Sinninghe Damsté, J. S. (2012). The Organic Geochemistry of Glycerol Dialkyl Glycerol Tetraether Lipids: A Review. *Org. Geochem.* 54, 19–61. doi:10.1016/j.orggeochem.2012.09.006

Schubert, B. A., and Jahren, A. H. (2015). Global Increase in Plant Carbon Isotope Fractionation Following the Last Glacial Maximum Caused by Increase in Atmospheric pCO2. *Geology* 43, 435–438. doi:10.1130/g36467.1

Sinninghe Damsté, J. S. (2016). Spatial Heterogeneity of Sources of Branched Tetraethers in Shelf Systems: The Geochemistry of Tetraethers in the Berau River delta (Kalimantan, Indonesia). *Geochim. Cosmochim. Acta* 186, 13–31. doi:10.1016/j.gca.2016.04.033

Sugimoto, A., Higuchi, K., and Kusakabe, M. (1988). Relationship between δD and δ18O Values of Falling Snow Particles from a Separate Cloud. *Tellus* 40B, 205–213. doi:10.1111/j.1600-0889.1988.tb00290.x

Tipple, B. J., and Pagani, M. (2013). Environmental Control on Eastern Broadleaf forest Species' Leaf Wax Distributions and D/H Ratios. *Geochim. Cosmochim. Acta* 111, 64–77. doi:10.1016/j.gca.2012.10.042

Yamamoto, M., Oba, T., Shimamune, J., and Ueshima, T. (2004). Orbital-Scale Anti-Phase Variation of Sea Surface Temperature in Mid-Latitude North Pacific Margins During the Last 145,000 Years. *Geophys. Res. Lett.* 31, L16311. doi:10.1029/2004gl020138

Yamamoto, M. (2009). Response of Mid-Latitude North Pacific Surface Temperatures to Orbital Forcing and Linkage to the East Asian Summer Monsoon and Tropical Ocean-Atmosphere Interactions. *J. Quat. Sci.* 24, 836–847. doi:10.1002/jqs.1255

Yamamoto, M., Suemune, R., and Oba, T. (2005). Equatorward Shift of the Subarctic Boundary in the Northwestern Pacific During the Last Deglaciation. *Geophys. Res. Lett.* 32, L05609. doi:10.1029/2004gl021903

Conflict of Interest: The authors declare that the research was conducted in the absence of any commercial or financial relationships that could be construed as a potential conflict of interest.

frontiers in Earth Science

ORIGINAL RESEARCH
published: 07 July 2021
doi: 10.3389/feart.2021.710797

Orbital and Millennial Variations in Sea Ice in the Southwestern Okhotsk Sea Since the Last Interglacial Period and Their Implications

Anqi Wang[1], Zhengquan Yao[1,2], Xuefa Shi[1,2]*, Kunshan Wang[1,2], Jianjun Zou[1,2], Yanguang Liu[1,2], Yonghua Wu[1,2] and Sergey A. Gorbarenko[3]*

[1]Key Laboratory of Marine Geology and Metallogeny, First Institute of Oceanography, Ministry of Natural Resources, Qingdao, China, [2]Laboratory for Marine Geology, Pilot National Laboratory for Marine Science and Technology, Qingdao, China, [3]V.I. Il'ichev Pacific Oceanological Institute, Far East Branch of Russian Academy of Science, (FEB of RAS), Vladivostok, Russia

OPEN ACCESS

Edited by:
Min-Te Chen,
National Taiwan Ocean University, Taiwan

Reviewed by:
Fengming Chang,
Institute of Oceanology (CAS), China
Jianguo Liu,
South China Sea Institute of Oceanology (CAS), China

***Correspondence:**
Zhengquan Yao
yaozq@fio.org.cn
Xuefa Shi
xfshi@fio.org.cn

Specialty section:
This article was submitted to Quaternary Science, Geomorphology and Paleoenvironment, a section of the journal Frontiers in Earth Science

Received: *17 May 2021*
Accepted: *24 June 2021*
Published: *07 July 2021*

Citation:
Wang A, Yao Z, Shi X, Wang K, Zou J, Liu Y, Wu Y and Gorbarenko SA (2021) Orbital and Millennial Variations in Sea Ice in the Southwestern Okhotsk Sea Since the Last Interglacial Period and Their Implications.
Front. Earth Sci. 9:710797.
doi: 10.3389/feart.2021.710797

Sea ice in the Okhotsk Sea plays a significant role in global climate change. However, the history and mechanism of changes in sea ice spanning the last glacial cycle remain controversial. In this study, an 8.8 m core (LV55-40-1) was recovered from the southwestern Okhotsk Sea that contains a continuous sea ice record over the past ~110 kyr. The sand fraction and dropstones were used as ice-rafted debris proxies to reconstruct the history of sea ice variations over the last ~110 kyr and to determine the underlying causes on orbital and millennial timescales. Sea ice expansions occurred during MIS 5b, MIS 4, mid-MIS 3, and early MIS 1, which were controlled mainly by decreased autumn insolation on an orbital timescale. Superimposed on the orbital-scale changes, millennial-scale variations in sea ice were also observed, with 19 expansion events that coincided with cold Dansgaard-Oeschger stadials. Millennial scale sea ice variations were most likely controlled by both the Arctic oscillation and the East Asian summer monsoon. During periods of negative Arctic oscillation patterns, decreased air temperatures over the Okhotsk Sea caused more active sea ice formation. Such conditions could have been reinforced, by a reduced influence of warm advection at the surface of the Okhotsk Sea caused by decreased discharge from the Amur River that resulted from a weakened East Asian summer monsoon during cold stadials.

Keywords: sea ice, ice-rafted debris, orbital scale, millennial scale, the Okhotsk Sea, the Amur River

INTRODUCTION

Sea ice is widespread in the subarctic North Pacific, and its expansion and retreat impact local and global climate changes by modulating the sea ice-induced albedo and energy budgets at both high and low latitudes (Turner et al., 2015; Serreze et al., 2016). Variations in sea ice influence the primary productivity in the Okhotsk Sea (Seki et al., 2004; Iwasaki et al., 2012; Jimenez-Espejo et al., 2018), as well as global ocean circulation and ventilation (Itaki, 2004). Consequently, sea ice variations on geologic timescales have played a significant role in paleoclimatic changes (Harada et al., 2012).

The Okhotsk Sea is located at the southernmost boundary of the region influenced by sea ice, and approximately two-thirds of the sea are covered by sea ice during the winter (Sakamoto et al., 2006). Therefore, sea ice coverage in the Okhotsk Sea is very sensitive to local and global changes in oceanography and climate (Nürnberg and Tiedemann, 2004; Seki et al., 2004; Sakamoto et al., 2005, Sakamoto et al., 2006; Nürnberg et al., 2011; Vasilenko et al., 2017; Vasilenko et al., 2019). The history of sea ice variations and their underlying causes have attracted attention from the paleoceanography research community (e.g., Nürnberg and Tiedemann, 2004; Sakamoto et al., 2006; Nürnberg et al., 2011; Vasilenko et al., 2017; Vasilenko et al., 2019; Lo et al., 2018). However, sea ice variations and their driving mechanisms over the last glacial cycle remain controversial. Some studies have suggested that the entire Okhotsk Sea has been influenced by seasonal/annual sea ice since the last interglacial period (Gorbarenko et al., 2003; Seki et al., 2004; Sakamoto et al., 2005; Sakamoto et al., 2006; Vasilenko et al., 2019; Gorbarenko et al., 2020), while other studies have demonstrated that perennial sea ice was present during severe cold stages, such as MIS 4, MIS 2 (Wang and Wang, 2008; Vasilenko et al., 2019), and at ~30 ka (Lo et al., 2018). Moreover, the mechanisms driving sea ice variations on orbital and millennial timescales are still debated. Previous studies have suggested that sea ice variations on orbital scales are controlled largely by glacial–interglacial cycles (Gorbarenko et al., 2002; Gorbarenko et al., 2003; Nürnberg and Tiedemann, 2004; Sakamoto et al., 2005). However, C_{25} highly branched isoprenoid (IP_{25})-derived sea ice records suggest that variations in sea ice in the central Okhotsk Sea were controlled by both insolation and atmospheric CO_2 concentrations (Lo et al., 2018). In contrast, sea ice variations on millennial scales are more complex. Vasilenko et al. (2017) demonstrated that millennial-scale sea ice expansion was controlled by the velocity of geostrophic winds that dominated over the Okhotsk Sea, as the direction of ice drift coincided with the wind direction. The Arctic Oscillation (AO) is a dynamic atmospheric process in which the associated pressure changes over the Arctic influence atmospheric circulation over the Eurasian continent and adjacent areas (Thompson, 1998). It has been suggested that polar atmospheric circulation in the northern hemisphere is a key process that affects sea ice expansion on millennial scales (Sakamoto et al., 2006). Sakamoto et al. (2006) also inferred that discharge from the Amur River and polar atmospheric dynamics were potential factors that control sea ice expansion on millennial scales. Based on sea ice extents and inter-annual variations in Amur River discharge, Ogi et al. (2001) found a strong correlation between sea ice extent in the Okhotsk Sea and monsoon-induced fluvial discharge. However, there is no evidence suggesting that such a mechanism operates on geologic timescales. In addition, most of the sedimentary records related to sea ice changes during the last glacial cycle were from the central and eastern parts of the Okhotsk Sea, records from the southwestern Okhotsk Sea that are sensitive to fluvial effects are scarce. The southwestern Okhotsk Sea is subject to the influence of fluvial discharge *via* the East Sakhalin Current (Zhabin et al., 2010). Therefore, this is an ideal region for studying the history of sea ice cover and its potential connections with fluvial discharge. In this study, we analyzed an 8.8 m long core (LV55-40-1) collected from the southwestern Okhotsk Sea to determine the history of sea ice variations since ~110 ka. Combined with previous results, we attempted to determine the dominant factors that control sea ice variations at orbital and -millennial timescales during the last glacial cycle.

REGIONAL SETTING

The Okhotsk Sea is the second largest marginal sea in the Pacific Ocean. It is surrounded by the Asian continent, Sakhalin Island, the Kamchatka Peninsula, the Kuril Islands and the island of Hokkaido. The Okhotsk Sea is connected to the North Pacific and the Japan Sea by the Straits of the Kuril Islands and by the Tatar and Soya straits, respectively (**Figure 1**).

Surface circulation in the Okhotsk Sea is characterized by a cyclonic gyre composed of the West Kamchatka Current (WKC), East Sakhalin Current (ESC), and the salty Soya Warm Current (SWC). The ESC flows along Sakhalin Island southward toward the Kuril Islands, and finally leaves the Okhotsk Sea through the Bussol Strait (Lapko and Radchenko, 2000). The water mass at 300–800 m depth in the Okhotsk Sea is called the Okhotsk Sea Intermediate Water (OSIW) and is characterized by low-density ($26.7–27\sigma_\theta$), low-salinity (33.8‰), and oxygen-rich water (Morley and Hays, 1983; Talley, 1993; Yang and Honjo, 1996). The OSIW has similar characteristics to the North Pacific Intermediate Water (NPIW) and is regarded as the present source of NPIW (Talley, 1991; Yasuda, 1997; Freeland et al., 1998; Martin and Kawase, 1998; Wong et al., 1998). Below the OSIW, ancient deep Pacific water masses enriched in CO_2 flow into the Okhotsk Sea through the Krusenstherna Strait and flow out through the Bussol Strait (Nürnberg and Tiedemann, 2004).

The Amur River is the largest river in East Siberia and is adjacent to the northwestern continental shelf of the Okhotsk Sea. The drainage area of the Amur River is $\sim 1.85 \times 10^6\,km^2$ (Mclennan, 2013). The river delivers $\sim 14\,t\,km^{-2}$ of sediment to the northern Okhotsk Sea annually, which is two to three times higher than that of other Siberian rivers, including those that drain into the Arctic Ocean (Anikiev et al., 2001). Freshwater input from the Amur River is approximately $310\,km^3$ per year (Vörösmarty et al., 1996) and is mainly affected by the East Asian Summer Monsoon (EASM). Due to EASM precipitation and melting snow at high altitudes, the Amur River discharge is the highest during August–October, also producing the warmest water in the Okhotsk Sea (~20°C) during the same period (Ogi et al., 2001). The formation of a low-salinity layer in the Okhotsk Sea is mainly due to inflow from the Amur River (Freeland et al., 1998).

Sea ice in the Okhotsk Sea initially forms in November, starting in the northwestern part of the basin and repeatedly expanding southward (Sakamoto et al., 2005) due to transport by the northerly winds and the southward flow of the Okhotsk Sea (Ohshima et al., 2001; Wang et al., 2021). This creates a polynya along the coast and forms new sea ice (Sakamoto et al., 2005; Sakamoto et al., 2006). Sea ice in the Okhotsk Sea reaches its maximum extent during March, with a maximum thickness of ~1 m (Rycroft, 1995). The sea ice disappears entirely in June, with ice-free conditions from July to October (Parkinson et al., 1987). The expansion and retreat of sea ice are influenced not only by ocean–atmosphere interactions, but also by the density of the

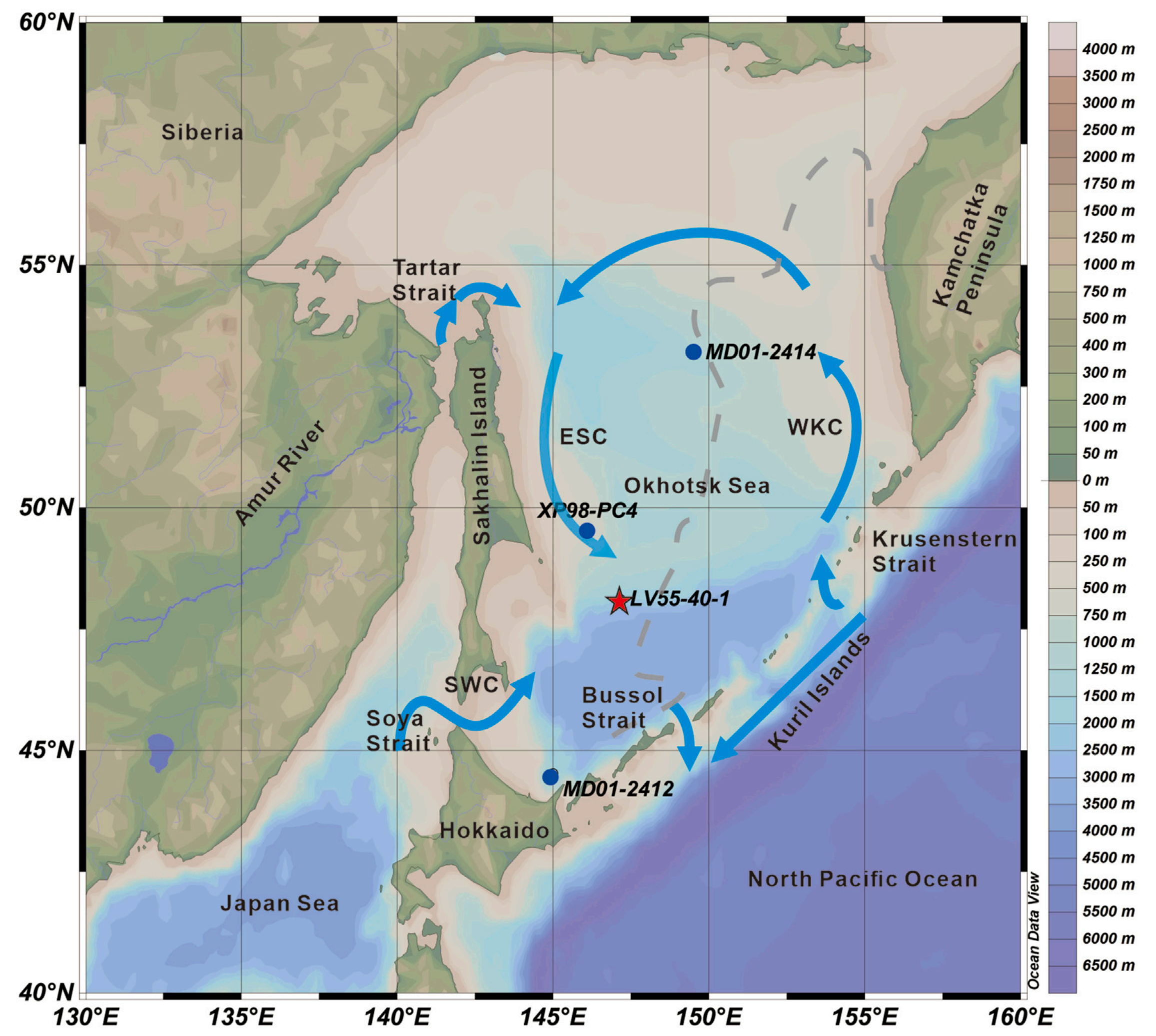

FIGURE 1 | Map of the Okhotsk Sea showing the locations of the core used in this study (LV55-40-1, red star) and other cores (blue dots) mentioned in the text (Sakamoto et al., 2006; Harada et al., 2008; Lo et al., 2018). Blue arrows indicate the East Sakhalin Current (ESC), West Kamchatka Current (WKC), and Soya Warm Current (SWC). The dashed line represents the average sea ice boundary from November to June according to Lo et al. (2018). Map generated using Ocean Data View version 4 (Schlitzer, 2021).

surface water that influences ocean circulation (Ohtani and Nagata, 1990). Intense sea ice formation causes brine rejection and forms Dense Shelf Water on the northern Okhotsk Sea shelves (Martin and Kawase, 1998; Gladyshev, 2003) and contributes to the formation and ventilation of the NPIW (Ohtani and Nagata, 1990; Talley, 1991; Wong et al., 1998).

MATERIALS AND METHODS

Core Description

Core LV55-40-1 (48.12°N, 147.15°E) was recovered from the northern Kuril Basin in the southwestern Okhotsk Sea at a water depth of 1,730 m (**Figure 1**). The 8.8 m thick deposits were composed of homogeneous olive gray (5Y 4/2) silty clay with distinctive layers dominated by coarse-grained sand and gravel at 340–345 cm and 385–388 cm depths. These layers were also characterized by extremely high magnetic susceptibility, and abundant volcanic glass (**Figure 2**).

Accelerator Mass Spectrometer ^{14}C Dating

Mixed samples of the planktonic foraminifera *Neogloboquadrina pachyderma* (sinistral) and *Globigerina bulloides* larger than 145 μm were collected from the core for accelerator mass spectrometer (AMS) ^{14}C dating (**Table 1**). The AMS ^{14}C analyses were performed by Beta Analytic Laboratory. Calibrated calendar ages were converted using CALIB 8.20 (Stuiver and Reimer, 1993) with the MARINE20 database (Heaton, 2020) and a calculated weighted mean $\triangle R$ = 450 ± 90 a (Lo et al., 2018).

X-Ray Fluorescence Scanning Analyses

X-ray fluorescence (XRF) scanning was performed at 0.5 cm intervals using an Itrax XRF core scanner with a 20 s count time, an X-ray voltage of 30 kV, and an X-ray current of 40–55 mA, which

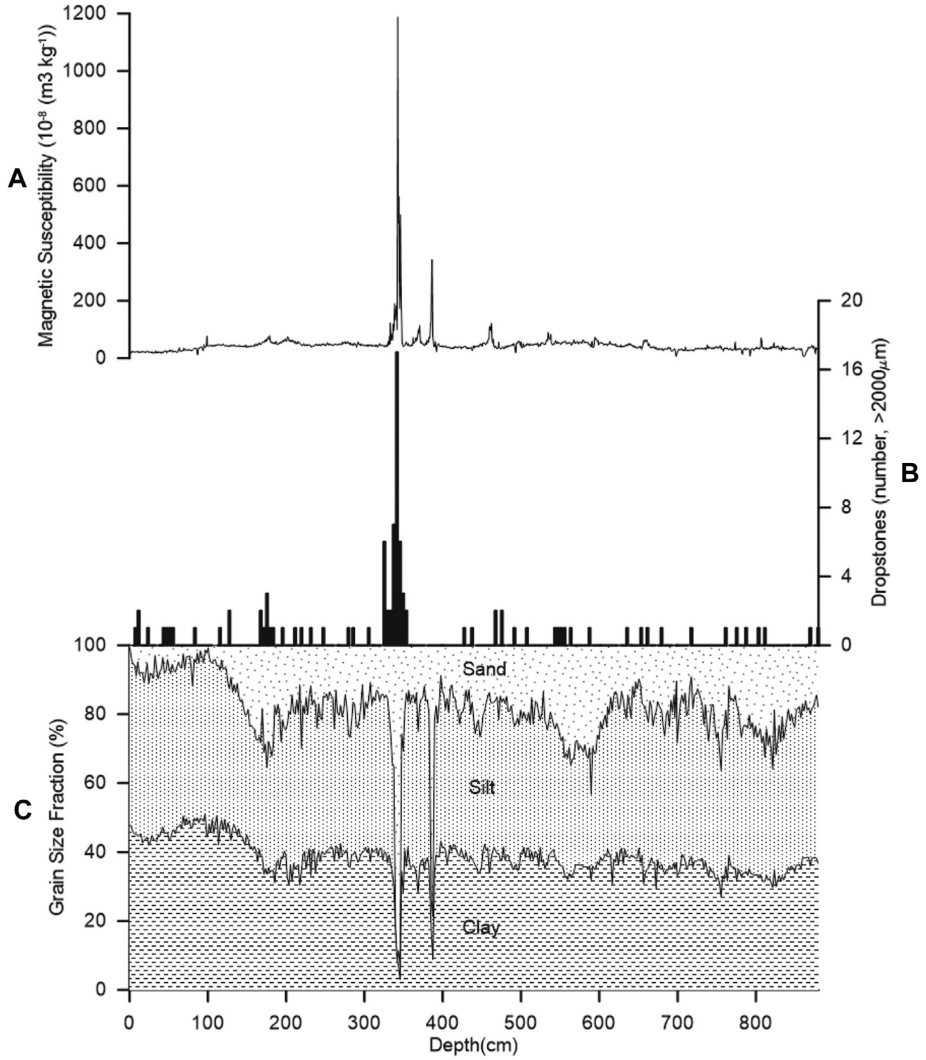

FIGURE 2 | Variations in **(A)** Magnetic Susceptibility, **(B)** Numbers of dropstones, and **(C)** Grain-size compositions with depth in core LV55-40-1.

TABLE 1 | AMS^{14}C ages and calendar ages obtained from core LV55-40-1.

Laboratory number	Core depth (cm)	Conventional radiocarbon age (a. BP)	±Error(a)	Cal BP age range (95.4%)	Median cal BP age (95.4%)
Beta-577768	111.5	6,360	30	5,891–6,367	6,127
Beta-576614	199.5	12,990	40	13,636–14,311	13,957
Beta-577769	262.5	17,960	60	19,893–20,558	20,243
Beta-577770	378.5	27,130	110	29,737–30,372	30,042

allowed for rapid, non-destructive, high-resolution elemental analyses of the sedimentary cores (Jansen et al., 1998).

Biogenic Silica Analyses

Biogenic silica (opal) analyses were performed on 440 samples using molybdate blue with modified pretreatments (Mortlock and Froelich, 1989). Opal was extracted using 40.0 ml of 0.2 mol/L $NaCO_3$ solution at 85°C for 6 h. During the analyses, 2 ml of $C_2H_2O_4$ was added to avoid interference by P and As. The opal contents were quantified using a Mettler UV5 spectrophotometer. The relative standard deviation (RSD) was less than 3%.

Chlorin Analyses

A total of 440 samples were analyzed to determine the chlorin concentrations with modified pretreatments (Harris and Maxwell, 1995). Briefly, ~1 g of each sample was extracted using 20 ml of 90% acetone and stored at 4°C for 24 h in the dark. The extracted liquor was centrifuged and filtered through GF/F membranes. The chlorin concentrations were determined using a TD-700 fluorometer. The RSD was less than 2%.

Ice-Rafted Debris Analyses

In the Okhotsk Sea, coarse sediment fractions with grain sizes larger than 63 μm in the Okhotsk Sea have been defined as ice-rafted debris (IRD) according to previous studies based on samples from sediment traps, surface sediments, and sediment cores from the region (Sakamoto et al., 2005). Laser diffraction and sieving of the IRD were performed, both of which were used to describe the grain size fractions in the core (Sakamoto et al., 2005, Sakamoto et al., 2006). Both of these methods were used in order to make the results more credible.

Laser Diffraction Grain-Size Analysis

Grain-size analyses were performed on 442 samples at ~1–2 cm intervals to characterize the sediment texture using a Malvern Master size laser particle sizer (Malvern 3000) with a range of ~0.02–2,000 μm. Carbonates, organic material, and diatoms were removed before analysis following the procedure introduced by Vasilenko et al. (2017). Briefly, ~0.1 g of sediment was pre-treated with excess 15% H_2O_2 to remove organic matter, and with excess 10% HCl to remove $CaCO_3$. The liquid was centrifuged three times at pH = 7, then 20 ml of 2 mol/L Na_2CO_3 was added and water-bathed at 85°C for 8 h to remove diatoms. Representative samples were observed under a microscope to ensure that the diatoms were completely removed. The accuracy of the measurements was 99% and the repeatability error was less than 0.1%.

Sieve Analysis

Approximately 3–10 g of dry samples were weighed before sieving and washed with water passing through a 63 μm mesh sieve. The residual samples on the sieve were dried at 60°C and passed through a 2,000 μm mesh sieve, and every fraction was weighed (Sakamoto et al., 2006; Nürnberg et al., 2011). The >2,000 μm grains (dropstones) were collected during core description, sampling and sieving, and were counted.

Time-Series Analysis

The IRD (vol%) time series analysis was performed using the wavelet transform in Acycle (Li et al., 2019) and a 95% confidence level was chosen. Cross-wavelet analysis visualizes the continuous variations in power and coherence in the time-frequency domain (Asahi et al., 2016). Prior to spectral analysis, all of the analyzed data were resampled at 0.2 kyr for wavelet transform and cross-wavelet analysis, which was the mean resolution of the sequence based on linear interpolation.

RESULTS

Chronology

The age model for core LV55-40-1 was constructed based on AMS ^{14}C dating of planktonic foraminifera and on correlation of the productivity proxies, such as Ba/Ti, chlorin and opal contents with marine and Greenland ice sheet oxygen isotopic records (**Figure 3**; Andersen et al., 2004; Lisiecki and Raymo, 2005). The Ba/Ti ratio was assumed to indicate the relative contribution of biological and terrestrial inputs into the Okhotsk Sea, which co-vary with glacial–interglacial cycles with higher Ba/Ti values during the interglacial periods (**Figure 3C,F**; Lo et al., 2018). Similarly, opal contents exhibited cyclic variations, with high abundances during interglacial periods and low abundances during glacial periods (**Figure 3D**). The correlation between opal contents and marine oxygen isotopes has been widely used to construct age models for deposits in the Okhotsk Sea (Narita et al., 2002; Sakamoto et al., 2006). In addition, magnetic susceptibility correlated with LR04 (Lisiecki and Raymo, 2005) and exhibited good correlations with log (Ba/Ti) and opal contents (**Figure 3C-E**).

The chlorin content in the Okhotsk Sea increased during Dansgaarde-Oeschger interstadials (DOIs), and have also been used to construct high-resolution age models in the Okhotsk Sea (Gorbarenko et al., 2007; Gorbarenko et al., 2009; Gorbarenko et al., 2010; Gorbarenko et al., 2012; Vasilenko et al., 2017; Gorbarenko et al., 2020). Thus, the resolution of the age model was improved further by correlating the chlorin content to DOIs in Greenland ice cores. In core LV55-40-1, the peaks in chlorin content correlated well with long-lasting DOIs 8, 12, 14, 19, and 21 within established MISs (**Figure 2F,G**). The 8.8 m core thus revealed orbital and millennial variations with a basal age of 110 kyr (early MIS 5d; **Figure 3**).

Variations in Ice-Rafted Debris in Core LV55-40-1

The IRD (vol%) content determined by laser diffraction was calculated as the volume percentage of the total terrigenous materials and excludes the influence of biological material. The IRD (wt%) content determined by sieving includes both terrigenous grains and biogenic fractions. However, in the Okhotsk Sea, the biogenic fraction is insignificant (Sakamoto et al., 2006) and can be ignored in the sand fraction. Moreover, the variations in the IRD fraction between these two analytical methods were consistent in core LV55-40-1 (**Figures 4C,D**), which confirms the above inference, and indicates that both are suitable as proxies.

Variations in IRD (vol%) ranged from 0.36 to 46.7% (**Figures 4D**, **5D**). In general, IRD (vol%) exhibited strong cyclic variations from ~110 to ~10 ka (**Figure 4D**), mostly ranging from ~5 to ~15%. High-frequency fluctuations were observed at 105, 94, 87, 80, 78, 74, 70, 62, 58, 48, 40, 37, 34, 31, 29, 27, 22, 17, and 12 ka (**Figure 5D,E**). Two significant peaks in IRD (vol%), with values of 46.7 and 39.3%, corresponded to ~31 and ~27 ka, respectively. The IRD (vol%) was low during the Holocene, with a mean of 4.7%. The variations in IRD (wt%) ranged from ~2 to ~52% throughout the core, and exhibited a similar pattern to those of the IRD (vol%) (**Figures 4D**, **5D**).

A total of 99 dropstones were collected from the core sequence (**Figure 2B**), with diameters ranging from 2 to 60 mm. The presence of dropstones verifies the presence of sea ice, as ice rafting is the main transport method for grains larger than 2 mm

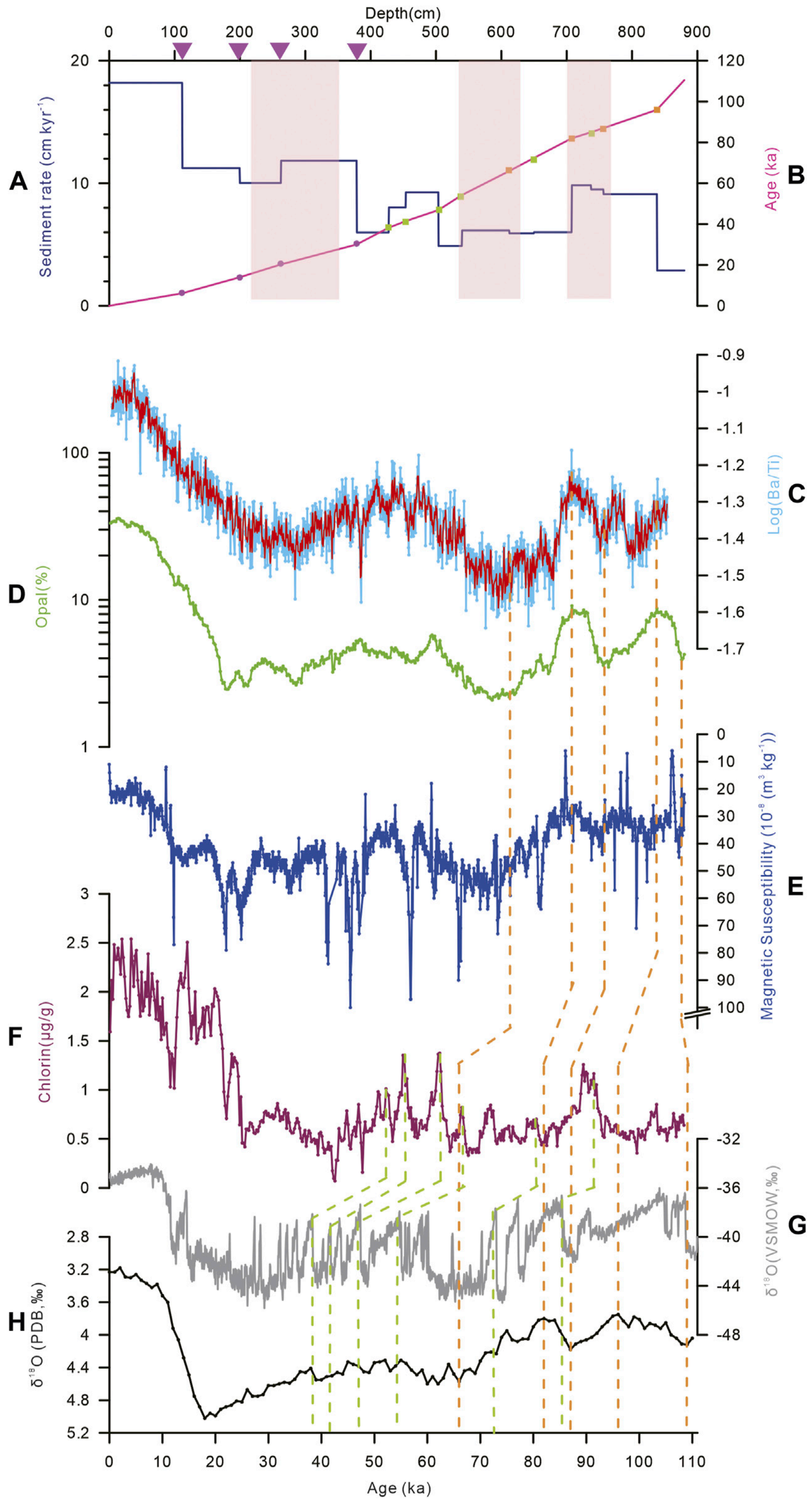

FIGURE 3 | Age model for core LV55-40-1. **(A)** Linear sedimentation rate, **(B)** Age-depth plot, **(C)** XRF-scanning log (Ba/Ti) ratio (blue line) with a 3-point running average (red line), **(D)** Opal content, **(E)** Magnetic susceptibility, **(F)** Chlorin concentration, **(G)** Oxygen isotopes from the NGRIP ice core (Andersen et al., 2004), and **(H)** LR04 $\delta^{18}O$ stack (Lisiecki and Raymo, 2005). Purple triangles represent age model tie point using AMS ^{14}C, orange and green dashed lines represent age control points obtained using correlations between the log (Ba/Ti) ratio, opal content, magnetic susceptibility, and LR04 $\delta^{18}O$, and using correlations between chlorin concentrations and oxygen isotopes from the NGRIP ice core. Pink shadows represent glacial periods.

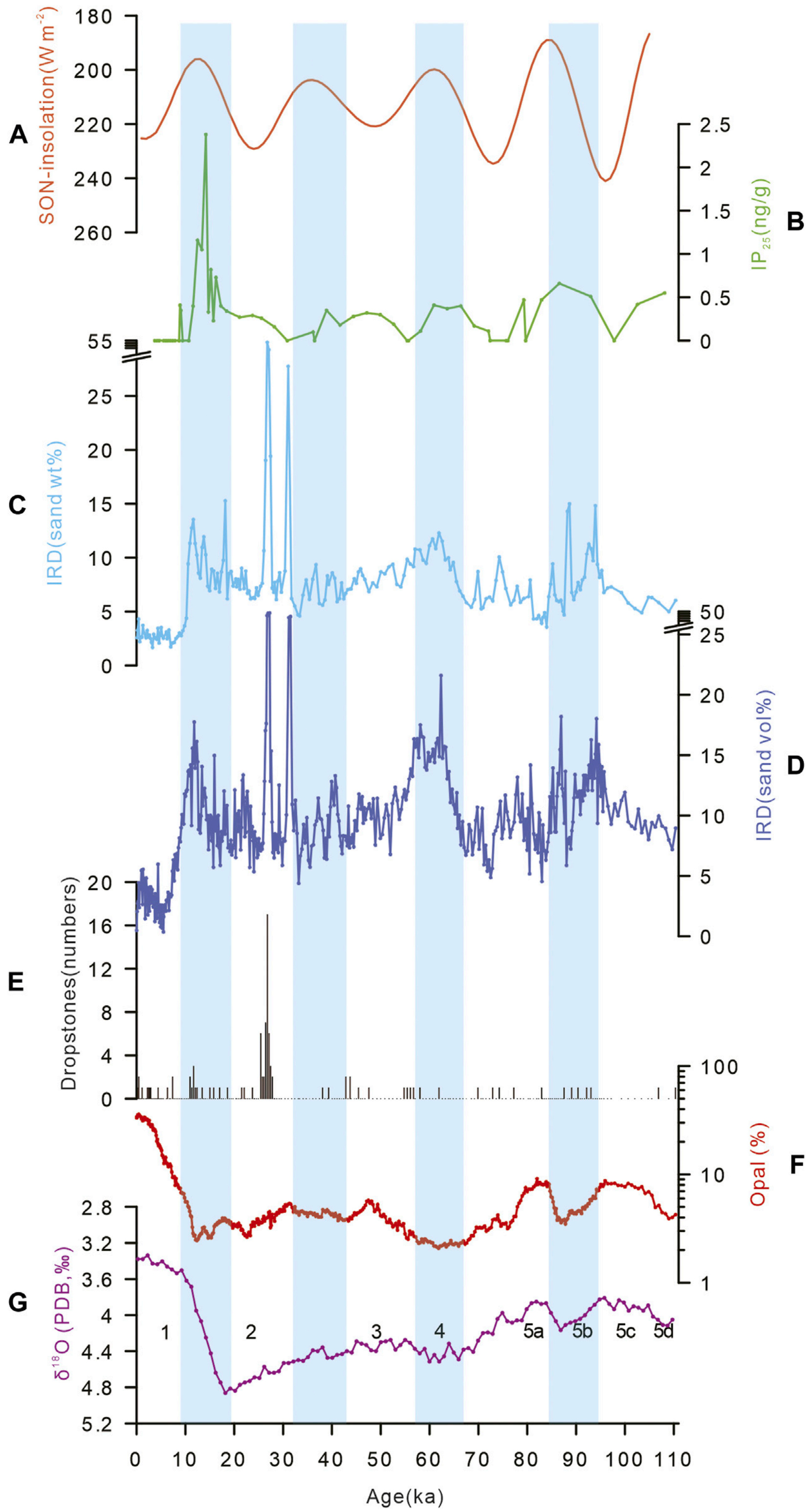

FIGURE 4 | Comparisons between variations in IRD proxies in core LV55-40-1 and other proxies. **(A)** SON-insolation (48°N; September, October, and November mean insolation), **(B)** IP_{25} content in core MD01-2414 from the central Okhotsk Sea, a proxy of sea ice (Lo et al., 2018), **(C)** IRD (wt%) in core LV55-40-1, **(D)** IRD (vol%) in core LV55-40-1, **(E)** Number of dropstones in core LV55-40-1, **(F)** Opal content in core LV55-40-1, and **(G)** LR04 $\delta^{18}O$ stack (Lisiecki and Raymo, 2005). Blue shadows represent intervals of sea ice expansion.

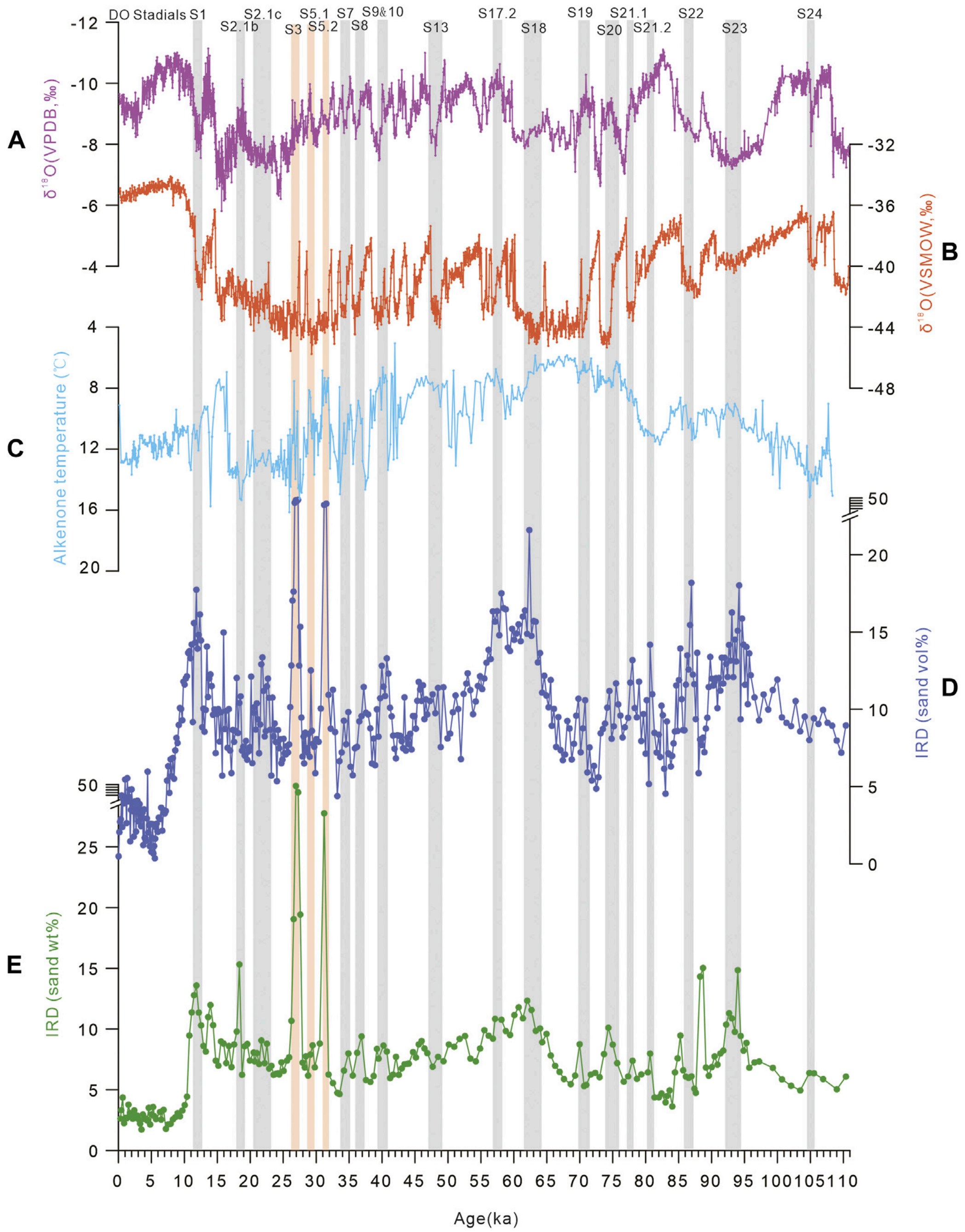

FIGURE 5 | Comparison between millennial-scale changes in IRD proxies in core LV55-40-1 and other proxies. **(A)** Oxygen isotopes from stalagmites (Cheng et al., 2016), a proxy for the East Asian summer monsoon (EASM), **(B)** Oxygen isotopes of the NGRIP ice core (Andersen et al., 2004), a proxy for air temperature, **(C)** Alkenone-derived temperature (°C) (Harada et al., 2008), indicating AO variations, **(D)** IRD (vol%) and **(E)** IRD (wt%) in core LV55-40-1. Grey shadows represent DOSs intervals, orange shadows represent intervals potentially affected by volcanic eruptions.

to hemipelagic regions, especially in areas influenced by seasonal sea ice (Sakamoto et al., 2006). Dropstones mostly occurred in intervals with high IRD contents, and the maximum number of dropstones (17) was observed at ~27 ka, which may have also been influenced by volcanic eruption as suggested by the extremely high magnetic susceptibility (**Figure 2A**).

DISCUSSION

Sea Ice Variations in the Okhotsk Sea on Orbital Timescale

Ice rafting is the dominant method of transport for coarse-grained terrigenous material and dropstones to hemipelagic regions in the Okhotsk Sea (Sakamoto et al., 2006; Nürnberg et al., 2011). However, turbidity currents, gravity flows, and volcanic eruptions can also transport coarse materials into the sea (Nürnberg et al., 2011; Wang et al., 2017). Evidence of turbidity currents or gravity flows was not observed in core LV55-40-1, and has not been recorded in cores from nearby regions (Karp, 1996; Biebow, 1999). The extremely high magnetic susceptibility (**Figure 2A**) and volcanic glass observed at ~31 and ~27 ka implies that abundant volcanic materials were brought by either directly volcanic eruption or by sea ice, which was difficult to distinguish and may have affected the IRD content only during early MIS 2 (**Figures 4D,G**, **5D**); however, this disturbance may be negligible because the abundant coarse volcanic material occurred as very thin layers in the core. The obvious effects of volcanic material on the IRD in the rest of the core could also be precluded due to the relatively low magnetic susceptibility values (**Figure 2A**).

The presence of IRD is generally the result of the expansion of sea ice under cold climatic conditions (Nürnberg and Tiedemann, 2004; Seki et al., 2004; Sakamoto et al., 2005, Sakamoto et al., 2006; Nürnberg et al., 2011). During cold stages, lower sea levels resulted in greater exposure of the surrounding continental shelf; thus, more terrigenous grains were captured and transported by sea ice to the ocean (Sakamoto et al., 2005). It has been suggested that perennial sea ice or ice-free conditions occur when IRD contents are 0% or approximately 0% (Seki et al., 2004; Sakamoto et al., 2005; Sakamoto et al., 2006). Seasonal sea ice is the only method that can transport dropstones to the ocean by ice rafting (Sakamoto et al., 2006), which is supported by the presence of dropstones during both warm and cold stages (**Figures 2B**, **4E-G**). Even in the modern southwestern Okhotsk Sea, there is a small area of seasonal sea ice cover at the study site (**Figures 4C,D**). IRD was abundant throughout the sequence in core LV55-40-1, suggesting that seasonal sea ice was predominant in the southwestern Okhotsk Sea over the past ~110 kyr. This is supported by analyses of IRD in cores MD01-2412 (Sakamoto et al., 2006) and XP98-PC4 (Sakamoto et al., 2005) from the southwestern Okhotsk Sea, which demonstrated that seasonal sea ice cover was present during the past ~100 kyr. However, conditions were different in other regions. The diatom records from the central Okhotsk Sea suggested perennial sea ice conditions during MIS 2 and MIS 4 (Wang and Wang, 2008), whereas IRD records from the eastern Okhotsk Sea indicate a seasonal to perennial sea ice cover (Nürnberg et al., 2011). Other IRD records indicate that during MIS 2 perennial sea ice covered the Okhotsk Sea only near the northwestern and western coasts (Vasilenko et al., 2019). However, perennial sea ice conditions were not present at our study site, even during the Last Glacial Maximum (LGM). Instead, a seasonal sea ice cover was present (**Figures 4C,D**). This implies that sea ice variations in the Okhotsk Sea are spatially heterogeneous on geologic timescales (Gorbarenko et al., 2014; Bosin et al., 2015; Vasilenko et al., 2019).

Generally, sea ice variations in the Okhotsk Sea exhibit cyclic glacial–interglacial patterns on an orbital scale, with expanding sea ice extents during glacials and retreating sea ice extents during interglacials (Nürnberg and Tiedemann, 2004; Sakamoto et al., 2005; Nürnberg et al., 2011; Zou et al., 2015; Wang et al., 2017; Jimenez-Espejo et al., 2018). Variations in core LV55-40-1 do not strictly follow the glacial-interglacial cycles, and four obvious sea ice expansions were observed during MIS 5b, MIS 4, mid-MIS 3, and early MIS 1, as indicated by high IRD contents (**Figure 4D**). The reconstructed sea ice variations from this core are mostly consistent with the IP_{25} record from core MD01-2414 in the central Okhotsk Sea (Lo et al., 2018; **Figures 4B,D**).

Sea ice formation in the modern Okhotsk Sea mainly occurs during the winter (Parkinson et al., 1987; Rycroft, 1995). Previous studies have demonstrated that air temperature and sea-surface conditions during autumn play an important role in sea ice formation during the subsequent winter (Ogi et al., 2001; Ogi and Tachibana, 2006). Therefore, local autumn insolation may be related to sea ice formation during the winter. This inference is confirmed by a good correlation between the variations in sea ice derived from IRD and autumn insolation in the study area (48°N; September, October, and November mean insolation, SON-insolation). Four sea ice expansions corresponded to either declining or minimum SON-insolation (**Figures 4A,D**). This suggests that seasonal sea ice variations on an orbital scale in the Okhotsk Sea were controlled by local autumn insolation, which exhibits a strong precession cycle. This inference is further supported by the wavelet transform analysis of IRD (**Figure 6A**) and a cross-wavelet analysis between IRD and SON-insolation (**Figure 6B**), which exhibited a strong 20-kyr cycle throughout the sequence (**Figure 4D**).

Sea Ice Variations in the Okhotsk Sea on Millennial Timescale

High-resolution variations in IRD revealed millennial-scale sea ice fluctuations over the past ~110 ka, which are superimposed on the variability at the orbital scale. In total, 19 IRD peaks were observed throughout the sequence, which correspond with cold Dansgaarde-Oeschger stadials (DOS) recorded by the Greenland ice sheet (Andersen et al., 2004; **Figures 5B,D**). Previous studies have reported that millennial-scale sea ice variations can be correlated with millennial climatic changes, such as DO cycles (Gorbarenko et al., 2003; Sakamoto et al., 2005; Sakamoto et al., 2006; Nürnberg et al., 2011; Vasilenko et al., 2017). A recent study suggested that the velocity of geostrophic winds over the Okhotsk Sea dominated sea ice drift, thereby causing the expansion of sea ice on millennial scales (Vasilenko et al., 2017). Mayewski et al. (1994) attributed rapid climatic changes to significant reorganization of atmospheric circulation, which stimulated changes in sea ice cover in the ocean. A study of the history of sea ice variations derived from IRD analyses also highlighted the importance of millennial-scale variations in polar atmospheric circulation for driving sea ice changes in the Okhotsk Sea (Sakamoto et al., 2005). Therefore, atmospheric circulation in the polar region and its correlation with pressure in the mid-latitudes might be related to sea ice changes in the Okhotsk Sea on a millennial scale (Sakamoto et al., 2005; Sakamoto et al., 2006; Harada et al., 2008).

The AO is a dynamic atmospheric process, and the associated pressure changes over the Arctic are opposite to those over the mid-latitude region in the Northern Hemisphere (Thompson, 1998). The AO exerts a strong influence on atmospheric circulation over the Eurasian continent and adjacent areas. Modern data suggests that sea ice cover in winter is strongly affected by the annual integrated AO in the Okhotsk Sea (Ogi and

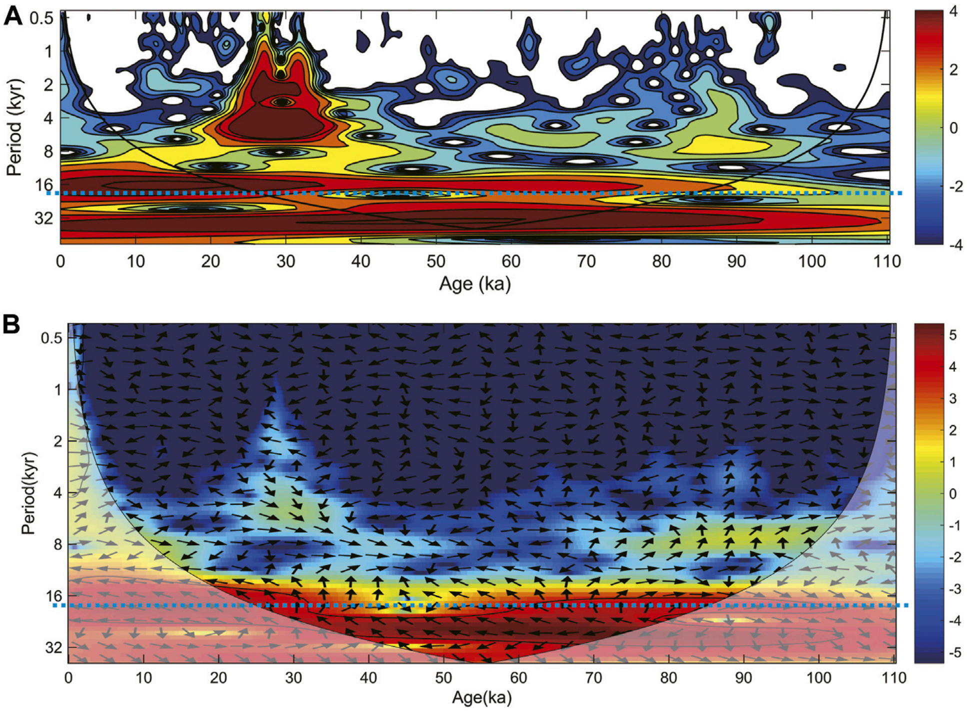

FIGURE 6 | (A) Continuous wavelet transform analysis of IRD (vol%) in core LV55-40-1 and **(B)** Cross-wavelet analysis of IRD (vol%) in core LV55-40-1 and SON-insolation. Blue dashed lines represent main orbital cycle of 20-kyr.

Tachibana, 2006). An IRD record from the central Okhotsk Sea also indicated that sea ice expansions in DOSs during the past ~100 kyr were the result of variations in polar atmospheric circulation in the Northern Hemisphere (Sakamoto et al., 2005). Therefore, the Arctic atmospheric processes must contribute to sea ice variations in the study area on a millennial scale. It has been suggested that the alkenone-derived ocean surface temperatures corresponded with AO on geologic timescales (Harada et al., 2008) and were coupled with temperature changes in the Arctic, with low temperatures indicating a negative AO, and vice versa. Therefore, negative AO during stadials plays a dominant role in sea ice expansion in the Okhotsk Sea, as negative AO patterns are closely correlated with cold DOSs (Harada et al., 2008; **Figures 5C,D**). During these sea ice expansion intervals, cold air masses could have easily penetrated through the Arctic region during periods with negative AO pattern, lowering the air temperatures over the Okhotsk Sea and causing more active sea ice formation (Thompson and Wallace, 1998; Harada et al., 2008).

In addition to the effects of AO, thermal anomalies at the ocean surface may have also influenced the sea ice formation in the Okhotsk Sea (Ogi et al., 2001; Sakamoto et al., 2005; Sakamoto et al., 2006; Harada et al., 2008). Such thermal anomalies are closely related to the discharge of warm freshwater (Ogi et al., 2001; Harada et al., 2008). In the modern Okhotsk Sea, the Amur River discharge brings warm water advection to the surface seawater, thereby reducing the sea ice formation during the subsequent winter (Ogi et al., 2001). On geologic timescales, the Amur River discharge is a potential factor that controlled sea ice variations during warm periods (Sakamoto et al., 2006). Core LV55-40-1 is located in an area east of the Sakhalin Islands, which is influenced by freshwater discharge from the Amur River that is transported by the ESC (Itoh and Ohshima, 2000; Sakamoto et al., 2005; **Figure 1**). Therefore, the discharge from the Amur River may have also contributed to sea ice variations during interglacial periods in the study area by modulating the sea-surface thermal conditions. As fluctuations in the Amur River discharge were controlled by the intensity of the EASM (Harada et al., 2008), the reconstructed variations in sea ice also corresponded well with the EASM variability on the millennial scale, with decreased sea ice formation during warm stages (Cheng et al., 2016; **Figures 5A,D**). During periods of enhanced EASM, increased monsoon precipitation would increase the discharge from the Amur River. The advection of this warm freshwater to the southwestern Okhotsk Sea caused thermal anomalies at the ocean surface (Ogi et al., 2001), thereby suppressing subsequent sea ice formation. In contrast, less warm freshwater input during cold stadials in the interglacials due to weak monsoonal conditions would allow more sea ice formation in the study area.

CONCLUSION

We reconstructed the history of sea ice variations in the southwestern Okhotsk Sea over the last ~110 kyr and investigated the factors controlling sea ice changes on orbital and -millennial timescales based on the IRD proxy. Seasonal sea ice was predominant in the southwestern Okhotsk Sea during the past ~110 kyr. Sea ice expansion occurred during MIS 5b, MIS 4, mid-MIS 3, and early MIS 1, which corresponded to period of less SON-insolation. Combined with the strong 20-kyr cycles in the IRD proxy, we suggest that orbital-scale sea ice variations in the southwestern Okhotsk Sea were controlled primarily by local autumn insolation. The millennial-scale sea ice variations are related to DO cycles, with sea ice expansion corresponding to cold DOSs. We suggest that sea ice variations were impacted by both the AO and the EASM. During intervals of sea ice expansion, cold air masses could have easily penetrated through the Arctic region during periods of negative AO pattern, thereby lowering the air temperature in the Okhotsk Sea latitudes and causing more active sea ice formation. In addition, the high discharges of warm freshwater transported by the Amur River to the southwestern Okhotsk Sea during warm interstadials caused thermal anomalies at the ocean surface, thereby suppressing the subsequent sea ice formation. In contrast, lower warm freshwater input during cold stadials would allow more sea ice formation in the study area.

DATA AVAILABILITY STATEMENT

The original contributions presented in the study are included in the article/supplementary material, further inquiries can be directed to the corresponding authors.

AUTHOR CONTRIBUTIONS

AW, ZY, and XS designed the study, synthesized and analyzed the data, and wrote the manuscript with contributions from all authors. KW and YW analyzed the data related to sedimentology. YL, JZ, and SG helped collect the core. All authors contributed to the manuscript and approved its submission.

FUNDING

This work was jointly supported by the National Key Research and Development Program of China (No: 2016YFA0601903), NSFC-Shandong Joint Fund for Marine Science Research Centers (U1606401), the National Program on Global Change and Air-Sea Interaction (Grant No. GASI-GEOGE-03), the Taishan Scholar Program of Shandong (XS), the Russian Science Foundation, Russia (Grant N_19-05-00663A), and the Russian state budget 121021700342-9 of the Pacific Oceanological Institute, Far East Branch of the Russian Academy of Sciences.

ACKNOWLEDGMENTS

We thank the Editor and two reviewers for their valuable suggestions.

REFERENCES

Andersen, K. K., Azuma, N., Barnola, J. M., Bigler, M., Biscaye, P., Caillon, N., et al. (2004). High-resolution Record of Northern Hemisphere Climate Extending into the Last Interglacial Period. *Nature* 431, 147–151. doi:10.1038/nature02805

Anikiev, V. V., Dudarev, O. V., Kolesov, G. M., Botsul, A. I., and Utkin, I. V. J. G. I. (2001). Factors of Mesoscale Variability in the Distribution of the Particulate Matter and Chemical Elements in the Amur River Estuary-Sea of Okhotsk Waters. *Geochem. Int.* 39, 64–87. doi:10.1134/S001670290905005X

Asahi, H., Kender, S., Ikehara, M., Sakamoto, T., Takahashi, K., Ravelo, A. C., et al. (2016). Orbital-scale Benthic Foraminiferal Oxygen Isotope Stratigraphy at the Northern Bering Sea Slope Site U1343 (IODP Expedition 323) and its Pleistocene Paleoceanographic Significance. *Deep Sea Res. Part Topical Stud. Oceanography* 125-126, 66–83. doi:10.1016/j.dsr2.2014.01.004

Biebow, N. (1999). KOMEX (Kurile Okhotsk Sea Marine Experiment). Cruise Reports: KOMEX I and II: RV Professor Gagarinsky Cruise 22, RV Akademik Lavrentyev Cruise 28. Geomar Reports.

Bosin, A., Gorbarenko, S., Xuefa, S., Liu, Y., and Zou, J. (2015). Regionalized Primary Paleoproduction Variability in the Sea of Okhotsk during Late Pleistocene and Holocene. *J. Asian Earth Sci.* 114, 534–540. doi:10.1016/j.jseaes.2015.07.019

Cheng, H., Edwards, R. L., Sinha, A., Spötl, C., Yi, L., Chen, S., et al. (2016). The Asian Monsoon over the Past 640,000 Years and Ice Age Terminations. *Nature* 534, 640–646. doi:10.1038/nature18591

Freeland, H. J., Bychkov, A. S., Whitney, F., Taylor, C., Wong, C. S., and Yurasov, G. I. (1998). WOCE Section P1W in the Sea of Okhotsk: 1. Oceanographic Data Description. *J. Geophys. Res.* 103, 15613–15623. doi:10.1029/98jc00368

Gladyshev, S. (2003). Distribution, Formation, and Seasonal Variability of Okhotsk Sea Mode Water. *J. Geophys. Res.* 108, 3186. doi:10.1029/2001jc000877

Gorbarenko, S. A., Artemova, A. V., Goldberg, E. L., and Vasilenko, Y. P. (2014). The Response of the Okhotsk Sea Environment to the Orbital-Millennium Global Climate Changes during the Last Glacial Maximum, Deglaciation and Holocene. *Glob. Planet. Change* 116, 76–90. doi:10.1016/j.gloplacha.2014.02.002

Gorbarenko, S. A., Goldberg, E. L. v., Kashgarian, M., Velivetskaya, T. y. A., Zakharkov, S. P., Pechnikov, V. S., et al. (2007). Millennium Scale Environment Changes of the Okhotsk Sea during Last 80 Kyr and Their Phase Relationship with Global Climate Changes. *J. Oceanogr.* 63, 609–623. doi:10.1007/s10872-007-0054-1

Gorbarenko, S. A., Harada, N., Malakhov, M. I., Vasilenko, Y. P., Bosin, A. A., and Gol'dberg, E. L. (2009). Millennial-scale Climatic and Environmental Oscillations in the Sea of Okhotsk in Response to Global Changes during the Last 190 Ka. *Dokl. Earth Sc.* 423, 1410–1413. doi:10.1134/s1028334x08090183

Gorbarenko, S. A., Harada, N., Malakhov, M. I., Vasilenko, Y. P., Bosin, A. A., and Goldberg, E. L. (2010). Orbital and Millennial-Scale Environmental and Sedimentological Changes in the Okhotsk Sea during the Last 350kyr. *Glob. Planet. Change* 72, 79–85. doi:10.1016/j.gloplacha.2010.03.002

Gorbarenko, S. A., Harada, N., Malakhov, M. I., Velivetskaya, T. A., Vasilenko, Y. P., Bosin, A. A., et al. (2012). Responses of the Okhotsk Sea Environment and Sedimentology to Global Climate Changes at the Orbital and Millennial Scale during the Last 350kyr. *Deep Sea Res. Part Topical Stud. Oceanography* 61-64, 73–84. doi:10.1016/j.dsr2.2011.05.016

Gorbarenko, S. A., Khusid, T. A., Basov, I. A., Oba, T., Southon, J. R., and Koizumi, I. (2002). Glacial Holocene Environment of the southeastern Okhotsk Sea: Evidence from Geochemical and Palaeontological Data. *Palaeogeogr. Palaeoclimatol. Palaeoecol.* 177, 237–263. doi:10.1016/s0031-0182(01)00335-2

Gorbarenko, S. A., Yanchenko, E. A., Psheneva, O. g. Y., Harada, N., Bosin, A. A., Artemova, A. V., et al. (2020). Orbital and Millennial-Scale Environmental and Hydrological Changes of the central Okhotsk Sea over the Last 136 Kyr Inferred from Micropaleontological (Radiolarian and Benthic Foraminifera), Geochemical and Lithological Proxies and the Mechanisms Responsible for Them. *Quat. Sci. Rev.* 247, 106569. doi:10.1016/j.quascirev.2020.106569

Gorbarenko, S., Leskov, V. Y., Artemova, A., Tiedemann, R., Nicole, B., and Nuernberg, D. (2003). Ice Cover of the Okhotsk Sea during Last Glaciating and Holocene. *Doklady Akademii Nauk* 388, 678–682.

Harada, N., Sato, M., and Sakamoto, T. (2008). Freshwater Impacts Recorded in Tetraunsaturated Alkenones and Alkenone Sea Surface Temperatures from the

Okhotsk Sea across Millennial-Scale Cycles. *Paleoceanography* 23, PA3201. doi:10.1029/2006pa001410

Harada, N., Takahashi, K., Timmermann, A., and Sakamoto, T. (2012). Climate Change Dynamics of Present and Past in the North Pacific and its Northern Marginal Seas. *Deep Sea Res. Part Topical Stud. Oceanography* 61-64, 1–3. doi:10.1016/j.dsr2.2012.01.001

Harris, P. G., and Maxwell, J. R. (1995). A Novel Method for the Rapid Determination of Chlorin Concentrations at High Stratigraphic Resolution in marine Sediments. *Org. Geochem.* 23, 853–856. doi:10.1016/0146-6380(95)80007-e

Heaton, T. (2020). Marine20 – the marine Radiocarbon Age Calibration Curve (0-55, 000 Cal BP). *Radiocarbon*, 1–42. doi:10.1017/rdc.2020.68

Itaki, T. (2004). Middle to Late Holocene Changes of the Okhotsk Sea Intermediate Water and Their Relation to Atmospheric Circulation. *Geophys. Res. Lett.* 31, L24309. doi:10.1029/2004gl021384

Iwasaki, S., Takahashi, K., Maesawa, T., Sakamoto, T., Sakai, S., and Iijima, K. (2012). Paleoceanography of the Last 500kyrs in the central Okhotsk Sea Based on Geochemistry. *Deep Sea Res. Part Topical Stud. Oceanography* 61-64, 50–62. doi:10.1016/j.dsr2.2011.03.003

Jansen, J. H. F., Van Der Gaast, S. J., Koster, B., and Vaars, A. J. (1998). CORTEX, a Shipboard XRF-Scanner for Element Analyses in Split Sediment Cores. *Mar. Geology* 151, 143–153. doi:10.1016/s0025-3227(98)00074-7

Jimenez-Espejo, F. J., García-Alix, A., Harada, N., Bahr, A., Sakai, S., Iijima, K., et al. (2018). Changes in detrital input, ventilation and productivity in the central Okhotsk Sea during the marine isotope stage 5e, penultimate interglacial period. *J. Asian Earth Sci.* 156, 189–200. doi:10.1016/j.jseaes.2018.01.032

Karp, B. Y. (1996). RV Akademik M.A. Lavrentyev Cruise 27: Cruise Report GREGORY, German Russian Expedition for Geological/Geophysical Okhotsk Sea Research, Vladivostok - Pusan - Okhotsk Sea - Pusan - Vladivostok, September 7 - October 12, 1995. Geomar Reports.

Lapko, V. V., and Radchenko, V. I. (2000). Sea of Okhotsk. *Mar. Pollut. Bull.* 41, 179–187. doi:10.1016/s0025-326x(00)00109-0

Li, M., Hinnov, L., and Kump, L. (2019). Acycle: Time-Series Analysis Software for Paleoclimate Research and Education. *Comput. Geosciences* 127, 12–22. doi:10.1016/j.cageo.2019.02.011

Lisiecki, L. E., and Raymo, M. E. (2005). A Pliocene-Pleistocene Stack of 57 Globally Distributed Benthic δ18O Records. *Paleoceanography* 20, PA1003. doi:10.1029/2004pa001071

Lo, L., Belt, S. T., Lattaud, J., Friedrich, T., Zeeden, C., Schouten, S., et al. (2018). Precession and Atmospheric CO2 Modulated Variability of Sea Ice in the central Okhotsk Sea since 130,000 Years Ago. *Earth Planet. Sci. Lett.* 488, 36–45. doi:10.1016/j.epsl.2018.02.005

Martin, S., and Kawase, M. (1998). The Southern Flux of Sea Ice in the Tatarskiy Strait, Japan Sea and the Generation of the Liman Current. *J. Mar. Res.* 56, 141–155. doi:10.1357/002224098321836145

Mayewski, P. A., Meeker, L. D., Whitlow, S., Twickler, M. S., Morrison, M. C., Bloomfield, P., et al. (1994). Changes in Atmospheric Circulation and Ocean Ice Cover over the North Atlantic During the Last 41,000 Years. *Science* 263, 1747–1751. doi:10.1126/science.263.5154.1747

Mclennan, S. M. (2013). Sediments and Soils: Chemistry and Abundances. *Rock Physics & Phase Relations*. Washington: American Geophysical Union (AGU).

Morley, J. J., and Hays, J. D. (1983). Oceanographic Conditions Associated with High Abundances of the Radiolarian Cycladophora Davisiana. *Earth Planet. Sci. Lett.* 66, 63–72. doi:10.1016/0012-821x(83)90126-7

Mortlock, R. A., and Froelich, P. N. (1989). A Simple Method for the Rapid Determination of Biogenic Opal in Pelagic marine Sediments. *Deep Sea Res. A. Oceanographic Res. Pap.* 36, 1415–1426. doi:10.1016/0198-0149(89)90092-7

Narita, H., Sato, M., Tsunogai, S., Murayama, M., Ikehara, M., Nakatsuka, T., et al. (2002). Biogenic Opal Indicating Less Productive Northwestern North Pacific during the Glacial Ages. *Geophys. Res. Lett.* 29, 22–31. doi:10.1029/2001gl014320

Nürnberg, D., Dethleff, D., Tiedemann, R., Kaiser, A., and Gorbarenko, S. A. (2011). Okhotsk Sea Ice Coverage and Kamchatka Glaciation over the Last 350ka - Evidence from Ice-Rafted Debris and Planktonic δ18O. *Palaeogeogr. Palaeoclimatol. Palaeoecol.* 310, 191–205. doi:10.1016/j.palaeo.2011.07.011

Nürnberg, D., and Tiedemann, R. (2004). Environmental Change in the Sea of Okhotsk during the Last 1.1 Million Years. *Paleoceanography* 19, PA4011. doi:10.1029/2004pa001023

Ogi, M., and Tachibana, Y. (2006). Influence of the Annual Arctic Oscillation on the Negative Correlation between Okhotsk Sea Ice and Amur River Discharge. *Geophys. Res. Lett.* 33. doi:10.1029/2006gl025838

Ogi, M., Tachibana, Y., Nishio, F., and Danchenkov, M. A. (2001). Does the Fresh Water Supply from the Amur River Flowing into the Sea of Okhotsk Affect Sea Ice Formation? *J. Meteorol. Soc. Jpn.* 79, 123–129. doi:10.2151/jmsj.79.123

Ohshima, K. I., Mizuta, G., Itoh, M., Fukamachi, Y., Watanabe, T., Nabae, Y., et al. (2001). Winter Oceanographic Conditions in the Southwestern Part of the Okhotsk Sea and Their Relation to Sea Ice. *J. Oceanogr.* 57, 451–460. doi:10.1023/a:1021225303621

Ohtani, K., and Nagata, Y. (1990). The Role of the Okhotsk Sea on the Formation of the Oyashio Water. *EOS Trans. Am. Geophys. Union* 71 (28), 811.

Parkinson, C. L., Comiso, J. C., Zwally, H. J., Cavalieri, D. J., Gloersen, P., Campbell, W. J. J. S., et al. (1987). *Arctic Sea Ice, 1973-1976: Satellite Passive-Microwave observations*. Washington: NASA SP-459.

Rycroft, M. J. (1995). Arctic and Antarctic Sea Ice, 1978-1987: Satellite Passive-Microwave Observations and Analysis. *J. Atmos. Terrestrial Phys.* 57, 445. doi:10.1016/0021-9169(95)90010-1

Sakamoto, T., Ikehara, M., Aoki, K., Iijima, K., Kimura, N., Nakatsuka, T., et al. (2005). Ice-rafted Debris (IRD)-based Sea-Ice Expansion Events during the Past 100kyrs in the Okhotsk Sea. *Deep Sea Res. Part Topical Stud. Oceanography* 52, 2275–2301. doi:10.1016/j.dsr2.2005.08.007

Sakamoto, T., Ikehara, M., Uchida, M., Aoki, K., Shibata, Y., Kanamatsu, T., et al. (2006). Millennial-scale Variations of Sea-Ice Expansion in the Southwestern Part of the Okhotsk Sea during the Past 120 Kyr: Age Model and Ice-Rafted Debris in IMAGES Core MD01-2412. *Glob. Planet. Change* 53, 58–77. doi:10.1016/j.gloplacha.2006.01.012

Schlitzer, R. (2021). Ocean Data View. Available at: odv.awi.de

Seki, O., Ikehara, M., Kawamura, K., Nakatsuka, T., Ohnishi, K., Wakatsuchi, M., et al. (2004). Reconstruction of Paleoproductivity in the Sea of Okhotsk over the Last 30 Kyr. *Paleoceanography* 19, PA1016. doi:10.1029/2002pa000808

Serreze, M. C., Stroeve, J., Barrett, A. P., and Boisvert, L. N. (2016). Summer Atmospheric Circulation Anomalies over the Arctic Ocean and Their Influences on September Sea Ice Extent: A Cautionary Tale. *J. Geophys. Res. Atmos.* 121 (11), 11463–11485. doi:10.1002/2016jd025161

Stuiver, M., and Reimer, P. J. (1993). Extended 14C Data Base and Revised CALIB 3.0 14C Age Calibration Program. *Radiocarbon* 35, 215–230. doi:10.1017/S0033822200013904

Talley, L. D. (1993). Distribution and Formation of North Pacific Intermediate Water. *J. Phys. Oceanogr.* 23, 517–537. doi:10.1175/1520-0485(1993)023<0517:Dafonp>2.0.Co;2

Talley, L. D. (1991). An Okhotsk Sea Water Anomaly: Implications for Ventilation in the North Pacific. *Deep Sea Res. Part A. Oceanographic Res. Pap.* 38, S171–S190. doi:10.1016/s0198-0149(12)80009-4

Thompson, D. W. J., and Wallace, J. M. (1998). The Arctic Oscillation Signature in the Wintertime Geopotential Height and Temperature fields. *Geophys. Res. Lett.* 25, 1297–1300. doi:10.1029/98GL00950

Turner, J., Hosking, J. S., Marshall, G. J., Phillips, T., and Bracegirdle, T. J. (2015). Antarctic Sea Ice Increase Consistent with Intrinsic Variability of the Amundsen Sea Low. *Clim. Dyn.* 46, 2391–2402. doi:10.1007/s00382-015-2708-9

Vasilenko, Y. P., Gorbarenko, S. A., Bosin, A. A., Artemova, A. V., Yanchenko, E. A., Shi, X.-F., et al. (2019). Orbital-scale Changes of Sea Ice Conditions of Sea of Okhotsk during the Last Glaciation and the Holocene (MIS 4-MIS 1). *Palaeogeogr. Palaeoclimatol. Palaeoecol.* 533, 109284. doi:10.1016/j.palaeo.2019.109284

Vasilenko, Y. P., Gorbarenko, S. A., Bosin, A. A., Shi, X.-F., Chen, M.-T., Zou, J.-J., et al. (2017). Millennial Mode of Variability of Sea Ice Conditions in the Okhotsk Sea during the Last Glaciation (MIS 4-MIS 2). *Quat. Int.* 459, 187–200. doi:10.1016/j.quaint.2017.09.039

Vörösmarty, C., Fekete, B. M., and Tucker, B. A. (1996). Global River Discharge Database RivDis v1.0. Technical Documents in Hydrology, UNESCO. 1–1008.

Wang, K.-S., Shi, X., Zou, J., Kandasamy, S., Gong, X., Wu, Y., Yan, Q., et al. (2017). Sediment Provenance Variations in the Southern Okhotsk Sea over the Last 180 Ka: Evidence from Light and Heavy Minerals. *Palaeogeogr. Palaeoclimatol. Palaeoecol.* 479, 61–70. doi:10.1016/j.palaeo.2017.04.017

Wang, K., Shi, X., Zou, J., Liu, Y., Yao, Z., and Gorbarenko, S. A. (2021). Spatial Distribution and Provenance of Detrital Minerals of Surface Sediment in the Okhotsk Sea. *Front. Earth Sci.* 9, 636850. doi:10.3389/feart.2021.636850

Wang, W., and Wang, L. (2008). Reconstruction of Oceanographic Changes Based on the Diatom Records of the Central Okhotsk Sea over the Last 500000 Years. *Terr. Atoms. Ocean. Sci.* 19, 403–411. doi:10.3319/tao.2008.19.4.403

Wong, C. S., Matear, R. J., Freeland, H. J., Whitney, F. A., and Bychkov, A. S. (1998). WOCE Line P1W in the Sea of Okhotsk: 2. CFCs and the Formation Rate of Intermediate Water. *J. Geophys. Res.* 103, 15625–15642. doi:10.1029/98jc01008

Yang, J., and Honjo, S. (1996). Modeling the Near-Freezing Dichothermal Layer in the Sea of Okhotsk and its Interannual Variations. *J. Geophys. Res.* 101, 16421–16433. doi:10.1029/96JC01091

Yasuda, I. (1997). The Origin of the North Pacific Intermediate Water. *J. Geophys. Res.* 102, 893–909. doi:10.1029/96jc02938

Zhabin, I. A., Abrosimova, A. A., Dubina, V. A., and Nekrasov, D. A. (2010). Influence of the Amur River Runoff on the Hydrological Conditions of the Amur Liman and Sakhalin Bay (Sea of Okhotsk) during the spring-summer Flood. *Russ. Meteorol. Hydrol.* 35, 295–300. doi:10.3103/s1068373910040084

Zou, J., Shi, X., Zhu, A., Chen, M.-T., Kao, S., Wu, Y., et al. (2015). Evidence of Sea Ice-Driven Terrigenous Detritus Accumulation and Deep Ventilation Changes in the Southern Okhotsk Sea during the Last 180ka. *J. Asian Earth Sci.* 114, 541–548. doi:10.1016/j.jseaes.2015.07.020

Conflict of Interest: The authors declare that the research was conducted in the absence of any commercial or financial relationships that could be construed as a potential conflict of interest.

frontiers
in Earth Science

ORIGINAL RESEARCH
published: 29 July 2021
doi: 10.3389/feart.2021.679689

Reconstructing the Climate Variability During the Last 5000 Years From the Banni Plains, Kachchh, Western India

Nisarg Makwana[1], S. P. Prizomwala[1], Archana Das[1], Binita Phartiyal[2], Aashima Sodhi[1,3] and Chintan Vedpathak[1,3]*

[1]Institute of Seismological Research, Gandhinagar, India, [2]Birbal Sahni Institute of Paleosciences, Lucknow, India, [3]Research Scholar, Gujarat University, Ahmedabad, India

The climatic conditions during the beginning of the last 5,000 years have been discussed, debated, and documented from various parts of the Indian subcontinent, due to the human–climate interrelationship. In the present study, we report a multi-proxy dataset encompassing the widely used ~ geochemical and mineral magnetic proxies supported by radiocarbon and optical chronologies from the Banni Plains of the Rann of Kachchh, western India. Our results support the earlier observations of the prolonged wetter climatic condition synchronous with the mature phase of Harappan era which witnessed a short and intense arid condition at the terminal part of the mature Harappan phase. The climate system dramatically fluctuated during the last five millennia from pulsating between relatively arid (4,800–4,400 years BP, 3,300–3,000 years BP, and at 2,400 years BP) and relatively humid phases (>4,800 years BP, 4,000–3,300 years BP, 1900–1,400 years BP, and 900–550 years BP). The multi-proxy dataset shows a gradual strengthening of the monsoonal conditions from the Banni Plains during the late Harappan phase. Apart from this, the high sedimentation rate (>1 mm/yr) recorded from the Banni Plains suggests it can be tapped as a robust archive to reconstruct multi-decadal to centennial climatic events spanning the Holocene epoch.

Keywords: paleoclimate, Banni plains, middle to late Holocene, Kachchh, Harappan civilization 2

Edited by:
Hema Achyuthan,
Anna University, India

Reviewed by:
Yu Li,
Lanzhou University, China
Aasif Mohmad Lone,
Indian Institute of Science Education and Research, India

****Correspondence:***
Archana Das
rchndas7@gmail.com

Specialty section:
This article was submitted to Quaternary Science, Geomorphology and Paleoenvironment, a section of the journal Frontiers in Earth Science

Received: *12 March 2021*
Accepted: *28 June 2021*
Published: *29 July 2021*

Citation:
Makwana N, Prizomwala SP, Das A, Phartiyal B, Sodhi A and Vedpathak C (2021) Reconstructing the Climate Variability During the Last 5000 Years From the Banni Plains, Kachchh, Western India. Front. Earth Sci. 9:679689. doi: 10.3389/feart.2021.679689

INTRODUCTION

Southwest Indian monsoon has a high socioeconomic impact as it plays a key role in delivering annual rainfall (nearly 80%) in the Indian subcontinent (Anderson et al., 2010; Berkelhammer et al., 2010). An understanding of the variability of Indian summer monsoon (ISM) rainfall for the Holocene epoch is vitally required to assess the speculated link between the climate deterioration and the decline in ancient civilization. The mid-Holocene, in particular, has witnessed several changes in climate with abrupt short events recorded globally as well as in the Indian subcontinent (Lamb, 1985; Bianchi and Mc Cave, 1999; Anderson et al., 2010; Sanwal et al., 2013; Quamar and Chauhan, 2014; Ngangom et al., 2016). Prasad et al. (2007), Prasad et al. (2014 b) reported wetter climate during the 5.5 to 2.8 ka BP from the lacustrine environments of Mainland Gujarat. Similarly, Laskar et al. (2013) reported subhumid climatic conditions from fluvial sediments of the Mainland Gujarat region. The period between 2.8 and 1.3 ka has reportedly experienced arid conditions from the lacustrine and fluvial records of Mainland Gujarat (Laskar et al., 2013a; Prasad V. et al., 2014; Sridhar et al., 2014a). Raja et al. (2019) reported paleoflood activity during 4,773 cal yr BP from the Parsons Valley Lake, Tamil Nadu. Consequently, the mid-to-late Holocene tend to have recorded various centennial scaled abrupt climatic variations. However, studies documenting the climatic variations on the centennial to decadal scale are still limited and need to be looked upon (Binanchi and Mc Cave, 1999; Gupta et al., 2003; Sinha et al., 2007; Chauhan et al., 2009; Makwana et al., 2019).

The Great Rann of Kachchh (GRK) in western India is a semi-enclosed basin and a dominantly depositional microenvironment, and hence the paleo-mudflats of Rann have proven to be useful to decipher past climatic oscillation in different timescales (Pillai et al., 2017, 2018; Basu et al., 2019; Makwana et al., 2019). The recent efforts have hinted that the Rann sediments remain a treasure trove for reconstructing Holocene paleoclimate (Ngangom et al., 2016; Pillai et al., 2017, 2018; Basu et al., 2019; Makwana et al., 2019; Sengupta et al., 2019; Sarkar et al., 2020). The Rann of Kachchh is believed to be a Holocene sediment depocenter (Maurya et al., 2013) and also has been a hotspot of mature and late Harappan occupation, which believed to be a riverine and trade-oriented civilization during 7000 BP to 3900 BP (Gaur et al., 2013; Sarkar et al., 2020). Large urban centers of mature Harappan settlements flourished along the Indus and Ghaggar-Hakra rivers (Possehl, 2002), and were considered to have abruptly ended around 3,900 years BP (Possehl, 2002). Also, the mid-Holocene climatic changes are coincident with the appearance of highly organized and urbanized civilizations from the Afro-Asiatic monsoonal region such as Egypt, Mesopotamia, Indus-Saraswati, and in northern China regions that form the bulk of the deserts today (Brooks, 2006; Prasad V. et al., 2014). However, the reasons for the decline of these civilizations, *viz.* abrupt climate change, sea level fluctuation, or reduction of natural resources, are still a question of debate for the researchers (Galili 1988; Staubwasser et al., 2003; Wright et al., 2008; Giosan et al., 2012; Dixit et al., 2014, 2018; Das et al., 2017; Sengupta et al., 2019).

Some of the intriguing questions regarding the paleoclimatic conditions, particularly, in the Kachchh region of western India are as follows: 1) What were the paleoenvironmental conditions that existed in the Banni Grassland during the middle-to-late Holocene? 2) How did the climatic fluctuations change since the mature Harappan times? In light of this, the objective of the present study is to reconstruct the past climatic events from the Banni Plains and explore their nature/boundary conditions during the last 5,000 years using a multi-proxy dataset.

STUDY AREA

The GRK is a unique and intriguing vast salt encrusted flat land, which is an E–W trending subbasin and occupies almost half of the area of the seismically active Kachchh paleo-rift basin (Burnes, 1834; Glennie and Evans, 1976; Biswas, 1987). The Banni Plain is a part of the extensive low-level hyper arid saline tract of the Great Rann that occupies the northern part of the seismically active Kachchh paleo-rift basin. The Banni grassland happens to be only the inhabited part of the Great Rann due to the fact that it occurs at the highest elevation and is free of present-day marine submergence (Roy and Merh, 1981). Large parts of the Banni get submerged during monsoon under a thin sheet of water by rainfall and rivers from the Kachchh mainland in the south.

The present study site BKR (23°32′48.12″N and 69°40′30.36″E) is situated in the central to the northern part of the Banni Plains (**Figure 1**). The Banni Plains and the GRK are covered by the quaternary deposits mostly comprising silt and clay sediments and considered as Holocene depocenters (Gupta, 1975; Maurya et al., 2013; Khonde et al., 2017a; Makwana et al., 2019) of three distinct sources, *viz.* Indus source from north, Aravalli in east, and Kachchh Mainland in south (Maurya et al., 2013; Khonde et al., 2017a, b). It experiences a hyper-arid to arid climate with annual rainfall less than 30 mm per year (**Figure 1**). However, till now there are limited data pertaining to the paleoclimate, provenance, and the nature of sediment comprising the Banni Plain. With an aim to study the evolution of these majestic landscape features, which probably beholds vital insights on middle-to-late Holocene climatic fluctuations, a shallow trench from the paleo-mudflat of the Banni Grassland has been investigated. Trench is 5.5 m deep (BKR site) and located on Bhuj-Khavda road (**Figure 1**) in the Banni Plains. Geomorphologically, the study site is surrounded by higher Banni surface with an elevation varying from 4 to 12 m amsl. The elevation of the trench site was 4.4 m above the present day mean sea level (msl) measured based on a D-GPS survey. The studied site is away from any human settlement, which assures negligible to nil anthropological effect.

ANALYTICAL METHODS

Sediment Geochemistry

Al_2O_3, Fe_2O_3, and TiO_2 are the major components of the aluminosilicate phase group and are useful to deduce the post depositional weathering and paleoenvironmental condition that prevailed in the region (Nesbitt and Young, 1982; Agnihotri et al., 2003; Tyagi et al., 2012; Das et al., 2017). Similarly, the ratio of K_2O/Al_2O_3 and CIA (Chemical Index of Alteration) has been used to measure the chemical weathering intensity in the region (Nesbitt and Young, 1982; Buggle et al., 2011; Pillai et al., 2018). The natural samples in the near-shore and marine-influenced environments may contain CaO content, originating from marine organisms. Hence, the samples collected from the field were treated with 1 N HCl until the CaO fraction was removed. These decarbonated samples were then used for estimating CIA, which represents the detrital content, originating due to the chemical weathering in the source region. A total of 55 samples were collected from the BKR site and dried at 50°C, crushed, homogenized, and sieved to <63 μm size. A part of this fraction was used for the analysis in XEPOS HE XRF instrument at the Institute of Seismological Research, India. The analytical precision of major oxide was better than 5% and that of trace elements was better than 10% (Das et al., 2017; Makwana et al., 2019).

Mineral Magnetic Measurements

Environmental magnetic properties of sediment samples were measured using standard rock magnetic methods (Walden et al.,

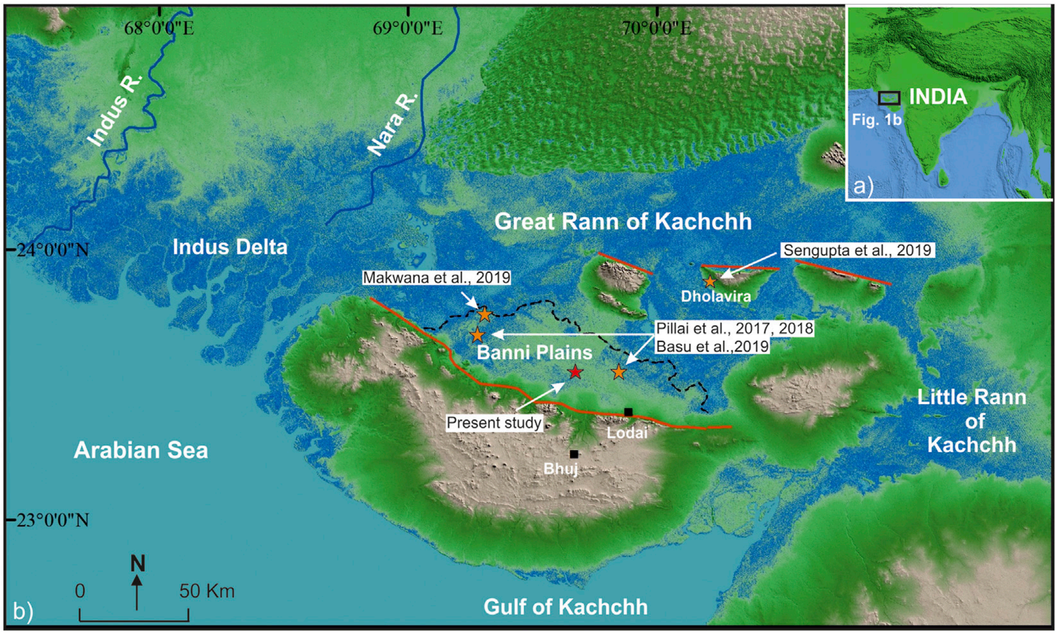

FIGURE 1 | Digital elevation model of Kachchh showing the location of the study area and trench site in Kachchh.

1999; Warrier and Shankar, 2009; Basavaiah, 2011). Selected samples were oven-dried and packed, ensuring no movement of magnetic minerals in nonmagnetic plastic bottles of 10 cm^3 for analysis. In the present study, we have measured magnetic susceptibility (χ), anhysteretic remnant magnetization (ARM), and isothermal remnant magnetization (IRM) at Birbal Sahni Institute of Palaeosciences, Lucknow, India. Low magnetic susceptibility (χ_{LF}) was measured using a Bartigton MS2B dual-frequency susceptibility meter at 976 Hz frequency. Samples were first demagnetized by using the AF demagnetizer, and then anhysteretic remnant magnetization (ARM) was calculated in a steady 0.05_{mT} field superimposed over decreasing alternating field (AF) up to 100_{mT} using the alternating field demagnetizer, D-2000 AF demagnetizer. The remnant magnetization of all ARMs and IRMs was measured using a AGICO JR-6 dual speed spinner magnetometer. Isothermal remnant magnetization (IRM) was measured at forward fields of 20 and 1000_{mT} and backward fields of −20, −40, −60, −100, and -300_{mT} using ASC scientific impulse magnetizer. IRM measured at 1_T field was considered as saturation isothermal remnant magnetization (SIRM). The S-ratio is indicative of the ferrimagnetic vs. anti-ferrimagnetic minerals, and the value close to one corresponds to the dominance of the ferrimagnetic minerals. S-ratio is often used as paleo-monsoonal proxy calculated using the formula $IRM_{-0.3T}$/SIRM (Basavaiah and Khadkikar, 2004).

AMS C-14 Dating

AMS is a modern and more efficient radiocarbon dating method for younger time frames to measure long-lived radionuclide that occurs naturally in environment. We have used two different samples of handpicked foraminifera from unit 2 to estimate the age of sediment deposition. Foraminifera tests were separated out from the samples and sent to Poznan Radiocarbon Laboratory, Poland, for AMS ^{14}C dating. For both the uncalibrated ages, we used a marine reservoir effect (ΔR) of −8 ± 37 from northern Arabian Sea, as it was the closest possible value available from the studied point and represented similar semi-enclosed environment (Dutta et al., 2001). We used the latest available online CALIB 8.2 program for Marine13 dataset (Stuiver et al., 2018). Calibrated ages are expressed as calendar years over a 2σ-error range (95.4%).

TABLE 1 | Lithostratigraphic information for the BKR trench site, Kachchh.

Litho-units	Thickness (in cm)	Textural class
Unit-3	170	Clayey silt horizon with faint laminations
Unit-2	330	Silty clay horizon
Unit-1	70	Sticky dark bluish clay horizon

RESULTS

Stratigraphy and Chronology of the BKR Trench

Based on the visual observations of sedimentological, textural, structures and variation in color, the entire succession was divided into three major litho-units (**Table 1**). At the BKR trench site, the bottommost exposed unit is a 70-cm-thick sticky dark bluish clay horizon (unit-1), followed by a 330-cm-thick brown silty clay deposit (unit-2). The foraminifera tests were collected from this unit, which yielded a calibrated AMS ^{14}C age of 3,157–3,520 cal yr BP (median value: 3,339 ± 181 cal yr BP)

TABLE 2 | AMS^{14}C ages and calibrated ages of the foraminifera from the BKR trench site, Kachchh.

Sample ID	Depth of sample (m)	Conventional C^{14} radiocarbon age (yr BP)	Calibrated age (cal yr BP, ± 2σ)	Median age (cal yr BP, ± 2σ)
POZ-101421	2.3	3,600 ± 35	3,157–3,520	3,339 ± 181
POZ-112296	4.1	4,460 ± 220	3,833–5,032	4,432 ± 600

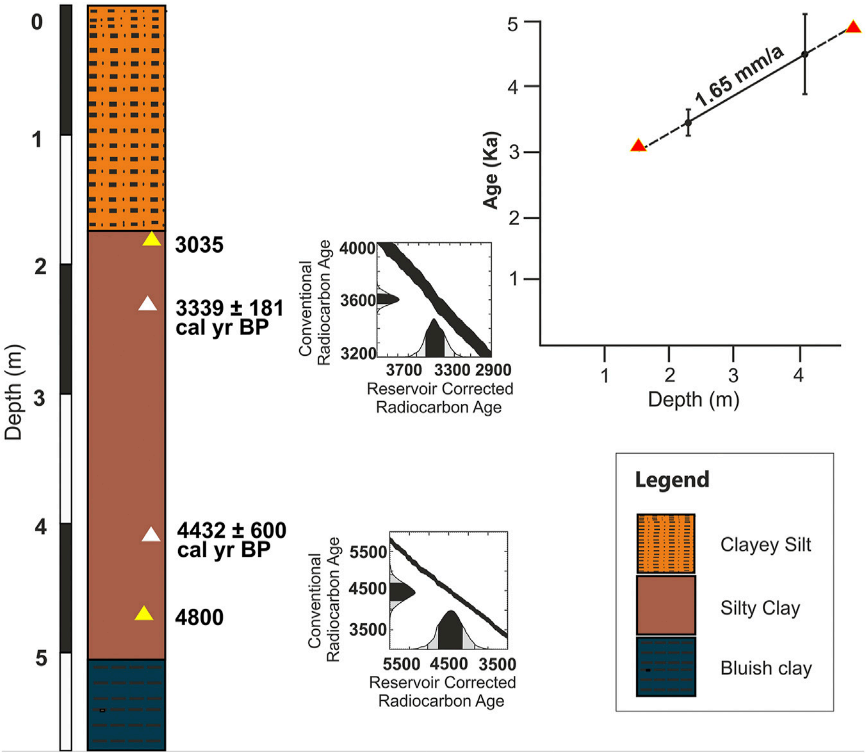

FIGURE 2 | Stratigraphy and the age depth model for the BKR trench site.

and 3,833–5,032 cal yr BP (median value: 4,432 ± 600 cal yr BP) (**Table 2**) at depth of 2.3 and 4.1 m, respectively, from the top of the trench surface. Unit-2 is overlain by 170-cm-thick clayey silt dominated horizon with faint laminations, that is, Unit-3 (**Figure 2**). Owing to the lack of datable material and negligible amount of foraminifers, the bottom age of 4,432 ± 600 cal yr BP shows a wider error scatter, due to mixing of foraminifer tests from two adjacent samples. Hence, due to the lack of available chronology, we assumed a relatively uniform sedimentary sequence in Unit-2 to extrapolate two ages, that is, 4,800 years BP and 3,035 years BP on the basis of the sedimentation rate between the dated depths.

Major Oxide Concentration and Their Elemental Ratio Variation

The concentration of major oxides and trace elements along with their ratios were studied and based on significant deviations in statistical parameters; a total of three relatively arid and four humid phases of paleoclimatic conditions are deduced (**Supplementary Table 1**).

Zone 1

Zone 1 encompassing the concentration variation of Al_2O_3, Fe_2O_3, and TiO_2 from 14.33 to 15.62%, 4.75 to 5.48%, and 0.73 to 0.80%, respectively. The oxide ratios of K_2O/Al_2O_3, Na_2O/TiO_2, CaO/TiO_2, and Fe_2O_3/TiO_2 varied from 0.17 to 0.19, 1.58 to 2.56, 11.34 to 12.52, and 6.50 to 6.91, respectively. Similarly, the elemental concentration of Sr and Ca varied from 202 to 211 ppm and 6.3 to 6.7%, respectively. The ratios of Zr/Al varied from 15.1 to 21.0. The values of weathering intensity CIA varied from 82 to 85 (**Supplementary Table 1**).

Zone 2

Zone 2 shows the concentration of Al_2O_3, Fe_2O_3, and TiO_2 varied from 13.9 to 15.2%, 4.2 to 5.4%, and 0.76 to 0.81%, respectively. The oxide ratios of K_2O/Al_2O_3, Na_2O/TiO_2, CaO/TiO_2, and Fe_2O_3/TiO_2 varied from 0.17 to 0.19, 1.6 to 2.1, 11.3 to 12.8, and 5.6 to 6.7, respectively. Similarly, the elemental concentration of Sr and Ca varied from 207 to 223 ppm and 6.4 to 6.9%, respectively. The ratios of Zr/Al varied from 19.0 to 26.5. The values of weathering intensity CIA varied from 79 to 83 (**Supplementary Table 1**).

Zone 3

Zone 3 suggests the concentration of Al_2O_3, Fe_2O_3, and TiO_2 varied from 16.0 to 16.7%, 5.3 to 6.9%, and 0.78 to 0.86%, respectively. The oxide ratios of K_2O/Al_2O_3, Na_2O/TiO_2, CaO/TiO_2, and Fe_2O_3/TiO_2 varied from 0.18 to 0.21, 1.3 to 1.6, 9.3 to 11.4, and 6.6 to 8.0, respectively. Similarly, the elemental concentration of Sr and Ca varied from 179 to 205 ppm and 5.7 to 6.5%, respectively. The ratios of Zr/Al varied from 10.0 to 15.4. The values of weathering intensity CIA varied from 84 to 88 (**Supplementary Table 1**).

Zone 4

Zone 4 suggests the concentration of Al_2O_3, Fe_2O_3, and TiO_2 varied from 14.3 to 15.3%, 4.1 to 5.1%, and 0.71 to 0.76%, respectively. The oxide ratios of K_2O/Al_2O_3, Na_2O/TiO_2, CaO/TiO_2, and Fe_2O_3/TiO_2 varied from 0.16 to 0.18, 1.7 to 2.1, 12.0 to 13.4, and 5.8 to 6.7, respectively. Similarly, the elemental concentration of Sr and Ca varied from 204 to 218 ppm and 6.5 to 6.8%, respectively. The ratios of Zr/Al varied from 16.5 to 20.2. The values of weathering intensity CIA varied from 82 to 85 (**Supplementary Table 1**).

Zone 5

Zone 5 suggests the concentration of Al_2O_3, Fe_2O_3, and TiO_2 varied from 13.7 to 16.4%, 3.9 to 5.1%, and 0.65 to 0.77%, respectively. The oxide ratios of K_2O/Al_2O_3, Na_2O/TiO_2, CaO/TiO_2, and Fe_2O_3/TiO_2 varied from 0.16 to 0.17, 1.72 to 1.88, 11.8 to 15.8, and 5.7 to 6.7, respectively. Similarly, the elemental concentration of Sr and Ca varied from 199 to 220 ppm and 6.3 to 7.3%, respectively. The ratios of Zr/Al varied from 14.8 to 21.2. The values of weathering intensity CIA varied from 82 to 86 (**Supplementary Table 1**).

Zone 6

Zone 6 suggests the concentration variation of Al_2O_3, Fe_2O_3, and TiO_2 between 13.2–13.5%, 3.4–3.8%, and 0.61–0.73%, respectively. The oxide ratios of K_2O/Al_2O_3, Na_2O/TiO_2, CaO/TiO_2, and Fe_2O_3/TiO_2 varied from 0.16 to 0.17, 1.5 to 1.9, 14.6 to 17.8, and 5.3 to 6.0, respectively. Similarly, the elemental concentration of Sr and Ca varied from 224 to 229 ppm and 7.3 to 7.7%, respectively. The ratios of Zr/Al varied from 16.5 to 24.2. The values of weathering intensity CIA varied from 79 to 81 (**Supplementary Table 1**).

Zone 7

Zone 7 suggests the concentration of Al_2O_3, Fe_2O_3, and TiO_2 varied between 14.5–16.8%, 4.5–7.0%, and 0.79–0.98%, respectively. The oxide ratios of K_2O/Al_2O_3, Na_2O/TiO_2, CaO/TiO_2, and Fe_2O_3/TiO_2 varied from 0.18 to 0.20, 0.9 to 1.4, 5.6 to 12.2, and 5.6 to 7.9, respectively. Similarly, the elemental concentration of Sr and Ca varied from 161 to 216 ppm and 3.7 to 6.9%, respectively. The ratios of Zr/Al varied from 11.5 to 24.8. The values of weathering intensity CIA varied from 83 to 89 (**Supplementary Table 1**).

Mineral Magnetic Variations

Zone 1

Zone 1 shows the magnetic susceptibility (χ_{LF}) values varied between $1.18 \times 10^{-8}\,\mathrm{m}^3/\mathrm{kg}$ and $1.97 \times 10^{-8}\,\mathrm{m}^3/\mathrm{kg}$, while the values of SIRM and χ_{arm} varied between 1.23–1.84 and 1.45×10^{-5}–5.88×10^{-5}, respectively. The increasing concentrations of $\chi_{\mathrm{LF.}}$ SIRM, and χ_{arm} are indicative of the ferrimagnetic mineral signals. However, decreasing concentration of these parameters implies dominance of the anti-ferrimagnetic minerals within the section. Values of the S-ratio varied from 0.62 to 0.74, indicating the presence of low coercivity minerals (**Supplementary Table 2**).

Zone 2

Zone 2 shows the magnetic susceptibility (χ_{LF}) values varied between $1.55 \times 10^{-8}\mathrm{m}^3/\mathrm{kg}$ and $1.56 \times 10^{-8}\mathrm{m}^3/\mathrm{kg}$, while the values of SIRM and χ_{arm} varied between 1.51–1.67 and 2.61×10^{-5}–3.60×10^{-5}, respectively. Values of the S-ratio varied from 0.63 to 0.66 (**Supplementary Table 2**).

Zone 3

Zone 3 suggests the magnetic susceptibility (χ_{LF}) values varied between $1.46 \times 10^{-8}\mathrm{m}^3/\mathrm{kg}$ and $1.87 \times 10^{-8}\mathrm{m}^3/\mathrm{kg}$, while the values of SIRM and χ_{arm} varied between 1.39–2.16 and 2.82×10^{-5}–10×10^{-5}, respectively. Values of the S-ratio varied from 0.60 to 0.74 (**Supplementary Table 2**).

Zone 4

Zone 4 suggests the magnetic susceptibility (χ_{LF}) values varied between $1.82 \times 10^{-8}\mathrm{m}^3/\mathrm{kg}$ and $1.88 \times 10^{-8}\mathrm{m}^3/\mathrm{kg}$, while the values of SIRM and χ_{arm} varied between 2.17–2.19 and 8.5×10^{-5}–8.9×10^{-5}, respectively. Values of the S-ratio varied from 0.76 to 0.77 (**Supplementary Table 2**).

Zone 5

Zone 5 suggests the magnetic susceptibility (χ_{LF}) values varied between $1.66 \times 10^{-8}\mathrm{m}^3/\mathrm{kg}$ and $1.86 \times 10^{-8}\mathrm{m}^3/\mathrm{kg}$, while the values of SIRM and χ_{arm} varied between 1.98–2.19 and 7.10×10^{-5}–8.50×10^{-5}, respectively. Values of the S-ratio varied from 0.73 to 0.74 (**Supplementary Table 2**).

Zone 6

Zone 6 suggests the magnetic susceptibility (χ_{LF}) values varied between 1.56×10^{-8}m3/kg and 1.58×10^{-8}m3/kg, while the values of SIRM and χ_{arm} varied between 1.76–1.79 and 5.71×10^{-5}–6.12×10^{-5}, respectively. Values of the S-ratio varied from 0.75 to 0.77 (**Supplementary Table 2**).

Zone 7

Zone 7 suggests the magnetic susceptibility (χ_{LF}) values varied between $1.68 \times 10^{-8}\mathrm{m}^3/\mathrm{kg}$ and $2.37 \times 10^{-8}\mathrm{m}^3/\mathrm{kg}$, while the values of SIRM and χ_{arm} varied between 1.91–2.76 and 6.82×10^{-5}–12.8×10^{-5}, respectively. Values of the S-ratio varied from 0.76 to 0.78 (**Supplementary Table 2**).

DISCUSSION

Approach: Role of Geochemistry and Magnetic Minerals in Paleoclimatic Reconstructions

The concentration of various oxides and elements is often derivative of weathering processes acting in the catchment of the basins. Major elemental concentration in sediments, mineral magnetics, and grain size often reflects the source of the origin, which were being used as effective proxies to demonstrate the intensity of chemical weathering, climate changes, and precipitation variations in the region (Staubwasser and Sirocko 2002; Yancheva et al., 2007; Tyagi et al., 2012; Clift et al., 2014; Das et al., 2017; Pillai et al., 2018; Ruifeng et al., 2020). The ratios like Na_2O/TiO_2, CaO/TiO_2, and Fe_2O_3/TiO_2 can be used to infer the changes in the paleoenvironmental condition (Pillai et al., 2018; Makwana et al., 2019). Increased values of Fe_2O_3/TiO_2 with lower values of Na_2O/TiO_2 and CaO/TiO_2 suggest increased precipitation, owing to the depletion of mobile elements like Ca and Na during erosion triggered by enhanced monsoon (Muhs et al., 2001; Kotlia and Joshi, 2013; Minyuk et al., 2013; Pillai et al., 2018). Hence, we assess the higher values of oxides like Al_2O_3, Fe_2O_3, and TiO_2 along with K_2O/Al_2O_3 and CIA (Chemical Index of Alteration) to mimic the enhanced monsoonal strength (Buggle et al., 2011; Pillai et al., 2018; Makwana et al., 2019). Similarly, concentration of magnetic minerals and their mineralogy have widely been used as surrogate to study the strength of the ISM (Basavaiah and Khadkikar, 2004; Warriar and Shankar, 2009). Magnetic susceptibility (χ) is controlled by the concentration and the grain-size distribution of ferromagnetic minerals and is strongly sensitive to variations of the local climate and constitutes an accurate proxy record, along with other parameters (Thompson and Oldfield, 1986; Phartiyal et al., 2003). The cumulative response of major oxide, elemental, CIA, and mineral magnetic properties is often touted to be a robust indicator of weathering intensity and is considered as a surrogate for reconstructing monsoonal strength (Warriar and Shankar, 2009; Prasad et al., 2007; 2014; Makwana et al., 2019).

Climatic Variability in Banni Plains Since the Mid-Holocene

Kachchh region in the western India experiences an arid climate and has attracted tremendous attention for its tectonic attributes (Chamyal et al., 2003). However, the landscape and its modulation with climatic forcings during the Holocene have been least explored (Pillai et al., 2017, 2018; Basu et al., 2019; Makwana et al., 2019; Sengupta et al., 2019). Our results reveal several alternate phases of wet and dry paleoclimatic conditions during the last five millennia from the Banni Plains (**Figure 3**).

Prior to 4,800 cal yr BP (Phase I)

The zone is marked by higher CIA values and other major elemental proxies, suggesting a higher chemical weathering under the relatively humid climatic regime (**Figure 4**). This is further indicated by the higher concentration of detrital components such as Al_2O_3, TiO_2, and Fe_2O_3 vs. reduction of Na_2O/TiO_2, CaO/TiO_2, Zr/Al, CaO, and Sr (Peterson et al., 2000; Luckge et al., 2001; Kotlia and Joshi 2013; Pillai et al., 2018). Thus, collectively, the geochemical proxies indicate a strengthened monsoonal condition and intense chemical weathering at period prior to 4,800 years BP in the Banni Plains region. The mineral magnetic proxies which provide information about the type and concentration of magnetic grains transported in the catchment (Oldfield et al., 1994) also support the inferences drawn from the geochemical data. The lower values of χ_{lf} in phase one signify strengthened monsoonal condition, which leads to higher erosion and weathering that lowered the concentration of magnetic minerals. The values of the S-ratio also suggest a combined anti-ferro to ferrimagnetic mineral assemblage with dominance of ferrimagnetic minerals in phase I. The complied results of multi-proxies recommend the deposition of sediments that occurred under the relatively humid climatic condition in phase I (i.e., period prior to 4,800 years BP).

Thakur et al. (2019) based on palynological study form Harshad, western Saurashtra, reported a higher ISM precipitation during the 5,400 to 5,100 years BP period. Similar observations were also made by Kathayat et al. (2017) from the composite Sahiya d^{18}O record from the Himalayas. Higher CIA and enhanced precipitation at 5.1 ka during the mature Harappan phase have also been reported by Ngangom et al (2016) from the nearby Eastern Great Rann of Kachchh. A similar, wet phase of ISM was recorded by Parsons Valley Lake, Tamilnadu, southern India (Raja et al., 2019).

4,400–4,800 cal yr BP Period (Phase II)

The zone is marked by abrupt changes to lower CIA values and other major elemental proxies, suggesting a weaker chemical weathering under arid climatic conditions (**Figure 4**). This abrupt aridity around 4,400 years BP has been one of the most discussed, although debated, causative factor for the deurbanization and decentralization of Harappans as a community that was primarily thriving on river-based resources (Staubwasser et al., 2003; Madella and Fuller, 2006; Dixit et al., 2014, 2018; Sengupta et al., 2019). Several studies have shown that the brief phase of aridity experienced in western India as well as the Himalayas led to the drying of water resources and speculated that this might have led the Harappan migrations to explore alternate water resources and settlement to smaller centers (Madella and Fuller, 2006). Based on our proxy data, which shows excessive deficient moisture conditions during this period (4,400–4,800 years BP), we support the earlier view that the prevalence of drought-like conditions affected the deurbanization of the Harappan settlement from the Western India.

Period Between 4,400 cal yr BP and 3,300 cal yr BP (Phase III)

Phase III is marked by fluctuating but an overall increasing value of mineral magnetic parameters, higher concentration of major, and lower ratios of geochemical proxies. An increase in CIA

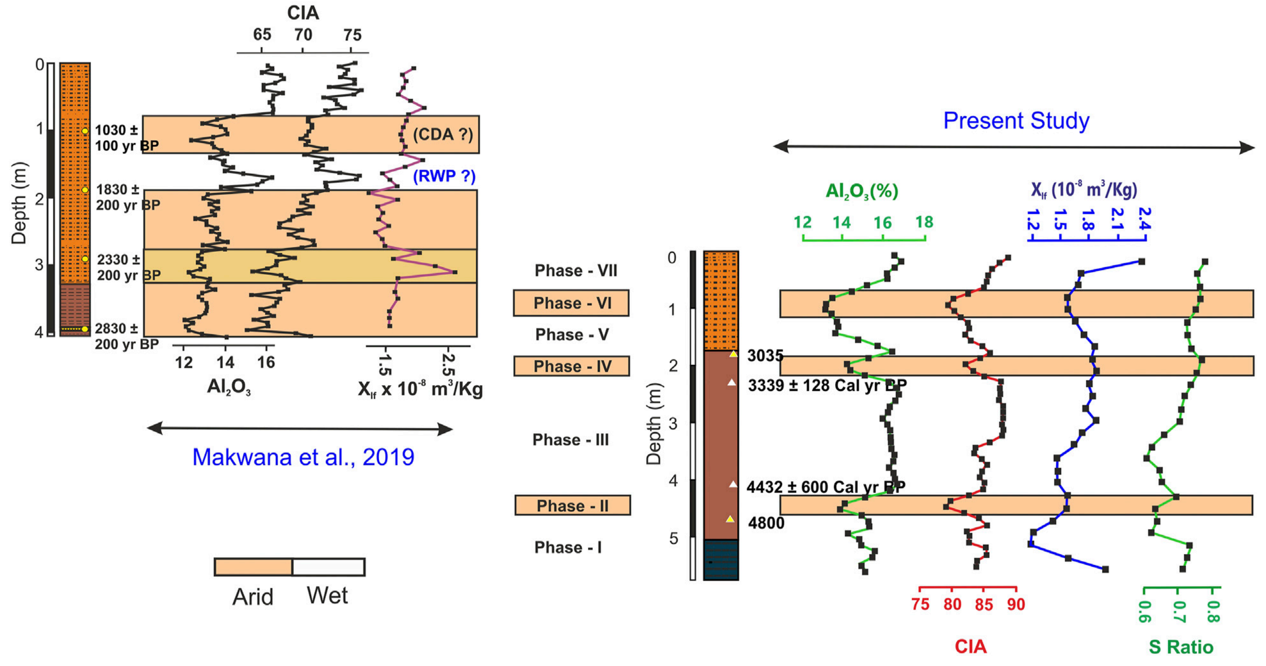

FIGURE 3 | Climatic fluctuations since the mature Harappan times (~5,000 years) from the Banni Plains; complied observation from Makwana et al. (2019) and BKR trench ~ present study.

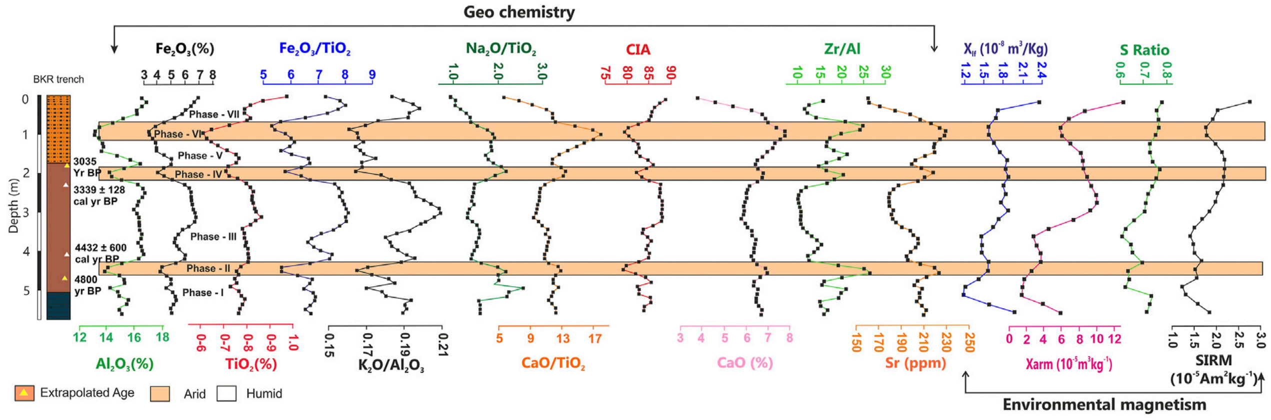

FIGURE 4 | Temporal variation of major elements, their ratios, and mineral magnetic properties from the BKR sediments of Banni Plains, GRK.

(>83%) hints an enhancement of chemical weathering signifying higher precipitation, which is also reflected in increasing concentration of major oxides such as Al_2O_3, Fe_2O_3, and TiO_2 (Anderson et al., 2004). A significant increasing trend is also noticeable in the ratios of K_2O/Al_2O_3 and Fe_2O_3/TiO_2 with lower concentration of Na_2O/TiO_2 and CaO/TiO_2 (**Figure 4**). Mineral magnetic parameters, that is, χ_{lf} and S-ratio, showed progressive decrease and thereafter increase in phase III, which indicates fluctuating but overall gradual increased precipitation/monsoon (**Figure 4**). Similar results of enhanced monsoonal strength have also been reported by Pillai et al. (2017, 2018) from the Banni Plains during 4,600 and 2,500 years BP. This period was the initiation of deurbanization of the mighty Harappan civilization, which was marked by the migration of Harrapans from the well-established centers to other sites, owing to water source scarcity (Ponton et al., 2012; Dixit et al., 2014, 2018; Pokharia et al., 2017). On the contrary to this, recently, some studies have demonstrated change in farming pattern and other means for survival of the ancient settlers despite the aridity (Sarkar et al., 2020; Pokharia et al., 2017; Singh et al., 2018).

Period Between 3,300 cal yr BP and 3,000 cal yr BP (Phase IV)

The period from 3,300 years BP to 3,000 years BP experienced a relatively drier climate with reduced CIA values and abruptly decreasing concentration of major oxides such as Al_2O_3, Fe_2O_3, and TiO_2. The relative content of CaO, Sr, and Na_2O/TiO2 increases as these mobile elements remain at the site due to the lack of hydrolysis. Prasad et al. (2014a) from the Wadhwana Lake in alluvial plains of Gujarat reported a short phase of low precipitation during 3,238–2,709 cal yr BP. Similar arid conditions are also reported from Rann sediments in northwest of the present site by Ngangom et al. (2016).

Contrastingly, Pillai et al. (2017, 2018) reported the period from 4,600 to 2,500 years BP as the period of enhanced monsoonal strength, owing to the coexistence of C4 and C3 vegetation along with geochemical composition of sediments due to chemical weathering. Recent studies from the Bednikund Lake, Himalayas, based on mineral magnetics, organic geochemistry, and grain size assemblages, also suggested an enhanced monsoonal strength during 3,380 and 2,830 cal yr BP. (Rawat et al., 2021).

Period During the Last 3,000 years (Phases V, VI, and VII in BKR Trench and BB Trench)

Makwana et al., 2019

The depiction of last three millennia has been done based on phases V, VI, and VII of BKR trench and previously reported BB trench from the northwest of the Banni Plains (Makwana et al., 2019). As we do not have age control on the top section of BKR, we only report that the phases V and VII show signs of strengthened monsoonal condition with enhanced values of CIA and associated geochemical proxies, whereas on the contrary, phase VI shows a relatively dip in CIA values and other oxides, hinting at a weaker chemical weathering, that is, arid climatic conditions.

On the contrary, the period from 2,900 years to 1900 years from BB trench site also supports an overall fluctuating to arid climatic condition with peak of that aridity around 2,400 years BP (Makwana et al., 2019). Pillai et al. (2018) from Luna core reported arid climatic condition during 3,000 to 2,500 years BP. Similarly, Quamar et al. (2021) studied a lacustrine sequence from central India and based on the pollen study reported a decline in strength of ISM during 3,000 to 2,600 years BP period. Similarly studies from the mudflats of Diu, Gujarat, are suggestive of the arid conditions during 2,640–1930 cal yr BP (Banerjee et al., 2017). This is in agreement with a long drought in the Thar Desert, India, between 3,600 and 2000 years BP (Bryson and Bryson, 1996; Enzel et al., 1999).

The period from 1900 years BP to 200 years BP shows three phases of prominent arid/humid climatic conditions (Makwana et al., 2019). These periods of arid/humid conditions coincide their timing with globally known events like the medieval climatic anomaly (MCA). These events have also been reported from regional archives in the past (Gupta et al., 2003; Sinha et al., 2007; Ngangom et al., 2012; Rajamanickam et al., 2017; Rawat et al., 2021). All the fluctuations from arid to humid climatic conditions during the last three millennia are abrupt in nature with sharp changes in proxy data (**Figure 3**). Previously, Makwana et al. (2019) reported a sedimentation rate of 1–2.2 mm/yr from the BB trench in the northwestern Banni Plains. The present BKR trench based on two AMS ^{14}C ages yields a sedimentation rate of 1.6 mm/yr during 4,432 to 3,339 cal yr BP period. The high sedimentation rate from BB and BKR trenches (>1 mm/yr) also aides this endeavor. Despite the poor chronological control, the presence of abrupt arid and humid periods during last two millennia is suggestive of Banni Plains being capable of being used as potential archive for studying climatic reconstructions.

CONCLUSION

Based on the multi-proxy dataset from the Banni Plains of the Kachchh region spanning last 5,000 years, the salient findings are as follows:

1. The periods from 4,800 to 4,400 cal yr BP are marked by abrupt drier climatic conditions in a multi-proxy dataset, which has also been reported by several other studies from the regional archives owing to the initiation of synchronous deurbanization of Harappan settlements. This is followed by a period from 3,300 to 3,000 cal yr BP and around 2,400 cal yr BP with pronounced aridity in the Banni Plain region.
2. The relatively humid climatic conditions were observed during >4,800 cal yr BP, 4,400 to 3,300 cal yr BP, 1900 to 1,400 years BP, and 900–550 years BP in the multi-proxy record. The late Harappan phase envisaged in the present study shows an intriguing gradual strengthening of the monsoonal intensity.
3. Based on preliminary results, the Banni Plains as an archive shows a high sedimentation rate, that is, > 1 mm/yr, which suggests it can act as a robust archive which can be tapped to be an excellent sedimentary record to reconstruct multi-decadal to centennial climatic events spanning the Holocene epoch.

Future studies from Banni Plains with relatively deeper information could likely aide in reconstructing the dynamics of the region spanning the entire Holocene epoch, as the present study validates the archiving potential of Banni sediments for reconstructing short and long spells of paleomonsoonal conditions.

DATA AVAILABILITY STATEMENT

The original contributions presented in the study are included in the article/**Supplementary Material**; further inquiries can be directed to the corresponding author.

AUTHOR CONTRIBUTIONS

The paper was written by NM and AD. The idea was conceptualized by NM, AD and SPP. The magnetic rsults and data was worked upon by BP. CV and AS contributed in field investigation and laboratory analysis. SPP supervised the work and edited the paper.

ACKNOWLEDGMENTS

We thank DST, Government of Gujarat for funding. Director General ISR and Director BSIP are thanked for permission to publish this work and encouragement. The study forms part of Ph.D thesis of NM. We convey our grateful thanks to Gaurav Chauhan for his assistance in field. We thank SAIF, BSIP for providing infrastructural facilities. We thank two anonymous reviewers and Editor for their constructive comments, which improved the earlier version of the paper.

SUPPLEMENTARY MATERIAL

The Supplementary Material for this article can be found online at: https://www.frontiersin.org/articles/10.3389/feart.2021.679689/full#supplementary-material

REFERENCES

Agnihotri, R., Bhattacharya, S. K., Sarin, M. M., and Somayajulu, B. L. K. (2003). Changes in Surface Productivity and Subsurface Denitrification during the Holocene: a Multiproxy Study from the Eastern Arabian Sea. *The Holocene* 13 (5), 701–713. doi:10.1191/2F0959683603hl656rp

Anderson, D. M., Baulcomb, C. K., Duvivier, A. K., and Gupta, A. K. (2010). Indian Summer Monsoon during the Last Two Millennia. *J. Quat. Sci.* 25 (6), 911–917. doi:10.1002/jqs.1369

Anderson, P. O. D., Worden, R. H., Hodgson, D. M., and Flint, S. (2004). Provenance Evolution and Chemostratigraphy of a Palaeozoic Submarine Fan-Complex: Tanqua Karoo Basin, South Africa. *Mar. Pet. Geology* 21, 555–577. doi:10.1016/j.marpetgeo.2004.01.004

Banerji, U., Bhusan, R., and Jull, A. J. T. (2017). Mid-late Holocene Monsoonal Records from the Partially Active Mudflats of Diu Island, Southern Saurashtra, Gujarat, Western India. *Quat. Int.* 443, 200–201. doi:10.1016/j.quaint.2016.09.060

Basavaiah, N. (2011). *Geomagnetism: Solid Earth and Upper Atmosphere Perspectives*. Dordrecht, Netherlands: Springer, 410.

Basavaiah, N., and Khadkikar, A. S. (2004). Environmental Magnetism and its Application towards Palaeomonsoon Reconstruction. *J. Indian Geophys. Union* 8 (1), 1–14.

Basu, S., Prasanta, S., Pillai, A. S., and Ambili, A. (2019). Response of Grassland Ecosystem to Monsoonal Precipitation Variability during the Mid-late Holocene: Inferences Based on Molecular Isotopic Records from Banni Grassland, Western India. *PLOS ONE* 14 (4), 0212743. doi:10.1371/journal.pone.0212743

Berkelhammer, M., Sinha, A., Mudelsee, M., Cheng, H., Edwards, L. R., and Cannariato, K. (2010). Persistent Multidecadal Power of the Indian Summer Monsoon. *Earth Planet. Sci. Lett.* 290, 166–172. doi:10.1016/j.epsl.2009.12.017

Bianchi, G. G., and Mc Cave, I. N. (1999). Holocene Periodicity in North Atlantic Climate and Deep Ocean Flow South of Iceland. *Nature* 397, 515–517. Available at: https://www.nature.com/articles/17362.

Biswas, S. K. (1987). Regional Tectonic Framework, Structure and Evolution of the Western Marginal Basins of India. *Tectonophysics* 135, 307–327. doi:10.1016/0040-1951(87)90115-6

Brooks, N. (2006). Cultural Responses to Aridity in the Middle Holocene and Increased Social Complexity. *Quat. Int.* 151 (1), 29–49. doi:10.1016/j.quaint.2006.01.013

Bryson, R. U., and Bryson, R. A. (1996). Application of a Global Volcanicity Time-Series on High-Resolution Paleoclimatic Modeling of the Eastern Mediterranean. *Water Sci. Technol. Libr.* 31, 1–19. doi:10.1007/978-94-017-3659-6_1

Buggle, B., Glaser, B., Hambach, U., Gerasimenko, N., and Markovic, S. (2011). An Evaluation of Geochemical Weathering Indices in Loess–Paleosol Studies. *Quat. Int.* 240, 12–21. doi:10.1016/j.quaint.2010.07.019

Burnes, A. (1834). Memoir on the Eastern Branch of the River Indus, Giving an Account of the Alterations Produced on it by an Earthquake, Also a Theory of the Formation of the Runn, and Some Conjectures on the Route of Alexander the Great; Drawn up in the Years 1827-1828. *Trans. R. Asiatic Soc. Great Britain Ireland* 3, 550–588.

Chamyal, L. S., Maurya, D. M., and Rachna, R. (2003). Fluvial Systems of the Dry Lands of Western India: a Synthesis of Late Quaternary Environmental and Tectonic Changes. *Quat. Int.* 104, 69–86. doi:10.1016/s1040-6182(02)00136-2

Chauhan, O. S., Vogelsang, E., Basavaiah, N., and Syed, A. K. (2009). Reconstruction of the Variability of the Southwest Monsoon during the Past 3 Ka, from the continental Margin of the southeastern Arabian Sea. *J. Quat. Sci.* 25, 798–807. doi:10.1002/jqs.1359

Clift, P. D., Wan, S., and Blusztajn, B. (2014). Reconstructing Chemical Weathering, Physical Erosion and Monsoon Intensity since 25 Ma in the Northern South China Sea: A Review of Competing Proxies. *Earth Sci. Rev.* 130, 86–102. doi:10.1016/j.earscirev.2014.01.002

Das, A., Prizomwala, S., Makwana, N., and Thakkar, M. (2017). Late Pleistocene-Holocene Climate and Sea Level Changes Inferred Based on the Tidal Terrace Sequence, Kachchh, Western India. *Palaeogeogr. Palaeoclimatol. Palaeoecol.* 473, 82–93. doi:10.1016/j.palaeo.2017.02.026

Dixit, Y., Hodell, D. A., Giesche, A., Tandon, S. K., Gázquez, F., Saini, H. S., et al. (2018). Intensified Summer Monsoon and the Urbanization of Indus Civilization in Northwest India. *Nat. Scientific Rep.* 8, 4225. doi:10.1038/s41598-018-22504-5

Dixit, Y., Hodell, D. A., Sinha, R., and Petrie, C. A. (2014). Abrupt Weakening of the Indian Summer Monsoon at 8.2 Kyr B.P. *Earth Planet. Sci. Lett.* 391, 16–23. doi:10.1130/G35236.1

Dutta, K., Bhushan, R., and Somayajulu, B. L. K. (2001). ΔR Correction Values for the Northern Indian Ocean. *Radiocarbon*. 43, Nr 2A, 483–488. doi:10.1017/s0033822200038376

Enzel, Y., Ely, L. L., Mishra, S., Ramesh, R., Amit, R., Lazar, B., et al. (1999). High Resolution Holocene Environmental Changes in the Thar Desert, Northwestern India. *Science* 284, 125–127. doi:10.1126/science.284.5411.125

Galili, E., Weinstein-Evron, M., and Ronen, A. (1988). Holocene Sea-Level Changes Based on Submerged Archaeological Sites off the Northern Carmel Coast in Israel. *Quat. Res.* 29, 36–42. doi:10.1016/0033-5894(88)90069-5

Gaur, A. S., Vora, K. H., Sundaresh, R., Murali, R. M., and Jaya kumar, S. (2013). Was the Rann of Kachchh Navigable during the Harappan Times (Middle Holocene)? an Archaeological Perspective. *Curr. Sci.* 105, 1485–1491.

Giosan, L., Clift, P. D., Macklin, M. G., Fuller, D. Q., Constantinescu, S., Durcan, J. A., et al. (2012). Fluvial Landscape of the Harappan Civilization. *Proc. Natl. Acad. Sci.* 109 (26), 1688–1694. doi:10.1073/pnas.1112743109

Glennie, K. W., and Evans, G. (1976). A Reconnaissance of the Recent Sediments of the Ranns of Kutch, India. *Sedimentology* 23, 625–647. doi:10.1111/j.1365-3091.1976.tb00098.x

Gupta, A., Anderson, D., and Overpeck, J. (2003). Abrupt Changes in the Asian Southwest Monsoon during the Holocene and Their Links to the North Atlantic Ocean. *Lett. Nat.* 421 (6921), 354–357. doi:10.1038/nature01340

Gupta, S. K. (1975). Silting of the Rann of the Kutch during the Holocene. *Indian J. Earth Sci.* 2, 163–175.

Khatayat, G., Cheng, H., Sinha, A., Yi, L., Xianglei, Li., Zhang, H., et al. (2017). The Indian Monsoon Variability and Civilization Changes in the Indian Subcontinent. *Sci. Adv.* 3 (12). doi:10.1126/sciadv.1701296

Khonde, N., Maurya, D. M., and Chamyal, L. S. (2017a). Late Pleistocene-Holocene clay mineral Record from the Great Rann of Kachchh basin, Western India: Implications for Palaeoenvironments and Sediment Sources. *Quat. Int.* 443, 86–98. doi:10.1016/j.quaint.2016.07.024

Khonde, N., Singh, S., Maurya, D. M., Rai, V. K., Chamyal, L. S., and Giosan, L. (2017b). Tracing the Vedic Saraswati River in the Great Rann of Kachchh. *Scientific Rep.* 7 (1). doi:10.1038/s41598-017-05745-8

Kotlia, B, S., and Joshi, L. M. (2013). Late Holocene Climatic Changes in Garhwal Himalaya. *Curr. Sci.* 104, 7.

Lamb, H. H. (1985). *Climatic History and the Future*. Princeton University Press.

Laskar, A. H., Yadava, M. G., Sharma, N., and Ramesh, R. (2013a). Late-Holocene Climate in the Lower Narmada valley, Gujarat, Western India, Inferred Using Sedimentary Carbon and Oxygen Isotope Ratios. *The Holocene* 23 (8), 1115–1122. doi:10.1177/2F0959683613483621

Lückge, A., Doose-Rolinski, H., Khan, A. A., Schulz, H., and Von Rad, U. (2001). Monsoonal Variability in the Northeastern Arabian Sea during the Past 5000 years: Geochemical Evidence from Laminated Sediments. *Palaeogeogr. Palaeoclimatol. Palaeoecol.* 167 (3-4), 273–286. doi:10.1016/S0031-0182(00)00241-8

Madella, M., and Fuller, D. Q. (2006). Palaeoecology and the Harappan Civilisation of South Asia: Reconsideration. *Quat. Sci. Rev.* 25 (11-12), 1283–1301. doi:10.1016/j.quascirev.2005.10.012

Makwana, N. M., Prizomwala, S. P., Chauhan, G., Phartiyal, B., and Thakkar, M. G. (2019). Late Holocene Palaeo-Environmental Change in the Banni Plains, Kachchh, Western India. *Quat. Int.* 507, 197–205. doi:10.1016/j.quaint.2018.11.028

Maurya, D., Khonde, N., Das, A., Chowksey, V., and Chamyal, L. (2013). Subsurface Sediment Characteristics of the Great Rann of Kachchh, Western India Based on Preliminary Evaluation of Textural Analysis of Two Continuous Sediment Cores. *Curr. Sci.* 104 (8), 1071–1077. Available at:

Minyuk, P. S., Borkhodoev, V. Ya., and Wennrich, V. (2013). Inorganic Data from El'gygytgyn Lake Sediments: Stages 6-11. *Clim. past Discuss.* 9, 393–433. doi:10.5194/cpd-9-393-2013

Muhs, D. R., Bettis, E. A., Been, J., and Mc Geehin, J. P. (2001). Impact of Climate and Parent Material on Chemical Weathering in Loess Derived Soils of the Mississippi River Valley. *Soil Sci. Soc. America J.* 65, 1761–1777. doi:10.2136/sssaj2001.1761

Nesbitt, H. W., and Young, G. M. (1982). Early Proterozoic Climates and Plate Motions Inferred from Major Element Chemistry of Lutites. *Nature* 299, 5885715–5885717. doi:10.1038/299715a0

Ngangom, M., Bhandari, S., Thakkar, M. G., Shukla, A. D., and Juyal, N. (2016). Mid-Holocene Extreme Hydrological Events in the Eastern Great Rann of Kachchh, Western India. *Quat. Int.* 443, 188–199. doi:10.1016/j.quaint.2016.10.017

Ngangom, M., Thakkar, M., Bhushan, R., and Juyal, N. (2012). Continental–marine Interaction in the Vicinity of the Nara River during the Last 1400 years, Great Rann of Kachchh, Western India. *Curr. Sci.* 103 (11), 1339–1342. Available at: https://www.jstor.org/stable/24089154.

Oldfield, F. (1994). Toward the Discrimination of fine-grained Ferrimagnets by Magnetic Measurements in lake and Near-shore marine Sediments. *J. Geophys. Res. Solid Earth* 99 (B5), 9045–9050. doi:10.1029/93JB03137

Petterson, L. C., Haug, G. H., Hughen, K. A., and Rohl, U. (2000). Rapid Changes in the Hydrologic Cycle of the Tropical Atlantic during the Last Glacial. *Science* 290, 1947–1951. doi:10.1126/science.290.5498.1947

Phartiyal, B., Appel, E., Blaha, U., Hoffmann, V., and Kotlia, B. S. (2003). Palaeoclimatic Significance of Magnetic Properties from Late Quaternary Lacustrine Sediments at Pithoragarh, Kumaun Lesser Himalaya, India. *Quat. Int.* 108, 51–62. doi:10.1016/S1040-6182(02)00193-3

Pillai, A. S., Ambili, A., Prasad, V., Manoj, M. C., Varghese, S., Prasanta, S., et al. (2018). Multi-proxy Evidence for an Arid Shift in the Climate and Vegetation of the Banni Grasslands of Western India during the Mid to Late Holocene. *The Holocene* 28 (7), 1057–1070. doi:10.1177/0959683618761540

Pillai, A. S., Ambili, A., Sankaran, M., Prasanta, S., Jha, D., and Ratnam, J. (2017). Mid-late Holocene Vegetation Response to Climatic Drivers and Biotic Disturbances in the Banni Grasslands of Western India. *Palaeogeogr. Palaeoclimatol. Palaeoecol.* 485, 869–878. doi:10.1016/j.palaeo.2017.07.036

Possehl, G. (2002). *The Indus Civilization: A Contemporary Perspective*. Lanham, MD: Altamira Press.

Prasad, S., Anoop, A., Riedel, N., Sarkar, S., Menzel, P., Basavaiah, N., et al. (2014b). Prolonged Monsoon Droughts and Links to Indo-Pacific Warm Pool: A Holocene Record Rom Lonar Lake, central India. *Earth Planet. Sci. Lett.* 391, 171–182. doi:10.1016/j.epsl.2014.01.043

Prasad, V., Farooqui, A., Sharma, A., Phartiyal, B., Chakraborty, S., Raj, R., et al. (2014a). Mid-late Holocene Monsoonal Variations from mainland Gujarat, India: a Multi-Proxy Study for Evaluating Climate Culture Relationship. *Palaeogeogr. Palaeoclimatol. Palaeoecol.* 397, 38–51. doi:10.1016/j.palaeo.2013.05.025

Prasad, V., Phartiyal, B., and Sharma, A. (2007). Evidence of Enhanced winter Precipitation and the Prevalence of a Cool and Dry Climate during the Mid to Late Holocene in mainland Gujarat, India. *The Holocene* 17 (7), 889–896. doi:10.1177/0959683607082403

Quamar, M. F., and Chauhan, M. S. (2014). Signals of Medieval Warm Period and Little Ice Age Southwestern Madhya Pradesh (India): A Pollen-Inferred Late-Holocene Vegetation and Climatic Change. *Quat. Int.* 325, 74–82. doi:10.1016/j.quaint.2013.07.011

Quamar, M. F., Kar, R., and Thakur, B. (2021). Vegetation Response to the Indian Summer Monsoon (ISM) Variability during the Late-Holocene from the central Indian Core Monsoon Zone. *The Holocene* 31 (7), 1197–1211. doi:10.1177/09596836211003191

Raja, P., Achyuthan, H., Farooqui, A., Ramesh, R., Kumar, P., and Chopra, S. (2019). Tropical Rainforest Dynamics and Palaeoclimate Implications since the Late Pleistocene, Nilgiris, India. *Quat. Res.* 91 (1), 367–382. doi:10.1017/qua.2018.58

Rajmanickam, V., Achyuthan, H., Eastoe, C., and Farooqui, A. (2017). Early-Holocene to present palaeoenvironmental shifts and short climate events from the tropical wetland and lake sediments, Kukkal Lake, Southern India: Geochemistry and palynology. *The Holocene* 27 (3), 404–417. doi:10.1177/0959683616660162

Rawat, V., Rawat, S., Srivastava, P., Negi, P. S., Prakasam, M., and Kotlia, B. S. (2021). Middle Holocene Indian Summer Monsoon Variability and its Impact on Cultural Changes in the Indian Subcontinent. *Quat. Sci. Rev.* 255, 106825. doi:10.1016/j.quascirev.2021.106825

Roy, B., and Merh, S. (1981). The Great Rann of Kutch: Intriguing Quaternary Terrain. *Recent Researches Geology.* 9, 100.

Ruifeng, M., Wei1, Z., and Chanyu, Y. (2020). Multi-proxy Records of Holocene Fluvio-Lacustrine Sediments in the Southern Liaodong Peninsula, China. *E3S Web of Conferences* 165, 03023. doi:10.1051/e3sconf/202016503023

Sanwal, J., Kotlia, B., Rajendran, C., Ahmad, S., Rajendran, K., and Sandiford, M. (2013). Climatic Variability in Central Indian Himalaya during the Last ~ 1800 years: Evidence from a High Resolution Speleothem Record. *Quat. Int.* 304, 183–192. doi:10.1016/j.quaint.2013.03.029

Sarkar, A., Mukherjee, A. D., Sharma, S., Sengupta, T., Ram, F., Bera, M. K., et al. (2020). New Evidence of Early Iron Age to Medieval Settlements from the Southern Fringe of Thar Desert (Western Great Rann of Kachchh), India: Implications to Climate-Culture Co-evolution. *Archaeological Res. Asia* 21, 2352–2267. doi:10.1016/j.ara.2019.100163

Sengupta, T., Mukherjee, A. D., Bhusan, R., Ram, F., Bera, M. K., Raj, H., et al. (2019). Did the Harappan Settlement of Dholavira (India) Collapse during the Onset of Meghalayan Stage Drought? *J. Quat. Sci.* 35 (3), 382–395. doi:10.1002/jqs.3178

Sinha, A., Cannariato, K. G., Stott, L. D., Cheng, H., Edwards, R. L., Yadava, M. G., et al. (2007). A 900-year (600 to 1500 AD) Record of the Indian Summer Monsoon Precipitation from the Core Monsoon Zone of India. *Geophys. Res. Lett.* 34, 16707. doi:10.1029/2007GL030431

Sridhar, A., Chamyal, L. S., and Patel, M. (2014a). Palaeoflood Record of High-Magnitude Events during Historical Time in the Sabarmati River, Gujarat. *Curr. Sci.* 107 (4), 675–679. Available at: https://www.jstor.org/stable/24103542

Staubwasser, M., Sirocko, F., Grootes, P. M., and Segl, M. (2003). Climate Change at the 4.2 Ka BP Termination of the Indus valley Civilization and Holocene South Asian Monsoon Variability. *Geophys. Res. Lett.* 30 (8), 14–25. doi:10.1029/2002GL016822

Stuiver, M., Reimer, P. J., and Reimer, R. W., (2018). CALIB 7.1 [WWW program] at http://calib.org, accessed. 8-13.

Thakur, B., Seth, P., Sharma, A., Pokharia, A. K., Spate, M., and Farooqui, S. (2019). Linking Past Cultural Developments to Palaeoenvironmental Changes from 5000 BP to Present: A Climate-Culture Reconstruction from Harshad Estuary, Saurashtra, Gujarat, India. *Quat. Int.* 507, 188–196. doi:10.1016/j.quaint.2019.01.019

Thompson, R., and Oldfield, F. (1986). *Environmental Magnetism*. London: Allen & Unwin, 227.

Tyagi, A. K., Shukla, A. D., Bhushan, R., Thakker, P. S., Thakkar, M. G., and Juyal, N. (2012). Mid-Holocene Sedimentation and Landscape Evolution in the Western Great Rann of Kachchh, India. *Geomorphology* 151-152, 89–98. doi:10.1016/j.geomorph.2012.01.018

Walden, J. (1999). "Remanence Measurements," in *Environmental Magnetism - A Practical Guide, Technical Guide No. 6*. Editors J. Walden, J. P. Smith, and F. Oldfield (London: Quaternary Research Association), 63–88.

Warrier, A., and Shankar, R. (2009). Geochemical Evidence for the Use of Magnetic Susceptibility as a Paleorainfall Proxy in the Tropics. *Chem. Geology* 265, 553–562. doi:10.1016/j.chemgeo.2009.05.023

Wright, R. P., Bryson, R., and Schuldenrein, J. (2008). Water Supply and History: Harappa and the Beas Regional Survey. *Antiquity* 8, 37–48. doi:10.1017/S0003598X00096423

Yancheva, G., Nowaczyk, N. R., Mingram, J., Dulski, P., Schettler, G., Negendank, F. W., et al. (2007). Influence of the Intertropical Convergence Zone on the East Asian Monsoon. *Nat. Lett.* 445 (7123), 74–77. doi:10.1038/nature05431

Conflict of Interest: The authors declare that the research was conducted in the absence of any commercial or financial relationships that could be construed as a potential conflict of interest.

frontiers
in Earth Science

BRIEF RESEARCH REPORT
published: 23 August 2021
doi: 10.3389/feart.2021.680180

Asian Winter Monsoon Imprint on the Water Column Structure at the Northern South China Sea Coast

Yancheng Zhang[1,2]*, Kai Zhu[2], Chao Huang[3,4], Deming Kong[4], Yuxin He[5], Huanye Wang[6], Weiguo Liu[6], Zhouqing Xie[7], Gangjian Wei[3] and Zhonghui Liu[2]

[1]School of Marine Sciences, Sun Yat-sen University, Zhuhai, China, [2]Department of Earth Sciences, The University of Hong Kong, Hong Kong, China, [3]State Key Laboratory of Isotope Geochemistry, Guangzhou Institute of Geochemistry, Chinese Academy of Sciences, Guangzhou, China, [4]Guangdong Province Key Laboratory for Coastal Ocean Variation and Disaster Prediction, Guangdong Ocean University, Zhanjiang, China, [5]School of Earth Sciences, Zhejiang University, Hangzhou, China, [6]State Key Laboratory of Loess and Quaternary Geology, Institute of Earth Environment, Chinese Academy of Sciences, Xi'an, China, [7]Anhui Key Laboratory of Polar Environment and Global Change, Department of Environmental Science and Engineering, University of Science and Technology of China, Hefei, China

Edited by:
Shengfa Liu,
Ministry of Natural Resources, China

Reviewed by:
Kefu Yu,
Guangxi University, China
Hong Yan,
Institute of Earth Environment (CAS), China
Qian Li,
Qingdao National Laboratory for Marine Science and Technology, China

Correspondence:
Yancheng Zhang
zhangych99@mail.sysu.edu.cn

Specialty section:
This article was submitted to Quaternary Science, Geomorphology and Paleoenvironment, a section of the journal Frontiers in Earth Science

Received: *13 March 2021*
Accepted: *12 July 2021*
Published: *23 August 2021*

Citation:
Zhang Y, Zhu K, Huang C, Kong D, He Y, Wang H, Liu W, Xie Z, Wei G and Liu Z (2021) Asian Winter Monsoon Imprint on the Water Column Structure at the Northern South China Sea Coast. Front. Earth Sci. 9:680180. doi: 10.3389/feart.2021.680180

Coastal regions of the northern South China Sea (SCS) strongly interact with the Asian monsoon circulation (AMC). Thus, variations of sea surface temperature (SST) here are newly suggested to document AMC changes in an effective manner, but additional physical parameters of oceanic conditions, probably also in relation to the AMC system, remain poorly understood. In this study, we analyzed glycerol dialkyl glycerol tetraethers (GDGTs) from a well-dated sediment core YJ, retrieved at the northern SCS coast, to further scrutinize the intrinsic response of water column to winter AMC strength. It shows that within the time frame of past ~1,000 years, the tetraether index of lipids with 86 carbon atoms (TEX_{86}) and published alkenone ($U^{K'}_{37}$) temperature records together confirm a reduced thermal gradient during the Little Ice Age (LIA), in comparison to that during the Medieval Climate Anomaly (MCA). Considering concurrent variations of the branched and isoprenoid tetraether (BIT) and the ratio of archaeol to caldarchaeol (ACE), for example, with decreased values (<~0.3) for the former and relatively high values for the latter at the LIA, indicative of stratification and salinity changes, respectively, these multiple lines of evidence thereby call for well mixing of onsite water at site YJ correspondingly. Our results suggest that winter AMC strength is a critical factor for mixing subsurface waters and modifying thermal/saline conditions at the northern SCS coasts through the last millennium and also, perhaps, on longer timescales.

Keywords: South China Sea, coastal conditions, GDGTs, last millennium, Asian winter monsoon

INTRODUCTION

The Asian monsoon circulation (AMC), as triggered by large-scale thermal contrast between ocean and land, characterizes a seasonal reversal of prevailing wind directions. In the summertime, it carries an enormous amount of moisture from the Indian and Pacific Oceans toward southern and northeastern Asia, and, consequently, exerts a considerable influence over the water cycle and the terrestrial ecosystem (Wang et al., 2017; Zhang et al., 2017). In this regard, much attention has been drawn until now to explore summer AMC variability and the physical mechanism(s) from seasonal to orbital timescales (e.g., Hu et al., 2008; An et al., 2011; Liu et al., 2015; Xie et al., 2015;

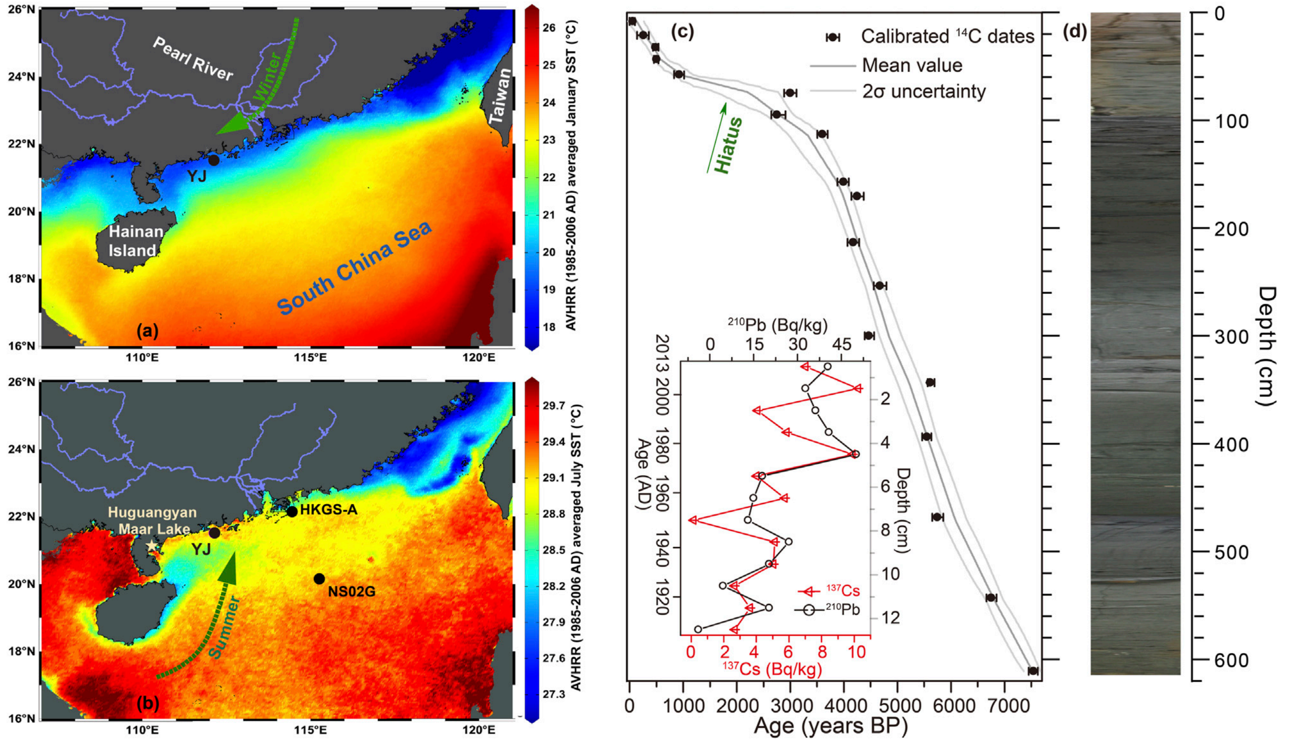

FIGURE 1 | Regional setting and the site of core YJ, existing paleorecords in the northern South China Sea (black dots) and at Huguang Maar Lake (orange star) as mentioned in the main text, are plotted against long-term (1985–2006 AD) averaged January **(A)** and July **(B)** sea surface temperature (SST, color scale) from the AVHRR dataset (Casey, 2013). Chronology **(C)** and lithology **(D)** of core YJ are cited from Huang et al. (2018) and Zhang et al. (2019). Note that the core-top **(C)** is calculated based on ^{210}Pb/^{137}Cs dates, to be 2013 AD when our core YJ was retrieved.

Cheng et al., 2016). In contrast, the winter component of the AMC itself often diverges cold-dry air from the Asian countries such as Siberia-Mongolia toward oceans, thus with little potential to deliver water vapor directly. Despite such fact, winter AMC is still of importance in transporting eolian dust and/or aerosol, and therefore in regulating the regional (and global) climate system (Maher et al., 2010; Kok et al., 2018). Combined with its impact upon the summer AMC precipitation subsequently (Bollasina et al., 2011; Li et al., 2016; Cai et al., 2019), a complete understanding of winter AMC variations at present and, if possible, before the instrumental era (after ~1850 AD) (e.g., Wen et al., 2016; Kang et al., 2020) would provide constructive insight into their intrinsic link against both anthropogenic and natural backgrounds. Abundant analyses based on the grain size and geochemical proxies from Chinese loess sequences at available sparse sites (Stevens et al., 2007; Li and Morrill 2015), on the one hand, have indeed advanced our knowledge about this topic, but on the other hand, these paleorecords, distributed across continental interiors, rather face difficulty to draw a clear picture of winter AMC behavior, for example, its far-field effect on terrestrial ecosystem especially. For example, at Huguangyan Maar Lake, winter AMC intensity, as inferred from diatom assemblages (Wang et al., 2012) and magnetic susceptibility (Yancheva et al., 2007), respectively, presents controversial temporal features during the Holocene (since ~11,700 years ago before present, “yr BP” hereafter).

Next to Huguangyan Maar Lake, the South China Sea (SCS) is also strongly involved into the AMC coupling process (e.g., Xie et al., 1998; Lau and Nath 2009; Wang et al., 2009; Liu and Zhu 2016) and hence well suited to fingerprint its variability. In fact, along the SCS northern coasts, sea surface temperature (SST) apparently exhibits shore-parallel gradient and intensive vertical mixing in winter, while horizontal homogenization and vertical stratification in summer (**Figures 1A,B**; Wang, 2007; Jing et al., 2009). Such seasonality of SST variations and their difference, for example, at both horizontal and vertical scales, are readily capable of revealing winter AMC signals across different timescales (e.g., Tian et al., 2010; Huang et al., 2011; Steinke et al., 2011; Kong, 2014a, Kong et al., 2014b). Particularly, our recent study (Zhang et al., 2019), based on a well-dated sediment core YJ, ~200 km far away from the Pearl River delta (**Figure 1**), has shown extraordinary decrease (by up to ~4°C) of alkenone SSTs and remarkable increase (by two to four orders of magnitude) of wind-borne terrigenous hopane contents during the Little Ice Age (LIA, ~150–550 years BP), consequently demonstrating an overall intensification of winter AMC, relative to the Medieval Climate Anomaly (MCA, ~700–1,100 years BP) and other intervals in the context of Holocene. This explanation, albeit well corroborated by a growing number of terrestrial paleorecords (e.g., Yancheva et al., 2007; Kang et al., 2020), still deserves independent evidence of oceanic conditions which, as inherently linked to SST change, would offer excellent

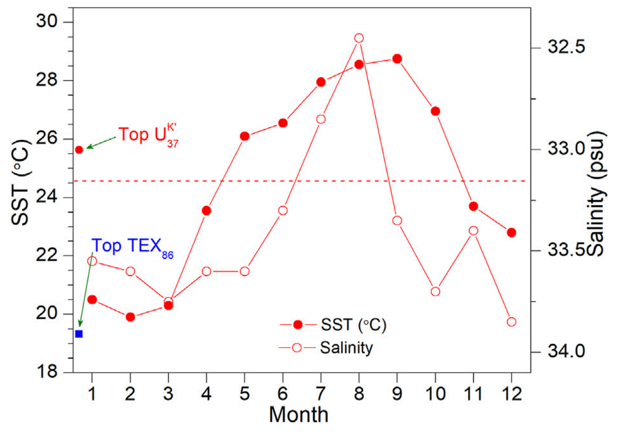

FIGURE 2 | Comparison between temperature estimates at the topmost sample based on $U^{K'}_{37}$ and TEX_{86} proxies, respectively. Observational SSTs and salinity near the core site (112.125°N, 21.625°E, Casey, 2013; Zweng et al., 2013) are also shown. The dashed line represents the annual mean SST value.

opportunity to further illustrate the fundamental role of winter AMC variations in affecting coastal waters. To this end, the time window of last millennium covering both the LIA and MCA, two well-identified climate anomaly intervals during the late Holocene (Mann et al., 2008), is specifically focused here for a tentative attempt to examine how the northern SCS coastal conditions, for example, in terms of both salinity and thermal properties, would have responded to winter AMC change at multi-centennial timescales.

Taking the advantage of sediment core YJ, including i) high-quality control of the chronological framework (**Figures 1C,D**) and ii) limited influence of the Pearl River freshwater discharge (**Figure 2**), we hence directly analyzed glycerol dialkyl glycerol tetraether (GDGT) lipid biomarkers on its uppermost ~65 cm section. Together with the existing measurements of the alkenone unsaturation index ($U^{K'}_{37}$, see definition in Prahl et al., 1988) and hopane components, as earlier reported by Zhang et al. (2019), this study aimed to investigate the hydrological properties of the onsite water column. We hereby present proxy records of the ratio of archaeol to caldarchaeol (ACE), the branched and isoprenoid tetraether (BIT), respectively, and the tetraether index of lipids with 86 carbon atoms (TEX_{86}) over the past ~1,000 years. These results, although potentially associated with various parameters in view of their original interpretations, are utilized to manifest salinity (Turich and Freeman 2011; Wang et al., 2013), stratification (Yamamoto et al., 2013; Wang et al., 2021), and integrated temperature of the whole water column (Xing et al., 2015; Wei et al., 2020), respectively. On this basis, the difference of our paired $U^{K'}_{37}$-TEX_{86} values, a rough measure of vertical thermal gradient, could be used to infer the water column structure changes induced by the winter AMC. Overall, this study helps clarify the dynamical interplay between winter AMC strength and northern SCS coastal conditions throughout the last millennium and, as a result, evoke a careful consideration of regional environmental settings in properly interpreting proxy-based temperature signals.

MATERIAL AND METHODS

Core Site and Chronology

Geographically, sediment core YJ (112°8.08′ E, 21°31.44′ N) is raised at a water depth of ~21 m from the inner continental shelf offshore Yangjiang city with a distance of ~200 km to the southwest of the Pearl River estuary. This site, according to modern observations (e.g., Dunn and Ridgway 2002; Casey, 2013), characterizes prominent SST variations between ~28.3°C in summer (June-July-August, JJA) and ~20.9°C in winter (December–January–February, DJF), but small changes in sea surface salinity (i.e., ~32.4 psu in JJA and ~33.4 psu in DJF; **Figure 2**) due to limited influence of the Pearl River discharge. Most importantly, it is located at the coastal sector outside ~1°C cooling effect of summer upwelling (e.g., to the east of the Pearl River delta and northeast of the Hainan Island, **Figure 1B**), while surface cooling here is largely determined by vertical mixing of the onsite water column in winter (**Figure 1A**). This site is hence well suited to examine the response of northern SCS coastal conditions to winter AMC changes, for example, by using the $U^{K'}_{37}$ SST record in our previous study (Zhang et al., 2019).

The age model of this core, as already published before by Huang et al. (2018) and Zhang et al. (2019), was achieved by combining both lead (^{210}Pb)/cesium (^{137}Cs) and radiocarbon (^{14}C) methods. To summarize, measurements of 13 $^{210}Pb/^{137}Cs$ radionuclide activity and 18 ^{14}C dates (at Beta Analytic Inc., United States) were implemented on samples of bulk sediments above 13 cm and complete shells below this depth, respectively. These age control points were then operated within R script BACON software (version 2.2, Blaauw and Christen 2011) and the Marine 13 calibration curve (Reimer et al., 2013), using default parameters and a 252-year correction of regional reservoir age (Southon et al., 2002; Yu et al., 2010), to compute the mean age and 2σ uncertainty at 1 cm resolution. Such a chronological framework hints a possible hiatus of sedimentary deposit at the depth between ~65 and 85 cm (**Figure 1C**; see details in Zhang et al., 2019). Hence, we mainly focus on the topmost 65 cm of the core YJ, roughly spanning the past ~1,000 years, to analyze GDGT biomarkers for detecting the AMC signal across the LIA and MCA.

Organic Biomarkers

Core YJ was sampled continuously with a step of 1 cm down its uppermost 65 cm, which, based on our chronology as stated in *Core Site and Chronology* section, guaranteed a temporal resolution of ~10–15 years per sample for the past ~1,000 years. Afterward, bulk sediment samples (~5 g) were freeze-dried, then grounded, and soaked to extract total lipids by solvent dichloromethane (DCM): methanol (MeOH) (9:1; v/v) in 60 ml vials, under an ultrasonic wave in the 40°C water bath for three cycles (~15 min each). The extract was subsequently hydrolyzed with 6% KOH in MeOH to remove alkenoates and separated into three fractions *via* silica gel column chromatography with successive eluents of *n*-hexane, DCM,

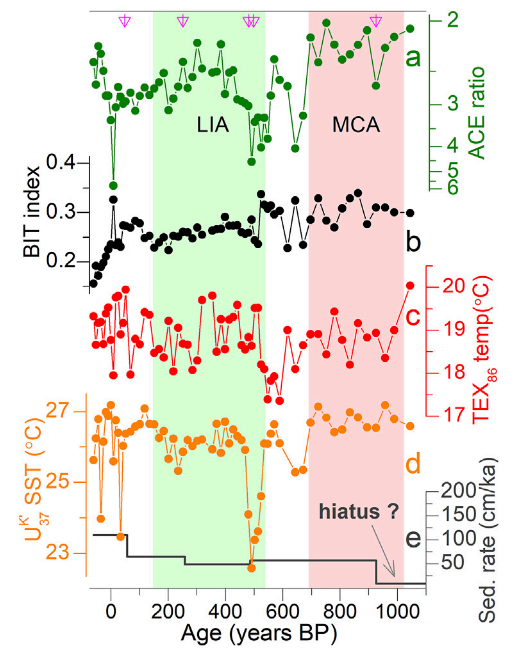

FIGURE 3 | GDGT proxies of sediment core YJ during the last millennium, for example, **(A)** ratio of archaeol to caldarchaeol (ACE) (higher values downward), **(B)** the branched and isoprenoid tetraether (BIT), **(C)** TEX_{86}-based temperatures, **(D)** $U^{K'}_{37}$-SST record, and **(E)** sedimentation rates (Zhang et al., 2019). Color bars outline the Little Ice Age (LIA, ~150–550 years BP) (green) and Medieval Climate Anomaly (MCA, ~700–1,100 years BP) (red), and triangles denote ^{14}C age control points.

and MeOH, respectively. Finally, GDGTs were isolated in MeOH fraction, alkenones in DCM fraction, and *n*-alkanes in hexane fraction.

Analyses of MeOH fraction were conducted on high-performance liquid chromatography atmospheric pressure chemical ionization (HPLC-APCI)-mass spectrometry (e.g., Liu et al., 2013). An aliquot of the fraction was directly dried under N_2, and then redissolved in hexane: isopropanol (99:1; v/v) and filtered after mixing with a known amount of C_{46} internal standard (Huguet et al., 2006). Selected ion monitoring (SIM), which targets specific mass numbers for GDGT components (membrane lipids biosynthesized as multiple homolog series of isoprenoid or methyl-branched isomers, termed isoprenoid-GDGTs, and branched-GDGTs, respectively, see detailed description in Schouten et al., 2013), was used to enhance the detection sensitivity. Quantification was carried out by integrating the peak area of $[M + H]^+$ ions in the extracted ion chromatogram and comparing with the C_{46} internal standard. We then calculated the ACE, BIT, and TEX_{86} indices using equations as given below:

$ACE = \frac{archaeol}{archaeol+caldarchaeol\times10} \times 100$ (Turich and Freeman 2011; Wang et al., 2013),

$BIT = \frac{I+II+III}{I+II++III+cren}$ (Hopmans et al., 2004),

$TEX_{86} = \frac{GDGT_2+GDGT_3+cren'}{GDGT_1+GDGT_2+GDGT_3+cren'}$ (Schouten et al., 2002).

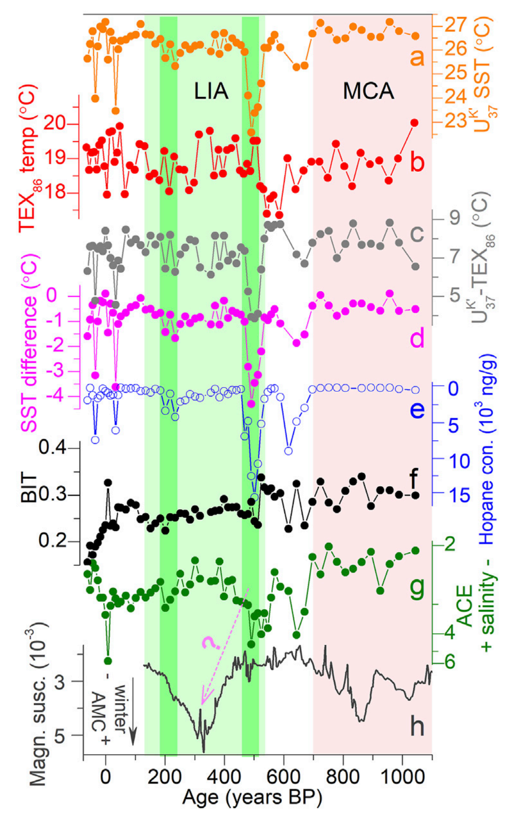

FIGURE 4 | Organic geochemical proxies of core YJ over the last millennium, including **(A)** $U^{K'}_{37}$-SST record (Zhang et al., 2019), **(B)** TEX_{86}-based temperature, **(C)** vertical thermal gradient at site YJ ($U^{K'}_{37}$ – TEX_{86} values), **(D)** $U^{K'}_{37}$-SST difference between two sites YJ and NS02G (YJ minus NS02G), **(E)** hopane compounds (Zhang et al., 2019), **(F)** the branched and isoprenoid tetraether (BIT), and **(G)** the ratio of archaeol to caldarchaeol (ACE). Note that magnetic susceptibility at Lake Huguangyan Maar (higher values downward, Yancheva et al., 2007) is also plotted **(H)** for comparison (with a possible shift of their peaks due to the age uncertainty). Color bars mark the same intervals as in **Figure 3** (two cold epochs within the LIA, e.g., ~250 years BP and ~500 years BP, are further highlighted).

TEX_{86} values were then converted to temperature estimates, using the calibration equation: SST = 68.4 ×log (TEX_{86})+38.6 (Kim et al., 2010). Analytical uncertainties for our laboratory standards are typically less than 5% for the BIT and ACE values and 0.01 unit for TEX_{86}.

RESULTS

Throughout the past millennium, ACE values appear to be relatively high during the LIA, especially at its onset (centered around ~500 years BP), as compared to the MCA (**Figure 3A**). In contrast, the BIT index generally experiences a gradual declining trend from ~0.3 during the MCA (and the earlier epochs, marked by a possible hiatus in sediment accumulation and hence not shown here) toward ~0.15 in the recent years (**Figure 3B**). Unlike these two modes, TEX_{86}-based temperatures, although fluctuated within a large range (nearly about 3°C in terms of magnitude, **Figure 3C**), are apparently trendless over the investigated interval. However, when placed together with the existing $U_{37}^{K'}$-based SST record of the same core YJ (**Figures 3D,E**), there exists certain similarity in the overall temporal patterns between SST (despite a substantial cooling of up to ~4°C, Zhang et al., 2019) and TEX_{86} temperatures over the LIA (e.g., increase at the first half and decrease at the second half), but for the MCA, variations of these two independent records are clearly featured by different structures. Collectively, the LIA interval characterizes increase in ACE values and wind-borne hopane compounds (Zhang et al., 2019), and decrease in BIT ratios, SST, and vertical temperature gradient ($U_{37}^{K'} - TEX_{86}$values), relative to those during the MCA (**Figure 3** and **Figure 4**).

DISCUSSION

Recent studies have shown that the possible source of brGDGTs, for example, terrigenous originated (e.g., soil) or *in situ* synthesized (mainly at subsurface waters), is critical to determine the BIT index and thus its proper explanation (Weijers et al., 2014; Xiao et al., 2016; Wang et al., 2021). For example, more subsurface production of brGDGTs in the Qiongzhou Strait is suggested to be responsible for higher BIT values (~0.4–0.6), which, as a result, reflect enhanced stratification of the onsite water column and thus change in summer AMC strength (Wang et al., 2021). At our study site YJ, BIT values, primarily subjected to crenarchaeol (one major component of isoGDGTs) rather than brGDGT variations (**Supplementary Figure 1**), also imply water column stratification. A set of field surveys, based on collection of both the sediment trap and core-top samples, show that, at the transition zones between the Pearl River estuary and the SCS northern coast, the bloom of autotrophic ammonia-oxidizing *Thaumarchaeota*, main producers of isoGDGTs with limited brGDGTs, tends to preferably occur under the hydrological conditions in the coldest months, like low light levels (e.g., Zhang et al., 2013; Wang et al., 2015; Jia et al., 2017) and less stratified water. Meanwhile, at normal marine settings, including those on the continental shelf, light and redox conditions can also yield redistribution of *Euryarchaeota*/*Archaea* community, leading to stratification of archaeal membrane lipids (with relatively high archaeol in subsurface waters, Turich et al., 2007; Weijers et al., 2014; Xiao et al., 2016; Zhu et al., 2016). In this sense, the coeval variations of isoGDGTs and archaeol abundance in our particular case may cause opposite temporal patterns of BIT and ACE indices (**Supplementary Figures 1, 2**). This fact, in contrary to a recent study presented by Wang et al. (2021) who have applied the concomitant increase in these two proxies to represent enhanced stratification of the northern SCS coastal water, thereby calls for other interpretation(s) to reconcile competing patterns of our BIT and ACE proxies (**Figures 3A,B**). Considering the small variations of BIT values and brGDGTs (**Supplementary Figure 1**), we thus interpret relatively low BIT ratios during the LIA as increased production of the ubiquitous *Thaumarchaeota*, relative to other *Euryarchaeota*/*Archaea*. Besides, it is also worth stressing that despite similar features of changes in crenarchaeol and caldarchaeol (GDGT-0) (**Supplementary Figures 1, 2**), two most abundant components of isoGDGTs, the observed ACE values here may still primarily respond to *Euryarchaeota*/*Archaea* community changes, therefore no longer being an indicator of water column stratification (e.g., Wang et al., 2021).

Based on the results of previous studies (Turich and Freeman, 2011; He et al., 2020), the ACE index might represent salinity if it mainly responds to *Euryarchaeota*/*Archaea* community changes. This prerequisite indeed exists in our case, because one could apparently see a major control of *Euryarchaeota*/*Archaea* on the ACE record (**Supplementary Figure 2**). Due to the different characteristics of BIT and ACE records that strongly exclude the latter as a tracer of stratification (Wang et al., 2021), we instead assume ACE to manifest salinity. As such, multi-centennial–scale variations in our ACE record, as depicted in **Figure 4G**, suggest increased (decreased) salinity of the onsite water column across the LIA (MCA) (Turich and Freeman, 2011). Together with the inference of the available $U_{37}^{K'}$-SST record and wind-borne hopane contents, as earlier reported (**Figures 4A,E**), relatively saline conditions at our site, although only qualitatively estimated (if also taking into account the small range of vertical salinity gradient, **Figure 2**), took place along with an intensification of winter AMC strength during the LIA, and *vice versa* for the MCA. Indeed, observational datasets confirm that, on seasonal timescales, there is a homogeneous structure of *in situ* salinity and temperature changes in winter (i.e., ~33.4 psu and ~20°C down the entire water column, respectively, **Supplementary Figure 3**), relative to those in summer (i.e., ~32.4 psu/28.3°C at surface and ~33.4 psu/27.1°C at ~10–15 m water depth; Zweng et al., 2013). In analogy with this scenario, it is possible that a stronger winter AMC during the LIA would have promoted vertical mixing of the onsite water column which; as a result, it would have brought more cold waters and production of (halophilic) *Euryarchaeota*/*Archaea* community (archaeol, the major driver of ACE values) at the subsurface layers toward upward, thereby decreasing SSTs while increasing its salinity. Notably, during the LIA cold interval, a less input of riverine discharge like the Pearl River drainage, due to the concomitant reduction of summer AMC intensity, as effectively corroborated by a growing body of compelling and independent evidence (e.g., Dykoski et al., 2005; Wang et al., 2005; Zhang et al., 2008; Wang et al., 2012; Lee et al., 2019), may have also somewhat contributed to the inferred salinity increase here. Because these two processes are naturally coupled together from a climatological perspective, it is still difficult to assuredly claim which should play a major role in driving the higher salinity during the LIA. Still, an in-depth examination of winter (*via* mixing of subsurface waters) and/or summer (*via* decrease of riverine discharge) AMC impact on *in situ* salinity will need additional work in the future, for example, model simulations in particular. Regardless, variations in winter AMC strength, as inferred from both magnetic susceptibility at Huguangyan Maar Lake (Yancheva et al., 2007) (**Figure 4H**), the $U_{37}^{K'}$ SST record and wind-borne hopane contents at site YJ, are strongly suggested to modulate the water column structure at the SCS northern coasts, for example, by superimposing additional cooling effect on the top of the LIA cold climate background (Zhang et al., 2019).

The physical mechanism for our inference is further substantiated by the BIT index and TEX_{86}-derived temperature records (**Figures 3B,C**). Based on the observations of i) more isoGDGT abundance at the northern SCS shelf in winter (e.g., roughly three times higher than in summer, Jia et al., 2017) and ii) its primary role (without contribution of terrigenous lipid input as represented by hopane contents, **Figure 4E**, and brGDGTs, **Supplementary Figure 1**) in regulating variations in the BIT index in our case, lower (higher) BIT values during the LIA (MCA) hence probably result from increased (decreased) production of the *Thaumarchaeota*, which is in good support of more (less) prevalence of wintertime conditions (Zhang et al., 2013; Wang et al., 2015; Jia et al., 2017). Combined with small BIT values downcore (roughly <0.3), terrigenous materials thus exert little (if any) impact on the TEX_{86} proxy (and its calibrated temperature). For the TEX_{86} thermometer, recent studies by Jia et al. (2017) and Wei et al. (2020) have also suggested that at the northern SCS coast, its estimates are commonly comparable to or slightly lower than winter SSTs, hence indicative of temperature signals in cold season (**Figure 2**). This interpretation, if true in our case, could explain the overall resemblance between our TEX_{86} values and the $U_{37}^{K'}$ SST record over the LIA (**Figure 3**), as it strongly indicates the homogeneity of thermal signals, in line with enhanced vertical mixing of onsite water due to a stronger AMC then. However, we still note that prior to the LIA interval, there existed slightly cooler (~0.5°C) values of TEX_{86} proxy during the MCA (**Figure 3**). Such observation, based on the winter temperature signals as earlier asserted (Jia et al., 2017; Wei et al., 2020), should necessitate a strengthening of winter AMC strength during the MCA (relative to the LIA), evidently contradicting not only our $U_{37}^{K'}$ SST and hopane records (Zhang et al., 2019) but also other terrestrial paleorecords (e.g., Yancheva et al., 2007; Kang et al., 2020). Therefore, additional parameter(s) must also be included here for completely understanding our TEX_{86} record.

In our case, downcore TEX_{86} values, calculated to be ~18.8 ± 1.2°C (**Figure 3C**, and roughly ~2°C higher if using regional equation developed by Jia et al., 2017), are obviously lower than the *in situ* instrumental SST in winter (**Figure 2**) considering that ~20% of *Thaumarchaeota* is actually produced in other seasons (Wang et al., 2015; Jia et al., 2017; Wei et al., 2020). Further, in light of i) its different features with the $U_{37}^{K'}$ SST record, ii) lower BIT values (<~0.3), and iii) use of the TEX_{86} proxy to manifest the temperature of subsurface rather than surface waters, for example, over the western Pacific marginal sea (Xing et al., 2015), we here apply TEX_{86} values as temperature indicators of an integrated water column but also biased toward winter season and subsurface waters (**Figure 2**). Although it is quite difficult to differentiate the inhabit depths of *Haptophyceae algae* (alkenone-producing species) and *Thaumarchaeota* at site YJ with ~21 m water depth, the use of $U_{37}^{K'}$- and TEX_{86}-derived temperatures to reflect the surface and subsurface thermal signals has been confirmed at the shallow water column in the northern SCS coast (e.g., ~50 m in Wang et al., 2021). Following such interpretation, within the LIA, an overall similarity in the temporal patterns of these two paired records (**Figure 3C** and **Figure 4A**) indicates the homogeneity of thermal signature down the entire water column here, thus calling for an intensification of vertical mixing due to a stronger winter AMC influence (Zhang et al., 2019). In contrast, during the MCA, a weaker winter AMC would have reduced vertical mixing which, together with a stronger summer AMC simultaneously (Dykoski et al., 2005; Zhang et al., 2008), intensified stratification of the water column and then eliminated the similar imprint of thermal conditions at different water depths, as extracted by $U_{37}^{K'}$-SST and TEX_{86} temperature records, respectively (**Figure 3C** and **Figure 4A**).

Since $U_{37}^{K'}$ mainly documents annual mean SST toward summer biases (Zhang et al., 2019) while the TEX_{86} index is largely controlled by winter temperature and the subsurface signal (**Figure 2**), the difference between our paired $U_{37}^{K'}$- and TEX_{86}-values, roughly ~6–7°C, can be used as a rough measure to represent thermal contrast at both seasonal and vertical scales (**Figure 4C**). As such, it shows that thermal gradient at the LIA was relatively small, for example, particularly down to ~4°C at a few short-lived epochs such as ~250 years BP, and ~500 years BP when the $U_{37}^{K'}$-SST record underwent abnormal cooling (of up ~4°C, **Figure 4A**), in comparison to that at the MCA (e.g., roughly ~8°C, **Figure 4C**). Together with similar variations of $U_{37}^{K'}$ and TEX_{86} records during the LIA, these multiple lines of independent evidence call for more influence of stronger AMC on the vertical mixing of subsurface water and thereby reduced stratification of the water column. Notably, considering the evolutionary role of winter AMC in regulating vertical mixing of subsurface waters at multi-centennial timescales, as discussed above, it is reasonable that, at our site YJ, the $U_{37}^{K'} - TEX_{86}$ gradient during the MCA is also likely amplified by an intensified stratification of the water column (and thus characterized by relatively larger errors) simultaneously. Reduction of vertical mixing, due to a weaker winter AMC (than during the LIA), would yield less influence of the subsurface cooling signal on surface temperature (generated by the $U_{37}^{K'}$ proxy, for example, Zhang et al., 2019). Water column stratification could also reshape *Euryarchaeota*/*Archaea* community and thus potentially drive TEX_{86} to lower values. This could have also contributed to the TEX_{86} values during the MCA, not particularly high as compared to the $U_{37}^{K'}$-SST values (**Figure 3C**). On the other hand, the TEX_{86} proxy well captures the temporal pattern of temperature changes within the LIA. Despite the potential contribution from *Euryarchaeota*/*Archaea* community changes, our calculation of vertical thermal gradient apparently resembles the temporal patterns of SST difference between the coast and open ocean (e.g., using $U_{37}^{K'}$-SST records at two sites YJ and NS02G, **Figure 4D**), whereas the SST difference is used to track winter AMC variability (Kong et al., 2017; Zhang et al., 2019). Assuming that the open sea SST represents "original" temperature signal that is not strongly impacted by the winter AMC, the temperature difference between the two locations could indicate the winter AMC impact. The difference of our $U_{37}^{K'}$ and TEX_{86} values captures most of the features in the two $U_{37}^{K'}$-SST difference (**Figures 4C,D**), suggesting that the TEX_{86} proxy largely manifests the integrated water column/subsurface temperature at this site, despite its complicated nature. Hence, vertical thermal difference at the site YJ, associated with the strengthening (weakening) of onsite vertical mixing, facilitates our explanation of enhanced (reduced) winter AMC strength during the LIA (MCA). Altogether, secular changes in winter AMC intensity, for example, its intensification during the LIA, are capable of i) transporting terrigenous biomass, as substantiated by exponential increase of wind-borne hopane compounds (**Figure 4E**); ii) exerting additional cooling signals upon typical cold climate background (through both atmospheric and oceanic processes, Zhang et al., 2019), as seen by abnormal SST decrease (**Figure 4A**); and iii) enhancing vertical mixing (thereby reducing stratification) of the onsite water column, as reinforced by the similarity in $U_{37}^{K'}$ and TEX_{86} temperatures and decrease in their difference (**Figure 4C**), as well as lower BIT values.

CONCLUSION

We used a sediment core YJ, collected from the northern SCS coast, to analyze GDGT lipid biomarkers during the past millennium. These proxies, together with published alkenone ($U_{37}^{K'}$)-SST and hopane records from the same core, help constrain the dynamical interplay between northern SCS coastal conditions and winter AMC intensity at multi-centennial timescales. In general, variations in ACE and BIT indices, although characterized by opposite features, indicate a more prevalent regime of the winter season at the LIA (than the MCA). Further comparison of paired $U_{37}^{K'}$ and TEX_{86} temperature records, with the caution that the latter might be additionally affected by non-thermal factor, shows decrease (increase) in the vertical thermal gradient during the LIA (MCA), thereby calling for a well (less)-mixing of the onsite water column. Therefore, winter AMC changes would have greatly regulated both thermal and saline properties of the shallow waters at northern SCS coasts. Our results necessitate a careful examination of the AMC coupling processes for better understanding coastal environment in the past, for example, during the LIA and MCA, and also in the near future.

DATA AVAILABILITY STATEMENT

The original contributions presented in the study are included in the article/**Supplementary Material**; further inquiries can be directed to the corresponding author.

AUTHOR CONTRIBUTIONS

Conceptualization: ZL; investigation: KZ, CH, DK, YH, HW, and ZX; formal analysis: YZ and ZL; resources: WL, GW, and ZL; funding acquisition: WL and ZL; writing: YZ and ZL led the writing with intellectual contributions from all coauthors.

FUNDING

This work was supported by the National Key Research and Development Program of China (2016YFA0601204) and Hong Kong RGC Grant 17325516.

ACKNOWLEDGMENTS

We sincerely thank guest editors for inviting contribution to this special issue and anonymous referees for providing insightful comments to improve our manuscript.

SUPPLEMENTARY MATERIAL

The Supplementary Material for this article can be found online at: https://www.frontiersin.org/articles/10.3389/feart.2021.680180/full#supplementary-material

REFERENCES

An, Z., Clemens, S. C., Shen, J., Qiang, X., Jin, Z., Sun, Y., et al. (2011). Glacial-interglacial Indian Summer Monsoon Dynamics. *Science* 333, 719–723. doi:10.1126/science.1203752

Blaauw, M., and Christen, J. A. (2011). Flexible Paleoclimate Age-Depth Models Using an Autoregressive Gamma Process. *Bayesian Anal.* 6, 457–474. doi:10.1214/ba/1339616472

Bollasina, M. A., Ming, Y., and Ramaswamy, V. (2011). Anthropogenic Aerosols and the Weakening of the South Asian Summer Monsoon. *Science* 334, 502–505. doi:10.1126/science.1204994

Cai, W., Wu, L., Lengaigne, M., Li, T., McGregor, S., Kug, J.-S., et al. (2019). Pantropical Climate Interactions. *Science* 363, eaav4236. doi:10.1126/science.aav4236

Casey, K. (2013). *US DOC/NOAA/NESDIS > National Oceanographic Data Center, AVHRR Pathfinder Version 5.0 Global 4km Sea Surface Temperature (SST) Cloud-Screened Monthly Climatologies for 1985-2006 (NODC Accession 0110657)*. NOAA: National Oceanographic Data Center.

Cheng, H., Edwards, R. L., Sinha, A., Spötl, C., Yi, L., Chen, S., et al. (2016). The Asian Monsoon over the Past 640,000 Years and Ice Age Terminations. *Nature* 534 (7609), 640–646. doi:10.1038/nature18591

Dunn, J. R., and Ridgway, K. R. (2002). Mapping Ocean Properties in Regions of Complex Topography. *Deep Sea Res. Oceanographic Res. Pap.* 49 (3), 591–604. doi:10.1016/s0967-0637(01)00069-3

Dykoski, C., Edwards, R., Cheng, H., Yuan, D., Cai, Y., Zhang, M., et al. (2005). A High-Resolution, Absolute-Dated Holocene and Deglacial Asian Monsoon Record from Dongge Cave, China. *Earth Planet. Sci. Lett.* 233, 71–86. doi:10.1016/j.epsl.2005.01.036

He, Y., Wang, H., Meng, B., Liu, H., Zhou, A., Song, M., et al. (2020). Appraisal of Alkenone- and Archaeal Ether-Based Salinity Indicators in Mid-latitude Asian Lakes. *Earth Planet. Sci. Lett.* 538, 116236. doi:10.1016/j.epsl.2020.116236

Hopmans, E. C., Weijers, J. W. H., Schefuss, E., Herfort, L., Sinninghe Damsté, J. S., and Schouten, S. (2004). A Novel Proxy for Terrestrial Organic Matter in

Sediments Based on Branched and Isoprenoid Tetraether Lipids. *Earth Planet. Sci. Lett.* 224, 107–116. doi:10.1016/j.epsl.2004.05.012

Hu, C., Henderson, G. M., Huang, J., Xie, S., Sun, Y., and Johnson, K. R. (2008). Quantification of Holocene Asian Monsoon Rainfall from Spatially Separated Cave Records. *Earth Planet. Sci. Lett.* 266, 221–232. doi:10.1016/j.epsl.2007.10.015

Huang, C., Zeng, T., Ye, F., Xie, L., Wang, Z., Wei, G., et al. (2018). Natural and Anthropogenic Impacts on Environmental Changes over the Past 7500 Years Based on the Multi-Proxy Study of Shelf Sediments in the Northern South China Sea. *Quat. Sci. Rev.* 197, 35–48. doi:10.1016/j.quascirev.2018.08.005

Huang, E., Tian, J., and Steinke, S. (2011). Millennial-scale Dynamics of the winter Cold Tongue in the Southern South China Sea over the Past 26 Ka and the East Asian winter Monsoon. *Quat. Res.* 75, 196–204. doi:10.1016/j.yqres.2010.08.014

Huguet, C., Hopmans, E. C., Febo-Ayala, W., Thompson, D. H., Sinninghe Damsté, J. S., and Schouten, S. (2006). An Improved Method to Determine the Absolute Abundance of Glycerol Dibiphytanyl Glycerol Tetraether Lipids. *Org. Geochem.* 37, 1036–1041. doi:10.1016/j.orggeochem.2006.05.008

Jia, G., Wang, X., Guo, W., and Dong, L. (2017). Seasonal Distribution of Archaeal Lipids in Surface Water and its Constraint on Their Sources and the TEX86 Temperature Proxy in Sediments of the South China Sea. *J. Geophys. Res. Biogeosci.* 122, 592–606. doi:10.1002/2016jg003732

Jing, Z.-y., Qi, Y.-q., Hua, Z.-l., and Zhang, H. (2009). Numerical Study on the Summer Upwelling System in the Northern continental Shelf of the South China Sea. *Continental Shelf Res.* 29, 467–478. doi:10.1016/j.csr.2008.11.008

Kang, S., Du, J., Wang, N., Dong, J., Wang, D., Wang, X., et al. (2020). Early Holocene Weakening and Mid- to Late Holocene Strengthening of the East Asian winter Monsoon. *Geology* 48 (11), 1043–1047. doi:10.1130/g47621.1

Kim, J.-H., van der Meer, J., Schouten, S., Helmke, P., Willmott, V., Sangiorgi, F., et al. (2010). New Indices and Calibrations Derived from the Distribution of Crenarchaeal Isoprenoid Tetraether Lipids: Implications for Past Sea Surface Temperature Reconstructions. *Geochimica et Cosmochimica Acta* 74, 4639–4654. doi:10.1016/j.gca.2010.05.027

Kok, J. F., Ward, D. S., Mahowald, N. M., and Evan, A. T. (2018). Global and Regional Importance of the Direct Dust-Climate Feedback. *Nat. Commun.* 9, 241. doi:10.1038/s41467-017-02620-y

Kong, D. (2014a). *Climatic Changes in the Northern South China Sea since the Last Glacial Maximum. PhD Thesis*. Hong Kong: University of Hong Kong. doi:10.5353/th_b5312314

Kong, D., Wei, G., Chen, M.-T., Peng, S., and Liu, Z. (2017). Northern South China Sea SST Changes over the Last Two Millennia and Possible Linkage with Solar Irradiance. *Quat. Int.* 459, 29–34. doi:10.1016/j.quaint.2017.10.001

Kong, D., Zong, Y., Jia, G., Wei, G., Chen, M.-T., and Liu, Z. (2014b). The Development of Late Holocene Coastal Cooling in the Northern South China Sea. *Quat. Int.* 349, 300–307. doi:10.1016/j.quaint.2013.08.055

Lau, N.-C., and Nath, M. J. (2009). A Model Investigation of the Role of Air-Sea Interaction in the Climatological Evolution and ENSO-Related Variability of the Summer Monsoon over the South China Sea and Western North Pacific. *J. Clim.* 22, 4771–4792. doi:10.1175/2009jcli2758.1

Lee, W.-M., Poon, K.-C., Kong, D., Sewell, R. J., Zong, Y., Zhang, Y., et al. (2019). Summer Monsoon-Induced Upwelling Dominated Coastal Sea Surface Temperature Variations in the Northern South China Sea over the Last Two Millennia. *The Holocene* 29 (4), 691–698. doi:10.1177/0959683618824715

Li, Y., and Morrill, C. (2015). A Holocene East Asian winter Monsoon Record at the Southern Edge of the Gobi Desert and its Comparison with a Transient Simulation. *Clim. Dyn.* 45, 1219–1234. doi:10.1007/s00382-014-2372-5

Li, Z., Lau, W. K. M., Ramanathan, V., Wu, G., Ding, Y., Manoj, M. G., et al. (2016). Aerosol and Monsoon Climate Interactions over Asia. *Rev. Geophys.* 54, 866–929. doi:10.1002/2015rg000500

Liu, B., and Zhu, C. (2016). A Possible Precursor of the South China Sea Summer Monsoon Onset: Effect of the South Asian High. *Geophys. Res. Lett.* 43, 11072–11079. doi:10.1002/2016gl071083

Liu, J., Chen, J., Zhang, X., Li, Y., Rao, Z., and Chen, F. (2015). Holocene East Asian Summer Monsoon Records in Northern China and Their Inconsistency with Chinese Stalagmite δ18O Records. *Earth-Science Rev.* 148, 194–208. doi:10.1016/j.earscirev.2015.06.004

Liu, W., Wang, H., Zhang, C. L., Liu, Z., and He, Y. (2013). Distribution of Glycerol Dialkyl Glycerol Tetraether Lipids along an Altitudinal Transect on Mt. Xiangpi, NE Qinghai-Tibetan Plateau, China. *Org. Geochem.* 57, 76–83. doi:10.1016/j.orggeochem.2013.01.011

Maher, B. A., Prospero, J. M., Mackie, D., Gaiero, D., Hesse, P. P., and Balkanski, Y. (2010). Global Connections between Aeolian Dust, Climate and Ocean Biogeochemistry at the Present Day and at the Last Glacial Maximum. *Earth-Science Rev.* 99, 61–97. doi:10.1016/j.earscirev.2009.12.001

Mann, M. E., Zhang, Z., Hughes, M. K., Bradley, R. S., Miller, S. K., Rutherford, S., et al. (2008). Proxy-based Reconstructions of Hemispheric and Global Surface Temperature Variations over the Past Two Millennia. *Proc. Natl. Acad. Sci.* 105 (36), 13252–13257. doi:10.1073/pnas.0805721105

Prahl, F. G., Muehlhausen, L. A., and Zahnle, D. L. (1988). Further Evaluation of Long-Chain Alkenones as Indicators of Paleoceanographic Conditions. *Geochimica et Cosmochimica Acta* 52, 2303–2310. doi:10.1016/0016-7037(88)90132-9

Reimer, P. J., Bard, E., Bayliss, A., Beck, J. W., Blackwell, P. G., Ramsey, C. B., et al. (2013). IntCal13 and Marine13 Radiocarbon Age Calibration Curves 0-50,000 Years Cal BP. *Radiocarbon* 55, 1869–1887. doi:10.2458/azu_js_rc.55.16947

Schouten, S., Hopmans, E. C., Schefuss, E., and Sinninghe Damsté, J. S. (2002). Distributional Variations in marine Crenarchaeotal Membrane Lipids: a New Tool for Reconstructing Ancient Sea Water Temperatures? *Earth Planet. Sci. Lett.* 204, 265–274. doi:10.1016/s0012-821x(02)00979-2

Schouten, S., Hopmans, E. C., and Sinninghe Damsté, J. S. (2013). The Organic Geochemistry of Glycerol Dialkyl Glycerol Tetraether Lipids: a Review. *Org. Geochem.* 54, 19–61. doi:10.1016/j.orggeochem.2012.09.006

Southon, J., Kashgarian, M., Fontugne, M., Metivier, B., and W-S Yim, W. (2002). Marine Reservoir Corrections for the Indian Ocean and Southeast Asia. *Radiocarbon* 44, 167–180. doi:10.1017/s0033822200064778

Steinke, S., Glatz, C., Mohtadi, M., Groeneveld, J., Li, Q., and Jian, Z. (2011). Past Dynamics of the East Asian Monsoon: No Inverse Behaviour between the Summer and winter Monsoon during the Holocene. *Glob. Planet. Change* 78, 170–177. doi:10.1016/j.gloplacha.2011.06.006

Stevens, T., Thomas, D., Armitage, S., Lunn, H., and Lu, H. (2007). Reinterpreting Climate Proxy Records from Late Quaternary Chinese Loess: A Detailed OSL Investigation. *Earth-Science Rev.* 80, 111–136. doi:10.1016/j.earscirev.2006.09.001

Tian, J., Huang, E., and Pak, D. K. (2010). East Asian winter Monsoon Variability over the Last Glacial Cycle: Insights from a Latitudinal Sea-Surface Temperature Gradient across the South China Sea. *Palaeogeogr. Palaeoclimatol. Palaeoecol.* 292, 319–324. doi:10.1016/j.palaeo.2010.04.005

Turich, C., and Freeman, K. (2011). Archaeal Lipids Record Paleosalinity in Hypersaline Systems. *Org. Geochem.* 42, 1147–1157.

Turich, C., Freeman, K., Freeman, K. H., Bruns, M. A., Conte, M., Jones, A. D., et al. (2007). Lipids of marine Archaea: Patterns and Provenance in the Water-Column and Sediments. *Geochimica et Cosmochimica Acta* 71, 3272–3291. doi:10.1016/j.gca.2007.04.013

Wang, B., Huang, F., Wu, Z., Yang, J., Fu, X., and Kikuchi, K. (2009). Multi-scale Climate Variability of the South China Sea Monsoon: A Review. *Dyn. Atmospheres Oceans* 47, 15–37. doi:10.1016/j.dynatmoce.2008.09.004

Wang, H., Liu, W., Zhang, C. L., Jiang, H., Dong, H., Lu, H., et al. (2013). Assessing the Ratio of Archaeol to Caldarchaeol as a Salinity Proxy in highland Lakes on the Northeastern Qinghai-Tibetan Plateau. *Org. Geochem.* 54, 69–77. doi:10.1016/j.orggeochem.2012.09.011

Wang, J.-X., Wei, Y., Wang, P., Hong, Y., and Zhang, C. L. (2015). Unusually Low TEX86 Values in the Transitional Zone between Pearl River Estuary and Coastal South China Sea: Impact of Changing Archaeal Community Composition. *Chem. Geology.* 402, 18–29. doi:10.1016/j.chemgeo.2015.03.002

Wang, L., Li, J., Lu, H., Gu, Z., Rioual, P., Hao, Q., et al. (2012). The East Asian winter Monsoon over the Last 15,000 Years: its Links to High-Latitudes and Tropical Climate Systems and Complex Correlation to the Summer Monsoon. *Quat. Sci. Rev.* 32, 131–142. doi:10.1016/j.quascirev.2011.11.003

Wang, M., Wang, H., Zhu, Z., Yang, X., Zhang, K., Zhang, Y., et al. (2021). Late Miocene-Pliocene Asian Summer Monsoon Variability Linked to Both Tropical Pacific Temperature and Walker Circulation. *Earth Planet. Sci. Lett.* 561 (116823), 116823. doi:10.1016/j.epsl.2021.116823

Wang, P. X., Wang, B., Cheng, H., Fasullo, J., Guo, Z., Kiefer, T., et al. (2017). The Global Monsoon across Time Scales: Mechanisms and Outstanding Issues. *Earth-Science Rev.* 174, 84–121. doi:10.1016/j.earscirev.2017.07.006

Wang, Y., Cheng, H., Edwards, R., He, Y., Kong, X., An, Z., et al. (2005). The Holocene Asian Monsoon: Links to Solar Changes and North Atlantic Climate. *Science* 308, 854–857. doi:10.1126/science.1106296

Wei, B., Jia, G., Hefter, J., Kang, M., Park, E., Wang, S., et al. (2020). Comparison of the U37K′, LDI, TEX86H, and RI-OH Temperature Proxies in Sediments from the Northern Shelf of the South China Sea. *Biogeosciences* 17, 4489–4508. doi:10.5194/bg-17-4489-2020

Weijers, J. W. H., Schefuß, E., Kim, J.-H., Sinninghe Damsté, J. S., and Schouten, S. (2014). Constraints on the Sources of Branched Tetraether Membrane Lipids in Distal marine Sediments. *Org. Geochem.* 72, 14–22. doi:10.1016/j.orggeochem.2014.04.011

Wen, X., Liu, Z., Wang, S., Cheng, J., and Zhu, J. (2016). Correlation and Anti-correlation of the East Asian Summer and winter Monsoons during the Last 21,000 Years. *Nat. Commun.* 7. doi:10.1038/ncomms11999

W. Wang (2007). *Study on the Coastal Geomorphological Sedimentation of the South China Sea* (Guangzhou, China: Guangdong Economy Publishing House), 344 in Chinese.

Xiao, W., Wang, Y., Zhou, S., Hu, L., Yang, H., and Xu, Y. (2016). Ubiquitous Production of Branched Glycerol Dialkyl Glycerol Tetraethers (brGDGTs) in Global marine Environments: a New Source Indicator for brGDGTs. *Biogeosciences* 13, 5883–5894. doi:10.5194/bg-13-5883-2016

Xie, A., Chung, Y., Liu, X., and Ye, Q. (1998). The Interannual Variations of Summer Monsoon Onset Over the South China Sea. *Theor. Appl. Climatol.* 59, 201–213.

Xie, S.-P., Deser, C., Vecchi, G. A., Collins, M., Delworth, T. L., Hall, A., et al. (2015). Towards Predictive Understanding of Regional Climate Change. *Nat. Clim Change* 5, 921–930. doi:10.1038/nclimate2689

Xing, L., Sachs, J. P., Gao, W., Tao, S., Zhao, X., Li, L., et al. (2015). TEX 86 Paleothermometer as an Indication of Bottom Water Temperature in the Yellow Sea. *Org. Geochem.* 86, 19–31. doi:10.1016/j.orggeochem.2015.05.007

Yamamoto, M., Kishizaki, M., Oba, T., and Kawahata, H. (2013). Intense winter Cooling of the Surface Water in the Northern Okinawa Trough during the Last Glacial Period. *J. Asian Earth Sci.* 69, 86–92. doi:10.1016/j.jseaes.2012.06.011

Yancheva, G., Nowaczyk, N. R., Mingram, J., Dulski, P., Schettler, G., Negendank, J. F. W., et al. (2007). Influence of the Intertropical Convergence Zone on the East Asian Monsoon. *Nature* 445, 74–77. doi:10.1038/nature05431

Yu, K., Hua, Q., Zhao, J.-x., Hodge, E., Fink, D., and Barbetti, M. (2010). Holocene marine14C Reservoir Age Variability: Evidence from230Th-Dated Corals in the South China Sea. *Paleoceanography* 25. doi:10.1029/2009PA001831

Zhang, C., Tang, Q., Chen, D., Li, L., Liu, X., and Cui, H. (2017). Tracing Changes in Atmospheric Moisture Supply to the Drying Southwest China. *Atmos. Chem. Phys.* 17, 10383–10393. doi:10.5194/acp-17-10383-2017

Zhang, J., Bai, Y., Xu, S., Lei, F., and Jia, G. (2013). Alkenone and Tetraether Lipids Reflect Different Seasonal Seawater Temperatures in the Coastal Northern South China Sea. *Org. Geochem.* 58, 115–120. doi:10.1016/j.orggeochem.2013.02.012

Zhang, P., Cheng, H., Edwards, R. L., Chen, F., Wang, Y., Yang, X., et al. (2008). A Test of Climate, Sun, and Culture Relationships from an 1810-year Chinese Cave Record. *Science* 322, 940–942. doi:10.1126/science.1163965

Zhang, Y., Zhu, K., Huang, C., Kong, D., He, Y., Wang, H., et al. (2019). Asian winter Monsoon Imprint on Holocene SST Changes at the Northern Coast of the South China Sea. *Geophys. Res. Lett.* 46, 13363–13370. doi:10.1029/2019gl085617

Zhu, C., Wakeham, S. G., Elling, F. J., Basse, A., Mollenhauer, G., Versteegh, G. J. M., et al. (2016). Stratification of Archaeal Membrane Lipids in the Ocean and Implications for Adaptation and Chemotaxonomy of Planktonic Archaea. *Environ. Microbiol.* 18, 4324–4336. doi:10.1111/1462-2920.13289

Zweng, M., Reagan, J., Antonov, J., Locarnini, R., Mishonov, A., Boyer, T., et al. (2013). "World Ocean Atlas," in *NOAA Atlas NESDIS*. Editors S. L. Salinity and A. Mishonov, 39.

Conflict of Interest: The authors declare that the research was conducted in the absence of any commercial or financial relationships that could be construed as a potential conflict of interest.

The reviewer (YH) declared a shared affiliation with several of the authors, (HW, WL, ZX), to the handling editor at time of review.

frontiers in Earth Science

ORIGINAL RESEARCH
published: 20 September 2021
doi: 10.3389/feart.2021.708578

Oxygen Isotope Equilibrium of the Shallow-Water Benthic Foraminifer *Hanzawaia nipponica* Asano in Tosa Bay, Southwest Japan

Minoru Ikehara[1,2]*, *Shigetaka Kita*[2] *and Shungo Kawagata*[3]

[1]Center for Advanced Marine Core Research, Kochi University, Kochi, Japan, [2]Graduate School of Integrated Arts and Sciences, Kochi University, Kochi, Japan, [3]College of Education, Yokohama National University, Yokohama, Japan

Oxygen isotopic compositions ($\delta^{18}O$) of benthic foraminifer tests are widely used for reconstructing paleoceanographic changes, such as global ice volumes during glacial–interglacial cycles. Although deep-sea benthic foraminifers have been well characterized and are considered reliable indicators, little attention has been paid to the geochemistry of shallow-water benthic foraminifers. In this study we evaluated $\delta^{18}O$ in the shallow-water benthic foraminifer *Hanzawaia nipponica* Asano, which lives in surface sediments on continental shelves and upper slopes under the influence of two warm currents, the Kuroshio and Tsushima currents, in the East China Sea, northwest Pacific, and southwestern Japan Sea. To evaluate oxygen isotope equilibrium, we analyzed $\delta^{18}O$ of *H. nipponica* and ambient seawater on the continental shelf in Tosa Bay, southwest Japan. Seawater $\delta^{18}O$ and salinity in Tosa Bay are similar to those of surface and subsurface waters in the Kuroshio region in the Okinawa Trough and the northwest Pacific. Vertical profiles of seawater $\delta^{18}O$ show no variation with water depth (0–200 m) in Tosa Bay. However, tests of living *H. nipponica* (as determined by staining with Rose Bengal) and fossil (non-stained) *H. nipponica*, picked from samples of the top centimeter of seafloor sediment, yielded carbonate $\delta^{18}O$ values that clearly increase with water depth, suggesting a temperature-dependent relationship. A comparison of carbonate $\delta^{18}O$ values in living *H. nipponica* and those predicted on the basis of seawater $\delta^{18}O$ and annual mean bottom temperature shows that *H. nipponica* tests are in oxygen isotopic equilibrium with ambient seawater. We determined the linear equations of $\delta^{18}O$–temperature relationship, and the slope of –5.26 (0.19‰°C^{-1}) for living and –4.50 (0.22‰°C^{-1}) for the fossil *H. nipponica*, respectively. The carbon isotopic compositions ($\delta^{13}C$) of *H. nipponica* also closely match seawater $\delta^{13}C$. Thus, we propose that the carbonate $\delta^{18}O$ and $\delta^{13}C$ of *H. nipponica* are useful proxies to reconstruct shallow-water paleoenvironmental changes in the northwest Pacific and its marginal seas.

Keywords: benthic foraminifer, *Hanzawaia nipponica* Asano, oxygen isotopic equilibrium, Tosa Bay, continental shelf, Kuroshio

Edited by:
Min-Te Chen,
National Taiwan Ocean University,
Taiwan

Reviewed by:
Tadamichi Oba,
Hokkaido University, Japan
Hong-Chun Li,
National Taiwan University, Taiwan

***Correspondence:**
Minoru Ikehara
ikehara@kochi-u.ac.jp

Specialty section:
This article was submitted to
Quaternary Science, Geomorphology
and Paleoenvironment,
a section of the journal
Frontiers in Earth Science

Received: *12 May 2021*
Accepted: *02 September 2021*
Published: *20 September 2021*

Citation:
Ikehara M, Kita S and Kawagata S
(2021) Oxygen Isotope Equilibrium of
the Shallow-Water Benthic Foraminifer
Hanzawaia nipponica *Asano in Tosa*
Bay, Southwest Japan.
Front. Earth Sci. 9:708578.
doi: 10.3389/feart.2021.708578

INTRODUCTION

The oxygen isotopic composition ($\delta^{18}O$) of the carbonate tests of benthic foraminifers is widely used in studying the geologic history of the oceans, especially the deep ocean. For example, early researchers argued that the deep-sea benthic foraminifer *Uvigerina* spp. appears to record $\delta^{18}O$ of calcite in isotopic equilibrium with seawater (Shackleton, 1974) and that *Cibicidoides wuellerstorfi* deviates from equilibrium by −0.64‰ in the Pacific (Shackleton and Opdyke, 1973). Bemis et al. (1998) countered their argument by compiling published $\delta^{18}O$ data for *Uvigerina* and *Cibicidoides* species from core tops in the Atlantic, Pacific, and Indian oceans and comparing them with predictions from the paleotemperature equation established by experimental results from planktic foraminifers, finding that *Cibicidoides* $\delta^{18}O$ data were in excellent agreement with the equation whereas *Uvigerina* data were scattered. They concluded that the relative ^{18}O enrichment of *Uvigerina* over *Cibicidoides* tests reflects the habitat differences of the genera: *Uvigerina* is infaunal and experiences low pH and decreased [CO_3^{2-}] in pore waters, whereas *Cibicidoides* inhabits the sediment surface where bottom water pH and [CO_3^{2-}] are higher (Bemis et al., 1998). As a result of these and other advances, much paleoceanographic research has made use of $\delta^{18}O$ analyses of epifaunal deep-sea benthic foraminifers. In contrast, shallow-water benthic foraminifers have seen little application in paleoceanographic studies because it is assumed that $\delta^{18}O$ in these species would be affected by freshwater input and larger temperature variations in the shallow-water environment. Although $\delta^{18}O$ records from shallow-water settings are very important evidence of past environmental changes of the coastal ocean, there is presently no useful species of shallow-water benthic foraminifer to aid in reconstructing past $\delta^{18}O$ changes.

Hanzawaia nipponica is a species of benthic foraminifer that was first reported from Pliocene strata in Kawasaki, on the Pacific coast of Japan, by Asano (1944) and has been subsequently reported from Pliocene to Pleistocene sedimentary sequences around Japan, such as in Okinawa (LeRoy, 1964), Kochi (Katto et al., 1953), and Shizuoka (Aoshima, 1978). Outside Japan, it has been recorded from upper Pliocene to lower Pleistocene shallow-marine deposits on Jeju Island in the Korea Strait (Li et al., 1999; Kang et al., 2010) and from a Holocene marine core in the Yellow Sea (Xiang et al., 2008). The living species is abundant in surface sediment on the continental shelf in the East China Sea (Inoue, 1989), off the San'in district in the southwest Japan Sea (Inoue, 1989), and in the Pacific Ocean near Japan off Kyushu Island (Akimoto and Torii, 1996), off Shikoku Island (Ishiwada, 1964; Inoue, 1989), off the Kii Peninsula (Uchio, 1968; Akimoto, 1990), in Suruga Bay (Akimoto, 1990), and off the Boso Peninsula (Kuwano, 1963). Living *H. nipponica* have been recorded at water depths ranging from 23 to 235 m (mainly at ~40 m) off the Pacific coast of western Japan (Aoshima, 1978). These records suggest that the main habitat of this species is the shallow continental shelf along southwestern Japan, where the seafloor is influenced by two major warm currents, the Kuroshio and Tsushima currents (Ishiwada, 1964; Matoba, 1976; Matoba and Honma, 1986; Inoue, 1989; Hasegawa, 1993).

TABLE 1 | Sampling sites in Tosa Bay, southwest Japan.

Site	Latitude	Longitude	Water depth (m)
St.5	32°25.133′N	133°30.667′E	40
St.25	32°19.0′N	133°35.25′E	100
St.26	32°15.0′N	133°38.25′E	200

Oxygen and carbon isotope compositions have been reported for fossil specimens of *H. nipponica* from one horizon of middle Pleistocene age in the lower Seogwipo Formation on Jeju Island (Li et al., 1999); however, there is no published evidence bearing on the oxygen isotope equilibrium of this species with seawater. In this study, we analyzed the $\delta^{18}O$ of ambient seawater on the continental shelf in Tosa Bay, off Shikoku Island, Japan, and contemporary *H. nipponica* tests from seafloor surface sediment in Tosa Bay, and we determined that the tests were in isotopic equilibrium with seawater. Our findings indicate that isotopic analyses of *H. nipponica*, a regionally abundant species recorded from the late Neogene to the present, can be valuable for paleoceanographic studies in shallow-marine environments.

METHODS

Sediment was collected with a Smith–McIntyre grab sampler from three sites (sites 5, 25, and 26) on the continental shelf of Tosa Bay (**Table 1**; **Figure 1**) by T/S *Toyohata-maru* and T/S *Neptune* operated by Kochi University. Sediment samples for this study were collected from the uppermost centimeter of the sediment in the grab sampler. These were stored in a refrigerator and stained with Rose Bengal to identify living individuals of *Hanzawaia nipponica* Asano. After 2 days, the stained sediments were washed with water through a 150-μm mesh sieve and the fractions remaining on the sieve were dried at 50°C in an oven. Stained tests larger than 150 μm, representing mature living foraminifers, were then picked for isotope analysis (**Figure 2**). These tests (7–10 specimens) were baked at 450°C in an electric oven to remove organic matter from the tests (e.g. Erez and Luz, 1983). Fossil individuals of *H. nipponica* (50 specimens) were also picked for isotope analysis. All tests were cleaned with methanol by ultrasonication, slightly crushed in a glass vial and weighed, and then cleaned carbonate fragments weighing approximately 100 μg were reacted with 100% phosphoric acid at 90°C in a vacuum. The released CO_2 was purified and analyzed for $\delta^{18}O$ in carbonate ($\delta^{18}O_c$) and carbon isotopic composition ($\delta^{13}C$) using the isotope ratio mass spectrometer (IsoPrime, GV Instruments Ltd.), with its MultiPrep automated sample preparation module, at the Center for Advanced Marine Core Research, Kochi University. The results are expressed in relation to the Vienna Pee Dee Belemnite (VPDB) standard. The estimated analytical precisions were better than 0.1‰ for both $\delta^{18}O$ and $\delta^{13}C$ measurements.

Seawater samples were collected at depths representing the entire water column (**Table 2**) at sites 5, 25, and 26 using a

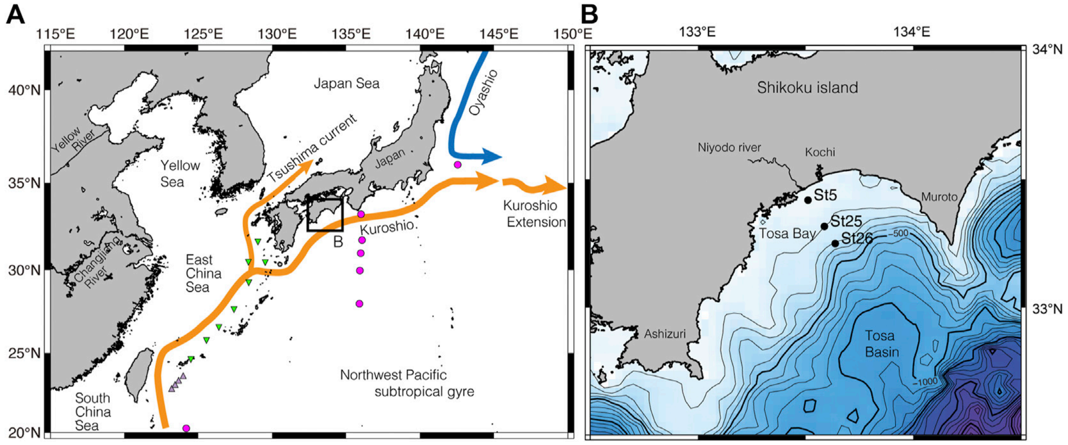

FIGURE 1 | Site location maps. **(A)** Index map with major surface currents in the northwest Pacific and marginal seas. The red circles indicate the location of the isotope data in Horibe and Ogura (1968), and light purple triangles show the location of the isotope data at Kuroshio sites in Horikawa et al. (2015). Green triangles show same at Okinawa Trough sites in Horikawa et al. (2015). **(B)** Bathymetric map showing site locations of surface sediment and seawater samples on the continental shelf in Tosa Bay; map location shown in **(A)**. Contour interval, 100 m.

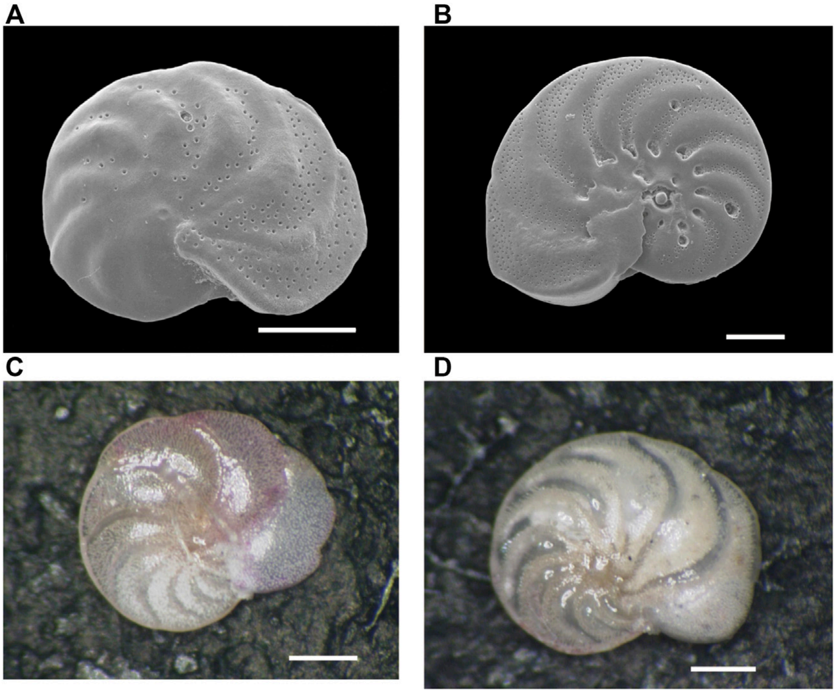

FIGURE 2 | Scanning Electron Microscope (SEM) and stereo microscopic images of the benthic foraminifer *Hanzawaia nipponica* (Asano) from surface sediment in Tosa Bay. **(A)** SEM image of living (stained) *H. nipponica* from site 25, **(B)** SEM image of living *H. nipponica* from site 5, **(C)** photomicrograph of living *H. nipponica* from site 5, **(D)** photomicrograph of fossil (non-stained) *H. nipponica* from site 25. Scale bars are 100 μm in **(A)** and **(B)** and 200 μm in **(C)** and **(D)**.

conductivity–temperature–depth (CTD)/rosette multi-sampler system with Niskin bottles on November 20, 2009 during a cruise by T/S *Toyohata-maru*. These samples were placed in 6-ml glass vials without bubbles and stored in a refrigerator until isotopic measurements were made. Subsamples measuring 200 μL were transferred into 10-ml vials containing CO_2 gas (99.999%) and allowed to reach CO_2–H_2O exchange equilibrium at 25°C. The equilibrium CO_2 gas was purified and analyzed for seawater $\delta^{18}O$ ($\delta^{18}O_{sw}$) using the IsoPrime system at Kochi University. The results are expressed in relation to Vienna Standard Mean Ocean Water (VSMOW). The estimated analytical precision was better than 0.1‰.

Profiles of water temperature and salinity were measured at 0.5-m depth intervals from the surface to the seafloor during the same cruise using a Compact-CTD system (Alec Electronics Ltd.). CTD profiles at these three sites were also measured

TABLE 2 | Temperature, salinity, and oxygen isotopic composition in seawater ($\delta^{18}O_{sw}$) from three sites in Tosa Bay (November 20, 2009).

Site	Water depth (m)	Temperature (°C)	Salinity	$\delta^{18}O_{sw}$ (‰, VSMOW)	Std.dev (‰)
St.5	0	22.24	34.01	0.180	0.02
	10	22.43	34.05	0.154	0.03
	25	22.37	34.18	0.173	0.03
	40	22.14	34.41	0.236	0.06
St.25	0	22.67	34.25	0.321	0.02
	10	22.71	34.25	0.169	0.03
	25	22.71	34.26	0.286	0.04
	50	22.71	34.27	0.292	0.03
	75	22.71	34.27	0.167	0.01
	100	20.87	34.52	0.244	0.02
St.26	0	22.86	34.23	0.259	0.04
	10	22.87	34.28	0.295	0.03
	25	22.87	34.28	0.233	0.04
	50	22.83	34.29	0.295	0.06
	75	22.62	34.27	0.271	0.03
	100	21.25	34.54	0.263	0.02
	150	18.31	34.60	0.274	0.02
	200	16.22	34.61	0.209	0.03
Analytical error:		±0.02	±0.03	<0.1	

TABLE 3 | Seasonal maximum, minimum, and annual mean value of bottom water temperature and salinity from three sites in Tosa Bay.

Site	Water depth (m)	Bottom water temperature (°C)			Bottom water salinity		
		max	min	annual mean	max	min	annual mean
St.5	40	27.5	16.1	20.8	34.6	33.8	34.4
St.25	100	21.8	13.8	17.9	34.6	34.3	34.5
St.26	200	16.2	9.4	12.5	34.6	34.3	34.5

each month from April 2009 to February 2010 by the research group of Usa Marine Biological Institute, Kochi University (**Table 3**). In this study, the nominal depths of the seafloor were 40 m at site 5, 100 m at site 25, and 200 m at site 26, although actual depths varied slightly from month to month. Accuracy of temperature and salinity measurements are ±0.02°C and ±0.03, respectively.

RESULTS AND DISCUSSION

Oceanic Structure and $\delta^{18}O_{sw}$ in Shallow Tosa Bay

Vertical profiles of monthly seawater temperature and salinity on the continental shelf in Tosa Bay show typical seasonal variations (**Figure 3**). Sea surface temperatures are about 28°C in summer and 17°C in winter at the three study sites (**Figure 3**). The surface water is thermally stratified during spring to summer, vertical mixing begins in October to November, and the temperature profile is almost uniform during January to March (Ichikawa and Hirota, 2004). The vertical temperature gradients on the day of sampling (November 20, 2009) were steeper than that of the annual mean temperature (**Figure 3**). The annual mean salinity in surface water was approximately 34.0 at site 5 and approximately 34.2 at sites 25 and 26 (**Figure 3**). Although the salinity of surface water in Tosa Bay decreased from July to September as a result of freshwater input from the Asian summer monsoon, the low-salinity layer was limited to the upper 80–90 m of the water column at sites 25 and 26. The sea surface salinity on the sampling day was slightly lower at site 5 (34.0) than at sites 25 (34.2) and 26 (34.2), but near the seafloor the salinity at site 5, the shallowest site (34.4), was similar to those at sites 25 (34.5) and 26 (34.6).

Although Tosa Bay is an open bay with a semicircular shelf–slope topography (**Figure 1**), the warm water of the Kuroshio does not flow directly through the bay. The most dominant current pattern is a counterclockwise circulation interacting with a cold eddy (Fujimoto, 1987; Kuroda et al., 2008). This circulation appears to be induced by the combined effect of changes in the position of the Kuroshio axis and the irregular topography of the continental margin (Awaji et al., 1991). The surface current, subsurface temperature, and vertical thermal structure on the continental slope in Tosa Bay are markedly influenced by the position of the Kuroshio axis, the counterclockwise circulation being enhanced as the Kuroshio axis moves near shore south of the Ashizuri and Muroto peninsulas (Kuroda et al., 2008). Therefore, the seafloor environment is affected by low-salinity coastal water only at depths shallower than 80–90 m in Tosa Bay, and the seafloor below 100 m is predominantly influenced by water originating from the Kuroshio.

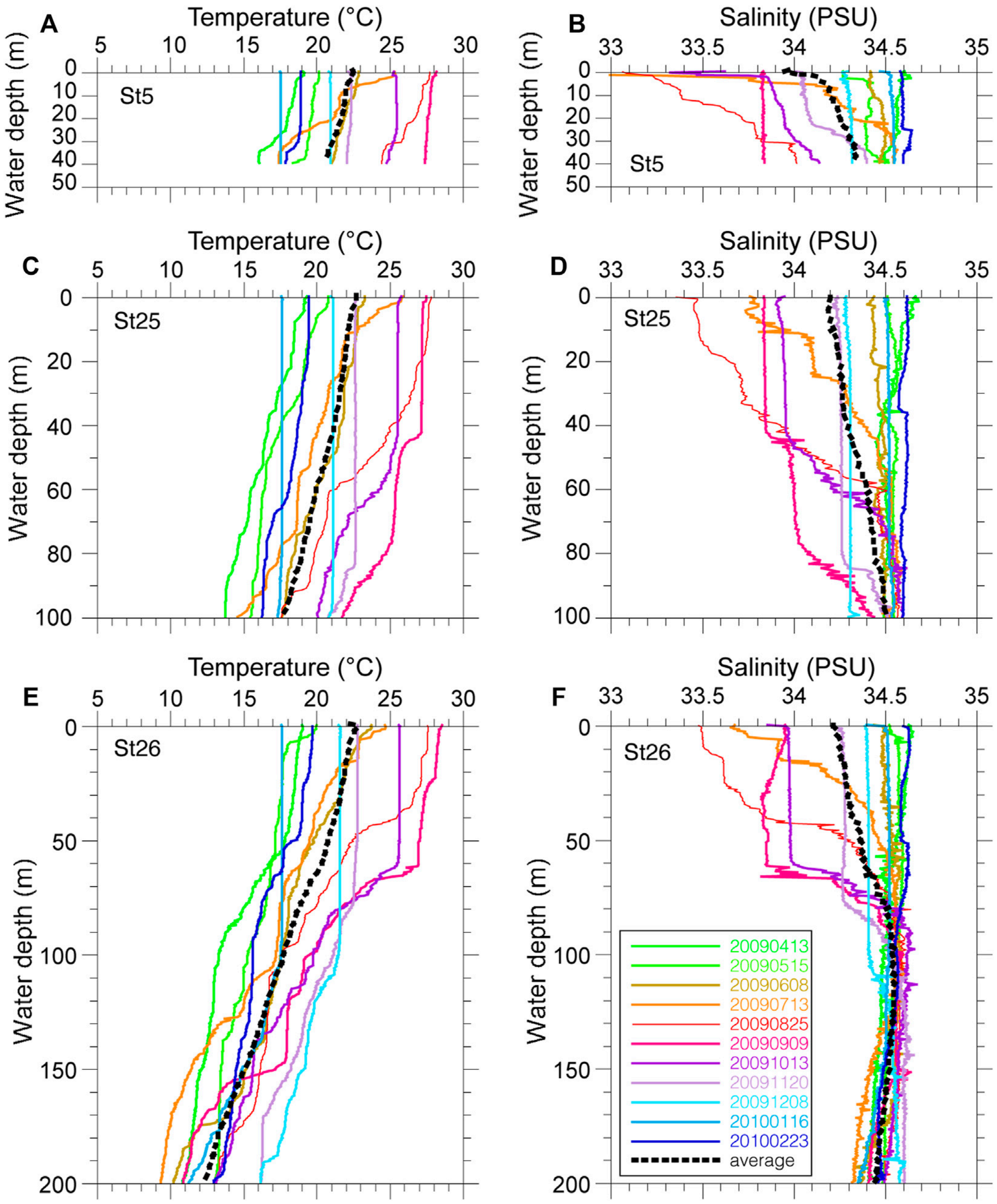

FIGURE 3 | Measured temperature and salinity profiles at three sites in Tosa Bay. **(A)** temperature and **(B)** salinity at site 5, **(C)** temperature and **(D)** salinity at site 25, **(E)** temperature and **(F)** salinity at site 26. Thin colored lines are monthly values, heavy dashed lines are annual mean values (April 2009 to February 2010).

On the date of sampling, the three sites in Tosa Bay had $\delta^{18}O_{sw}$ ranging from 0.15 to 0.32‰ (**Table 2**; **Figure 4**). Although not all of the Tosa Bay data lie on the regression lines of surface water from the East China Sea to the Kuroshio region (Oba, 1990; Horikawa et al., 2015) and their $\delta^{18}O_{sw}$ values appear relatively high (**Figure 4**), the $\delta^{18}O_{sw}$–salinity data appear to be consistent with previously published results. These $\delta^{18}O_{sw}$ values and salinity values in Tosa Bay are very close to those of Kuroshio surface water from east of Taiwan (salinity = 34.2–34.4 and $\delta^{18}O_{sw}$ = 0.1–0.2‰) and Kuroshio subsurface water (40–100 m) in the Okinawa Trough (salinity = 34.4–34.7 and $\delta^{18}O_{sw}$ = 0.15–0.35‰) (Horikawa et al., 2015). The $\delta^{18}O_{sw}$ values in Tosa Bay are also consistent with those in surface and subsurface waters (0.25‰–0.4‰; 0–200 m) from the Kuroshio Extension and subtropical gyre (Oba and Yasuda, 1992). There is little available $\delta^{18}O_{sw}$–salinity data of typical Kuroshio waters, but data from the Kuroshio region south of Japanese Islands show that Kuroshio water has higher salinity and $\delta^{18}O$ there than in the localities just described (Horibe and Ogura, 1968) (**Figure 4**). The $\delta^{18}O$ data from Horibe and Ogura (1968) were converted from

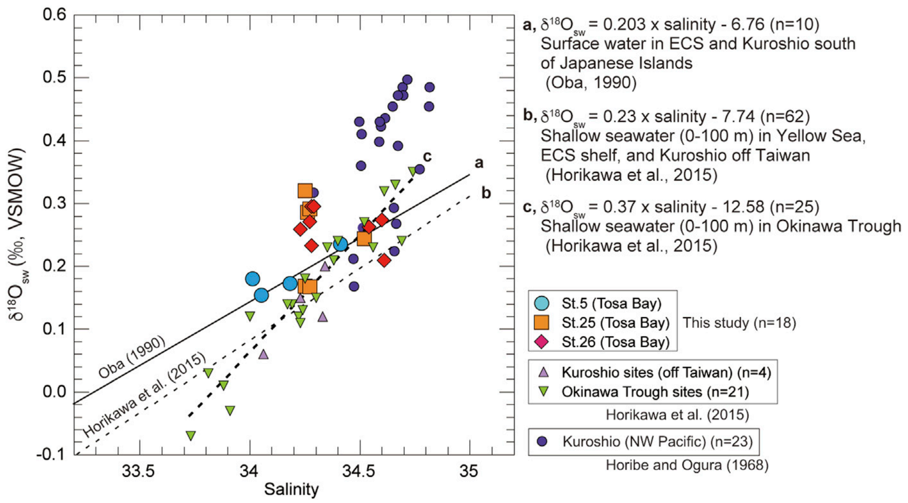

FIGURE 4 | Plot of seawater $\delta^{18}O_{sw}$ against salinity (0–200 m) in Tosa Bay during November and published data from other northwest Pacific and East China Sea sites. Regression line **(A)** is derived from surface-water data in the East China Sea and the Kuroshio south of the Japanese Islands (Oba 1990). Regression line **(B)** is from shallow water (0–100 m) data in the Yellow Sea, East China Sea, and the Kuroshio off Taiwan (Horikawa et al., 2015). Regression line **(C)** is derived from shallow water (0–100 m) data in the Okinawa Trough (Horikawa et al., 2015). Equations from the literature are also shown. Equation of regression line c is calculated from data in the Okinawa Trough sites in Horikawa et al. (2015). End-member data for the Kuroshio are from northwest Pacific (Horibe and Ogura 1968).

TABLE 4 | Oxygen and carbon isotopic compositions of living (stained) and fossil (non-stained) *H. nipponica* from three sites in Tosa Bay.

Site	Water depth (m)	living *Hanzawaia nipponica*			fossil *Hanzawaia nipponica*		
		Specimens	$\delta^{18}O$ (‰, VPDB)	$\delta^{18}C$ (‰, VPDB)	Specimens	$\delta^{18}O$ (‰, VPDB)	$\delta^{13}C$ (‰, VPDB)
St.5	40	10	−0.89	0.03	50	−1.00	0.77
St.25	100	9	−0.35	0.99	50	−0.38	0.94
St.26	200	7	0.68	0.80	50	0.83	0.63

Analytical error: <0.1‰

δD data via the formula $\delta^{18}O = \delta D/8.03$. Slope 8.03 is derived from the relationship between $\delta^{18}O$ and δD of observed global data (Mathieu et al., 2002).

The $\delta^{18}O_{sw}$ values averaged over the water column are 0.19‰ at site 5, 0.25‰ at site 25, and 0.26‰ at site 26. These results suggest that site 5 might be affected by freshwater with lower $\delta^{18}O$ values from the Niyodo River. The $\delta^{18}O$ values of surface water (river, stream, and spring water) in southern Shikoku are ranging from −5.9‰ to −7.9‰ (calculated average value −6.6‰) (Mizota and Kusakabe, 1994), indicating that the freshwater $\delta^{18}O$ from Shikoku is almost consistent with the intercept of regression line a (**Figure 4**), which was derived from surface water in East China Sea and Kuroshio region in south of Japanese Islands (Oba, 1990). However, the discrepancy at site 5 is much smaller in water near the seafloor (**Table 2**), which suggests that freshwater influences only the surface mixed layer near the mouth of the Niyodo River. We lack data to assess the impact of seasonal changes, but because the seasonal salinity variation in bottom-water is small (**Figure 3**), we assume that the seasonal variation of $\delta^{18}O_{sw}$ in bottom water is negligible.

Oxygen Isotope Equilibrium of *H. nipponica*

The $\delta^{18}O_c$ values of living and fossil *H. nipponica* increase with water depth in Tosa Bay, even though the vertical profile of $\delta^{18}O_{sw}$ is almost constant (**Table 4**; **Figure 5**). The differences in $\delta^{18}O_c$ with depth may depend on water temperature, given that $\delta^{18}O_{sw}$ varies so little with depth (**Figure 5A**). However, $\delta^{18}O_c$ in many foraminifer species differs from the equilibrium state (e.g., Shackleton, 1973; Bemis et al., 1998), and a specific offset value should be calculated to assess the temperature dependence of $\delta^{18}O_c$ in *H. nipponica*. Although the biology of *H. nipponica* is not documented in detail, the life span of shallow-water benthic foraminifers is typically from several months to a year (Murray, 1991). For example, the life cycle of *Planoglabratella opercularis*, a benthic inhabitant of rocky shore environments, is completed in 40–65 days (Tsuchiya et al., 2014). We assumed that the life span of *H. nipponica* is more than 3 months, and on that basis we estimated the effect on calcification in the shallow ambient environment in Tosa Bay. Predicted $\delta^{18}O_c$ values were calculated, assuming oxygen isotopic equilibrium in foraminiferal calcite, from

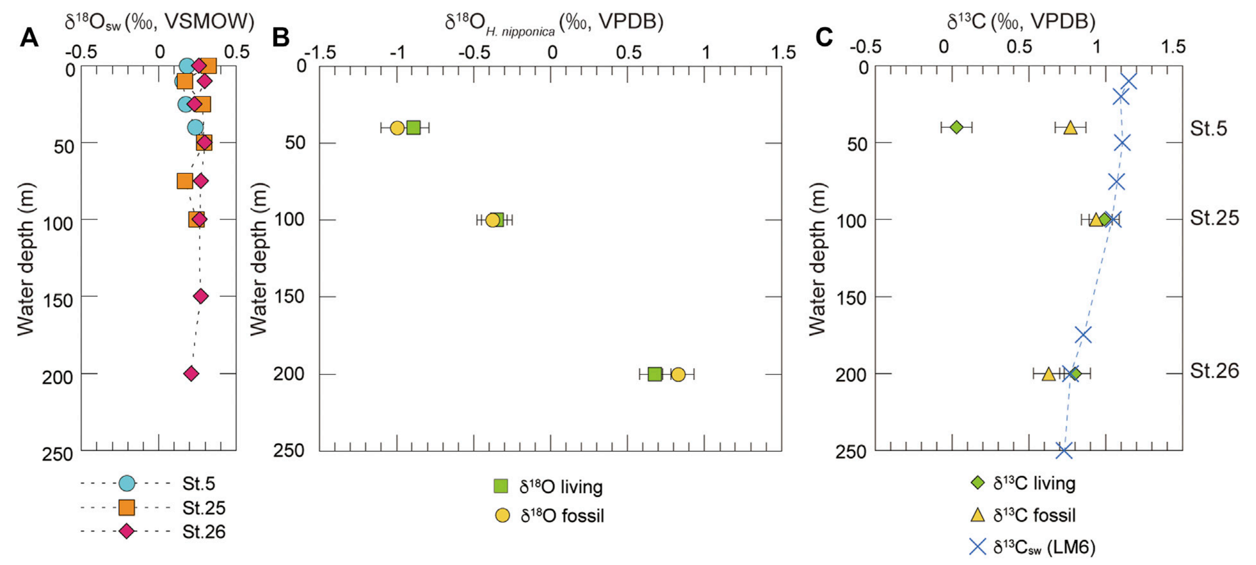

FIGURE 5 | Oxygen and carbon isotopic compositions of seawater and *H. nipponica* at three sites in Tosa Bay. **(A)** Vertical profiles of oxygen isotopic compositions of seawater. **(B)** Oxygen and **(C)** carbon isotopic compositions of living and fossil *H. nipponica* specimens. Horizontal bars represent analytical error of 0.1‰. The $\delta^{13}C$ values of seawater at station LM6 (34°67′N, 142°05′E) in the Kuroshio region off the Boso Peninsula (Oba et al., 2006) are also plotted in **(C)**.

$$T(^{\circ}C) = 16.5 - 4.8\left(\delta^{18}O_C - \left(\delta^{18}O_{SW} - 0.27\right)\right) \qquad (1)$$

This equation was determined from culturing experiments with a symbiont-bearing planktic foraminifer, *Orbulina universa*, grown under low-light conditions (Bemis et al., 1998). The adjustment of −0.27‰ to the seawater term compensates for the $\delta^{18}O$ difference between the VSMOW and PDB standards. We calculated $\delta^{18}O_c$ from the $\delta^{18}O_{sw}$ values at each of our three study sites and various bottom-water temperatures for each site: monthly values, the annual mean value, and average values for the 3-month period September to November, based on measurements from April 2009 to February 2010.

The results (**Figure 6**) show that the $\delta^{18}O_c$ values of living *H. nipponica* lie well within the seasonal variation of predicted $\delta^{18}O_c$ at every site and are nearly equal to the predicted $\delta^{18}O_c$ values based on the annual mean bottom temperature. They also suggest that the $\delta^{18}O_c$ values of living *H. nipponica* are heavier than the predicted $\delta^{18}O_c$ values from the 3-months average. Because we assumed a life span of 3 months for this species, the discrepancy indicates that *H. nipponica* has a much longer life cycle. This finding is also supported by the fact that $\delta^{18}O_c$ values of living and fossil *H. nipponica* are very close to each other (**Figure 5B**). From these results, we conclude that the carbonate tests of *H. nipponica* are in oxygen isotopic equilibrium with the ambient seawater. Although there are only three sites in this study, it is possible to evaluate the relationship between $\delta^{18}O_c$ of benthic foraminifer and bottom water temperature. **Figure 7** shows the relationship $\delta^{18}O_c$ of living and fossil *H. nipponica* and annual mean bottom water temperature in Tosa Bay. It is clear that the relationship is linear in both cases. The slope of the linear function is −5.26 (0.19‰°C^{-1}) for the living and −4.50 (0.22‰°C^{-1}) for the fossil *H. nipponica*, respectively (**Figure 7**).

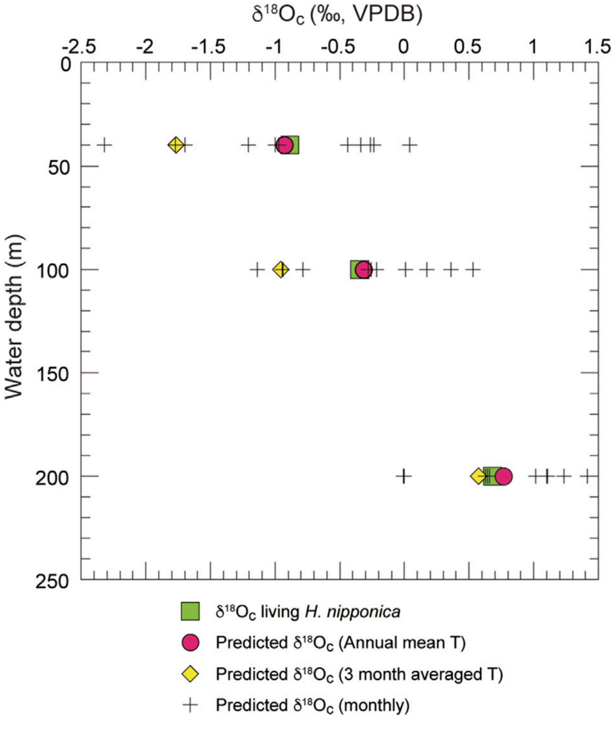

FIGURE 6 | Predicted and measured $\delta^{18}O_c$ of living *H. nipponica* plotted against water depth. Plus symbols show the monthly predicted $\delta^{18}O_c$ values at sites 5 (40 m), 25 (100 m), and 26 (200 m). Red filled circles and yellow filled diamond symbols show the predicted $\delta^{18}O_c$ values for annual mean temperatures and 3-months average temperature (September to November), respectively. The predicted $\delta^{18}O_c$ values are calculated from water temperature and $\delta^{18}O_{sw}$ in Tosa Bay using a calcite equilibrium equation (Bemis et al., 1998).

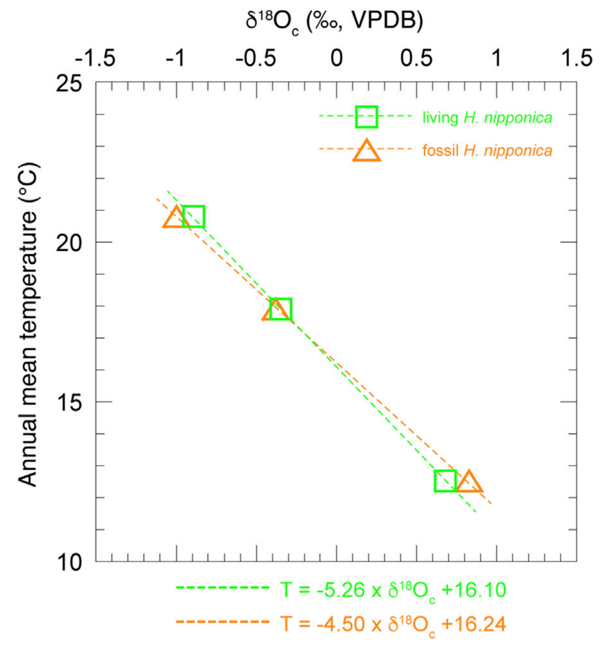

FIGURE 7 | Relationship between $\delta^{18}O_c$ of living and fossil *H. nipponica* and annual mean bottom water temperature at three sites in Tosa Bay. Green squares show data from living *H. nipponica* and orange triangles indicate data from fossil *H. nipponica*.

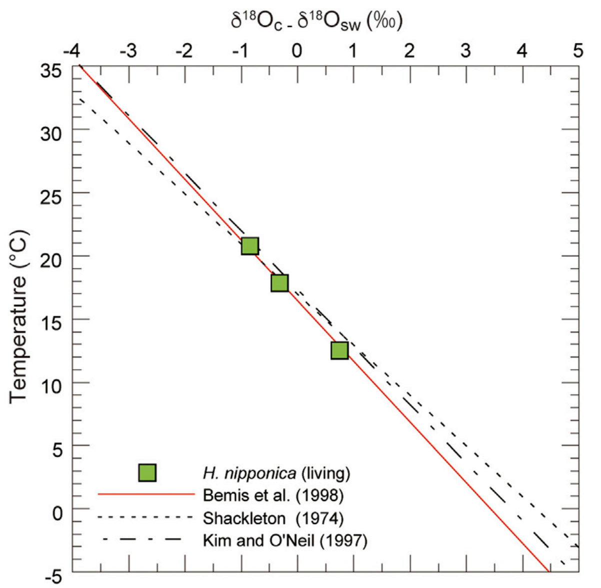

FIGURE 8 | Predicted $\delta^{18}O$ values for living *H. nipponica* from surface sediments on the continental shelf in Tosa Bay. Published relations between temperature and $\delta^{18}O$ are also plotted (Shackleton 1974; Kim and O'Neil 1997; Bemis et al., 1998). The *H. nipponica* data show a good fit to the equation of Bemis et al. (1998).

Although we applied the $\delta^{18}O_c$–temperature equation of Bemis et al. (1998) to our data, there are other $\delta^{18}O_c$–temperature relationships that yield various estimates for calcification of benthic foraminifers. For instance, Shackleton (1974) used core-top data to calibrate a $\delta^{18}O_c$–temperature relationship for the benthic foraminifer *Uvigerina* spp., and Zahn and Mix (1991) proposed that $\delta^{18}O_c$ in *Uvigerina peregrina* at water depths greater than 2 km could be described best by the equation of Erez and Luz (1983), derived from culture experiments with the planktic foraminifer *Globigerinoides sacculifer*. Both of these studies assumed that *Uvigerina* precipitates its test in oxygen isotope equilibrium with ambient seawater. Bemis et al. (1998) compared **Eq. 1** to an analysis of a compilation of published $\delta^{18}O$ data for the benthic foraminifers *Uvigerina* and *Cibicidoides* from core tops in the Atlantic, Pacific and Indian oceans, the Arabian Sea, and the Gulf of Mexico. They found that the $\delta^{18}O$ data for *Cibicidoides* were in excellent agreement with **Eq. 1**, which was based on culture experiments in low-light conditions with the planktic foraminifer *Orbulina universa*. Our data for *H. nipponica* show that the relationship between $\delta^{18}O_c$ and ambient temperature closely fits **Eq. 1** (**Figure 8**). The $\delta^{18}O$ data also show a similar trend with temperature in equations based on benthic foraminifers (Shackleton, 1974) and inorganic calcite (Kim and O'Neil, 1997). We conclude that the shallow-water benthic foraminifer *H. nipponica* precipitates its test close to oxygen isotopic equilibrium with seawater, as does the deep-sea benthic foraminifer *Cibicidoides*. The equation of Bemis et al. (1998) appears to be widely applicable to foraminifers, including benthic foraminifers in shallow and deep-sea environments. Although *H. nipponica* is restricted to continental shelves and upper slopes, this species may be very useful for elucidating paleoenvironmental changes in shallow-water settings affected by the Kuroshio and Tsushima current in the northwest Pacific and adjoining seas. Planktic foraminifer, which have been used in many isotope studies, have relatively large depth habitat (e.g. Schiebel and Hemleben, 2017), in contrast, benthic foraminifer have the advantage of being able to extract information on limited water depths, thus our new result is very important to advance paleoceanographic research in shallow water of past ocean.

Carbon Isotopes of *H. nipponica*

Our determinations showed that $\delta^{13}C$ of living *H. nipponica* ranged from 0.03 to 0.99‰, and those of fossil *H. nipponica* ranged from 0.63 to 0.94‰ (**Table 4**; **Figure 5C**). The differences between living and fossil specimens were small at site 25 (0.05‰) and site 26 (0.17‰) and much greater (0.74‰) at site 5, the shallowest site, where living specimens exhibited relatively depleted values (**Figure 5C**). Although $\delta^{13}C$ values of seawater in Tosa Bay have not been reported, values in the Kuroshio off the Boso Peninsula have been reported as a gradation from ~1.2‰ in surface water to ~0.8‰ in subsurface water at ~200 m depth (**Figure 5C**; Oba et al., 2006). Similarly, Kroopnick (1985) reported $\delta^{13}C$ values of 1.2‰ in surface water in the Kuroshio region off central Japan (station 224; 34°25′N, 142°00′E). Our results show that the $\delta^{13}C$ of *H. nipponica* is very close to these values in bottom water at site 25 (100 m) and site 26 (200 m) (**Figure 5C**), suggesting that $\delta^{13}C$ in *H. nipponica* reflects the $\delta^{13}C$ of ambient seawater. The depleted $\delta^{13}C$ values of *H. nipponica* at site 5 suggest that the $\delta^{13}C$ of benthic foraminifers in the surface mixed layer are greatly influenced by factors such as photosynthetic processes, local river input, and contributions of depleted $\delta^{13}C$ from terrestrial organic materials.

In general, the distribution of $\delta^{13}C$ in the ocean is controlled by the interaction of biological uptake at the sea surface, air–sea gas exchange, and decomposition in deeper water masses. Photosynthesis in shallow waters preferentially extracts ^{12}C from the carbon-bearing ions in seawater, enriching the ΣCO_2 of surface water in ^{13}C. The $\delta^{13}C$ value in seawater after primary producers have removed all nutrients, then, is controlled by the mean $\delta^{13}C$ and the mean nutrient concentration of the ocean (Broecker, 1982). Because the carbon taken up by phytoplankton has a $\delta^{13}C$ value of approximately −20‰, the surface reservoir is enriched by 2.0‰ relative to the mean $\delta^{13}C$ of deep water (Curry et al., 1988). Therefore, $\delta^{13}C$ data of fossil benthic foraminifers can be used to reconstruct past properties of deep water and infer past changes in ocean ventilation (e.g., Curry and Oppo, 2005; Ullerman et al., 2016).

Although further research will be necessary to better specify the dominant factors of $\delta^{13}C$ in *H. nipponica*, the $\delta^{13}C$ of this species is nearly identical to that of seawater. This similarity means that $\delta^{13}C$ of *H. nipponica* can be used to reconstruct the history of carbon circulation in subsurface to intermediate waters in the northwest Pacific and its marginal seas.

CONCLUSION

The main findings of this study are as follows:

1) The oxygen isotopic composition ($\delta^{18}O_{sw}$) and salinity of seawater samples from Tosa Bay generally overlap with those of the Kuroshio, which flows from the Okinawa Trough past Tosa Bay to the northwest Pacific. Although the surface and subsurface waters at site 5, the shallowest site, are influenced by freshwater input, the bottom water at all sites (40–200 m) is minimally influenced by less saline coastal water.
2) The $\delta^{18}O_c$ values increased with water depth in living and fossil specimens of the benthic foraminifer *Hanzawaia nipponica*, whereas $\delta^{18}O_{sw}$ did not vary with water depth in Tosa Bay. The $\delta^{18}O_c$ values of living *H. nipponica* were predicted well by the calcite equilibrium equation of Bemis et al. (1998) using the annual mean bottom-water temperature, indicating that the carbonate tests of *H. nipponica* form in oxygen isotopic equilibrium with ambient seawater. This result reinforces the utility of the equation of Bemis et al. (1998) for calculating $\delta^{18}O_{sw}$ and temperature for foraminifers, including benthic foraminifers in shallow and deep marine environments.
3) Tests of *H. nipponica* faithfully record the $\delta^{13}C$ of ambient seawater, although the $\delta^{13}C$ of this species in the surface mixed layer is difficult to interpret owing to the influence of various factors.
4) Data on $\delta^{18}O_c$ and $\delta^{13}C$ of *H. nipponica* are useful proxies to reconstruct paleoenvironmental changes in the shallow waters of the northwest Pacific and its marginal seas.

DATA AVAILABILITY STATEMENT

The original contributions presented in the study are included in the article/Supplementary Material, further inquiries can be directed to the corresponding author.

AUTHOR CONTRIBUTIONS

MI proposed the topic and conceived and designed the study. SKi carried out the sampling and the experimental study. SKa collaborated with the corresponding author in the identification of benthic foraminifers. MI and SKi analyzed the data and helped in their interpretation. All authors read and approved the final manuscript.

FUNDING

This work was supported by a research project grant of Kochi University.

ACKNOWLEDGMENTS

We thank Professor Emeritus Hiroshi Ueda, Makoto Yano, and Zenji Imoto (Usa Marine Biological Institute, Kochi University) and Daiki Kawata (Kochi University) for support during seawater and sediment sampling in Tosa Bay. We also acknowledge Michiyo Kobayashi and Sayaka Sakaguchi (Center for Advanced Marine Core Research, Kochi University) for analytical support. Discussions with Hitomi Wakaki-Uchimura (Kochi University), Hidetaka Nomaki (JAMSTEC), and Masashi Tsuchiya (JAMSTEC) on benthic foraminiferal habitats were helpful in improving the manuscript. We are grateful to Professor Emeritus Tadamichi Oba and one reviewer for their constructive comments.

REFERENCES

Akimoto, K. (1990). Distribution of Recent Benthic Foraminiferal Faunas in the Pacific off Southwest Japan and Around Hachijojima Island. *Sci. Rep. Tohoku Univ. Sendai, 2nd Ser. (Geology)* 60 (2). 139–223.

Akimoto, K., and Torii, M. (1996). Distribution of Recent Benthic Foraminiferal Assemblages in the Surface Sediments of the Hyuganada Area, off Kyushu and Shikoku, Japan. *Bull. Geol. Surv. Jpn.* 47, 41–59.

Aoshima, M. (1978). Depositional Environment of the Plio-Pleistocene Kakegawa Group, Japan —A Comparative Study of the Fossil and the Recent Foraminifera—. *J. Fac. Sci. Univ. Tokyo, Section Geology. mineralogy, Geogr. Geophys.* 19 (5). 401–441.

Asano, K. (1944). *Hanzawaia*, a New Genus of Foraminifera, from the Pliocene of Japan. *Jour. Geol. Soc. Jpn.* 51, 97–99. doi:10.5575/geosoc.51.97

Awaji, T., Akitomo, K., and Imasato, N. (1991). Numerical Study of Shelf Water Motion Driven by the Kuroshio: Barotropic Model. *J. Phys. Oceanogr.* 21, 11–27. doi:10.1175/1520-0485(1991)021<0011:nsoswm>2.0.co;2

Bemis, B. E., Spero, H. J., Bijma, J., and Lea, D. W. (1998). Reevaluation of the Oxygen Isotopic Composition of Planktonic Foraminifera: Experimental Results and Revised Paleotemperature Equations. *Paleoceanography* 13, 150–160. doi:10.1029/98pa00070

Broecker, W. S. (1982). Glacial to Interglacial Changes in Ocean Chemistry. *Prog. Oceanography* 11, 151–197. doi:10.1016/0079-6611(82)90007-6

Curry, W. B., Duplessy, J. C., Labeyrie, L. D., and Shackleton, N. J. (1988). Changes in the Distribution of $\delta^{13}C$ of Deep Water ΣCO_2 between the Last Glaciation and the Holocene. *Paleoceanography* 3, 317–341. doi:10.1029/pa003i003p00317

Curry, W. B., and Oppo, D. W. (2005). Glacial Water Mass Geometry and the Distribution of $\delta^{13}C$ of ΣCO_2 in the Western Atlantic Ocean. *Paleoceanography* 20. doi:10.1029/2004PA001021

Erez, J., and Luz, B. (1983). Experimental Paleotemperature Equation for Planktonic Foraminifera. *Geochimica et Cosmochimica Acta* 47, 1025–1031. doi:10.1016/0016-7037(83)90232-6

Fujimoto, M. (1987). On the Flow Types and Current Stability in Tosa Bay and Adjacent Seas. *Umi to Sora* 62, 15–27. (in Japanese with English abstract).

Hasegawa, S. (1993). Distribution of Recent Benthic Foraminifers as an Indicator of thermal Conditions of the Seas Around the Japanese Islands - an Approach to Reconstruction of Cenozoic Oceanic Condition. *Fossils* 55, 17–33. (in Japanese with English abstract).

Horibe, Y., and Ogura, N. (1968). Deuterium Content as a Parameter of Water Mass in the Ocean. *J. Geophys. Res.* 73, 1239–1249. doi:10.1029/jb073i004p01239

Horikawa, K., Kodaira, T., Zhang, J., and Murayama, M. (2015). δ_{sw}^{18O} Estimate for *Globigerinoides ruber* from Core-Top Sediments in the East China Sea. *Prog. Earth Planet. Sci.* 2, 19. doi:10.1186/s40645-015-0048-3

Ichikawa, T., and Hirota, Y. (2004). Seasonal Changes of Primary Productivity in Tosa Bay, Japan. *Oceanography Jpn.* 13, 259–269. (in Japanese with English abstract). doi:10.5928/kaiyou.13.259

Inoue, Y. (1989). Northwest Pacific Foraminifera as Paleoenvironmental Indicators, *Sci. Rep. Inst. Geosci. Univ. Tsukuba, Section B* 10, 57–162.

Ishiwada, Y. (1964). Benthonic Foraminifera off the Pacific Coast of Japan Referred to Biostratigraphy of the Kazusa Group. *Rep. Geol. Surv. Jpn.* 205, 1–45.

Kang, S., Lim, D., and Kim, S.-Y. (2010). Benthic Foraminiferal Assemblage of Seogwipo Formation in Jeju Island, South Sea of Korea: Implication for Late Pliocene to Early Pleistocene Cold Episode in the Northwestern Pacific Margin. *Quat. Int.* 225, 138–146. doi:10.1016/j.quaint.2010.04.009

Katto, J., Nakamura, J., and Takayanagi, Y. (1953). Stratigraphical and Paleontological Studies of the Tonohama Group, Kochi Prefecture, Japan, *Res. Rep. Kochi Univ.* 2 (32). 1–15.

Kim, S.-T., and O'Neil, J. R. (1997). Equilibrium and Nonequilibrium Oxygen Isotope Effects in Synthetic Carbonates. *Geochimica et Cosmochimica Acta* 61, 3461–3475. doi:10.1016/s0016-7037(97)00169-5

Kroopnick, P. M. (1985). The Distribution of ^{13}C of ΣCO_2 in the World Oceans. *Deep Sea Res. A. Oceanographic Res. Pap.* 32, 57–84. doi:10.1016/0198-0149(85)90017-2

Kuroda, H., Shimizu, M., Hirota, Y., Ambe, D., and Akiyama, H. (2008). Surface Current and Vertical thermal Structure on the continental Slope in Tosa Bay. *J. Oceanogr* 64, 81–91. doi:10.1007/s10872-008-0006-4

Kuwano, Y. (1963). Foraminiferal Biocoenosis of the Seas Around Japan: A Survey of Pacific Side Biocoenoses, III. Biocoenoses off Boso Peninsula. *Miscellaneous Rep. Res. Inst. Nat. Resour.* 60, 29–51.

LeRoy, L. W. (1964). Smaller Foraminifera from the Late Tertiary of Southern Okinawa. *Prof. Pap. U.S. Geol. Surv.* 454-F, 1–58. doi:10.3133/pp454f

Li, B., Park, B.-K., Kim, D., and Woo, H. J. (1999). The Geological Age and Paleoenvironment of the Lower Seogwipo Formation, Cheju Island, Korea. *Geosci. J.* 3, 181–190. doi:10.1007/bf02910489

Mathieu, R., Pollard, D., Cole, J. E., White, J. W. C., Webb, R. S., and Thompson, S. L. (2002). Simulation of Stable Water Isotope Variations by the GENESIS GCM for Modern Conditions. *J. Geophys. Res.* 107. doi:10.1029/2001JD900255

Matoba, Y. (1976). "Foraminifera from off Noshiro, Japan, and Postmortem Destruction of Tests in the Japan Sea," in *Progress on Micropaleontology*. Editors Y. Takayanagi and T. Saito (New York: Micropaleontology Press), 169–189.

Matoba, Y., and Honma, N. (1986). "Depth Distribution of Recent Benthic Foraminifera off Nishitsugaru, Eastern Sea of Japan," in *Studies on Cenozoic Benthic Foraminifera in Japan*. Editors Y. Matoba and M. Kato (Mining College, Akita University), 53–78. (in Japanese with English abstract).

Mizota, C., and Kusakabe, M. (1994). Spatial Distribution of δD-$\delta^{18}O$ Values of Surface and Shallow Groundwaters from Japan, south Korea and east China. *Geochem. J.* 28, 387–410. doi:10.2343/geochemj.28.387

Murray, J. W. (1991). "Ecology and Distribution of Benthic Foraminifera," in *Biology of Foraminifera*. Editors J. J. Lee and O. R. Anderson (Academic Press), 285–334.

Oba, T., Irino, T., Yamamoto, M., Murayama, M., Takamura, A., and Aoki, K. (2006). Paleoceanographic Change off central Japan since the Last 144,000 Years Based on High-Resolution Oxygen and Carbon Isotope Records. *Glob. Planet. Change* 53, 5–20. doi:10.1016/j.gloplacha.2006.05.002

Oba, T. (1990). "Paleoceanographic Information Obtained by Isotopic Measurement of Individual Foraminiferal Specimens," in *Proceedings of the First International Conference on Asian Marine Geology*. Editors P. Wang, Q. Lao, and Q. He (Beijing: China Ocean Press), 169–180.

Oba, T., and Yasuda, H. (1992). Paleoenvironmental Change of the Kuroshio Region since the Last Glacial Age. *Daiyonki-kenkyu* 31, 329–339. (in Japanese with English abstract). doi:10.4116/jaqua.31.329

Schiebel, R., and Hemleben, C. (2017). *Planktic Foraminifers in the Modern Ocean*. Berlin: Springer-Verlag.

Shackleton, N. J. (1974). Attainment of Isotopic Equilibrium between Ocean Water and the Benthonic Foraminifer Genus *Uvigerina*: Isotopic Changes in the Ocean during the Last Glacial. *C.N.R.S. Colloquium* 219, 203–209.

Shackleton, N. J., and Opdyke, N. D. (1973). Oxygen Isotope and Palaeomagnetic Stratigraphy of Equatorial Pacific Core V28-238: Oxygen Isotope Temperatures and Ice Volumes on a 10^5 Year and 10^6 Year Scale. *Quat. Res.* 3, 39–55. doi:10.1016/0033-5894(73)90052-5

Tsuchiya, M., Takahara, K., Aizawa, M., Suzuki-Kanesaki, H., Toyofuku, T., and Kitazato, H. (2014). "How Has Foraminiferal Genetic Diversity Developed? A Case Study of *Planoglabratella Opercularis* and the Species Concept Inferred from its Ecology, Distribution, Genetics, and Breeding Behavior," in *Approaches to Study Living Foraminifera. Environmental Science and Engineering*. Editors H. Kitazato and J. M. Bernhard (Tokyo: Springer), 133–162. doi:10.1007/978-4-431-54388-6_9

Uchio, T. (1968). Foraminiferal Assemblages in the Vicinity of the Seto Marine Biological Laboratory, Shirahama-Cho, Wakayama-Ken, Japan (PART 1). *Publications Seto Mar. Biol. Lab.* 15 (5), 399–417. doi:10.5134/175480

Ullermann, J., Lamy, F., Ninnemann, U., Lembke-Jene, L., Gersonde, R., and Tiedemann, R. (2016). Pacific-Atlantic Circumpolar Deep Water Coupling during the Last 500 Ka. *Paleoceanography* 31, 639–650. doi:10.1002/2016PA002932

Xiang, R., Yang, Z., Saito, Y., Fan, D., Chen, M., and Guo, Z. (2008). Paleoenvironmental Changes during the Last 8400 Years in the Southern Yellow Sea: Benthic Foraminiferal and Stable Isotopic Evidence. *Mar. Micropaleontology* 67, 104–119. doi:10.1016/j.marmicro.2007.11.002

Zahn, R., and Mix, A. C. (1991). Benthic Foraminiferal δ18O in the Ocean's Temperature-Salinity-Density Field: Constraints on Ice Age Thermohaline Circulation. *Paleoceanography* 6, 1–20. doi:10.1029/90pa01882

Conflict of Interest: The authors declare that the research was conducted in the absence of any commercial or financial relationships that could be construed as a potential conflict of interest.

frontiers
in Earth Science

REVIEW
published: 31 January 2022
doi: 10.3389/feart.2021.717420

Holocene Monsoonal Variations Over Southern India: Looking Into Its Antecedents

M. R. Resmi[1]*, *Hema Achyuthan*[2] *and Hritika Deopa*[1]

[1]*Department of Earth Sciences, Banasthali Vidyapith, Vanasthali, India,* [2]*Institute for Ocean Management (IOM), Anna University, Chennai, India*

A proper understanding of the paleoclimatic variability in the Southern Peninsular India demands a high-resolution paleoclimate reconstruction record. Hence, in this paper, we compiled all the available paleoclimate records from various locations across the Southern India that receives the southwest and the northeast monsoon. We delineated the southwest monsoon (SWMR) and Northeast monsoon (NEMR) variations within the Holocene Period based on the existing paleoclimatic record from this region. Paleoclimate records are primarily based on various paleoclimate archives and proxies. A detailed study of these variations unravels, (i) that SWMR gradually intensified since the younger dryas during the Early Holocene period. On the contrary, NEMR records indicate a dry phase during the same period. (ii) During the mid-late Holocene, precipitation in SWMR-dominated regions decreased, whereas precipitation in NEMR-dominated regions shows an increasing trend. (iii) Then, in the late Holocene Period, SWMR exhibits an overall wet phase with a few drier periods, and NEMR shows an intense dry period with shorter wet phases, which can be correlated to the demise of Chola dynasty, in the Southern India.

Keywords: southern India, SWMR and NEMR, MWP, LIA, ancient settlement

Edited by:
Xander Wang,
University of Prince Edward Island,
Canada

Reviewed by:
Yu Li,
Lanzhou University, China
Raj K. Singh,
Indian Institute of Technology
Bhubaneswar, India

***Correspondence:**
M. R. Resmi
resmiarun.mr@gmail.com

Specialty section:
This article was submitted to
Interdisciplinary Climate Studies,
a section of the journal
Frontiers in Earth Science

Received: *30 May 2021*
Accepted: *31 August 2021*
Published: *31 January 2022*

Citation:
Resmi MR, Achyuthan H and Deopa H
(2022) Holocene Monsoonal Variations
Over Southern India: Looking Into
Its Antecedents.
Front. Earth Sci. 9:717420.
doi: 10.3389/feart.2021.717420

INTRODUCTION

The tropical climate system in India is dominated by the Indian Summer Monsoon (ISM), which is characterised by regional irregularities in the general circulation of the atmosphere caused by land-sea contrasts and seasonal reversal in wind direction. The primary cause for monsoonal variation in the Indian subcontinent is differential heating of land and sea and/or manifestation of the seasonal migration of the intertropical convergence zone (ITCZ) (Charney, 1969). However, during the winter dry cold winds from Asia blow offshore (Colin et al., 1998). The interaction of these moisture regimes with various teleconnections (El Niño, La Nina, and IODM) have resulted in decadal to millennial-scale precipitation variations over India (Singhvi and Kale, 2010; Rajeevan et al., 2012).

The southwest or the summer monsoon (SWMR) and the northeast or winter monsoon (NEMR) are the two monsoons that bring copious amount of rain to South Asia. While the summer monsoon accounts for the majority of annual rainfall in India. Rainfall obtained during the northeast monsoon is also significant, particularly along the Coromandel Coast, South India, and Sri Lanka (**Figure 1**). During the summer monsoons withdrawal phase, lower-level winds in South Asia migrate from southwest to northeast (Rajeevan et al., 2012). This shift can be attributed to the southern trend of the tropical convergence zone. Hence, low-level winds over India switch their direction from southwesterly to northeasterly during the NEMR, and the region becomes a subset of the

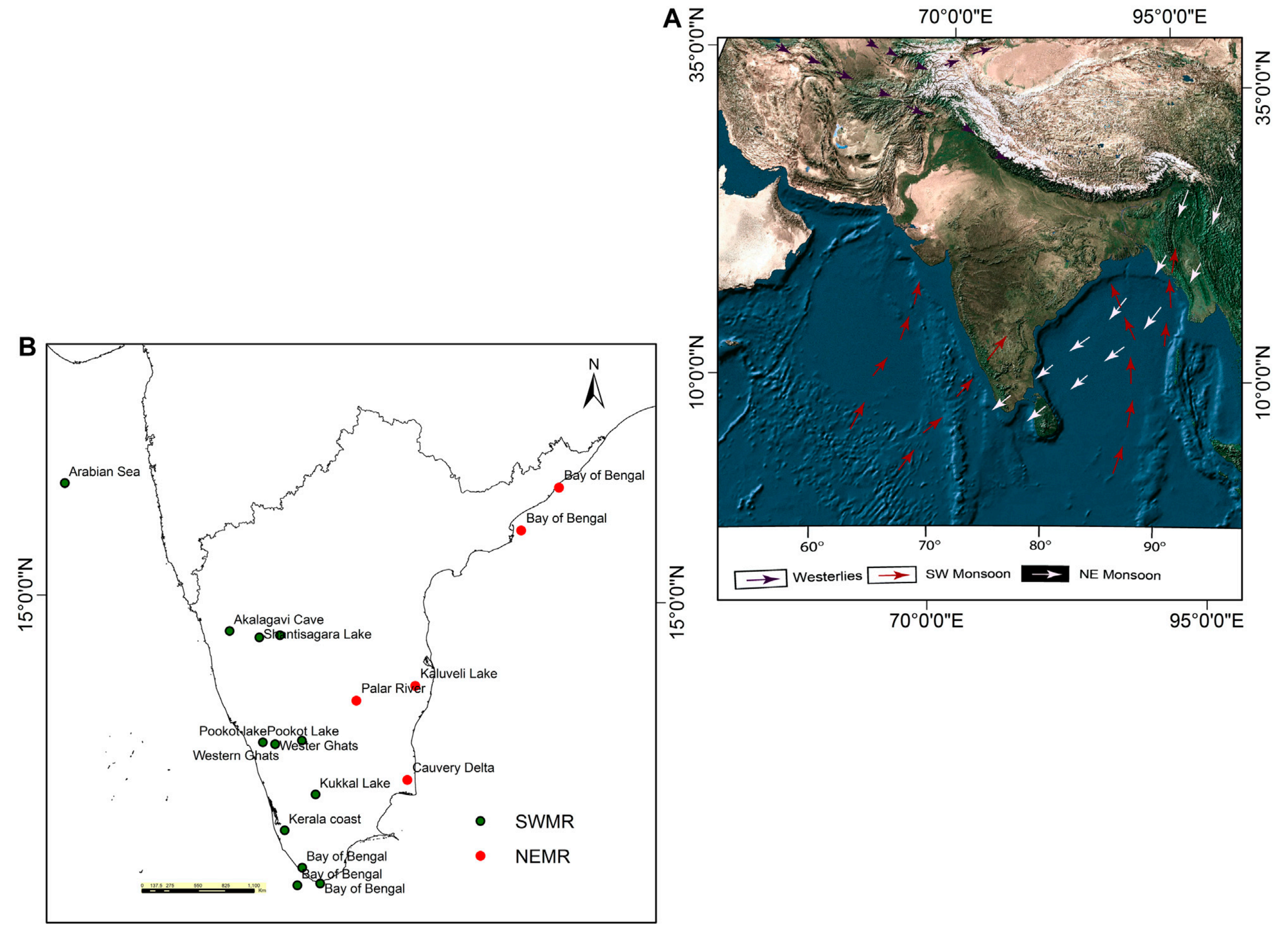

FIGURE 1 | (A) Represents Large-scale topographical maps with dominant seasonal hemispherical airflows (after Mishra 2014, Resmi and Achyuthan, 2018). **(B)** Geographical location of the selected site.

northeast trades, which is dry, persistent, and has a smaller vertical extent than the southwest monsoon. Hence, NEMR has a significant impact on agricultural practises in southern peninsular India (Rao Krishna and Jaganathan, 1953).

On a regional and temporal scale, several studies have been attempted to reconstruct the Holocene paleoclimatic variability (Stubwasser et al., 2003; Trauth et al., 2003; Ponton et al., 2012). From the Indian subcontinent, various records *viz.* lacustrine (Rajagopalan et al., 1997; Juyal et al., 2004; Prasad et al., 2014; Sarkar et al., 2015; Rajaminkam et al., 2016), marine (Gupta et al., 2003; Thamban et al., 2007; Achyuthan et al., 2014), and fluvial records (Kale, et al., 2010; Resmi et al., 2016; Resmi and Achyuthan, 2018) have been used to reconstruct the paleomonsoon variability during the Holocene period.

Geographic distribution in the monsoon rainfall are of particular implication; for instance, the southern region of India which receives both SWMR and NEMR, perhaps, is the only region that experiences both the monsoons (**Figures 1A,B, 2A,B**). In the Holocene period, the southern peninsular India witnessed multiple cultural and adaptive innovations, transitions, as well as the rise of several civilizations (**Figure 2C**; Gupta et al., 2003; Walker et al., 2012). These ancient civilizations developed and disappeared in tandem with climate shifts, the monsoons have caused a significant socioeconomic ramification.

DATA COLLECTION

Climatic reconstructions data considered for the present study is based on the following criteria: (1) The sites are located only in the Southern Peninsular India which is experiencing either NE or SW monsoon. (2) The proxy data were interpreted originally in terms of dry phase or wet phase (3) The records are within the Holocene period. However, owing to the paucity of high-resolution climatic records from the southern peninsular region, chronological uncertainty was not considered as the criteria for selection. We included and compiled all the records of lacustrine, fluvial and marine sediments. All records used in the compilation met the above-said criteria. To enable the comparison, the precipitation records were subdivided into the Southwest monsoon (SWMR) dominated region and Northeast monsoon (NEMR) dominated region. This strategy was adopted in the present study because of the spatial variability of SWMR and NEMR in the southern Peninsular India. Some of the precipitation records include isotope data, pollen data, sedimentation rate, geochemical records, clay mineralogy etc. We solely used proxy records of inferred climate shifts documented in previous records for the present study, and we did not reinterpret any original proxy data to a climate signal.

DATASETS

The Corg/N and $\delta^{13}C$ ratio help to differentiate the paleoenvironment in the catchment of a lake region (Chen et al., 2002). Corg/N ratio records are available from Shantisagara Lake (Sandeep et al., 2007) and Kukkal Lake (Rajamanickam et al., 2016) spanning the Holocene period. Lake sediments from Shantisagara, Sandynallah, Parsons Valley, and Akalagavi Cave Deposits have been assessed for $\delta^{13}C$ value (Sukumar et al., 1993; Rajagopalan et al., 1997; Yadava et al., 2004; Sandeep et al., 2017; Raja et al., 2018a). High rainfall periods are characterized by depleted $\delta^{13}C$ values (C_3 plants), whereas low rainfall periods are marked by less negative or enriched $\delta^{13}C$ values (C_4 plants). Speleothem records are available from Akalagavi cave, $\delta^{18}O$ value of the speleothem layers are a proxy for the past variations of precipitation (Yadava et al., 2004). Enrichment and depletion in $\delta^{18}O$ are the indicative of the past deficiency and excess in rainfall of Akalagavi cave deposit (**Table 1**). $\delta^{18}O$ variation in foraminifera is also used as proxy indicator for paleoclimatic studies (Thamban et al., 2001). Intensity of Chemical weathering (CWI) is also a proxy for understanding precipitation (Sun et al., 2010). In this review, CWI records from the Palar River (Resmi and Achyuthan, 2018) and Kukkal Lake (Rajamanickam et al., 2016) are also included. CWI is often higher in warm and humid climates than in cold and dry climates. The Cao/MgO, Rb/Sr records were used in this review: Under warm and dry climate conditions, increased CaO/MgO values in the Palar River (Resmi and Achyuthan, 2018) and Kukkal Lake (Rajamanickam et al., 2016) demonstrated higher carbonate of authigenic origin (Wang et al. 2004). Magnetic susceptibility (X_{lf}) is a major tool for assessing climatic variations (Da Silva et al., 2014). Low (X_{lf}) values suggest less rainfall, and vice versa (Bhattacharyya et al., 2015). Magnetic susceptibility (X_{lf}) data are available from Shantisagara Lake and Thimmannanayakanakere tank (**Table 1**).

Pollen inferred climate records from Shantisagara Lake, Pookode Lake, Ashtamudi- Sasthamkotta Lake, Kukkal Lake, Sandynallah Basin, Parsons Valley, Peat deposition in Kerala and Konkan coast and mangrove vegetation of Northern Konkan region provide a high-resolution paleoclimate data during Holocene (Sukumar et al., 1993; Rajagopalan et al., 1997; Kumaran et al., 2005; Nair et al., 2010; Limaye and Kumaran, 2012; Rajamanickam et al., 2016; Sandeep et al., 2017; Raja et al., 2018a) (**Table 1**). Arboreals and non-arboreals pollen provides insight into its climatic conditions of the past. Prevalence of non-arboreal pollen with sparce vegetation suggests wet, dynamic, and non-static climatic conditions, and vice versa. Clay mineral assemblages can be used to deduce paleoclimate. This review also includes clay mineralogy records from the Bay of Bengal and Kaliveli Lake (Pattanaik, 2009; Chauhan et al., 2010) Thecamoebians record from the Pichavaram Estuary used in this review, A high abundance of thecamoebians indicates a better marine environment, and vice versa (Srivastava et al., 2011) (**Table 1**).

DISCUSSION

Southwest Monsoon

Greenlandian Stage (Early Holocene)

Sukumar et al. (1993), Rajamanickam et al. (2016), and Sandeep et al. (2017) presented a detailed southwest monsoon variability on peat and lake sediments from southern Indian Peninsula spanning the Holocene period. Based on a high content of carbonate, Corg/N ratio, Corg, N, and depleted $\delta^{13}C$ values along with dominant C_4 plants indicate an overall dry phase as presented in Shanti Sagara Lake in the initial stage of the early Holocene period (11.1–10.7 ka) (Sandeep et al., 2017) (**Figure 3**) (**Table 1**). This decreasing tendency was perhaps due to the gradual transition from the Younger Dryas to the early Holocene wet phase (**Figure 3**). Subsequently, enhanced precipitation phase is marked during 10.7–8.6 ka, reflecting high abundance of C_3 plants as studied in the Shanti Sagara Lake (Sandeep et al., 2017), Kukkal Lake (Rajamanickam et al., 2016) (**Figure 3**), and peat deposits in the Nilgiris (Sukumar et al., 1993). The interpolated ages from the pollen data of Parsons Valley Lake, Nilgiris, indicate a dominance of arboreal, with a subsequent shift to a significant increase in non-arboreal, suggests a decrease in precipitation in the early Holocene (Raja et al., 2018a) (**Table 1**). Based on the $\delta_{13}C$ record, Sukumar et al. (1993) have marked a high dominance of C_3 vegetation at ~10.6 ka which indicate an intensified rainfall during this period, followed by a predominance of C_4 vegetation suggesting a dry period from 10 to 6 ka. Various terrestrial proxies, such as magnetic susceptibility and element concentration in marine core sediments extracted from the Arabian Sea (Thamban et al., 2007), have observed a sudden rise in the intensity of SWMR during 9.5–8 ka (**Table 1**), which is coeval with the maxima in the Kaveri River discharge (Kale et al., 2010) and the formation of thermocline anoxia in the Arabian Sea (Staubwasser et al., 2002). Sedimentological, palynological, and stable isotopes of sediments from the Kallada Bay Delta suggest a rise in sea level during the early Holocene period due to intense rainfall (Padmalal et al., 2013). The beginning of early Holocene, optimum ~ 10.65 ka, can be manifested from several parts of southern India (Sukumar et al., 1993; Rajagopalan et al., 1997; Caner et al., 2007; Kumaran et al., 2008; Sandeep et al., 2017; Raja et al., 2018b). Thamban et al. (2007) observed the cessation of the early Holocene climatic optimum (HCO) event occurred gradually at ~8.5 ka. Summer monsoons were intense in the early Holocene times, as shown by lake (Rawat et al., 2015a, 2015b; Sarkar et al., 2015) and sea (Kessarkar et al., 2013; Saraswat et al., 2016) sediments from the other part of Indian subcontinent. High-resolution speleothem records from northern Oman and the Oman margin support the

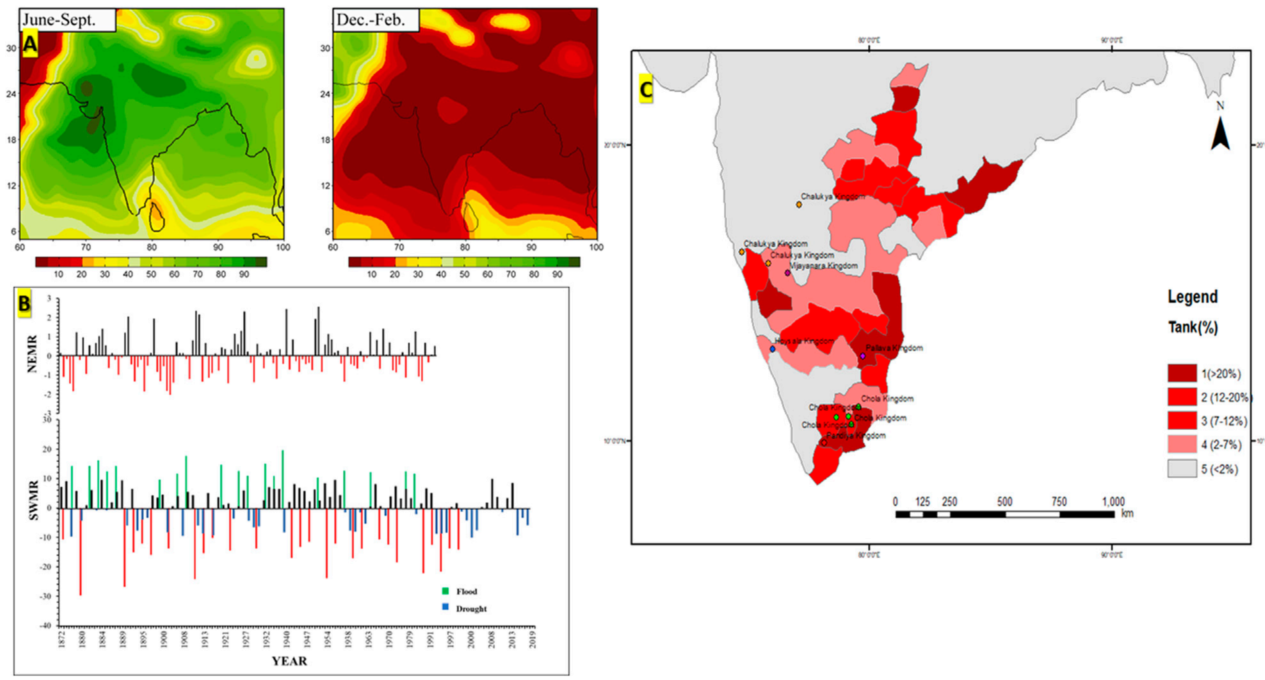

FIGURE 2 | (A) Maps showing the monsoon precipitation during **(A)** June–September and December- February. **(B)** Monsoonal History (SWMR & NEMR) **(C)** Tanks and climate in India, District-wise ratio of tank irrigation to net sown area. The Chola and Pallava tank kingdoms mostly expanded across regions (modified after Gunnell et al., 2007).

view that Early Holocene is marked by intense precipitation (Neff et al., 2001; Gupta et al., 2003; Fleitmann et al., 2007).

Northgrippian Stage (Mid Holocene)

During 8.6–4.5 ka, the high Corg/N ratio and the prevalence of C_4 plants indicate an overall decreasing trend of monsoon during the mid-Holocene period, which corresponds to the 8.2 ka cold event (Sandeep et al., 2017). Moreover, southward shift of the Inter-Tropical Convergence Zone (ITCZ) can be linked to a long-term drop in precipitation during the mid-Holocene (Fleitmann et al., 2007) (**Figure 3**). The period between 8 and 6 ka is marked a rise in sea level along the Kerala Coast and sinking areas of the mangroves which were flourished at that time, followed by a major regression at ~5 ka (Cronin et al., 2007).

Increased carbon (TOC), total nitrogen (TN), and the C/N ratio of Kukkal Lake are pointing towards an aridity at ~8 ka (**Figure 3**). On the contrary, the paleoclimatic data from the flood plain of the upper Kaveri River indicate that a major flood occurred at ~8 ka (Kale et al., 2010) (**Figure 1**) (**Table 1**). Enriched C/N ratio and dominant C_3 terrestrial input indicate an intense rainfall during 8.4–4.9 ka with short drier phases (Raja et al., 2018b). As a continuation of early climatic optimum in the Sandhyanallah Basin experienced an intense rainfall till 5 ka, gradually an increase in C_4 vegetation indicating a decreasing trend of monsoon during mid-Holocene (Sukumar et al., 1993; Rajagopalan et al., 1997) (**Figure 3**). High CaO and CaO/Al_2O_3 values indicated a lagoonal and/ or estuarine conditions between 6400 and 2600 cal year BP, which later on shifted to fresh water conditions at 2600 cal yr BP (Banerji et al., 2021).

Intense rainfall in southwest coastal plains during 6.5 ka leads to the enormous growth of forest in the abandoned river channels. The occurrence of pollen and peat deposits in these palaeoforests along the southwest coast of India suggests a warmer climate, which is consistent with a mid-Holocene thermal maximum (Kumaran et al., 2014). Studies based on geochemical proxies such as Fe, Al, and Ti, indicated that a most significant weaker monsoon during 6–5 Ka (Thamban et al., 2007) that corresponds with the foraminiferal oxygen isotope data from the sediment cores studied from the southwest coast of India (Sarkar et al., 2000; Thamban et al., 2001).

A substantial decrease in summer monsoon rainfall is also marked by a decrease in the kaolinite/chlorite ratio during 5.6 ka (Thamban et al., 2001; **Table 1**). In the mangroves of southern Konkan, Limaye and Kumaran (2012) suggested an increased rainfall and higher sea level from 5.6 to 5.33 ka. The marine sediment samples of Bay of Bengal marked a decrease in the intensity of SWM from 5 to 3.6 ka, which at ~4.8 ka signify an arid climate conditions (Chauhan and Suneethi 2001).

Southern Indian palaeo-monsoonal records indicate a dry climate phase throughout the mid-Holocene (Sukumar et al., 1993) followed by wet spells and a high sedimentation rate during late Holocene (Padmalal et al., 2013). Short-term abrupt climatic fluctuations of enhanced monsoon have been inferred at 8.5, 8.4, and 8.2 ka (Thamban et al., 2007; Kale et al., 2010; Limaye and Kumaran, 2012). However, the 8.2 ka cold event relates to the abrupt weakening of ISM and during this time, solar insolation shows a decreasing tendency (Sandeep et al., 2017).

TABLE 1 | List of proxy records (major) from terrestrial and marine climate archives compiled in this study.

Sl.No	Record	Latitude	Longitude	Altitude (m asl)	Proxy	Reconstructed climate	Reference
1	Shanti Sagara Lake	14°8′34″N	75°52′56″E	770	Magnetic parameters, the Corg/N ratio, and $\delta^{13}C$ values	SWMR	Sandeep et al. (2017)
2	Pookode Lake	11°32′35″N	76°01′40″E		Sediment texture, phytolith, major oxides, palynology, and the Chemical Weathering Index (CWI)	SWMR	Veena et al. (2014)
3	Pookode Lake	11°32′30″N	76°01′38″E	775	Palynology, particle size, and magnetic susceptibility	SWMR	Bhattacharaya et al. (2015)
4	Ashtamudi–Sasthamkotta Lake	08°45′–09°05′N	76°25′–76°45′E		Palynology, sedimentology, and a heavy mineral analysis	SWMR	Nair et al. (2010)
5	Kukkal Lake	10°16′N	77°22′E	1887	Geochemistry, a textural analysis, and palynology	SWMR	Rajamanickam et al. (2016)
6	Kaliveli Lake	12.11.97°N	79.8577°E		Sedimentation rate, clay mineralogy, and 10Be abundance	NEMR	Pattanaik (2009)
7	Pichavaram Lake	11°22′–11°32′N	79°45′–79°49′E		Sedimentology, marine and freshwater palynomorphs, and salinity	NEMR	Srivastava et al. (2011), Srivastava et al. (2012)
8	Sandynallah Basin	11°30′N	76°20′E		Textural analysis, palynology, and $\delta^{13}C$ values	SWMR	Sukumar et al. (1993)
9	Sandynallah Basin	11°30′N 7600’-	77^{0}20′E		Textural analysis, palynology, and $\delta^{13}C$ values	SWMR	Rajagopalan et al. (1997)
10	Parsons Valley Lake	11.39°N	76.60°E		Textural analysis, palynology, and $\delta^{13}C$ values	SWMR	Raja et al. (2018a)
11	Thimmanna Nayakana Kere	14°12′N	76°24′E		Particle size and magnetic susceptibility	SWMR	Shankar et al. (2006)
12	Cauvery Delta	11∘01.178′N	79∘50.446′E		Geochemistry and pollen studies	SWMR & NEMR	Mohaptra et al. (2021)
13	Bay of Bengal	17°54N	83°33E		Clay minerology	NEMR	Chauhan et al. (2010)
14	Arabian Sea	17°45′N	70°52′E		Foraminiferal studies	SWMR	Thamban et al. (2007)
15	Palar River	12°37′	78°22′		Sedimentology, geochemistry	NEMR	Resmi and Achyuthan (2018)
16	Akalagavi Cave	14° 16′ 48″N	75° 7′ 19.2″E		Oxygen (δ 180) and carbon (δ 3C)	SWMR	Yadava et al. (2004)
17	Kerala Coast	9°22′38″N–	76°36′05″E		Peat deposits	SWMR	Kumaran et al. (2014)
18	Cauvery River	12.30°N	75.87°E		Flood deposits	SWMR	Kale et al., 2010

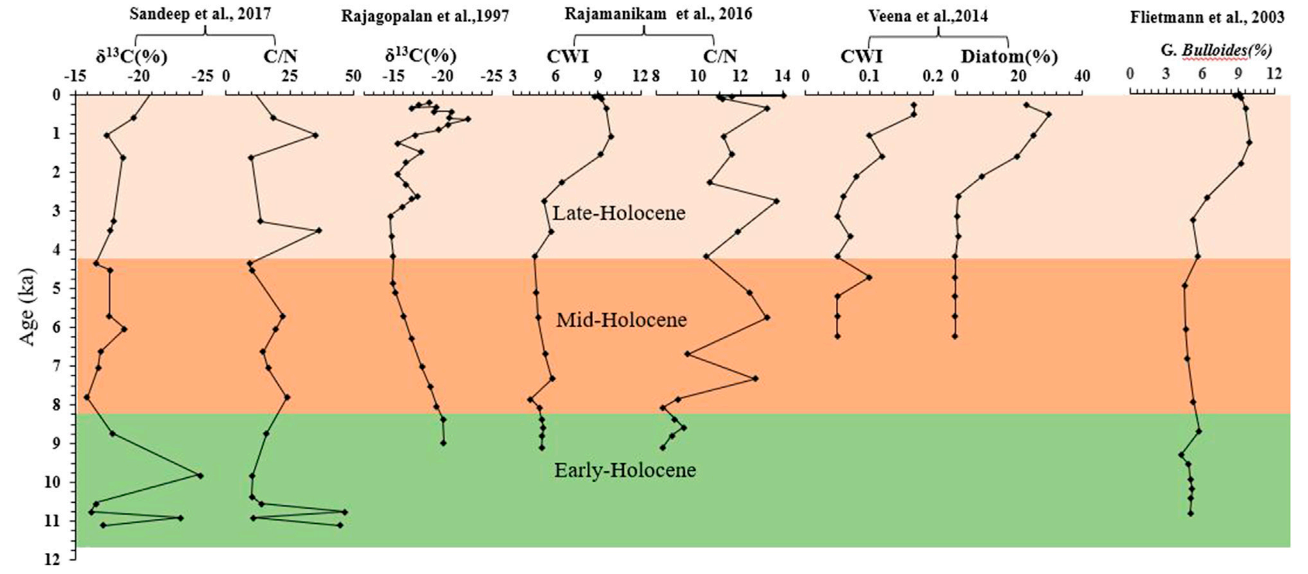

FIGURE 3 | Schematic diagram of climate variability during the Holocene from records in the region which experiences SWMR.

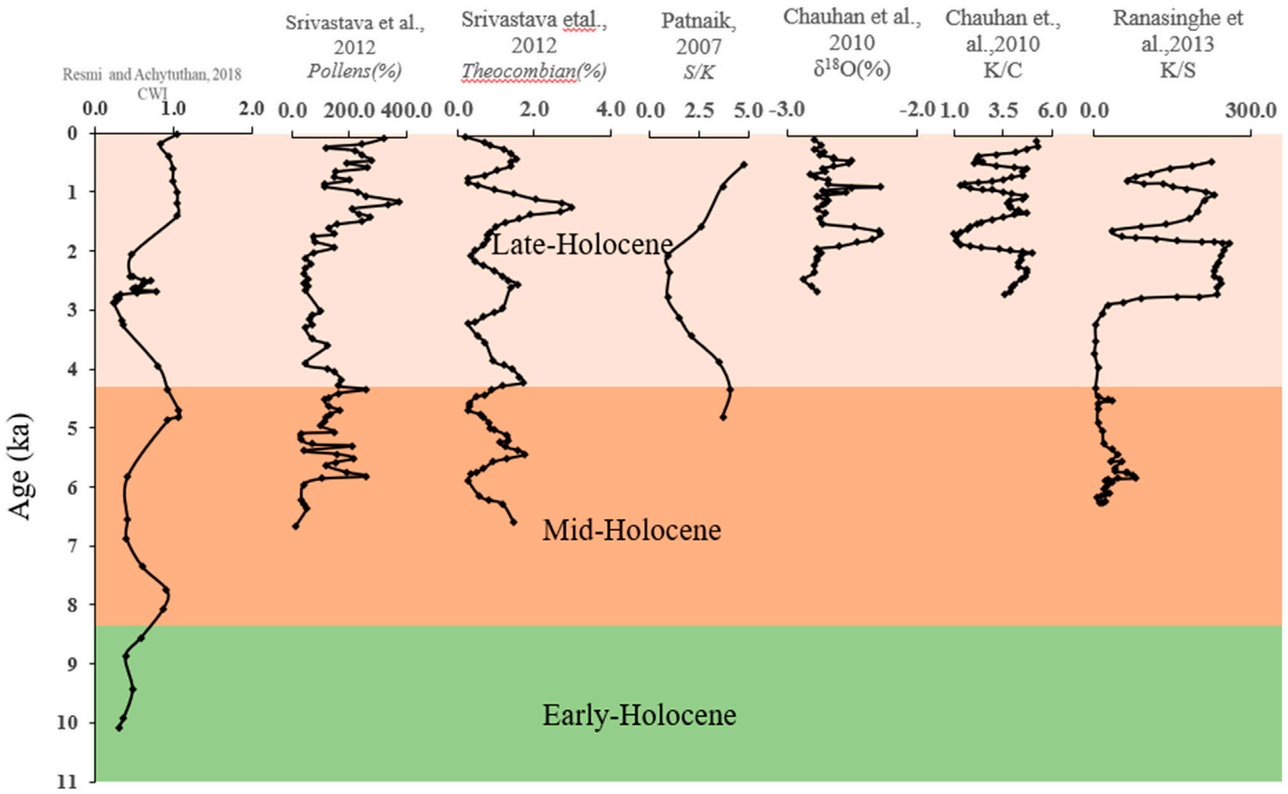

FIGURE 4 | Schematic diagram of climate variability during the Holocene from records in the region which experiences NEMR.

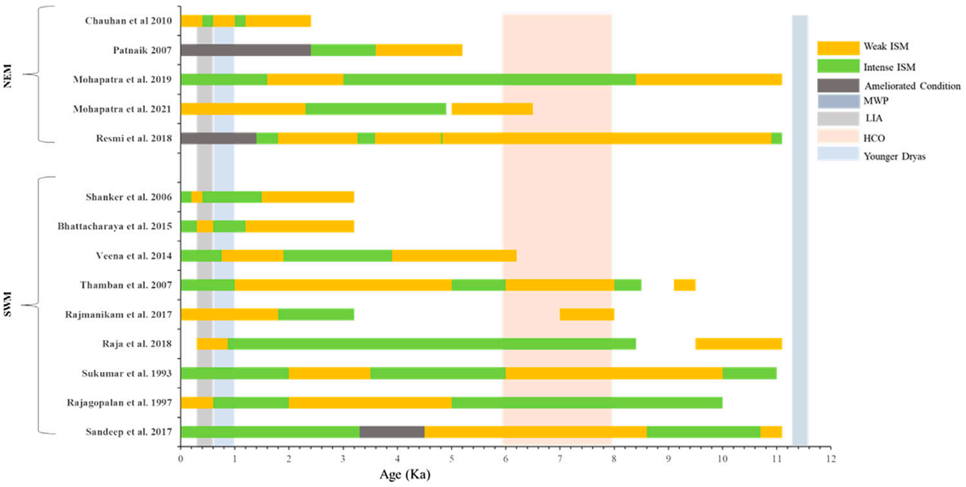

FIGURE 5 | Paleoclimate variability in Southern Peninsular India during Holocene.

Southwest monsoon paleo-records from the other part of the Indian subcontinent are also characterized by decreasing monsoonal precipitation during the mid-Holocene. Eventhough the records reveals that during the mid-Holocene, the monsoon precipitation was waning, a few climate records show an increasing trend in monsoon strength (Prasad and Enzel, 2006; Staubwasser and Weiss, 2006). Construction of man-made dams, ponds, and other structures along the slope of the river or on tributary courses allowed water to be stored during the drier periods of the SWM-dominated regions. Around 5 ka, archaeological evidence indicates that local populations were affected, and providing alternatives to rice which was the main staple, alternative development of tilling-based agriculture caused a surge in sedimentation rates near the foot of the continental slope in the Arabian Sea. It is striking that the change in sedimentation rates roughly corresponds to the early Bronze Age's significant cultural shifts and massive population migrations (Gourlan et al., 2020).

According to speleothem studies conducted by Fleitmann et al. (2007), the ITCZ migrated southward during the middle to late Holocene, and monsoon precipitation decreased gradually in response to decreased solar insolation; the same trend is also evident from the Indian and East Asian monsoon areas. Regardless of the fact that all monsoon records reveal unexpected and extreme monsoon events, they are short and dramatically superimposed on the consistent pattern of decreasing monsoon precipitation during mid- Holocene.

Meghalayan Stage (Late Holocene)

The high Corg/N ratio during 4.5–3.3 ka indicates a constant shift from plankton-dominated deep-water environments to entirely terrestrial vegetation as observed in the Shanti Sagara Lake. The paleomonsoon records of the Shanti Sagara Lake indicate a fluctuating monsoon condition from the beginning of late Holocene and decreasing trend from 4.5 ka, which corresponds to the 4.2 ka cold aridity event (Sandeep et al., 2017) (**Figure 3** and **Table 1**). In Kukkal Lake, an increase in the intensity of chemical weathering, together with enhanced preservation of arboreal pollens and ferns, suggests a period of increasing rainfall during late Holocene ~3.5 ka (**Figure 3**). Subsequently, a decrease in the sand deposition at ~1.7 ka and replacement of forest vegetation largely by grasslands point towards a rapid increase in SWM intensity during this period. This is further corroborated by the establishment of Shola Forest during 3.5–1.70 ka (Rajamanikam et al., 2016) (**Figure 3**). Veena et al. (2014) noticed an increase of evergreen and semi-evergreen pollen taxa like *Apocynaceae*, *Arenga*, *Artemisia* (2.6%), and *Calophyllum* (2.5%) and an increase of panicoid, chloridoid, and festucoid suggesting a wet climate phase during 1.4–0.760 ka (**Figure 3**). Bhattacharyya et al. (2015) suggest that the significant high X_{lf} along with high influx of sand and low influx of clay in Pookot Lake during 3.1–2.5 ka indicate high precipitation during this period. Pookot Lake also indicates an overall dry period during 2.5–1 ka, with a brief episodes of intense monsoon as indicated by a rise in X_{lf}, sand deposition, and a reduction in clay content. The high-rainfall environments in Pookot Lake from 1 to 0.5 ka enhanced the growth of vegetation, which resulted in increased pollen formation and preservation; this time period is most likely the Medieval Warm Period (MWP) in Pookot Lake. The 0.6–0.3 ka period is marked by lower Xlf values, possibly indicating LIA with a cold and arid climate. Pookot Lake witnessed substantial rainfall during the MWP and low rainfall during the LIA, the SWMR becomes more intense after the LIA (Bhattacharyya et al., 2015). Shankar et al. (2006) marked that aridity conditions prevailed between 1.55 and 2.5 ka in the Nilgiris region, while an intense SWMR is noted at ~1.7 ka BP (Raja et al., 2018b). Rajagopalan et al. (1997) noted the abundance of C_3 plants in the Sandynallah Basin, Nilgiris, while the lake sediment samples from Parsons Valley Lake indicate a period of weakened SWM.

Along the Kerala–Konkan Coast during the beginning of the late Holocene period, ~4 Ka, a decline in the distribution of the mangrove pollen, especially of *Cullenia exarillata*, and decrease in the organic matter content signifies an intense arid conditions (Kumaran et al., 2005) (**Table 1**). Recent studies carried out on mangrove vegetation from Northern Konkan suggest a reduced rainfall and drier climatic conditions (Limaye and Kumaran, 2012) in the late Holocene period (**Figure 3**).

Yadaava et al. (2004) noted that the stalagmite deposit of Akalagavi Cave shows an enrichment of $\delta^{18}O$ values that indicate a deficient in rainfall events (which occurred during the years AD 1982, 1979, 1941, 1925, 1918, 1915, 1905, 1899, 1877, 1854, 1777, and 1796), and a depletion of $\delta^{18}0$ designate an excess rainfall event (AD 1988, 1975, 1961, 1956, 1953, 1917, 1910, 1894, 1893, 1884, 1878, and 1664). The records shows that all deficient and excess rainfall years can be linked to countrywide rainfall as well as that the same extreme events occurring across the country (**Figure 2B**).

From the decadal averages, the SWMR shows a significant trend of increasing rainfall. From 1813–1820 to 1911–1920, there were 25 deficit years against 11 surplus years, but upto 2006 (86 years), there were 16 surplus years against seven deficit years, suggesting a trend of increasing rainfall than deficit. According to Verma and Bhatla (2021), the interannual variation in SWMR precipitation has been linked to El Nino in recent years, and this had a significant impact on the Eastern Ghats in the southern peninsular region. During the La Nina years, however, SWMR rainfall variation from the mean was large in the southern peninsular region. As a result of this, future flooding situation in the aforementioned places can be linked to the recurring and prolonged occurrences of La Nina events. Hari et al. (2020) suggested an increase in SWMR since 2002 because of the variations in the dynamics of the ITCZ that propagated northward since 2002.

North-East Monsoon (NEMR)

Greenlandian Stage: Greenlandian Stage (Early Holocene): Resmi and Achyuthan (2018) studied the Palar River paleochannel sediments to reconstruct NEMR variability over the Southern Indian Peninsular spanning the Holocene period (**Figure 1**). It is observed that during the Early Holocene period ~10 ka, a decrease in CWI values and higher CIA, Rb/Sr ratio of sediments indicate an enhanced NE monsoonal precipitation (**Figure 4**). During 10 to 4.83 ka suggests an increase in CWI values along with a decline in CIA values, and Rb/Sr ratio, pointing a decrease in rainfall in this period. However, some short pulses of enhanced NEM were also reported during this period (Resmi et al., 2017). Pollen data from the Cauvery delta sediments reveals that deposition occurred in a sub-aerial environment at the bottom of deltaic incised valleys between 11 and 9.3 ka (Mohapatra et al., 2021) (**Table 1**). This reveals that sea level was advanced during the LGM, as the region was 19 and 13 m below current mean sea level. From 9.3 to 6.5 ka, a rapid transgression occurred in this area, pushing the coastline 10 km inland.

Northgrippian Stage (Mid Holocene): During ~7.3 ka SE coast of India witnessed high stand sea level recorded from the emerged coral colony at Rameswaram (Banerjee, 2000). Later on, ~6.5 to 5 ka mangroves had established in the nearby region might be due to stabilization of sea-level. Subsequently, an increase in NEMR precipitation is noted during ~5.1 ka-2.5 ka from the high abundance of Poaceae, Cyperaceae along with the occurrence of aquatic taxa. Significant increase in CaO/MgO and CWI value are observed during 4.8-3.59 ka from the Palar River and its paleochannels implies a progressive rise in the precipitation. This inference is substantially corroborated by low Rb/Sr and Ba/Sr ratios (Resmi and Achyuthan, 2018).

Meghalayan Stage (Late Holocene): Resmi and Achyuthan (2018) noted a fluctuation in elemental concentrations with high sand percentage, Rb/Sr, K/Al, Ti/Al ratios and Lower CaO/MgO ratios during 3.59-3.26 ka indicating a rise in NEMR precipitation during this period. The period from 3.26 to 1.88 ka shows a significant decrease in elemental ratios of CaO/MgO, Ti/Al, CWI, and CIA values that indicate a reducing trend of NEMR. During 3.5 ka period, Srivastava et al. (2011) observed a decline in the abundance of thecamoebians studied from the Pichavaram Estuary (**Figure 4**). This was accompanied with significant tidal input from the Bay of Bengal and freshwater intake from the inland, indicating an increase in the monsoon conditions. This is further corroborated by smectite/kaolinite and Lower $_{10}$Be content in Kaluveli Lake representing a semi-arid to humid climate around 3.4 kyrs and humid to present day semi-arid conditions at ~2.24 ka (Patnaik, 2009; **Figure 4**). Chauhan et al. (2010) inferred that high contribution of chlorite and kaolinite into the Bay of Bengal during NEMR. Hence an enhanced flux of chlorite and reduced K/C ratio indicate a high monsoon precipitation during 2.2-1.8 ka, ~1 ka, ~0.45 ka-0.6 ka. Likewise, a weakening of NEMR is noted from 1.8-1.1 ka BP to 1.44 ka (**Figures 4**, **5**).

Only a few studies have been conducted around the globe to reconstruct the NEMR (winter) monsoon. Using chemical, biological, mineralogical, and physical proxies in coastal sediments from the Panama, Okanda, and Kirinda estuaries, Ranasinghe et al. (2013) noticed that intervals from >7.3 to 6.75, 4 to 3, 1.1 to 0.5 ka were marked by decreased NEMR, a short-wet interval around 6.5–6.25 ka, and a semi-arid interval between 6.25 and 4.6 ka were marked by decreased NEMR (**Figure 4**).

The decrease in NEMR intensity has a significant influence on paddy farming, mainly in the Cauvery delta. The Grand Anicut, also known as Kallanai, is a historic dam that spanning the Cauvery River in Srirangam in the Thiruchirapalli District. During the Sangam period (Singh, 2003; Hill, 2008), the dam was built to manage water for paddy agriculture and irrigation during the reign of Chola king Karikalan (c. 100 BC–c. 100 AD). It is India's oldest and still operational water-regulator construction. With the reduction in NEMR during the Pallava period in the 9th and 10th centuries AD, the region around Chennai, Kanchipuram, and Chengapttu witnessed warmer conditions (1000 AD). Further, the impacts of rainfall on the Chola Kingdom's wealth and prosperity (850–1280 ce) can correlate well with the Medieval Warm Period. However, instrumental and proxy climate data reveal that recurring El Nino-like events occurred between 850 and 1300 CE, which can be linked to a rise in NEMR, although SWMR suffered severe deficit during this time. The development of water harvesting infrastructure in the Chola Kingdom was concentrated in the NEMR-dominated area of southeastern India, with construction peaked during El Nino-dominated intervals. Because of the monumental architecture and proliferation of tanks in South India (**Figure 2C**), the Chola rulers are widely regarded as great supporters of culture, art, and architecture, and their dynasty is known as the 'Golden Age of Tanks' (Barah, 1996). Temple tanks were built to collect rainwater and supply it for home and agricultural use during the non-rainy season (Pandey et al., 2003; Ramachandran, 2006; Rajan, 2013; Meter et al., 2014). In addition to temple tanks, the Chola rulers favored the construction of multifunctional man-made lakes, also known as tanks, which were primarily used to collect runoff water for irrigation for example Veeranam Lake and Chembarambakkam Lake are two major man-made water bodies during the Chola period (Shanmugasundaram et al., 2017). Overall, the Chola's territory strengthened and adapted to the declining NEMR conditions. As a result, it can be concluded that the Chola Dynasty's water management system and infrastructure helped them to sustain extreme climatic conditions such as droughts and floods in the later part of its history.

The NEMR is connected to the ENSO and IOD ocean–atmospheric phenomena, and the variability of NEM rainfall reflects year-to-year change. NEMR rainfall variabilities reveals different period of high and low rainfall during the last two centuries. Furthermore, rainfall episodes near the tropical Indian Ocean be therefore a decade or more. As a result, there are no long-term trends in NEMR. In contrast, the variability of the Indian Ocean dipole moment (IODM) has shifted from a predominantly negative phase in previous decades to a predominantly positive phase in recent decades. The northeast monsoon activity is enhanced by the IODM's positive phase. Winds are converging in the positive phase of the anomalous flow pattern, indicating moisture transport from the southeast Indian Ocean and the Bay of Bengal to southern India. In the negative phase, however, winds diverge and moisture is moved away from the southern Indian subcontinent. A negative correlation between Indian NEM and the Southern Oscillation Index (SOI), as well as a positive relationship between NEM and El Niño, which is opposite of ENSO's relationship with Indian SWM rains. The anomalously warm SST in the western Indian Ocean, the cold SST in the eastern Indian Ocean, and the related large-scale convergence extending towards South India are all factors in the development of NEM rains during the positive dipole phase (Pattanaik and Mohapatra, 2017).

Overall, the NEMR and SWMR monsoon shows variability with important climatic events which demonstrates that the region's geographical positions have a considerable influence on monsoon strength (**Figure 5**). Furthermore, our review suffers from a lack of temporal data in many regions, particularly those experiencing NEMR. When comparing multiproxy data from various archives from different locations, there can be discrepancies in interpretation. It may be due to the sensitivity of the proxies used.

CONCLUSION

To get a comprehensive picture of climatic variations of SWMR and NEMR in southern peninsular India, we have considered all available terrestrial and marine records. SWMR paleoclimatic record shows a wet period in the early Holocene and a gradual decline in monsoon precipitation in the Mid-Holocene period. However, the NEMR reveals a rise in precipitation at the beginning of the Early Holocene, followed by a decrease in the Early Holocene period. The NEMR-dominated region experienced a significant increase in precipitation during the Mid Holocene. Then, SWMR indicates an overall wet phase with a few drier episodes in the late Holocene Period, but NEMR shows an overwhelming dry period with shorter wet phases, which corresponds with the demise of the chola dynasty. During intense NEMR; IODM and El Nino exhibits a positive correlation. However, NEM shows a opposite relation to Southern Oscillation which is opposite to the relation that ENSO exhibits with the SWM rainfall. Hence, we inferred that since Holocene an antiphase relationship has been existed between NEMR and SWMR as stated by Resmi and Achythan (2018).

The SWMR records suggest that the globally known climate event 'Younger Dryas', HCO, MWP and LIA is reported from Southern India also but not evident in all paleoclimatic records. NEMR records, on the other hand, reveals little evidence of major climatic events apart from the MWP. Since the region is experiencing both monsoon (mostly SWMR) though intensity is less, NEMR also plays a major role in especially in the SE part of India but most of the paleoclimate reconstruction record from this region is predominately considering SWMR influence not NEMR. Hence, the present study is pointing to the need of reconstructing high-resolution NEMR and SWMR records using a multi-proxy approach, and the role of monsoon in the demise of major dynasties has yet to be explored.

AUTHOR CONTRIBUTIONS

RM (corresponding author) has taken a leading role. Other authors also contributed significantly.

REFERENCES

Achyuthan, H., Nagasundaram, M., Gourlan, T. A., Eastoe, C., Ahmad, S. M., and Veena, M. P. (2014). Mid-Holocene Indian Summer Monsoon Variability off the Andaman Islands, Bay of Bengal. *Quat. Int.* 1e13. doi:10.1016/j.quaint.2014.07.041

Banerjee, P. K. (2000). Holocene and Late Pleistocene Relative Sea Level Fluctuations along the East Coast of India. *Mar. Geology* 167, 243–260. doi:10.1016/s0025-3227(00)00028-1

Banerji, U., Shaji, J., Arulbalaji, M., Vishnu, M., Dabhi, A. J., and Bhushan, R. (2021). Padmalal Mid-late Holocene evolutionary history and climate reconstruction of Vellayani lake, south India. *Quat. Int.* doi:10.1016/j.quaint.2021.03.018

Barah, B. C. (1996). *Traditional Water Harvesting Systems: An Ecological Economic Survey*. New Delhi: New Age International Limited.

Bhattacharyya, A., Sandeep, K., Misra, S., Shankar, R., Warrier, A. K., Weijian, Z., et al. (2015). Vegetational and Climatic Variations during the Past 3100 Years in Southern India: Evidence from Pollen, Magnetic Susceptibility and Particle Size Data. *Environ. Earth Sci.* 74, 3559–3572. doi:10.1007/s12665-015-4415-6

Caner, L., Seen, D. L., Gunnell, Y., Ramesh, B. R., and Bourgeon, G. (2007). Spatial Heterogeneity of Land Cover Response to Climatic Change in the Nilgiri highlands (Southern India) since the Last Glacial Maximum. *The Holocene* 17, 195–205. doi:10.1177/0959683607075833

Charney, J. G. (1969). The Intertropical Convergence Zone and the hadley Circulation of the Atmosphere. *Proc. Wmo/iucg Symp. Numer. Weather Predict. Jpn. Meteorol. Agency* III, 73–79.

Chauhan, O. S., Dayal, A. M., Basavaiah, N., and Kader, U. S. A. (2010). Indian Summer Monsoon Andwinter Hydrographic Variations over Past Millennia Resolved by clay Sedimentation. *Geochem. Geophys. Geosyst. Res. Lett.* 11, 12. doi:10.1029/2010gc003067

Chauhan, O. S., and Suneethi, J. (2001). 18 Ka BP Records of Climatic Changes, Bay of Bengal: Isotopic and Sedimentological Evidences. *Curr. Sci.* 81, 1231–1234.

Chen, J. a., Wan, G., Wang, F., Zhang, D. D., Huang, R., Zhang, F., et al. (2002). Environmental Records of Carbon in Recent lake Sediments. *Sci. China Ser. D-Earth Sci.* 45 (10), 875–884. doi:10.1360/02yd9086

Colin, C., Kissel, C., Blamart, D., and Turpin, L. (1998). Magnetic Properties of Sediments in the Bay of Bengal and the Andaman Sea: Impact of Rapid North Atlantic Ocean Climatic Events on the Strength of the Indian Monsoon. *Earth Planet. Sci. Lett.* 160, 623–635. doi:10.1016/s0012-821x(98)00116-2

Cronin, T. M., Vogt, P. R., Willard, D. A., Thunell, R., Halka, J., Berke, M., et al. (2007). Rapid Sea Level Rise and Ice Sheet Response to 8,200-year Climate Event. *Geophys. Res. Lett.* 34 (20), L20603. doi:10.1029/2007gl031318

Da Silva, A.-C., Whalen, M. T., Hladil, J., Koptikova, L., Chen, D., Spassov, S., et al. (2014). Application of Magnetic Susceptibility as a Paleoclimatic Proxy on Paleozoic Sedimentary Rocks and Characterization of the Magnetic Signal – IGCP-580 Projects and Events. *Episodes* 37 (2), 87–95.

Fleitmann, D., Burns, S. J., Mangini, A., Mudelsee, M., Kramers, J., Villa, I., et al. (2007). Holocene ITCZ and Indian Monsoon Dynamics Recorded in Stalagmites from Oman and Yemen (Socotra). *Quat. Sci. Rev.* 26, 170–188. doi:10.1016/j.quascirev.2006.04.012

Gourlan, T. A., Albarede, F., Achyuthan, H., and Campillo, S. (2020). The marine Record of the Onset of Farming Around the Arabian Sea at the Dawn of the Bronze Age. *Holocene* doi:10.1177/2F095968362090221810.1177/0959683620902218

Gupta, A. K., Anderson, D. M., and Overpeck, J. T. (2003). Abrupt Changes in the Asian Southwest Monsoon during the Holocene and Their Links to the North Atlantic Ocean. *Nature* 421, 354–357. doi:10.1038/nature01340

Gunnell, Y., Anupam, K., and Sultan, B. (2007). Response of the South Indian runoff-harvesting civilization to northeast monsoon rainfall variability during the last 2000 years: instrumental records and indirect evidence. The Holocene 17,2 (2007) pp. 207–215.

Hari, V., Villarini, G., Karmakar, S., Wilcox, L. J., and Collins, M. (2020). Northward Propagation of the Intertropical Convergence Zone and Strengthening of Indian Summer Monsoon Rainfall. *Geophys. Res. Lett.* 47, e2020GL089823. doi:10.1029/2020gl089823

Hill, C. (2008). *South Asia: An Environmental History*, 33. Santa Barbara: ABC-CLIO.

Juyal, N., Chamyal, L. S., Bhandari, S., Maurya, D. M., and Singhvi, A. K. (2004). Environmental Changes during Late Pleistocene in the Orsang

River basin, Western India. *J. Geol. Soc. India* 64, 471–479. doi:10.1016/j.palaeo.2004.07.017

Kale, V., Achyuthan, H., Jaiswal, M., and Sengupta, S. (2010). Palaeoflood Records from Upper Kaveri River, Southern India: Evidence for Discrete Floods during Holocene. *Geochronometria* 37, 49–55. doi:10.2478/v10003-010-0026-0

Kessarkar, P. M., Purnachadra Rao, V., Naqvi, S. W. A., and Karapurkar, S. G. (2013). Variation in the Indian Summer Monsoon Intensity during the Bølling-Ållerød and Holocene. *Paleoceanography* 28 (3), 413–425. doi:10.1002/palo.20040

Kumaran, K. P. N., Limaye, R. B., Nair, K. M., and Padmalal, D. (2008). Palaeoecological and Palaeoclimate Potential of Subsurface Palynological Data from the Late Quaternary Sediments of South Kerala Sedimentary Basin, Southwest India. *Curr. Sci.* 95, 515–526.

Kumaran, K. P. N., Nair, K. M., Shindikar, M., Limaye, R. B., and Padmalal, D. (2005). Stratigraphical and Palynological Appraisal of the Late Quaternary Mangrove Deposits of the West Coast of India. *Quat. Res.* 64, 418–431. doi:10.1016/j.yqres.2005.08.015

Kumaran, N. K. P., Padmalal, D., Nair, M. K., Limaye, R. B., Guleria, J. S., Srivastava, R., et al. (2014). Vegetation Response and Landscape Dynamics of Indian Summer Monsoon Variations during Holocene: An Eco-Geomorphological Appraisal of Tropical Evergreen Forest Subfossil Logs. *PLoS One* 9 (4), e93596. doi:10.1371/journal.pone.0093596

Laskar, A. H., Yadava, M. G., Ramesh, R., Polyak, V. J., and Asmerom, Y. (2013). A 4 Kyr Stalagmite Oxygen Isotopic Record of the Past Indian Summer Monsoon in the Andaman Islands. *Geochem. Geophys. Geosyst.* 14 (9), 3555–3566. doi:10.1002/ggge.20203

Limaye, R. B., and Kumaran, K. P. N. (2012). Mangrove Vegetation Responses to Holocene Climate Change along Konkan Coast of South-Western India. *Quat. Int.* 263, 114–128. doi:10.1016/j.quaint.2012.01.034

Meter, K. J. V., Basu, N. B., Tate, E., and Wyckoff, J. (2014). Monsoon Harvests: The Living Legacies of Rainwater Harvesting Systems in South India. *Environ. Sci. Technol.* 48 (8), 4217–4225. doi:10.1021/es4040182

Mishra, P. K. (2014). Late Quaternary climate variability in the Indian monsoon domain. PhD Thesis, Freie Universitt Berlin.

Mohapatra, P. P., Stephen, A., Prasad, S., and Anupama, K. (2021). Pollen based inference of Holocene Sea level changes, depositional environment and climatic history of Cauvery delta, Southern India, Catena 199, 105029. https://doi.org/10.1016/j.catena.2020.105029

Nagasundaram, M., Achyuthan, H., and Ahmad, S. M. (2014). Monsoonal Changes Inferred from the Middle to Late Holocene Sediments off Landfall Island, North Andaman. *Arab J. Geosci.* 7, 3513–3523. doi:10.1007/s12517-013-1010-6

Nair, K. M., Padmalal, D., Kumaran, K. P. N., Sreeja, R., Limaye, R. B., and Srinivas, R. (2010). Late Quaternary Evolution of Ashtamudi-Sasthamkotta lake Systems of Kerala, South West India. *J. Asian Earth Sci.* 37, 361–372. doi:10.1016/j.jseaes.2009.09.004

Neff, U., Burns, S. J., Mangini, A., Mudelsee, M., Fleitmann, D., and Matter, A. (2001). Strong Coherence between Solar Variability and the Monsoon in Oman between 9 and 6 Kyr Ago. *Nature* 411, 290–293. doi:10.1038/35077048

Padmalal, D., Kumaran, K. P. N., Nair, K. M., Baijulal, B., Limaye, R. B., and Mohan, S. V. (2011). Evolution of the Coastal Wetland Systems of SW India during the Holocene: Evidence from marine and Terrestrial Archives of Kollam Coast, Kerala. *Quat. Int.* 237 (1-2), 123–139. doi:10.1016/j.quaint.2010.12.021

Padmalal, D., Nair, K. M., Kumaran, K. P. N., Sajan, K., Mohan, S. V., Maya, K., et al. (2013). Climate and Sea Level Changes in a Holocene Bay Head Delta, Kerala, Southwest Coast of India. *Clim. Change Isl. Coastal Vulnerability*, 191–208. doi:10.1007/978-94-007-6016-5_13

Pandey, D. N., Gupta, A. K., and Anderson, D. M. (2003). Rainwater Harvesting as an Adaptation to Climate Change. *Curr. Sci.* 85 (1), 46–59.

Parthasarathy, B., Rupa Kumar, K., and Munot, A. A. 1993, Homogeneous Indian Monsoon Rainfall: Variability and Prediction. *Proc. Indian Acad. Sci. (Earth Planet. Sci.* 102 (1), 121–155.

Pattanaik, D. R., and Mohapatra, M. (2017). Active Northeast Monsoon over India during 2015 - an Assessment of Real-Time Extended Range Forecast. *Curr. Sci.* 112 (11), 2253–2262. doi:10.18520/cs/v112/i11/2253-2262

Pattanaik, J. (2009). *Sr Isotope and Geochemical Studies on Kaveri, Palar And Ponnaiyar Rivers, Southern India and 10Be Isotope Studies on Quaternary Sediments of Kaluveli Lake*. near Pondicherry, India. PhD Thesis: Pondicherry University.

Ponton, C., Giosan, L., Eglinton, T. I., Fuller, D. Q., Johnson, J. E., Kumar, P., et al. (2012). Holocene Aridification of India. *Geophys. Res. Lett.* 39 (3), n. doi:10.1029/2011gl050722

Prasad, S., Anoop, A., Riedel, N., Sarkar, S., Menzel, P., Basavaiah, N., et al. (2014). Prolonged Monsoon Droughts and Links to Indo-Pacific Warm Pool: a Holocene Record from Lonar Lake, central India. *Earth Planet. Sci. Lett.* 391, 171–182. doi:10.1016/j.epsl.2014.01.043

Prasad, S., and Enzel, Y. (2006). Holocene Paleoclimates of India. *Quat. Res.* 66, 442–453. doi:10.1016/j.yqres.2006.05.008

Prasad, S., Kusumgar, S., and Gupta, S. K. (1997). A Mid to Late Holocene Record of Palaeoclimatic Changes from Nal Sarovar: A Palaeodesert Margin lake in Western India. *J. Quat. Sci.* 12 (2), 153–159. doi:10.1002/(sici)1099-1417(199703/04)12:2<153:aid-jqs300>3.0.co;2-x

Prell, W. L., and Kutzbach, J. E. (1992). Sensitivity of the Indian Monsoon to Forcing Parameters and Implications for its Evolution. *Nature* 360, 647–652. doi:10.1038/360647a0

Raja, P., Achyuthan, H., Farooqui, A., Ramesh, R., Kumar, P., and Chopra, S. (2018b). Tropical Rainforest Dynamics and Paleoclimate Implications since the Late Pleistocene. India: Nilgiris. *Quat. Res.* doi:10.1017/qua.2018.58

Raja, P., Achyuthan, H., Geethanjali, K., Kumar, P., and Chopra, S. (2018a). Late Pleistocene Paleoflood Deposits Identified by Grain Size Signatures, Parsons Valley Lake, Nilgiris, Tamil Nadu. *J. Geol. Soc. India* 91, 517–644. doi:10.1007/s12594-018-0903-0

Rajagopalan, G., Sukumar, R., and Ramesh, R. (1997). Late Quaternary Vegetational and Climatic Changes from Tropical Peats in Southern India, an Extended Record up to 40,000 Years BP. *Curr. Sci.* 73, 60–63.

Rajan, P. (2013). Irrigation System, Water Management and Agrarian System in Southern Pennar valley under the Cholas. *Indian Streams Res. J.* 2 (12), 3–8.

Rajeevan, M., Unnikrishnan, C. K., Bhate, J., Niranjan Kumar, K., and Sreekala, P. P. (2012). Northeast Monsoon over India: Variability and Prediction. *Met. Apps* 19 (2), 226–236. doi:10.1002/met.1322

Rajmanickam, V., Achyuthan, H., Eastoe, C., and Farooqui, A. (2016). Early-Holocene to Present Palaeoenvironmental Shifts and Short Climate Events from the Tropical Wetland and lake Sediments, Kukkal Lake, Southern India: Geochemistry and Palynology. *Holocene* 27 (3), 404–417. doi:10.1177/0959683616660162

Ramachandran, K. (2006). *Third World Water Forum – Water and Cultural Diversity – 2003*. Tokyo: United Nations Educational Scientific and Cultural Organization, 113–130.

Ranasinghe, P., Ortiz, J., Smith, A., Griffith, E., Siriwardana, C., De Silva, S., et al. (2013). Mid- to late-Holocene Indian winter monsoon variability from a terrestrial record in eastern and southeastern coastal environments of Sri Lanka. *Holocene* 23, 945–960. doi:10.1177/0959683612475141

Rao Krishna, P. R., and Jagannathan, P. (1953). A Study of the Northeast Monsoon Rainfall of Tamilnadu. *Indian J. Meteorology Geophys.* 4, 22–43.

Rawat, S., Gupta, A. K., Sangode, S. J., Srivastava, P., and Nainwal, H. C. (2015b). Late Pleistocene-Holocene Vegetation and Indian Summer Monsoon Record from the Lahaul, Northwest Himalaya, India. *Quat. Sci. Rev.* 114, 167–181. doi:10.1016/j.quascirev.2015.01.032

Rawat, S., Gupta, A. K., Srivastava, P., Sangode, S. J., and Nainwal, H. C. (2015a). A 13,000 Year Record of Environmental Magnetic Variations in the lake and Peat Deposits from the Chandra valley, Lahaul: Implications to Holocene Monsoonal Variability in the NW Himalaya. *Palaeogeogr. Palaeoclimatol. Palaeoecol.* 440, 116–127. doi:10.1016/j.palaeo.2015.08.044

Resmi, M. R., Achyuthan, H., and Jaiswal, M. K. (2016). Middle to Late Holocene Paleochannels and Migration of the Palar River, Tamil Nadu: Implications of Neotectonic Activity. *Quat. Int.* 443, 211–222.

Resmi, M. R., and Achyuthan, H. (2018). Northeast Monsoon Variations during the Holocene Inferred from Palaeochannels and Active Channels of the Palar River basin, Southern Peninsular India. *The Holocene* 28 (6), 895–913. doi:10.1177/0959683617752839

Sandeep, K., Shankar, R., Warrier, A. K., Yadava, M. G., Ramesh, R., Jani, R. A., et al. (2017). A Multi-Proxy lake Sediment Record of Indian Summer Monsoon

Variability during the Holocene in Southern India. *Palaeogeogr. Palaeoclimatol. Palaeoecol.* 476, 1–14. doi:10.1016/j.palaeo.2017.03.021

Sandeep, S., Chandrasekar, A., and Dash, S. K. (2007). On the Prediction of Tropical Cyclones over the Indian Region Using a Synthetic Vortex Scheme in a Mesoscale Model. *Pure Appl. Geophys.* 164 (8-9), 1443–1463. doi:10.1007/s00024-007-0231-6

Saraswat, R., Naik, D. K., Nigam, R., and Gaur, A. S. (2016). Timing, Cause and Consequences of Mid-holocene Climate Transition in the Arabian Sea. *Quat. Res.* 86 (2), 162–169. doi:10.1016/j.yqres.2016.06.001

Sarkar, A., Ramesh, R., Somayajulu, B. L. K., Agnihotri, R., Jull, A. J. T., and Burr, G. S. (2000). High Resolution Holocene Monsoon Record from the Eastern Arabian Sea. *Earth Planet. Sci. Lett.* 177, 209–218. doi:10.1016/s0012-821x(00)00053-4

Sarkar, S., Prasad, S., Wilkes, H., Riedel, N., Stebich, M., Basavaiah, N., et al. (2015). Monsoon Source Shifts during the Drying Mid-holocene: Biomarker Isotope Based Evidence from the Core 'monsoon Zone' (CMZ) of India. *Quat. Sci. Rev.* 123, 144–157. doi:10.1016/j.quascirev.2015.06.020

Shankar, R., Prabhu, C. N., Warrier, A. K., Vijaya Kumar, G. T., and Sekar, B. (2006). A Multidecadal Rock Magnetic Record of Monsoonal Variations during the Past 3700 Years from a Tropical Indian Tank. *J. Geol. Soc. India* 68, 447–459.

Shanmugasundaram, J., Gunnell, Y., Hessl, A. E., and Lee, E. (2017). Societal Response to Monsoon Variability in Medieval South India: Lessons from the Past for Adapting to Climate Change. *Anthropocene Rev.* 4, 110–135. doi:10.1177/2053019617695343

Singh, V. P., and Ram Narayan, Y. (2003). *Water Resources System Operation: Proceedings of the International Conference on Water and Environment*, 508. Allied Publishers.

Singhvi, A. K., and Kale, V. S. (2010). Paleoclimate Studies in India: Last Ice Age to the Present. *Indian Natl. Sci. Acad. IGBP-WCRP-SCOPE-Report Ser.* 4.

Srivastava, J., Farooqi, A., and Hussain, S. (2011). Ecological Changes in Pichavaram Estuary during the Last 4 Millennium. *Int. J. Geology Earth Environ. Sci.* 1, 18–26.

Srivastava, J., Farooqui, A., and Hussain, S. M. (2012). Vegetation History and Salinity Gradient during the Last 3700 Years in Pichavaram Estuary, India. *J. Earth Syst. Sci.* 121 (5), 1229–1237. doi:10.1007/s12040-012-0215-5

Staubwasser, M., Sirocko, F., Grootes, P. M., and Erlenkeuser, H. (2002). South Asian Monsoon Climate Change and Radiocarbon in the Arabian Sea during Early and Middle Holocene. *Paleoceanography* 17, 15–21. doi:10.1029/2000PA000608

Staubwasser, M., Sirocko, F., Grootes, P. M., and Segl, M. (2003). Climate Change at the 4.2 Ka BP Termination of the Indus valley Civilization and Holocene South Asian Monsoon Variability. *Geophys. Res. Lett.* 30 (8). doi:10.1029/2002gl016822

Staubwasser, M., and Weiss, H. (2006). Holocene Climate and Cultural Evolution in Late Prehistoric-Early Historic West Asia. *Quat. Res.* 66 (3), 372–387. doi:10.1016/j.yqres.2006.09.001

Sukumar, R., Ramesh, R., Pant, R. K., and Rajagopalan, G. (1993). A δ13C Record of Late Quaternary Climate Change from Tropical Peats in Southern India. *Nature* 364, 703–706. doi:10.1038/364703a0

Sun, Y., Ding, Y., and Dai, A. (2010). Changing Links between South Asian Summer Monsoon Circulation and Tropospheric Land-Sea thermal Contrasts under a Warming Scenario. *Geophys. Res. Lett.* 37, L02704. doi:10.1029/2009gl041662

Thamban, M., Kawahata, H., and Rao, V. P. (2007). Indian Summer Monsoon Variability during the Holocene as Recorded in Sediments of the Arabian Sea: Timing and Implications. *J. Oceanogr.* 63, 1009–1020. doi:10.1007/s10872-007-0084-8

Thamban, M., Purnachandra Rao, V., Schneider, R. R., and Grootes, P. M. (2001). Glacial to Holocene Fluctuations in Hydrography and Productivity along the Southwestern continental Margin of India. *Palaeogeogr. Palaeoclimatol. Palaeoecol.* 165 (1-2), 113–127. doi:10.1016/s0031-0182(00)00156-5

Trauth, M. H., Deino, A. L., Bergner, A. G. N., and Strecker, M. R. (2003). East African Climate Change and Orbital Forcing during the Last 175 Kyr BP. *Earth Planet. Sci. Lett.* 206, 297–313. doi:10.1016/s0012-821x(02)01105-6

Veena, M. P., Achyuthan, H., Eastoe, C., and Farooqui, A. (2014). A Multi-Proxy Reconstruction of Monsoon Variability in the Late Holocene, South India. *Quat. Int.* 325, 63–73. doi:10.1016/j.quaint.2013.10.026

Verma, S., and Bhatla, R. (2021). Performance of RegCM4 for Dynamically Downscaling of El Nino/La Nina Events during Southwest Monsoon over India and its Regions. *Earth Space Sci.* 10, 1029. doi:10.1029/2020EA001474

Walker, M. J. C., Berkelhammer, M., Björck, S., Cwynar, L. C., Fisher, D. A., Long, A. J., et al. (2012). Formal Subdivision of the Holocene Series/Epoch: a Discussion Paper by a Working Group of INTIMATE (Integration of Ice-Core, marine and Terrestrial Records) and the Subcommission on Quaternary Stratigraphy (International Commission on Stratigraphy). *J. Quat. Sci.* 27 (7), 649–659. doi:10.1002/jqs.2565

Wang, H., Liu, H., Liu, Y., and Cui, H. (2004). Mineral Magnetism of Lacustrine Sediments and Holocene Paleoenvironmental Changes in Dali Nor area, Southeast Inner Mongolia Plateau, China. *Palaeogeogr. Palaeoclim. Palaeoecol.* 208, 175–193.

Yadava, M. G., Ramesh, R., and Pant, G. B. (2004). Past monsoon rainfall variations in peninsular India recorded in a 331-year-old speleothem. *Holocene* 14, 517–524.

Conflict of Interest: The authors declare that the research was conducted in the absence of any commercial or financial relationships that could be construed as a potential conflict of interest.

Advantages of publishing in Frontiers

OPEN ACCESS

Articles are free to read
for greatest visibility
and readership

FAST PUBLICATION

Around 90 days
from submission
to decision

HIGH QUALITY PEER-REVIEW

Rigorous, collaborative,
and constructive
peer-review

TRANSPARENT PEER-REVIEW

Editors and reviewers
acknowledged by name
on published articles

Frontiers
Avenue du Tribunal-Fédéral 34
1005 Lausanne | Switzerland

Visit us: www.frontiersin.org
Contact us: frontiersin.org/about/contact

REPRODUCIBILITY OF RESEARCH

Support open data
and methods to enhance
research reproducibility

DIGITAL PUBLISHING

Articles designed
for optimal readership
across devices

FOLLOW US

@frontiersin

IMPACT METRICS

Advanced article metrics
track visibility across
digital media

EXTENSIVE PROMOTION

Marketing
and promotion
of impactful research

LOOP RESEARCH NETWORK

Our network
increases your
article's readership